Double helicity asymmetry for π^0 production in polarized $p+p$ collisions at $\sqrt{s} = 200$ GeV : Implications for the polarized gluon distribution in the proton

Yoshinori Fukao

A Dissertation Submitted in Partial Fulfillment of
the Requirements for the Degree of
Doctor of Science

Department of Physics
Kyoto University

September, 2007

Abstract

We present a measurement of the double helicity asymmetry A_{LL} in neutral pion (π^0) production in proton-proton (pp) collisions at the center-of-mass energy of 200 GeV. Since it was revealed by polarized deep-inelastic scatterings (DIS) that quarks and antiquarks in a proton carry only one-quarter of the proton spin, it is one of the major interests in the study of the proton structure to investigate the gluon contribution to the proton spin. In pp collisions, the gluon can directly participate in the interaction unlike DIS. For this reason, measurements with pp collision is one of the most promising methods to probe the contribution of the gluon spin to the proton spin, which is represented as Δg.

The measurement was performed in the PHENIX experiment with polarized proton beams in the Relativistic Heavy Ion Collider (RHIC) at Brookhaven National Laboratory (BNL) in the U.S. The measured kinematical region was 0.5 to 9.0 GeV/c in transverse momentum and -0.35 to 0.35 in pseudorapidity of π^0. In the experiment, photons from π^0 decay were detected by electromagnetic calorimeters located at the central region of the PHENIX detector. The results of A_{LL} were obtained using the integrated luminosity of 2.3 pb^{-1} accumulated during the data taking period in 2005. Average beam polarization was about 50 % for the selected events. The PHENIX experiment has already published π^0 A_{LL} using data of 2003 and 2004. Compared to these measurements, the statistics in this thesis is about 25 times larger in terms of figure-of-merit for A_{LL} and the measured p_T range is extended.

The measured A_{LL} is consistent with zero within the present experimental uncertainty. The accuracy of the measurement is dominated by the statistics, and the uncertainty is 0.0017 at 1.0 – 1.5 GeV/c and 0.0257 at 7.0 – 9.0 GeV/c in p_T. Our results of A_{LL} are compared to theoretical calculations with various Δg inputs and reject the case that the gluon spin is maximally polarized. Moreover, an interpretation from A_{LL} to Δg is discussed in this thesis. An analysis with a simple model unveiled that our measurement constrains the allowed region of Δg extracted in the past experiments by half in the measured region of Bjorken x. The result with the model is consistent with a calculation of a global analysis.

As well as A_{LL}, the single helicity asymmetry A_L and the double transverse-spin asymmetry A_{TT} are also measured and reported in this thesis. Both results are consistent with zero within uncertainty of the measurement and have agreement with a theoretical calculation.

Contents

Chapter 1

Introduction

1.1 Overview

Since ancient times, we human beings have been interested in what are constituents of materials and how they form the world. Ancient people guessed that materials consist of a few elements, such as fire, water and so on. In modern age, scientists thought that the constituents are chemical elements. However, it turned out that many kinds of elements are comprised of only electron, proton and neutron. Subsequently, experiments utilizing a cosmic ray or a particle accelerator unveiled that the proton and the neutron are only a part of hadrons. Similarly to the case of the chemical elements, the hadrons were expected to have substructure. The constituents of the hadrons, quarks, were proved by deep inelastic-scattering experiments. Currently, quarks and leptons are considered as the minimum unit of materials. Another important question is how the quarks and the leptons form materials. In the field theory, the interaction between particles is explained by exchange of a particle. While the atom is formed from the nuclei and the electrons mainly by the electromagnetic interaction, the main role in formation of the nucleon from the quarks, as well as the nuclei from the nucleons, is played by the strong interaction which is mediated by the gluon.

A particle has its own features, which include mass, momentum and charge. One of the most important and basic variable is spin. Based on a symmetry in spacial rotation, total angular momentum, sum of spin and orbital angular momentum, is conserved. Therefore, if a particle consists of some constituents, spin of the particle must be reconstructed from spin and orbital angular momentum of the constituents. The subject of this thesis is how the proton are formed in terms of the spin. In particular, we focus on the contribution from the gluon to the proton spin.

Since constituents of the proton were discovered, study of the proton structure was also that of the constituents, the quark and the gluon. The study was mainly carried out through electron-proton deep inelastic scattering (ep DIS). In the results, the constituents with electric charge, which are quarks, turn to be a point particle (so far) and have spin of one-half, while neutral ones, gluons, have spin of one. At the same time, study about how much each kind of quark carries momentum of the proton was performed. Consequently, it was revealed that about half of the proton momentum is carried by the quarks. It was proved that the rest of the proton momentum is carried by the gluons in cooperation with experiments with proton-antiproton collisions. In contrast, for the spin, the quarks were expected to carry the most of the proton spin because of great success of static constituent-quark model. In the model, the hadrons consist of two or three quarks and no gluons are considered. The model quite well explains magnetic moment of the hadrons, as well as the masses. However, contrary to the

expectation, it was unveiled by DIS experiments with polarized electron beam and polarized proton target that the quarks (and the antiquarks) carry only one-quarter of the proton spin. Currently, source of the rest of the proton spin is unknown.

The leading contribution in the *ep* scattering is the electromagnetic interaction. However, the gluon is neutral in the electromagnetic interaction. For this reason, it is difficult to probe the gluon in the proton in DIS experiments. One of the promising methods to study the gluon in the proton is proton-proton (*pp*) collisions. In the *pp* collisions, the gluon in a proton can interact with another quark or gluon in the other proton through the strong interaction. Hence, the gluon in the proton can be directly probed in *pp* collisions. The experiment in this thesis was performed with the PHENIX detector at RHIC (Relativistic Heavy Ion Collider) at BNL (Brookhaven National Laboratory) in the U.S. RHIC is a unique collider in the world which can accelerate polarized protons. The data were taken in proton-proton (*pp*) collisions with both beams polarized at the center-of-mass energy ($\sqrt{s}$) of 200 GeV. To apply pQCD (perturbative quantum chromodynamics), which describes the strong interaction at short distance, for comparison between the data and the theoretical calculation, it is important to achieve high $\sqrt{s}$. This experiment with $\sqrt{s} = 200$ GeV is expected to satisfy the requirement.

Especially, production of neutral pion (π^0) with high transverse momentum (p_T) in *pp* collisions is the interest of this thesis. Kinematical range of the measured π^0 was 0.5 to 9 GeV/c in p_T and -0.35 to $+0.35$ in pseudorapidity (η). The high p_T is also a requirement of pQCD. Typically, a few GeV/c is required. π^0 with high p_T is produced in hadronization of the scattered quark or gluon. The QCD subprocess for π^0 production is dominated by gluon-gluon scatterings at $p_T < 3$ GeV/c and gluon-quark scatterings at $3 < p_T < 15$ GeV/c, and contribution of quark-quark scatterings is small in the measured p_T range. For this reason, π^0 is an effective probe to investigate the gluon in the proton. As experimental advantages, π^0s are obtained with large statistics and easily identified by reconstructing the invariant mass from decay photons.

To extract the gluon contribution to the proton spin, the double helicity asymmetry A_{LL} in π^0 production ($A_{LL}^{\pi^0}$) in *pp* collisions with both proton beams polarized longitudinally was measured. $A_{LL}^{\pi^0}$ is defined as

$$\begin{aligned} A_{LL}^{\pi^0} &\equiv \frac{d\sigma_{++} - d\sigma_{+-} - d\sigma_{-+} + d\sigma_{--}}{d\sigma_{++} + d\sigma_{+-} + d\sigma_{-+} + d\sigma_{--}} \\ &\sim P_2 \left[\frac{\Delta g}{g}\right]^2 + P_1 \left[\frac{\Delta g}{g}\right] + P_0. \end{aligned} \tag{1.1}$$

Here $d\sigma_{h_1 h_2}$ is spin-dependent cross section of π^0. h_1 and h_2 denote helicities of the proton beams. Denominator of the first equation corresponds to the spin-independent cross section. The second equation is quite rough approximation. The gluon contribution to the proton spin is represented by Δg. Meanwhile, g indicates the unpolarized contribution of the gluon to the proton momentum. P_0, P_1 and P_2 include other factors, such as the quark contributions, the QCD subprocesses and the hadronization to π^0. In the approximation, $A_{LL}^{\pi^0}$ is written as a quadratic function of $\frac{\Delta g}{g}$. This indicates that π^0 is produced via the QCD subprocesses of gluon-gluon, gluon-quark and quark-quark scatterings (the term of P_2, P_1 and P_0, respectively).

The first measurement of $A_{LL}^{\pi^0}$ was carried out by E704 experiment at FNAL (Fermi National Accelerator Laboratory) with proton-proton and proton-antiproton collisions at $\sqrt{s} = 19.4$ GeV [1]. p_T range of the measurement was $1 < p_T < 4$ GeV/c. But, the experimental uncertainty was too large to constrain the gluon contribution to the proton spin. The E704 experiment was followed by the RHIC-PHENIX experiment. PHENIX published

$A_{LL}^{\pi^0}$ at $\sqrt{s} = 200$ GeV using the data accumulated during 2003 and 2004 [2, 3]. The data covered 1 to 5 GeV/c in p_T. However, the uncertainty was too large to obtain meaningful constraints.

The data of this thesis was taken in the 2005 run aiming for much improved statistics and better beam polarization. Integrated luminosity of 2.3 pb^{-1} was accumulated with average beam polarization of about 50 %. The integrated luminosity was about 8 times higher than that of the 2003 and 2004 runs. The polarization was improved by 5 % from the previous year. In terms of figure-of-merit for A_{LL}, about 25 times higher statistics were obtained in 2005 than the previous years. Owing to the higher statistics, the measured p_T range was extended up to 9 GeV/c.

In this chapter, theoretical basis and current experimental knowledge on PDF are introduced. First, notations and conventions used in this thesis are described in Section 1.2. In Section 1.3, currently known elementary particles which comprise the world is briefly introduced. The formalism about the structure of the nucleon is described in Section 1.4 and 1.5. Especially in Section 1.5, parton distribution function which is the main topic of this thesis is described. Theoretical tools to analyze pp collision are introduced in Section 1.6 for factorization theorem and Section 1.7 for fragmentation function. Following Section 1.8 is devoted to display the current experimental knowledge in the spin structure in the proton. Some theoretical predictions for the gluon contribution to the proton spin are introduced in Section 1.9. In Section 1.10, specific feature in the measurement of π^0 with pp collisions are described. In Section 1.11 and 1.12, experimental procedure to obtain A_{LL} and other asymmetries are explained.

Following this chapter, the experimental setup is explained in Chapter 2 and the analysis procedure is described in Chapter 3. In Chapter 4, the results of this thesis appears and some discussions are presented. Finally, the conclusion is in Chapter 5.

1.2 Notations and Conventions

In this thesis, following notations are adopted. Relativistic 4-vector is described with indices of Greek alphabet like v^μ, where μ takes 0, 1, 2 and 3. v^μ is often simplified as v. Classical 3-vector is described as $\vec{v}$. The metric tensor is described as $g^{\mu\nu}$ and defined as

$$g^{\mu\nu} = g_{\mu\nu} \equiv \begin{pmatrix} 1 & 0 & 0 & 0 \\ 0 & -1 & 0 & 0 \\ 0 & 0 & -1 & 0 \\ 0 & 0 & 0 & -1 \end{pmatrix}. \tag{1.2}$$

The totally antisymmetric tensor (Levi Civita tensor) $\varepsilon^{\mu\nu\alpha\beta}$ is defined as

$$\varepsilon_{0123} = -\varepsilon^{0123} = 1. \tag{1.3}$$

When indices are the same label, summation is taken for the indices. We adopt the natural units $c = \hbar = 1$, where c is the light velocity and $\hbar$ is the Plank constant divided by 2π.

1.3 Elementary particles

In our best knowledge, everything in the world consists of quarks and leptons. Presently, six kinds of quarks and six kinds of leptons are discovered. The kind of the quarks and leptons are usually named "flavor". Table 1.1 and 1.2 list the quarks and the leptons, respectively.

	Name	Spin	Electric charge	Mass (MeV/c^2)
d	(down)	1/2	$-1/3$	3 – 7
u	(up)	1/2	$+2/3$	1.5 – 3.0
s	(strange)	1/2	$-1/3$	95±25
c	(charm)	1/2	$+2/3$	1250±90
b	(bottom)	1/2	$-1/3$	4200±70
t	(top)	1/2	$+2/3$	174000±3300

Table 1.1: The quark family [4]. The electric charge is assigned in the unit of electron charge. The mass is not for "constituent quark", but "current quark", which appears in hard processes such as deep inelastic-scattering described in Section 1.4.2.

	Name	Spin	Electric charge	Mass (MeV/c^2)
e	(electron)	1/2	-1	0.511
ν_e	(electron neutrino)	1/2	0	$\sim$0
μ	(muon)	1/2	-1	106
ν_μ	(muon neutrino)	1/2	0	$\sim$0
τ	(tauon)	1/2	-1	1780
ν_τ	(tau neutrino)	1/2	0	$\sim$0

Table 1.2: The lepton family [4]. The electric charge is assigned in the unit of electron charge.

Interaction	Gauge particle	Spin	Electric charge	Mass (MeV/c^2)
Strong interaction	g (gluon)	1	0	0
Electromagnetic interaction	γ (photon)	1	0	0
Weak interaction	$W^\pm$, Z^0	1	±1, 0	80400, 91200
Gravity	graviton	2	0	0

Table 1.3: The interactions and the gauge particles [4]. The electric charge is assigned in the unit of electron charge. The graviton which carries the gravity is not discovered and the values in the table is the prediction.

Another important concept in the particle physics is the interaction between particles. Currently, four kinds of interactions are known. Table 1.3 lists the interactions and the gauge particles which mediate the interactions.[1] The gauge particles are experimentally observed except for the graviton. These interactions are related to their own charge; electric charge for the electromagnetic interaction, for example. The charge is not only the quantum number but its magnitude also governs strength of the interaction. The quarks are coupled with all 4 interactions, while the leptons are not coupled with the strong interaction since they do not have color charge which is related to the strong interaction. Gluons interact with each other through the strong interaction and it results in confinement of the quarks in hadrons. Similarly, there is the self-coupling in the weak and electromagnetic interaction, which appears as $W^{\pm} - Z^0$ and $W^{\pm} - \gamma$ interactions. The weak interaction has features that violate the parity conservation and change flavor of the quarks. The latter characteristic is useful to select quark flavor in reaction, such as neutrino scattering. The gravity is assumed to be coupled with energy. However, because strength of the gravity is negligibly small compared with other interactions, it is ignored in this thesis as in other usual literature.

Particles listed in Table 1.1, 1.2 and 1.3 have their own antiparticles, which have same characteristic and mass as the corresponding particles except for the charge. Similarly, composite particles from quarks also have the antiparticles; the antiproton for the proton, for example. Sometimes, the antiparticle is identical to the particle, such as photon. We often describe an antiparticle as a character with overbar; the proton and the antiproton are written as p and $\bar{p}$, for example.

Presently, the electromagnetic, strong and weak interactions, except the gravity, are described by the quantum field theory.[2] The theory of the electromagnetic interaction is called QED (quantum electrodynamics). Similarly, the theory for the strong interaction is named QCD (quantum chromodynamics). The weak interaction is incorporated into QED and the unified framework is referred to as the electroweak theory. QCD and the electroweak theory are collectively called the standard model of particle physics.

1.4 Form factor and structure function

In this section and the following sections, structure of the nucleon is discussed.[3] Because the proton and the neutron are doublet in the isospin symmetry, their structures are also related each other. Therefore, description in this thesis is basically for the proton, following the usual way in other papers.

1.4.1 Form factor

It is proved by electron-proton (ep) elastic scattering that the proton is not a point particle. If the proton is a point particle with spin $\frac{1}{2}$, cross section with electron beam and proton target can be immediately calculated based on QED,

$$\frac{d\sigma^{point}}{d\Omega} = \frac{\alpha^2}{4E^2 \sin^4 \frac{\theta}{2}} \frac{E'}{E} \left[\cos^2 \frac{\theta}{2} - \frac{q^2}{2M_p^2} \sin^2 \frac{\theta}{2} \right]. \tag{1.4}$$

[1] Gauge particle is also called gauge boson because its spin is integer. Meanwhile, quarks and leptons have the spin of half-integer and belong to fermion.

[2] The study of the quantum theory for the gravity is on going but no conclusive theory is established so far.

[3] For contents in this section and the following sections about the nucleon structure, several review articles such as [5–11] are used as reference.

Solid angle $d\Omega$ and scattering angle θ are for the scattered electron beam. E and E' are energy of the incident and the scattered electron beam, respectively. E' is uniquely determined by the kinematics; $E' = E\left[1 + \frac{2E}{M_p}\sin^2\frac{\theta}{2}\right]^{-1}$ with the proton mass M_p. $q \equiv k - k'$ is momentum transfer, where k and k' are 4-momentum of the incident and the scattered electron. $\alpha = \frac{e^2}{4\pi}$ is the coupling constant of the electromagnetic interaction (fine structure constant). The electron mass is ignored in Equation (1.4).

However, the conjecture of the point-like proton is rejected by measurements. To describe the finite-size proton, Equation (1.4) is modified by replacing the current for a Dirac particle as follows;

$$J^\mu = \bar{\psi}\gamma^\mu\psi \rightarrow \bar{\psi}\left[F_1^p(q^2)\gamma^\mu + \frac{\chi_p}{2M_p}F_2^p(q^2)i\sigma^{\mu\nu}q_\nu\right]\psi. \tag{1.5}$$

γ^μ is Dirac gamma matrix and $\sigma^{\mu\nu}$ is defined as $\sigma^{\mu\nu} = \frac{i}{2}(\gamma^\mu\gamma^\nu - \gamma^\nu\gamma^\mu)$. ψ is Dirac field with mass M_p. $\chi_p \sim 1.79$ is anomalous magnetic moment of the proton and the magnetic moment is described as $(1+\chi^p)\frac{e}{2M_p}$. In the case of a Dirac particle, χ is equal to 0. The parameterization of Equation (1.5) is a general form based on the Lorentz invariance and form factors F_1^p and F_2^p are functions of q^2.

Figure 1.1-left displays diagram of ep elastic scattering. Using Equation (1.5), cross section of ep elastic scattering is calculated. The well-known Rosenbluth's formula is obtained on the laboratory frame (rest frame of the target proton).

$$\frac{d\sigma^{ep,ela.}}{d\Omega} = \frac{\alpha^2}{4E^2\sin^4\frac{\theta}{2}}\frac{E'}{E}\left[2\tau {G_M^p}^2\sin^2\frac{\theta}{2} + \frac{{G_E^p}^2 + \tau {G_M^p}^2}{1+\tau}\cos^2\frac{\theta}{2}\right], \tag{1.6}$$

The electron mass is again ignored in Equation (1.6). τ is defined as $\tau = -\frac{q^2}{4M_p}$. G_E^p and G_M^p are so-called electric and magnetic form factor of the proton, respectively, and introduced for convenience to eliminate the interference term of F_1^p and F_2^p. Relations between F_1^p, F_2^p, G_E^p and G_M^p are

$$G_E^p \equiv F_1^p + \frac{\chi_p q^2}{4M_p^2}F_2^p, \qquad G_M^p \equiv F_1^p + \chi_p F_2^p. \tag{1.7}$$

G_E^p and G_M^p are closely related to distribution of electric and magnetic moment of the proton.[4] Comparing Equation (1.6) with Equation (1.4), G_E^p and G_M^p are constant and equal to 1 if the proton is a point particle. The measured G_E^p and G_M^p have q^2 dependence and $G_E^p(q^2) \sim \frac{G_M^p(q^2)}{1+\chi^p} \sim \left(1 - \frac{q^2}{0.71}\right)^{-2}$ is obtained. This result indicates that the proton is not a point particle. From G_E^p and G_M^p measured, charge distribution of the proton turns out to be an exponential function of its radius and the mean square radius is obtained to be $\sim$0.8 fm.[5]

1.4.2 Structure function

To investigate structure of the proton in more detail, larger momentum transfer squared[6] $(-q^2)$ is required. However, The scattering with large $-q^2$ results in destructing the proton;

[4] When $|\vec{k} - \vec{k'}| \ll M_p^2$, G_E^p and G_M^p become Fourier transform of distribution of the electric and the magnetic moment.

[5] Form factors for the neutron, G_E^n and G_M^n, have been also measured. The obtained relation is $G_M^n(q^2)/(1+\chi^n) \sim G_E^p(q^2)$, where $\chi^n \sim -1.91$. Measured G_E^n is not 0 and implies that the neutron has inner structure and its constituent has electric charge.

[6] In the electron scattering, q^2 is always negative.

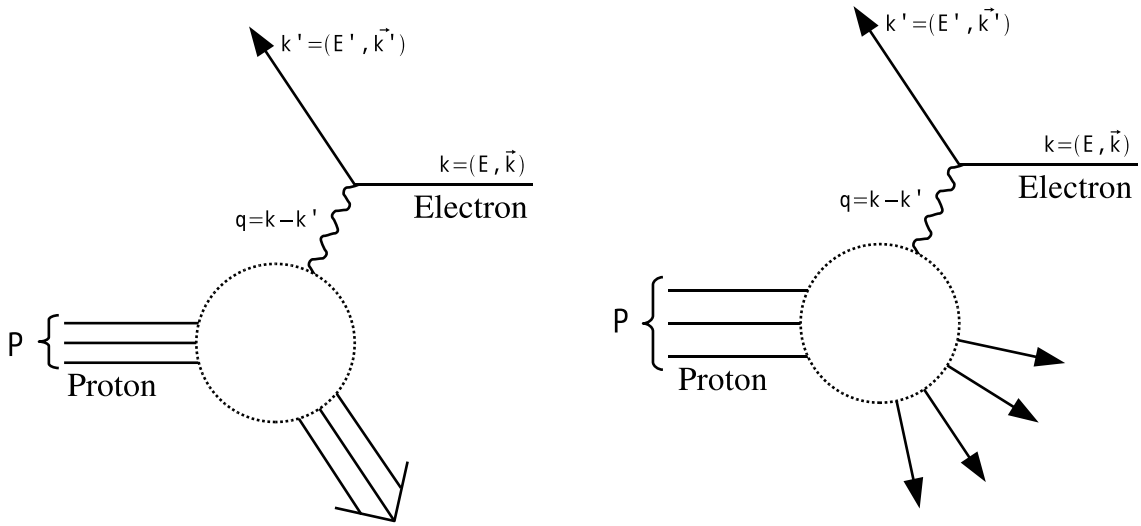

Figure 1.1: (Left) Diagram of ep elastic scattering. The final state of the target proton is still single particle described as a Dirac field. (Right) Diagram of ep inelastic scattering. The target proton is destructed by the scattering.

inelastic scattering. Therefore, formalization of the inelastic scattering is needed. Diagram of ep inelastic scattering is displayed in Figure 1.1. Because the current in Equation (1.5) is sandwiched by the Dirac field, it results in the process that both initial and final state are a proton (and an electron). To describe the inelastic scattering where the final state is no longer a proton, the calculation needs to be executed without parameterization like Equation (1.5). At the leading order, cross section of ep scattering is generally represented with the leptonic tensor $L^{\mu\nu}$ and the hadronic tensor $W^{\mu\nu}$ as follows;

$$\frac{d\sigma^{ep}}{dE'd\Omega} = \frac{\alpha}{q^4}\frac{E'}{E}L^{\mu\nu}W_{\mu\nu}. \tag{1.8}$$

The lepton part $L^{\mu\nu}$ is computable by QED and the leading term is

$$L^{\mu\nu} = 2(k^\mu k'^\nu + k'^\mu k^\nu - (kk' - m_e^2)g^{\mu\nu}) + 2im_e\varepsilon^{\mu\nu\alpha\beta}s_\alpha(k-k')_\beta, \tag{1.9}$$

where m_e is the electron mass and s^μ is spin vector of the incident electron. If the particle is an eigenstate of the helicity, the spin vector is defined as $s^\mu = h(\frac{|\vec{k}|}{m_e}, \frac{k^0\vec{k}}{m_e|\vec{k}|})$, where $h = \pm 1$ is the helicity. When the particle is relativistic, the spin vector becomes $m_e s^\mu \simeq hk^\mu$.

Since it is impossible (at least currently) to calculate the hadronic part $W_{\mu\nu}$ analytically, it is parameterized as is done in Equation (1.5). One can find out that $L^{\mu\nu}$ of the lepton part is divided into two parts, symmetric and asymmetric parts in an exchange of μ and ν. In consideration of this fact, $W_{\mu\nu}$ is divided into symmetric part $W^S_{\mu\nu}$ and asymmetric part $W^A_{\mu\nu}$ as

$$W_{\mu\nu} \equiv W^S_{\mu\nu} + W^A_{\mu\nu}. \tag{1.10}$$

The general form of $W_{\mu\nu}$ is written by the combination of the independent physics variables; 4-momentum P^μ and spin vector S^μ of the initial proton, and momentum transfer q^μ. In the rest frame of the proton, $S^\mu = (0, \vec{S})$, where $\vec{S}$ is direction of the proton spin with $|\vec{S}| = 1$.

Requiring the conservation of the current and the parity, $W^S_{\mu\nu}$ and $W^A_{\mu\nu}$ are written as follows;

$$W^S_{\mu\nu} = \left(-g_{\mu\nu} + \frac{q_\mu q_\nu}{q^2}\right) W_1(\nu, q^2) + \left(P_\mu - \frac{Pq}{q^2} q_\mu\right)\left(P_\nu - \frac{Pq}{q^2} q_\nu\right) \frac{W_2(\nu, q^2)}{M^2} \quad (1.11)$$

$$W^A_{\mu\nu} = i\varepsilon_{\mu\nu\alpha\beta} q^\alpha \left[M S^\beta G_1(\nu, q^2) + \Big((Pq)S^\beta - (Sq)P^\beta\Big) \frac{G_2(\nu, q^2)}{M} \right]. \quad (1.12)$$

M denotes the proton mass, where "p" in M_p is dropped for simplicity. W_1, W_2, G_1 and G_2 describe structure of the proton in the process of ep inelastic scattering.[7] These four structure functions are functions of two independent variables, ν and q^2, where ν is defined as $\nu = \frac{Pq}{M}$ and it is $\nu = E - E'$ on the laboratory frame.

Because the asymmetric part of Equation (1.9) is proportional to the spin vector of the incident electron, it disappears with unpolarized beam. At the same time, $W^A_{\mu\nu}$ for the proton part also disappears in Equation (1.8). Therefore, cross section with unpolarized beam on the laboratory frame is calculated to be

$$\frac{d\sigma^{ep}}{dE' d\Omega} = \frac{4E'^2\alpha^2}{Q^4} \left[2W_1 \sin^2\frac{\theta}{2} + W_2 \cos^2\frac{\theta}{2} \right], \quad (1.13)$$

where the positive variable $Q^2 = -q^2$ is used for convenience and the electron mass is ignored as usual. Meanwhile, to access G_1 and G_2, one need to measure spin dependent cross section. Instead of the cross section itself, difference of the spin dependent cross section is usually discussed.

$$\frac{d\Delta\sigma^{ep}}{dE' d\Omega} \equiv \frac{d\sigma^{ep}_{\rightarrow\Leftarrow}}{dE' d\Omega} - \frac{d\sigma^{ep}_{\rightarrow\Rightarrow}}{dE' d\Omega} = \frac{4\alpha^2}{Q^2}\frac{E'}{E} \Big[M(E + E'\cos\theta) G_1 - Q^2 G_2 \Big], \quad (1.14)$$

where subscripts of $d\sigma$ indicates the spin state of the incident electron and proton. $\rightarrow$ ($\leftarrow$) denotes positive (negative) helicity of the electron, and $\Rightarrow$ ($\Leftarrow$) indicates that the proton spin is parallel (antiparallel) to the momentum of the incident electron beam. Because the parity is conserved in the electromagnetic interaction, other two spin combinations are identical to those in Equation (1.14); $d\sigma^{ep}_{\leftarrow\Rightarrow} = d\sigma^{ep}_{\rightarrow\Leftarrow}$ and $d\sigma^{ep}_{\leftarrow\Leftarrow} = d\sigma^{ep}_{\rightarrow\Rightarrow}$. Again, Equation (1.14) is on the proton rest frame and the electron mass is ignored.

Equation (1.13) and (1.14) make it possible to analyze the inelastic scattering and it turns out that measurement of the unpolarized cross section and the difference of the spin-dependent cross section can determine the structure functions W_1, W_2, G_1 and G_2. With large Q^2 and ν, the ep scattering can gain information about constituents of the proton. The limit of $Q^2, \nu \rightarrow \infty$ with $\frac{Q^2}{2M\nu}$ fixed is called the Bjorken limit and ep scattering at the limit is called deep inelastic scattering (DIS). We will see clearly in Section 1.5.1 that the ratio $\frac{Q^2}{2M\nu}$ is momentum fraction of the constituent to that of the proton. For convenience, following dimensionless structure functions are often used in literature.[8]

$$F_1 = MW_1, \quad F_2 = \nu W_2, \quad g_1 = M^2\nu G_1, \quad g_2 = M\nu^2 G_2 \quad (1.15)$$

As described in the following sections, these functions are directly related to spin-independent and dependent momentum distribution of the constituents of the proton; quarks and gluons. Note that F_1 and F_2 in Equation (1.15) are not relevant to those in Equation (1.5).

[7] In process where the weak interaction plays a main role, such as neutrino scattering, additional terms are included in $W_{\mu\nu}$ which violate the parity conservation.

[8] Actually, the definition of W_1, W_2, G_1 and G_2 is different depending on papers. However, F_1, F_2, g_1 and g_2 seems to be universal.

1.5 Parton distribution function

Quarks are originally introduced to categorize many hadrons observed. Each quark carries various quantum numbers such as spin, charge, isospin, strangeness, etc., depending on its flavor. Hadrons are described as combination of quarks and the quantum numbers of hadrons are calculated from the quantum numbers of quarks forming the hadron. Baryons including proton and neutron consist of three quarks and mesons including pions and kaons consist of a pair of quark and antiquark. This simple model (constituent quark model) has been developed based on flavor-SU(3) symmetry of the light quarks; u, d and s quarks. Incorporating color-SU(3) symmetry, the model successfully categorizes hadrons, but it is not only for the categorization. Though the flavor-SU(3) is not an exact symmetry, it is approximately well satisfied due to small difference in mass of these three quarks. Owing to this feature, the model successfully explains various physics observables of hadrons, for example, mass and magnetic moment. However, it should be remarked that the model cannot explain everything completely.

In the constituent quark model, hadrons are understood by only two or three constituent quarks. In fact, however, creation and annihilation of quarks and gluons continuously happen in the hadrons; quarks radiate or absorb gluons, a gluon converts into a pair of quark and antiquark, and a quark antiquark pair evaporates into a gluon. What is proved by DIS process is such a dynamic "parton" (quarks and gluon) rather than the static constituent quarks. Therefore, it is possible that strange quarks, antiquarks or gluons contribute to the property of the proton which is described by uud quarks in the constituent quark model. Quarks which carry the quantum numbers of hadrons are named "valence quark", while quark and antiquark pairs generated by pair creation are named "sea quark". The values of the quark mass in Table 1.1 is for quarks observed in processes such as DIS. In contrast, the mass of u, d and s quark in the constituent quark model is $\sim$300, $\sim$300, $\sim$500 MeV/c^2, which is interpreted as that including effect of interaction between the quarks.

The discussion is advanced to understand constituent of the proton as parton. In this section, the parton distribution function is introduced in the model where motion of the partons in the proton is collinear and the interaction between partons are ignored.[9] Then, the interaction between partons are discussed in Section 1.5.4. To examine the framework on the basis of the parton and understand the structure of the proton by measurement, several types of experiments have been carried out, including DIS, e^+e^- collision and pp collision. To summarize various kinds of data, it is necessary to perform "global analysis". In the following subsections, theoretical tools to describe such physics processes are introduced. Present experimental knowledge is summarized in Section 1.8.

1.5.1 Unpolarized parton distribution function

When Q^2 becomes larger in DIS, the scattering seems to occur between the electron and a single parton in the proton. Figure 1.2 displays the diagram of ep inelastic scattering with this view. At the leading order, interaction between partons is ignored. It means that the parton corresponds to quark which carries electric charge in this approximation. We assume

[9] Some higher order effects such as higher-twist are discussed in [12].

that the parton in the proton carries fraction x of the proton momentum.

$$\begin{array}{ccc} & \text{Proton} & \text{Parton} \\ \text{Momentum} & P^\mu & p^\mu = xP^\mu \\ \text{Transverse momentum} & P_T = 0 & p_T = 0 \\ \text{Mass} & M & m = xM \end{array} \tag{1.16}$$

p^μ and m is 4-momentum and mass of the parton. Transverse momentum is defined as component of the momentum perpendicular to the direction of the proton's motion. When the proton with momentum $\vec{P}$ is moving along the z-axis, transverse momentum of the parton is $p_T = \sqrt{p_x^2 + p_y^2}$. Though it is strange that mass of the parton depends on the momentum fraction x in Equation (1.16), the discussion here is correctly verified on the system with infinite proton momentum, where mass of the proton and parton becomes vanishingly small and therefore p_T from such a proton also becomes negligible.

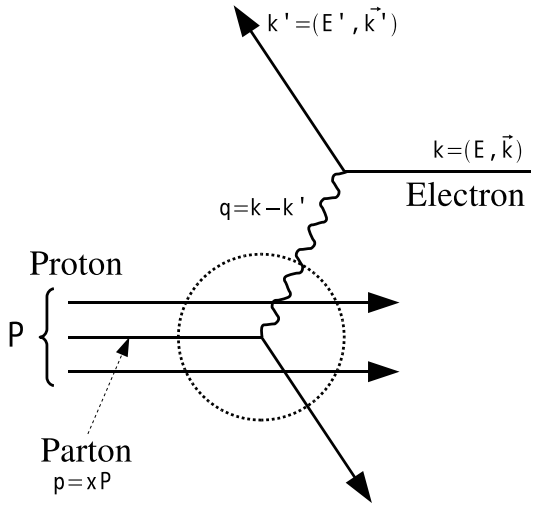

Figure 1.2: Diagram of ep inelastic scattering. It is assumed that the electron beam is scattered by a single parton in the proton. Interaction between partons is ignored in this approximation.

The structure function F_1 and F_2 in Equation (1.15) is related to the momentum distribution of the parton, $q(x)$, which is referred to as (unpolarized) "parton distribution function" (PDF). $q(x)dx$ is defined as the probability that quark with flavor q and momentum fraction x to $x+dx$ is observed in the scattering. Similarly, PDF for the gluon in the proton is defined as $g(x)$ and PDF for antiquark is $\bar{q}(x)$. By definition, sum of the parton momentum results in the proton momentum;

$$\int_0^1 x \left[\sum_q \Big(q(x) + \bar{q}(x) \Big) + g(x) \right] dx = 1. \tag{1.17}$$

In addition, because the quantum number of the proton is carried by uud constituent quarks, following equations are satisfied;

$$\int_0^1 \left[u(x) - \bar{u}(x) \right] dx = 2, \quad \int_0^1 \left[d(x) - \bar{d}(x) \right] dx = 1, \quad \int_0^1 \left[s(x) - \bar{s}(x) \right] dx = 0. \tag{1.18}$$

Though it is a little forceful, cross section of scattering between electron and parton in the proton is written on the proton rest frame as

$$\frac{d\sigma^{parton}}{dE'd\Omega} = \frac{4E'^2\alpha^2 e_q^2}{Q^4}\left[\frac{1}{M}\sin^2\frac{\theta}{2} + \frac{x}{\nu}\cos^2\frac{\theta}{2}\right]\delta\left(x - \frac{Q^2}{2M\nu}\right), \tag{1.19}$$

where e_q is electric charge of the parton in unit of the electron charge and summarized in Table 1.1. $\delta(x)$ is Dirac delta function. One can obtain Equation (1.4) by substituting $x = 1$ and $e_q = 1$, and integrating Equation (1.19) over E'. Assuming that cross section of ep scattering is described as superposition of the parton's cross section Equation (1.19), it is written as

$$\frac{d\sigma^{ep}}{dE'd\Omega} = \sum_{q,\bar{q}}\int_0^1 q(x)\frac{d\sigma^{parton}}{dE'd\Omega}dx. \tag{1.20}$$

Sum is computed for both quarks and antiquarks. One must remember that the reaction is in the Bjorken limit of $Q^2, \nu \to \infty$ to describe ep scattering as Equation (1.20). By comparing Equation (1.20), Equation (1.13) and Equation (1.15), the relation between F_1, F_2 and $q(x)$ is obtained.

$$F_1(\nu, Q^2) = \frac{1}{2x}F_2(\nu, Q^2) = \frac{1}{2}\sum_{q,\bar{q}} e_q^2 q(x), \qquad x = \frac{Q^2}{2M\nu}. \tag{1.21}$$

Because the reaction process is practically elastic scattering between an electron and a parton, momentum of the initial parton is kinematically determined by ν and Q^2 as described in Equation (1.19) as delta function. By definition, $0 \leq x \leq 1$ must be satisfied and it is also assured in Equation (1.21) by the kinematics. In this naive parton model, F_1 and F_2 are related each other (Callan-Gross relation) and the relation is confirmed by experiments at SLAC (the figure is found in [13]). At the same time, the confirmation of the relation means that the parton is a point particle with spin $\frac{1}{2}$ because the relation is satisfied when the parton is a Dirac particle.

Another important conclusion of Equation (1.21) is a scaling feature of F_1 and F_2. In general, F_1 and F_2 are functions of ν and Q^2. However, from Equation (1.21), they are only a function of $x = \frac{Q^2}{2M\nu}$. Therefore, when x is fixed, F_1 and F_2 is independent of Q^2. This feature is so-called Bjorken scaling and x is named the Bjorken scaling variable or simply Bjorken x. In fact, the scaling is proved by measurements except for small Q^2 dependence as displayed in Figure 1.6. The violation of the Bjorken scaling does not indicate substructure of the parton, but higher order effect such as interaction between partons, which is described in Section 1.5.4.

1.5.2 Polarized parton distribution function

To describe spin-dependent reaction such as Equation (1.14), unpolarized PDF needs to be extended to spin-dependent PDF. Spin-dependent PDF is defined as $q_H^h(x)$, where H and h denote helicity of the proton and that of the parton in the proton. In similar way to unpolarized PDF, $q_+^+(x)dx$ means the probability that in the scattering one observes the quark with flavor q, momentum fraction x to $x + dx$ and positive helicity in the proton with positive helicity. It's same for the gluon. It is easy to derive equations

$$q_+^+(x) = q_-^-(x), \qquad q_+^-(x) = q_-^+(x) \tag{1.22}$$

by Lorentz transformation (or one may imagine the proton rest frame). Obviously, unpolarized PDF is obtained by combine spin-dependent PDF as $q(x) = q_+^+(x) + q_+^-(x)$. Instead of

directly discussing spin-dependent PDF, we often use the difference of spin-dependent PDF;

$$\Delta q(x) \equiv q_+^+(x) - q_+^-(x). \tag{1.23}$$

$\Delta q(x)$ is named polarized PDF in this thesis. Based on the fact that the proton spin is $\frac{1}{2}$, sum of contributions from spin and orbital angular momentum of the parton in the proton should reconstruct the proton spin.

$$\frac{1}{2} = \int_0^1 \left[\frac{1}{2} \sum_q \Big(\Delta q(x) + \Delta \bar{q}(x) \Big) + \Delta g(x) \right] dx + L, \tag{1.24}$$

where L indicates contribution of the orbital angular momentum carried by quarks and gluons.

In ep scattering process, the polarized PDF is related to G_1 and G_2 in Equation (1.14) or g_1 and g_2 in Equation (1.15). Corresponding to Equation (1.19), the difference of the spin-dependent cross section with static parton target is

$$\frac{d\Delta\sigma^{parton}}{dE'd\Omega} \equiv \frac{d\sigma^{parton}_{\rightarrow\leftarrow}}{dE'd\Omega} - \frac{d\sigma^{parton}_{\rightarrow\rightarrow}}{dE'd\Omega} = \frac{2\alpha e_q^2}{MQ^2} \frac{E'}{E} \frac{E + E'\cos\theta}{\nu} \delta\left(x - \frac{Q^2}{2M\nu} \right), \tag{1.25}$$

where the spin state denoted at the subscripts of $d\sigma$ is for the electron beam and the parton target in the similar way to Equation (1.14). The cross section with the proton target of Equation (1.14) is written as superposition of that with the parton target of Equation (1.25) as follows.

$$\begin{aligned} \frac{d\Delta\sigma^{ep}}{dE'd\Omega} &= \int_0^1 \left[q_-^+(x) \frac{d\sigma^{parton}_{\rightarrow\rightarrow}}{dE'd\Omega} + q_-^-(x) \frac{d\sigma^{parton}_{\rightarrow\leftarrow}}{dE'd\Omega} \right] dx \\ &\quad - \int_0^1 \left[q_+^+(x) \frac{d\sigma^{parton}_{\rightarrow\rightarrow}}{dE'd\Omega} + q_+^-(x) \frac{d\sigma^{parton}_{\rightarrow\leftarrow}}{dE'd\Omega} \right] dx \\ &= \int_0^1 \Delta q(x) \frac{d\Delta\sigma^{parton}}{dE'd\Omega}\, dx, \end{aligned} \tag{1.26}$$

where the relation of Equation (1.22) is used. Comparing Equation (1.14), Equation (1.15) and Equation (1.26), one obtains

$$g_1(\nu, Q^2) = \frac{1}{2} \sum_{q,\bar{q}} e_q^2 \Delta q(x), \qquad g_2(\nu, Q^2) = 0, \qquad x = \frac{Q^2}{2M\nu}. \tag{1.27}$$

Again, the momentum fraction x of the parton is fixed kinematically.

Though this naive approximation results in $g_2 = 0$, it is predicted that g_2 is also related to polarized PDF in the second order calculation, where, for example, the interaction between partons in the proton or initial transverse momentum of the parton are considered. In the experiment, the measurement by the polarized DIS is insensitive to g_2 because the coefficient of g_2 compared to g_1 is $\frac{2Mx}{E+E'\cos\theta}$ from Equation (1.14) and it is suppressed by an order of $\frac{M}{E}$. In contrast, the spin-dependent cross section with the proton target polarized perpendicular to the electron spin is sensitive to g_2.

1.5.3 Transversity distribution

There is another kind of PDF which is independent of both $q(x)$ and $\Delta q(x)$. It is referred to as transversity distribution and often described as $\delta q(x)$.[10] The transversity is understood in

[10] In some literature, transversity distribution is denoted as $\Delta_T q(x)$.

the parton model when the proton with infinite momentum is polarized transversely (spin of the proton is perpendicular to the proton momentum) and can be written as

$$\delta q(x) \equiv q_{\uparrow}^{\uparrow}(x) - q_{\uparrow}^{\downarrow}(x), \tag{1.28}$$

where $q_{\uparrow}^{\uparrow(\downarrow)}$ is the probability to observe parton with its spin (anti)parallel to the proton spin. Significant difference from unpolarized and polarized PDF is that there is no gluon transversity for hadrons with spin one-half because of helicity conservation [14].[11] It is thought that the transversity is related to the transverse single-spin asymmetry A_N [15, 16]. Experimentally, several method is suggested and performed to access the transversity, including semi-inclusive DIS (SIDIS) where more than one particle produced in the reaction is observed in addition to the scattered electron [15, 16] and double spin asymmetry A_{TT} with transversely polarized pp collision. In the non-relativity, rotations and boosts commute. Therefore, when partons in the proton are non-relativistic, polarized PDF $\Delta q(x)$ and transversity $\delta q(x)$ become identical because series of rotations and boosts can transform the proton longitudinally polarized into the transversely polarized proton. However, the partons are not non-relativistic because contribution of gluons to property of the proton, which represent interaction between the partons, is not negligible as explained in Section 1.8. Hence $\Delta q(x)$ and $\delta q(x)$ is independent. Presently, there is almost no information based on measurements about the transversity. Only the relation between the transversity and other PDF, so-called the Soffer inequality, is theoretically known [17];

$$2|\delta q(x)| \leq q(x) + \Delta q(x). \tag{1.29}$$

1.5.4 QCD evolution for PDF (DGLAP equation)

In the sections 1.5.1 and 1.5.2, PDF are introduced at the first order approximation, where interaction between partons in the proton is ignored. Some results obtained above is based on the approximation. One is the Bjorken scaling; PDF is only a function of x which is determined in Equation (1.21) or (1.27). The interaction of partons results in violation of the Bjorken scaling and Q^2 dependence of PDF. Another feature at the first order approximation is that DIS is described with only charged partons (quarks) and neutral parton (gluon) does not contribute to the reaction. However, creation and annihilation of partons continuously happen in the proton and gluons can indirectly affect the DIS process by creating pairs of quarks and antiquarks. This phenomenon is also implemented by considering the interaction of partons.

The Q^2 dependence of PDF is understood as follows. As Q^2 of virtual photon from the electron beam becomes larger, resolution of the photon becomes better. Hence, single parton which is seen by the photon with small Q^2 is many partons like cloud for the photon with large Q^2. For this reason, the larger-Q^2 photon observes smaller-x partons, while the smaller Q^2 photon looks at larger-x partons. Qualitatively, as x increases, PDF becomes larger at small Q^2 and smaller at large Q^2. Structure function F_2 as a function of Q^2 for various x is measured by many experiments and part of its results are shown in Section 1.8.1.

Transition of PDF is logarithmic in Q^2 and equation to describe the Q^2 dependence of PDF can be obtained by QCD, which rules dynamics of the quarks and the gluons. It is called "evolution equation", or "DGLAP equation" from the names who derive the equation (Dokshitzer, Gribov, Lipatov, Altarelli, Parisi) [18–20]. The evolution equations for unpolarized

[11] On the helicity basis, the transversity is written as helicity-flip amplitude in a scattering of the parton and the parent hadron. Because the gluon have spin one, spin one-half hadron can not absorb the spin flip of the gluon. Therefore, there is no gluon transversity.

PDF is written as

$$\begin{aligned}\frac{dq(x,Q^2)}{d\log Q^2} &= \int_0^1 dy\ dz \left[P_{qq}(z)\ q(y,Q^2) + P_{qg}(z)\ g(y,Q^2)\right]\delta(x-zy) \\ \frac{dg(x,Q^2)}{d\log Q^2} &= \int_0^1 dy\ dz \left[\sum_{q,\bar{q}} P_{gq}(z)\ q(y,Q^2) + P_{gg}(z)\ g(y,Q^2)\right]\delta(x-zy), \end{aligned} \quad (1.30)$$

where $P_{ij}(z)$'s are named splitting functions and they govern the evolution of PDF. Figure 1.3 represents the first correction from the constituent quark model, where only the term of $P_{qq}(z)$ affects the DIS cross section. In general, $P_{ij}(z)$ is interpreted as probability function that parent parton converts into daughter parton. z indicates momentum fraction of the daughter parton compared to the parent parton. For example, $P_{qq}(z)$ is the probability that a quark with momentum p radiates a gluon and becomes a quark with momentum zp (see Figure 1.3). Obviously, to understand all kinds of $P_{ij}(z)$, one need to be away from the constituent quark model and consider the proton as an aggregation of quarks and gluons interaction each other. Based on the parton model, the right side of Equation (1.30) simply describes the process to generate parton with x from parent PDF, $q(y)$ and $g(y)$, following the probability $P_{ij}(z)$. By definition, x, y and z must satisfy the relation of $x = zy$, which is represented as delta function in Equation (1.30). In Equation (1.30), PDF is differentiated by $\log Q^2$, not Q^2. It implies large Q^2 dependence of PDF in low Q^2.

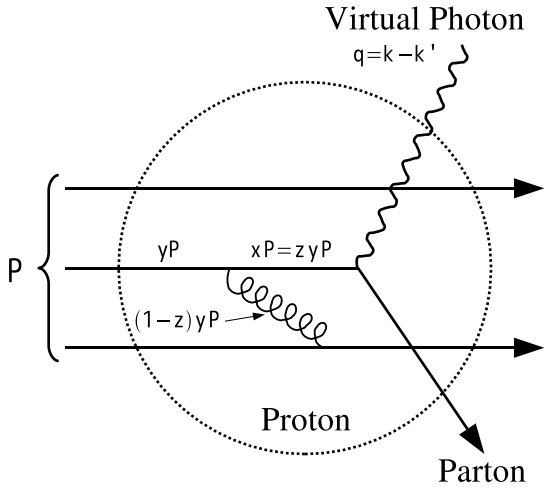

Figure 1.3: The first correction for DIS from the constituent quark model. The parent quark loses momentum by radiating gluon and then scattered by the virtual photon in the figure. Its contribution is described by the splitting function $P_{qq}(z)$ in the parton model.

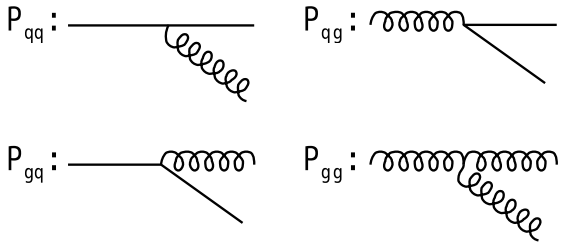

Figure 1.4: Diagrams for the leading order of $P_{ij}(z)$. By calculating these diagrams, one can obtain the specific function of $P_{ij}(z)$.

The splitting function $P_{ij}(z)$ is evaluated by QCD. $P_{ij}(z)$ is expanded by order of the coupling constant of the strong interaction, α_s.

$$P_{ij}(z) = \left(\frac{\alpha_s}{2\pi}\right) P_{ij}^{(0)}(z) + \left(\frac{\alpha_s}{2\pi}\right)^2 P_{ij}^{(1)}(z) + ... \quad (1.31)$$

Diagrams corresponding to the first term of $P_{ij}(z)$ are listed in Figure 1.4. The formulae are obtained by calculating the diagrams and summarized in Section A.1. Currently, the splitting function is calculated up to NNLO (next-to-next-to-leading order, an order of α_s^3) for unpolarized PDF (see [21, 22] and references given therein).

For polarized PDF, the evolution equation is derived in the same way.

$$\begin{aligned}\frac{d\Delta q(x,Q^2)}{d\log Q^2} &= \int_0^1 dy\ dz \left[\Delta P_{qq}(z)\ \Delta q(y,Q^2) + \Delta P_{qg}(z)\ \Delta g(y,Q^2)\right]\delta(x-zy) \\ \frac{d\Delta g(x,Q^2)}{d\log Q^2} &= \int_0^1 dy\ dz \left[\sum_{q,\bar{q}} \Delta P_{gq}(z)\ \Delta q(y,Q^2) + \Delta P_{gg}(z)\ \Delta g(y,Q^2)\right]\delta(x-zy).\end{aligned} \tag{1.32}$$

The spin-dependent splitting function $\Delta P_{ij}(z)$ is also expanded by order of α_s in the similar way to the unpolarized case. Presently, $\Delta P_{ij}(z)$ is obtained up to NLO (see [23, 24] and references given therein) and the first-order terms are summarized in Section A.1

1.6 Factorization theorem

In Equation (1.20) and (1.26), DIS process is described as superposition of the interaction between the virtual photon and a single parton in the proton. The same idea is available for "hard" *pp* scattering, where the initial protons are broken by the collision. Comparison of *ep* and *pp* scattering is displayed in Figure 1.5. In *ep* scattering, the reaction is divided into two parts. One is selection of a parton in the proton, which is confined in PDF due to difficulty of the theoretical calculation. The other part is scattering between the parton and the electron, which one can calculate precisely using perturbative QED.

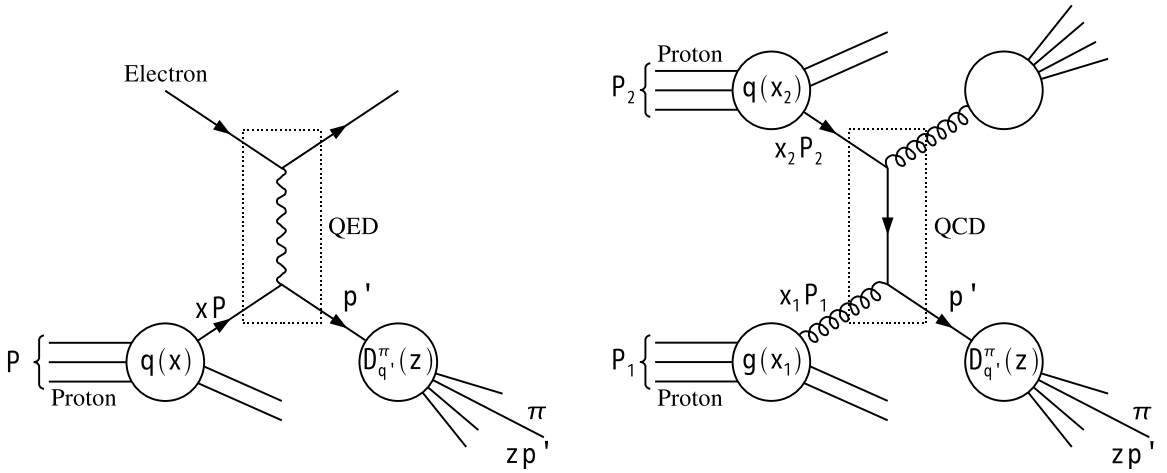

Figure 1.5: (Left) Diagram of DIS. In SIDIS experiment, one or more hadrons at the final state are detected. (Right) Diagram of hard *pp* scattering. Inclusive measurement of hadrons is often performed. In both SIDIS and *pp* scattering, the reaction is divided into three parts; PDF, FF and the partonic cross section.

When hadron at the final state is measured in DIS (SIDIS), it is necessary to formalize such a process. The hadronization from the scattered parton is "soft" QCD process, where

pQCD does not work due to low energy scale. Hence, the hadronization process is represented by fragmentation function (FF) like PDF. FF is described as a function of z (this is irrelevant to z in Section 1.5.4), which is energy fraction of the hadron detected compared to the parent parton. We explain the details of FF in Section 1.7. FF is displayed in Figure 1.5 as $D_q^h(z)$, where q denotes the parent parton and h denotes the hadron observed. Instead of Equation (1.20), for example, reaction of SIDIS with pion (π) measured in the final state is written as

$$d\sigma^{ep\to\pi X} = \sum_{q,q'} \int_0^1 dx \int_0^1 dz\ q(x)\ d\hat{\sigma}^{eq\to q'X}\ D_{q'}^{\pi}(z). \tag{1.33}$$

$d\hat{\sigma}$ indicates the cross section at the parton level. The summation is performed for possible combinations of the initial and the final parton (and anti-parton).

In the same way, reaction of pp can also be factorized as displayed in the right side of Figure 1.5. Inclusive measurement of pion in pp scattering is divided into three parts; PDF, FF and partonic cross section. Corresponding to the initial two protons, two PDFs appear. Unlike ep scattering, gluons in the proton directly participate in the reaction in pp scattering. The scattering between partons selected following PDF is calculated by pQCD instead of QED.[12] Then, the scattered parton is hadronized following FF. In formula, the process is written as

$$d\sigma^{pp\to\pi X} = \sum_{f_1,f_2,f'} \int dx_1\ dx_2\ dz\ f_1(x_1) f_2(x_2)\ d\hat{\sigma}^{f_1 f_2\to f'X}\ D_{f'}^{\pi}(z), \tag{1.34}$$

where f indicates type of the parton and includes both the quark and the gluon.

It is important to remember that, in ep scattering, this picture is valid at large Q^2 where the virtual photon interacts with a single parton in the proton. Similarly, large Q^2 is required in pp scattering and it is confirmed by production of hadron with high transverse momentum p_T.[13] Here, p_T is defined as the momentum component perpendicular to momentum of the initial protons in center-of-mass system. The large Q^2 results in small α_s, which assures validity of pQCD.

One of the noteworthy features of the factorization theorem is universality of PDF and FF. Owing to this feature, PDF or FF obtained by a certain experiment is available for other experiments and it results in versatility and predictability of the theory. In fact, FF is measured by e^+e^- collision which is free from the uncertainty of PDF. Then, DIS or SIDIS is utilized to determine PDF for quarks in which FF obtained by e^+e^- collision is used. To measure gluon PDF, pp collision is effective because gluon appears in the reaction at the leading order and PDF and FF obtained above is useful in analyzing pp scattering.

In the same way as the unpolarized case, cross section of polarized pp scattering can be also factorized. For example, when both initial protons have positive helicity in center-of-mass system of the protons, spin-dependent cross section is written as

$$\begin{aligned} d\sigma_{++}^{pp\to\pi X} = \sum_{f_1,f_2,f'} \int dx_1\ dx_2\ dz\ \Big[& \\ & f_{1+}^{+}(x_1)\ f_{2+}^{+}(x_2)\ d\hat{\sigma}_{++}^{f_1 f_2\to f'X} + f_{1+}^{+}(x_1)\ f_{2+}^{-}(x_2)\ d\hat{\sigma}_{+-}^{f_1 f_2\to f'X} + \\ & f_{1+}^{-}(x_1)\ f_{2+}^{+}(x_2)\ d\hat{\sigma}_{-+}^{f_1 f_2\to f'X} + f_{1+}^{-}(x_1)\ f_{2+}^{-}(x_2)\ d\hat{\sigma}_{--}^{f_1 f_2\to f'X} \Big] D_{f'}^{\pi}(z). \end{aligned} \tag{1.35}$$

[12] QED also contributes the process, but the contribution is small due to smaller coupling constant of the electromagnetic interaction than the strong interaction.

[13] Empirically, boundary for the validity of the factorization theorem is around 1 GeV/c in p_T.

+ or − at subscripts of $d\sigma$ denotes the helicity state of the initial protons. Similarly, those of partonic cross-section $d\hat{\sigma}$ are parton's helicity and the left and right sign is for f_1 and f_2, respectively. In the case that a pion is detected in the final state, FF is independent of spin state of the parent parton because the pion does not have spin and FFs for two spin state of the parent parton are transformed each other by the Lorentz transformation.

Polarized PDF Δf is related to appropriate linear combination of the spin-dependent cross section, which is named polarized cross section.

$$\begin{aligned} d\Delta\sigma^{pp\to\pi X} &\equiv \frac{1}{4}\left[d\sigma_{++}^{pp\to\pi X} - d\sigma_{+-}^{pp\to\pi X} - d\sigma_{-+}^{pp\to\pi X} + d\sigma_{--}^{pp\to\pi X}\right] \\ &= \sum_{f_1,f_2,f'} \int dx_1\ dx_2\ dz\ \Delta f_1(x_1)\ \Delta f_2(x_2)\ d\Delta\hat{\sigma}^{f_1 f_2\to f'X} D_{f'}^{\pi}(z), \end{aligned} \tag{1.36}$$

where $d\Delta\hat{\sigma}$ is polarized cross section on the parton level and defined as

$$d\Delta\hat{\sigma}^{f_1 f_2\to f'X} \equiv \frac{1}{4}\left[d\hat{\sigma}_{++}^{f_1 f_2\to f'X} - d\hat{\sigma}_{+-}^{f_1 f_2\to f'X} - d\hat{\sigma}_{-+}^{f_1 f_2\to f'X} + d\hat{\sigma}_{--}^{f_1 f_2\to f'X}\right]. \tag{1.37}$$

To obtain Equation (1.36), the relation of Equation (1.22) is used. In the same way as the unpolarized case, universality of PDF and FF is again available. Polarized PDF for the quarks and FF is obtained by polarized DIS and e^+e^- collision, respectively, while $d\Delta\hat{\sigma}$ is evaluated based on pQCD. Therefore, polarized pp collision can be an approach to measurement of polarized gluon PDF Δg, which DIS experiment is insensitive to.

1.7 Fragmentation function

In DIS or hard pp collision, a single parton with large momentum is knocked out from the proton. Since the quark or the gluon cannot exist by itself, such a parton is hadronized and generates a "jet", which consists of many hadrons with momentum almost parallel to that of the initial parton. The process of hadronization is described by "fragmentation function" (FF). FF is often represented as $D_f^h(z)$, where f and h indicate the parent parton and the hadron after the fragmentation, respectively, and z is energy fraction of the hadron to the parton. $D_f^h(z)dz$ is defined as the probability density that the hadron h with momentum of zp to $(z+dz)p$ is generated in the jet originating in the parton f with momentum of p. When the hadron at the final state has spin, polarized FF is defined in analogy with PDF. However, in the case of pion with no spin, which is measured in this thesis, FF is independent of helicity state of the parent parton because FFs for positive and negative helicity of the parton are transformed each other by the Lorentz transformation. Therefore, we don't refer to polarized FF.

As mentioned in Section 1.6, FF has the feature of universality and FF obtained by a certain measurement is available for other experiments. Based on this feature, e^+e^- collision is used as the common tool to research FF because the reaction of $e^+e^- \to q\bar{q}$ is precisely calculable by QED and there is no other theoretical uncertainty except for FF. In e^+e^- collision with center-of-mass system of the incident electrons, FF is related to cross section at the first order as follows.

$$\frac{1}{\sigma_{tot}^{e^+e^-\to X}} \frac{d\sigma^{e^+e^-\to hX'}}{dz} = \frac{\sum_{q,\bar{q}} e_q^2 D_q^h(z)}{\sum_{q,\bar{q}} e_q^2}, \qquad z = \frac{2E_h}{\sqrt{s}} = \frac{E_h}{E_q}. \tag{1.38}$$

σ_{tot} is the total cross section of e^+e^- collision. The summation is executed over possible quark flavors, while contribution from gluon does not appear at the first order. $\sqrt{s}$, E_h and E_q are center-of-mass energy, energy of the hadron and energy of the parton, respectively. $D_f^h(z)$ also depends on Q^2 like PDF. Though, in this equation, only FFs for the quarks appear and the cross section has scaling on z, FF depends on Q^2 with higher order QCD, like PDF, and evolves following DGLAP equation for FF [25–27].

To determine FF, several experiments of e^+e^- collision and analyses to unify the experimental data are performed (see [28–32] and references given therein). However, from Equation (1.38), one can notice that it is difficult to distinguish FFs for each quark flavor because the right-hand side of Equation (1.38) is always sum of FFs. For example, difference of d and s quarks is just slightly different mass. For this reason, to extract FF from measured data, symmetric properties and phenomenological assumptions are often adopted. Charge conjugation results in

$$D_f^h = D_{\bar{f}}^{\bar{h}}, \tag{1.39}$$

and additional isospin symmetry derives for positive pion

$$D_u^{\pi^+} = D_{\bar{d}}^{\pi^+}, \qquad D_{\bar{d}}^{\pi^+} = D_{\bar{u}}^{\pi^+}. \tag{1.40}$$

In addition to these "reliable" conditions, some constraints are imposed, such as $D_{\bar{d}}^{\pi^+} = D_s^{\pi^+} = D_{\bar{s}}^{\pi^+}$ based on symmetry for non-valence quarks [28,32]. Recently, flavor-decomposed FFs were published [31]. They are obtained utilizing experimental data where two hadrons are tagged at the final state. For instance, pion measured with D meson tagged lead to pion FF from c quark, D_c^π. It is also hard to extract gluon FF in simple measurement with one hadron tagged. To determine gluon FF, method with three jets tagged is applied. One of the three jets originates in the gluon radiated by the quark which is the source of other jets.

1.8 Current experimental knowledge on PDF

Many experiments have been performed to explore PDF. To extract PDFs from these huge data points, it is necessary to fit a certain theoretical model to the data. Such a study is called "global analysis". As discussed in Section 1.5.4, PDFs depend on Q^2 and the evolution follows the DGLAP equation, Equation (1.30) or (1.32), obtained by QCD. Therefore, in global analysis, model of PDF for the analysis is parameterized as a function of Bjorken x at fiducial Q^2, which is usually around a few GeV^2. The Q^2 dependence of the model is calculated based on the DGLAP equation. Though the parameterization is different in analysis groups, the number of the parameters for the fit is roughly 10 to 20. Generally, it is small for polarized PDF analysis simply because of poor number and precision of experimental data with polarization.

It is important to note about the isospin symmetry between the proton and the neutron. The isospin symmetry is well satisfied in current accuracy of measurements. The symmetry relate PDFs of the neutron to those of the proton;

$$u^p(x) = d^n(x), \qquad d^p(x) = u^n(x), \qquad s^p(x) = s^n(x). \tag{1.41}$$

p and n at superscript of PDF denote the proton and the neutron, respectively. The similar relation is obtained for antiquark PDFs and polarized PDFs. To extract structure function of the neutron, DIS experiment with deuteron target is utilized, assuming a deuteron as a proton and a neutron which are bound very weekly and almost independent. In addition to the isospin symmetry, analysis groups adopt some constraints between PDFs to obtain better efficiency and accuracy.

1.8.1 Unpolarized PDF

Figure 1.6 displays the structure function F_2 of the proton as a function of Q^2 for various x values [33]. In the figure, arbitrary offset is added to F_2, though the offset is common in the same x value. The lines under the data points show results of the global analysis by H1 collaboration [34] and ZEUS collaboration [35]. The data is well represented by the fit and it indicates validity of the Q^2 evolution based on QCD.

Since DIS experiments can measure only F_2 which is sum of PDFs, it is hard to separate F_2 into PDFs of each flavor. To disentangle F_2, several kinds of experiments are utilized in addition to DIS with the proton or the deuteron target. DIS with neutrino beam [36] is useful because charged weak current (W boson coupling) selects quark flavor. For example, the reaction with negative lepton detected on the final state selects s, d or $\bar{u}$ quarks (in light quarks). Similarly, W boson production in collision of the proton and the antiproton ($p\bar{p}$) [37] is used for the separation of u and d quarks. PDF of c quark is tagged by SIDIS with D meson detected on the final state [38–42]. Lepton pair production (Drell-Yang process) in pp or pd (proton-deuteron) collision [43, 44] is available to distinguish PDFs of $\bar{u}$ and $\bar{d}$ since lepton pair is produced by annihilation of the quark and the antiquark. Measurement of inclusive jet production in $p\bar{p}$ collision [45–48] contributes to determination of gluon PDF, especially at higher x region ($x >\sim 0.01$). DIS measurements with wide Q^2 range also contribute to constraint of gluon PDF through the Q^2 evolution at small x region ($x <\sim 0.1$).

There are several groups extracting PDF from the experimental data [34, 35, 49–52]. The results from the groups have reasonable agreement each other. Figure 1.7 displays unpolarized PDF as a function of Bjorken x at $Q^2 = 4$ GeV^2 extracted by CTEQ group [49]. PDFs are parameterized at $Q^2 = (1.3)^2$ GeV^2 since the Q^2 evolution is unstable at too low Q^2. The band in the figure indicates uncertainty of PDF. The gluon PDF is scaled by 0.2 for convenience. There is a bump at $x \sim 0.2$ for u and d quarks because they are valence quark. About sea quarks, PDF of $\bar{u}$ and $\bar{d}$ is similar, while that of $\bar{s}$ and $\bar{c}$ is suppressed compared to $\bar{u}$ and $\bar{d}$ because of difference of their masses. Large gluon PDF indicates that large amount of proton momentum is carried by the gluons.

1.8.2 Polarized PDF

It is difficult to theoretically calculate x dependence of PDF from the first principle. However, there are some prediction about integral of PDF over x, which is called sum rule. Some sum rules are often used for global analysis as constraints, as well as for the examination of Equation (1.24). For example, some trivial sum rules are Equation (1.17) and (1.18), in addition to Equation (1.24).

The most fundamental sum rule for polarized PDF is derived by Bjorken [53, 54] based on the isospin symmetry of the nucleon.

$$\int_0^1 g_1^p(x) - g_1^n(x)dx = \frac{1}{6}\left|\frac{g_A}{g_V}\right|\left[1 - \frac{\alpha_s(Q^2)}{\pi} + ...\right], \qquad \left|\frac{g_A}{g_V}\right| = 1.2695 \pm 0.0029 \tag{1.42}$$

where g_1^p and g_1^n are structure functions defined at Equation (1.15) for the proton and the neutron, respectively. g_V and g_A are the vector and the axial-vector weak coupling constants of the neutron β-decay and determined precisely by experiments [4].[14] The term $1 - \frac{\alpha_s}{\pi} + ...$

[14] β-decay of the neutron is described by the vector and the axial-vector current as $\left[\bar{\psi}_p(g_V\gamma^\mu - g_A\gamma^\mu\gamma^5)\psi_n\right]\left[\ \textit{lepton part}\ \right]$, where ψ_p and ψ_n is field of the proton and the neutron, respectively. The

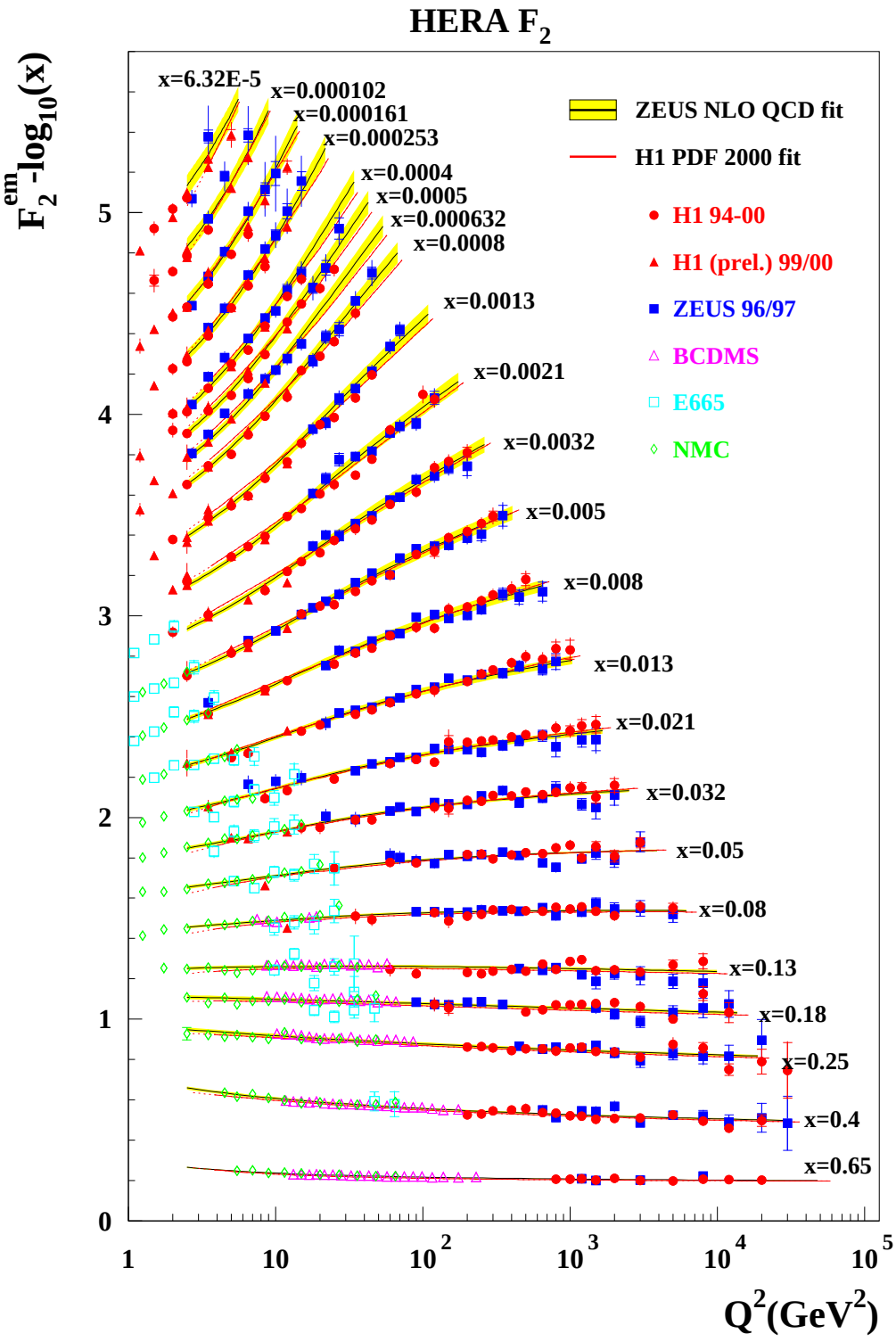

Figure 1.6: Structure function F_2 for the proton at various x values as a function of Q^2 [33]. Offsets, which is common in the same x value, are added to F_2. The results of the global analysis by H1 [34] and ZEUS collaborations [35] are also displayed in the figure.

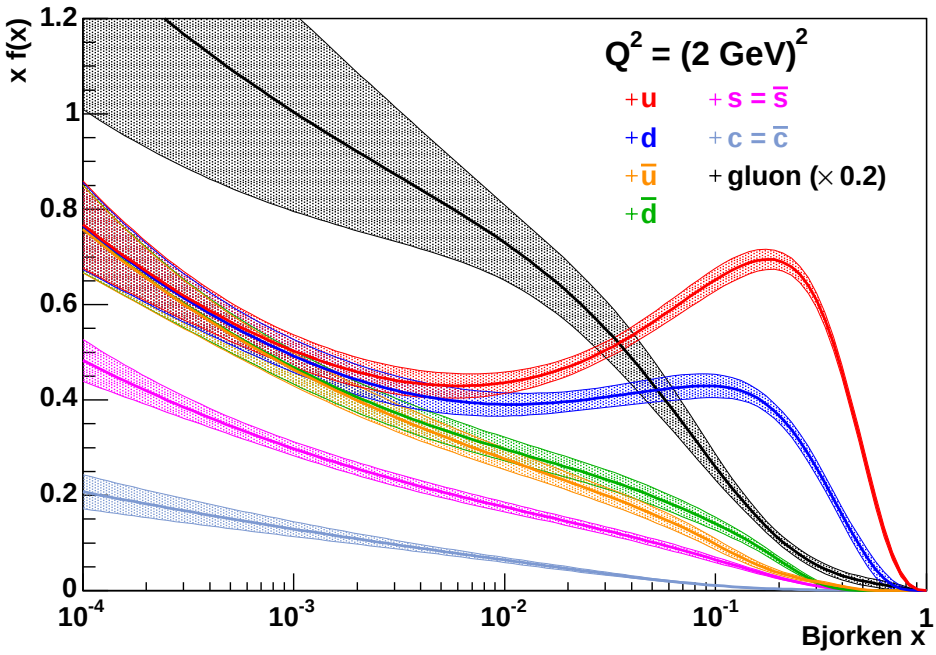

Figure 1.7: Unpolarized PDF at $Q^2 = 4$ GeV^2 as a function of Bjorken x obtained by CTEQ group [49]. For gluon PDF, $g(x) \times 0.2$ is displayed in this figure for convenience.

in the right hand side is from higher order correction of QCD. This Bjorken sum rule is well verified by measurements [55, 56].

By assuming flavor-SU(3) symmetry for the spin-$\frac{1}{2}$ baryon octet, the β-decay of hyperons can be described by two parameters, F and D [57,58]. At the same time, certain combinations of integral of the polarized PDF is related to F and D as follows.

$$\int_0^1 \left[u(x) + \bar{u}(x)\right] - \left[d(x) + \bar{d}(x)\right] dx = F + D = \left|\frac{g_A}{g_V}\right|, \tag{1.43}$$

$$\int_0^1 \left[u(x) + \bar{u}(x)\right] + \left[d(x) + \bar{d}(x)\right] - 2\left[s(x) + \bar{s}(x)\right] dx = 3F - D = 0.586 \pm 0.031. \tag{1.44}$$

It is noticeable that these linear combinations of PDF is independent of Q^2 in up to NLO. Equation (1.43) is identical to the Bjorken sum rule of Equation (1.42). Since the isospin symmetry is included in the flavor-SU(3) symmetry, the Bjorken sum rule also appears in this model. The right-hand side of Equation (1.44) is evaluated using measured $\frac{g_A}{g_V}$ for hyperon decays ($\Lambda \to p$, $\Xi \to \Lambda$ and $\Sigma \to n$) [4], where F and D is fixed by Equation (1.43). Chi-square of the fit of 2.1 with degree-of-freedom of 2 is reasonable and it supports validity of the assumption of the flavor-SU(3) symmetry.

In experiments, instead of measuring $d\Delta\sigma$ of Equation (1.36) or Equation (1.26) directly, ratio to the unpolarized cross section, "asymmetry", is often measured to reduce normalization uncertainty. In DIS experiments, longitudinal double spin asymmetry $A_{||}$ is an effective

nucleon spin vector is also described by the axial-vector current as $2M_p S^\mu = \langle P, S|\bar{\psi}\gamma^\mu\gamma^5\psi|P, S\rangle$. The fields of the proton and the neutron are related by the isospin symmetry.

way to determine g_1. $A_{||}$ is defined as an asymmetry between the cross section with helicities of the electron and the proton antiparallel and that with parallel helicities.

$$A_{||} \equiv \frac{d\sigma^{ep}_{\rightarrow\Leftarrow} - d\sigma^{ep}_{\rightarrow\Rightarrow}}{d\sigma^{ep}_{\rightarrow\Leftarrow} + d\sigma^{ep}_{\rightarrow\Rightarrow}} = \frac{d\Delta\sigma^{ep}}{2d\sigma^{ep}}, \tag{1.45}$$

where $d\Delta\sigma^{ep}$ and $d\sigma^{ep}$ are defined in Equation (1.13) and (1.14), respectively. By substituting Equation (1.13) and (1.14), $A_{||}$ can be written by structure functions. At the Bjorken limit, $A_{||}$ is simply proportional to ratio of g_1 and F_1 as

$$A_{||} \sim D\frac{g_1}{F_1} \sim D\frac{g_1}{F_2}2x(1+R). \tag{1.46}$$

D called depolarization factor represents polarization of virtual photon emitted by the electron beam and is determined kinematically. R is a function of x and Q^2, and relates F_1 and F_2 [59]. As described in Equation (1.21), $R = 0$ in the first-order parton model. More detail is described in Section A.2.

Following pioneering experiments at SLAC [60–63] to measure g_1, EMC (European Muon Collaboration) at CERN measured g_1 over 0.01 – 0.7 in Bjorken x with polarized muon beam and extracted integral of g_1 [64, 65]. As described in Equation (1.27), g_1 is written in linear combination of polarized PDFs of the quarks (and the antiquarks). When only three light-flavor quarks, u, d and s, are taken into account, integral of each polarized PDF of the quarks are extracted by assuming Equation (1.43) and Equation (1.44) based on the flavor-SU(3) symmetry. Thus, contribution from the quarks to the proton spin in Equation (1.24) is evaluated by measurements of g_1. The EMC results were interpreted as meaning that quarks and antiquarks carry only ∼10 % of the proton spin, even though the uncertainty is large. This conclusion is a contrast to that constituent quarks carry quantum numbers of hadrons and well describe magnetic moment of hadrons. It is noteworthy that about half of the proton momentum is carried by gluons.

Many experiments have been performed to confirm the EMC results (see references in [66–71]). The obtained g_1 of the proton at various Bjorken x are displayed in Figure 1.8 as a function of Q^2. In this figure, arbitrary offsets which is common for same x value are added to g_1. Compared with Figure 1.6, precision of the experimental data is poorer and the measured range of Q^2 and x is much smaller than the unpolarized structure function F_2. The small Q^2 and x range measured is related to poor knowledge on polarized gluon PDF, in contrast to the unpolarized case where large kinematical coverage constrain the uncertainty of gluon PDF. Resulting curve of global analysis by AAC (Asymmetry Analysis Collaboration) [70] is also displayed in Figure 1.8.[15] The contribution of the quarks and the antiquarks to the proton spin is obtained by the recent analyses [66–71] to be 20 – 35 % at $Q^2 = 1$ GeV^2. Remaining ∼70 % of the proton spin is expected to be carried by gluons or orbital angular momentum of the parton. But, currently, no definite experimental knowledge on them is obtained.

In global analysis, some constraints, which is generally tighter than the unpolarized case due to poor experimental precision, are imposed depending on analysis groups. What is frequently adopted are sum rules of Equation (1.42), (1.43) and (1.44). Symmetric sea quark distributions, $\bar{u}(x) = \bar{d}(x) = \bar{s}(x) = s(x)$, are also often assumed. Figure 1.9 displays polarized PDF at $Q^2 = 1$ GeV^2 obtained by AAC with above constraints[15]. Valence u quark

[15] AAC has already analyzed data including preliminary results of A_{LL} in π^0 production in this thesis [70] and the resulting curve is displayed in Figure 1.8. However, polarized PDFs in Figure 1.9 are produced without our data [72].

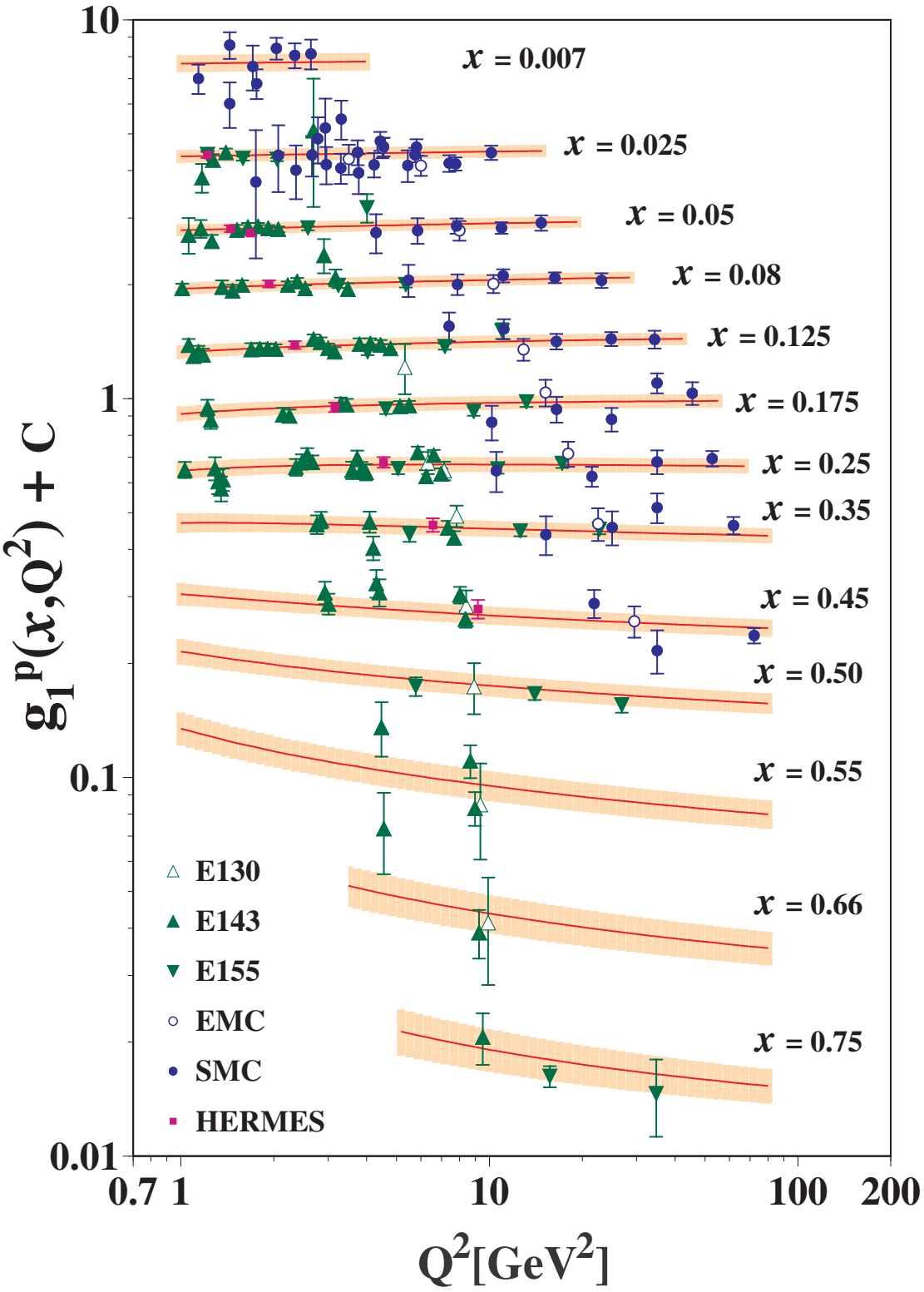

Figure 1.8: g_1 at various Bjorken x region as a function of Q^2. Curve displays result of global analysis by [70]. Offsets which is common for the same x range are added to g_1 for convenience.

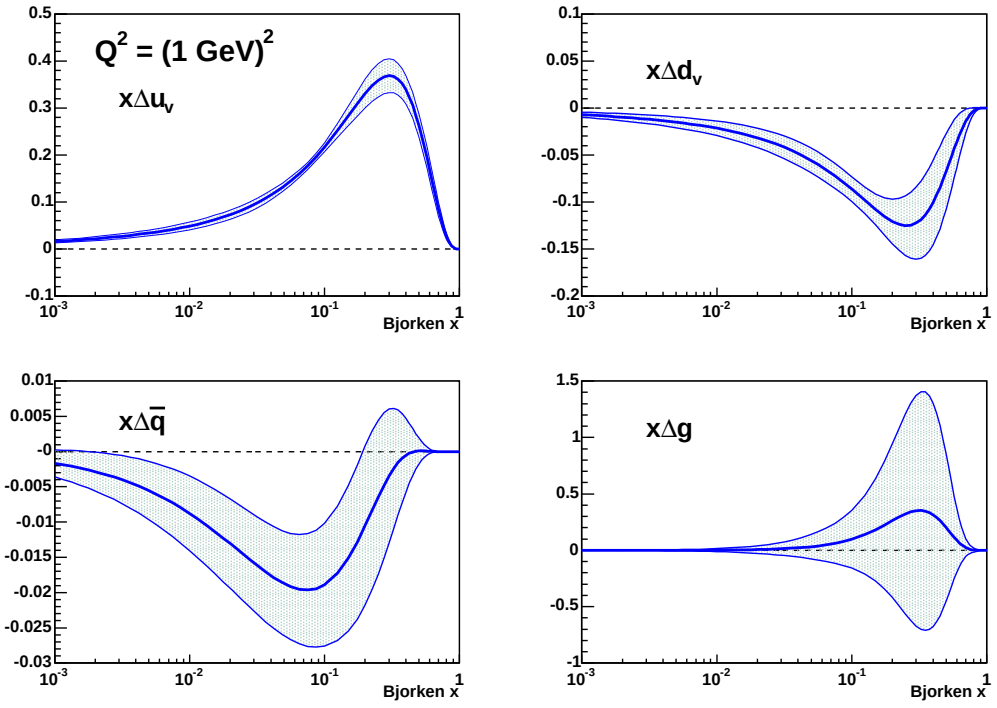

Figure 1.9: Polarized PDF at $Q^2 = 1$ GeV^2 obtained by global analysis by AAC[15]. u_v (d_v) indicates valence u (d) quark. The distributions of the sea quarks and the strange quark are labeled as $\Delta\bar{q}$. The band represents uncertainty of polarized PDF. The sum rules of Equation (1.42), (1.43) and (1.44) are used in the fitting, and assumption of symmetric sea-quark distributions is applied.

aligns parallel to spin of the proton, while polarization of valence d quark and the sea quarks are slightly negative. Since most data are currently obtained by DIS experiments, there is almost no capability to determine polarized gluon PDF as huge uncertainty is assigned to it in Figure 1.9.

Other processes such as SIDIS and pp collisions are available to constrain Δg. In such experiments, asymmetry is usually measured. In the case of pp collisions, especially for inclusive π^0 production, the detail is described in Section 1.10. Currently, SMC [73], HERMES [74] and COMPASS [75] collaborations published the results of Δg based on SIDIS. Their results have moderate precision and are consistent with the global analysis including our data as shown in Section 4.4. Further experimental activities are ongoing including π^0 A_{LL}. For example, A_{LL} in jet production with pp collisions was published by the STAR experiment at RHIC [76]. Such efforts are discussed in Section 4.5.

1.9 Theoretical works to predict Δg

As mentioned before, it is hard to predict PDF from the first principle. Nevertheless, since the EMC experiment revealed that most of the proton spin is not carried by the spin of quarks and antiquarks unexpectedly, theorists have worked to estimate the contribution of the gluon, which is the possible part in the rest of the proton spin. Most of them are model dependent

and derive only first moment of Δg, which we describe as ΔG; $\Delta G(Q^2) = \int_0^1 \Delta g(x, Q^2)\ dx$. One of the theoretical works is based on the QCD sum rule and $\Delta G = 2.1 \pm 1.0$ at $Q^2 = 1$ GeV^2 is predicted by [77]. Following sum rule, another group [78] extracted the total angular momentum J_g of the gluon, sum of spin and orbital angular momentum, to be $J_g \sim 0.35 \pm 1.3$ at $Q^2 = 1$ GeV^2. Brodsky et al. [79] adopted hypothesis that a parton with large momentum fraction of the proton also retain the helicity of the proton. In this hypothesis, they presume the shape of Δg as a function of Bjorken x. Finally, they derived $\Delta G \sim 0.5$ in their model. Barone et al. [80] extracted ΔG based on non-relativistic constituent quark model. In the model, the proton is regarded as three quarks floating in the classical gluon color field, which is analogous to the electromagnetic field. They obtained $\Delta G = 0.24$ at $Q^2 = 0.25$ GeV^2. In addition, they predicted that the orbital angular momentum of the gluon is similar in size. Instead of constituent quark model, Lee et al. [81] adopted the bag model. The bag for the proton is filled with color charge and field in the model. Their prediction was $\Delta G \sim 0.2$. Recently, the studies based on the non-relativistic quark model and the bag model were updated by [82]. They estimated that ΔG is 0.2 to 0.3 at $Q^2 = 1$ GeV^2. They also provided x dependence of Δg and the shape is similar to that obtained by the global analysis. The lattice QCD, which is only model independent way so far, attempted to derive ΔG. However, the accuracy is still not sufficient and only the limit is obtained to be $\frac{3\alpha_s}{2\pi}|\Delta G| < 0.05$ [83]. The predictions introduced here are different depending on the models. Moreover, the values extracted include uncertainty of the model, or they assign large error. It is quite important to determine Δg in experiments.

1.10 Δg measurement via A_{LL} in π^0 production

In pp collisions, the double helicity asymmetry A_{LL} is an orthodox method to approach polarized PDF. In this thesis, A_{LL} in inclusive π^0 production ($A_{LL}^{\pi^0}$) is measured. $A_{LL}^{\pi^0}$ is defined as

$$A_{LL}^{\pi^0} \equiv \frac{d\sigma_{++}^{pp\to\pi^0 X} - d\sigma_{+-}^{pp\to\pi^0 X} - d\sigma_{-+}^{pp\to\pi^0 X} + d\sigma_{--}^{pp\to\pi^0 X}}{d\sigma_{++}^{pp\to\pi^0 X} + d\sigma_{+-}^{pp\to\pi^0 X} + d\sigma_{-+}^{pp\to\pi^0 X} + d\sigma_{--}^{pp\to\pi^0 X}} = \frac{d\Delta\sigma^{pp\to\pi^0 X}}{d\sigma^{pp\to\pi^0 X}}. \tag{1.47}$$

Here $d\sigma^{pp\to\pi^0 X}$ is the cross section of inclusive π^0 production and its subscripts indicate helicities of the initial protons. The denominator corresponds to four times of the unpolarized cross section. Using Equation (1.34) and (1.36), Equation (1.47) is rewritten as

$$A_{LL}^{\pi^0} = \frac{\sum_{f_1,f_2,f'} \int dx_1\ dx_2\ dz\ \Delta f_1(x_1)\ \Delta f_2(x_2)\ d\Delta\hat{\sigma}^{f_1 f_2\to f' X} D_{f'}^{\pi^0}(z)}{\sum_{f_1,f_2,f'} \int dx_1\ dx_2\ dz\ f_1(x_1) f_2(x_2)\ d\hat{\sigma}^{f_1 f_2\to f' X}\ D_{f'}^{\pi^0}(z)}. \tag{1.48}$$

As shown in this equation, $A_{LL}^{\pi^0}$ is written as convolution of unpolarized and polarized PDF, the cross section at the parton level and FF to π^0. Owing to the universality of PDF and FF, PDF and FF measured in other processes are available for $A_{LL}^{\pi^0}$. It should be noted that each component depends on Q^2, which usually takes p_T^2 of produced π^0 in theoretical calculations. As described in Section 1.8.1, unpolarized PDFs are well known by the past experiments. For the polarized case, polarized DIS experiments constrain polarized PDF of quarks and antiquarks as described in Section 1.8.2. Meanwhile, FF to π^0 is determined by experiments with e^+e^- collisions, where no uncertainty of PDF contribute (see [28–32] and references given therein). In addition, the partonic cross section can be calculated by pQCD. Therefore,

only Δg is the unknown factor in Equation (1.48). This means that the measurement of $A_{LL}^{\pi^0}$ can directly constrain Δg.

It is the most significant advantage of $A_{LL}^{\pi^0}$ that Δg appears at the leading order in pp collisions. In DIS, Δg is a contribution of the next-to-leading order because the gluon can not be probed via electromagnetic interaction which is the leading effect in DIS. One of the concerns in $A_{LL}^{\pi^0}$ is whether pQCD is applicable because pQCD is a framework to compare the data and theoretical calculations. It is important to achieve large $\sqrt{s}$ and detect π^0 with high p_T to apply pQCD to the data. This experiment was performed with the collider. This make it possible to reach $\sqrt{s} = 200$ GeV. Usually, $\sqrt{s}$ of 200 GeV is expected to satisfy the requirement of pQCD. In terms of p_T, pQCD require more than a few GeV. Since the p_T range of the measurement was 0.5 to 9 GeV/c, pQCD is applicable to the data in the higher p_T range. For the test of pQCD, the calculation of the cross section in π^0 production is compared with the measurement in Section 4.2.

Another concern in $A_{LL}^{\pi^0}$ is how much gluons in a proton contribute to π^0 production. In terms of QCD subprocess, π^0 is produced via gluon-gluon, gluon-quark and quark-quark scatterings. Obviously, it is preferable that the fraction of gluon-gluon or gluon-quark subprocesses are large to probe gluons in a proton. Figure 1.10 displays the fraction of each subprocess in π^0 production. In the measured p_T range, 0.5 to 9 GeV/c, gluon-gluon scatterings are dominant at $p_T < 3$ GeV/c and the gluon-quark subprocess is significant at $p_T > 3$ GeV/c. Meanwhile, the contribution of quark-quark scatterings becomes large at $p_T > 15$ GeV/c. This tendency is understood by considering valence quarks in the proton. Most of partons with large Bjorken x is valence quarks as displayed in Figure 1.7 and, qualitatively, π^0s with high p_T are produced from partons with large Bjorken x. For this reason, the contribution of quarks becomes significant for high-p_T π^0 production, while the gluon contribution is dominant at low p_T region.

It must be kept in mind that each term in Equation (1.48) includes corresponding $d\Delta\hat{\sigma}$ to the subprocess. If $d\Delta\hat{\sigma}$ is small, the contribution from the corresponding subprocess is also small. Figure 1.11 displays the double helicity asymmetry for subprocesses ($\hat{a}_{LL}$) as a function of scattering angle on the partonic center-of-mass system. In the similar way to Equation (1.47), $\hat{a}_{LL}$ is defined as

$$\hat{a}_{LL} \equiv \frac{d\Delta\hat{\sigma}}{d\hat{\sigma}}, \tag{1.49}$$

where superscripts indicating parton flavors are abbreviated. Roughly speaking, our measurement looks at around $\cos\theta = 0$ because π^0s are detected at the central rapidity. There is no significant difference in any subprocesses except for the group E, in which $\hat{a}_{LL}$ is negative. However, in total, each $\hat{a}_{LL}$ for the gluon-gluon, gluon-quark, quark-quark scatterings becomes positive in the measured kinematical region.

In Section 1.1, we introduced that $A_{LL}^{\pi^0}$ can approximately be described as a quadratic function of $\frac{\Delta g}{g}$. The approximate relation of $A_{LL}^{\pi^0}$ and Δg is reintroduced;

$$A_{LL}^{\pi^0}(p_T) \sim P_2(p_T)\left[\frac{\Delta g(\xi)}{g(\xi)}\right]^2 + P_1(p_T)\left[\frac{\Delta g(\xi)}{g(\xi)}\right] + P_0(p_T),$$
$$\xi \equiv \langle x_1 \rangle = \langle x_2 \rangle, \quad \text{depends on } p_T. \tag{1.50}$$

To obtain the approximation, it is assumed that the integrals over x_1 and x_2 in Equation (1.48) is represented by the value at mean x_1 and x_2. In addition, because the kinematical coverage of our measurement is $\sim$0 in pseudorapidity, mean values of x_1 and x_2 is likely same. They are described as ξ and should depend on p_T of π^0 as written in the second line of Equation (1.50).

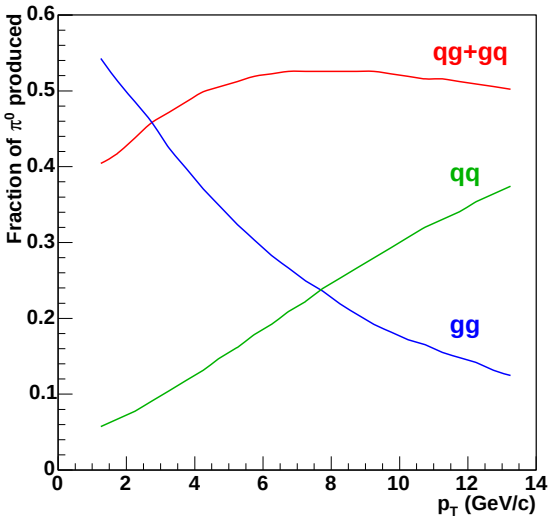

Figure 1.10: Fractions of the gluon-gluon, gluon-quark and quark-quark subprocesses in π^0 production as a function of π^0 p_T. Measured p_T range in this thesis is $0.5 - 9$ GeV/c.

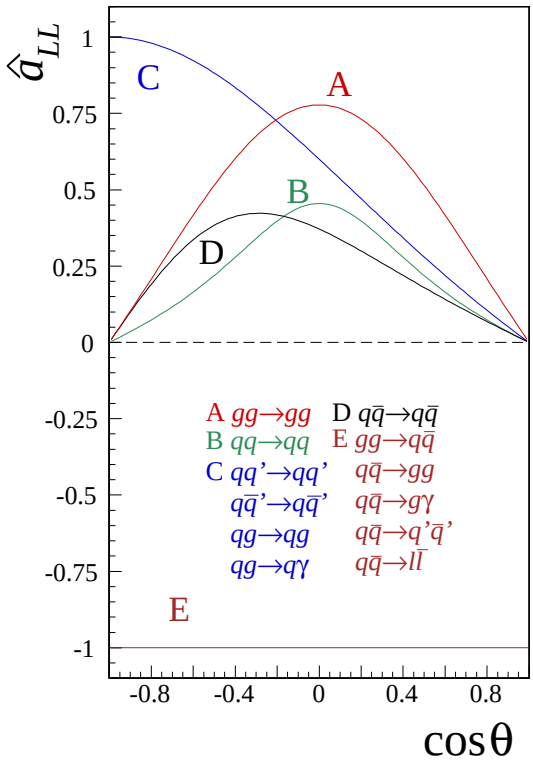

Figure 1.11: The double helicity asymmetry of the partonic cross section ($\hat{a}_{LL}$) as a function of the scattering angle on the partonic center-of-mass system. This is the leading order calculation. Our measurement covers central rapidity and it roughly corresponds to $\cos\theta \sim 0$.

Hence, Equation (1.48) can be written by the second, first and zeroth order term of $\Delta g(\xi)$. They correspond to terms of P_2, P_1 and P_0. Considering that Equation (1.48) includes $g(x)$ at the denominator, $\frac{\Delta g(\xi)}{g(\xi)}$ is used instead of just $\Delta g(\xi)$. Remaining part from FF, the partonic cross sections and PDF except for Δg are confined into $P_{0,1,2}$. In Equation (1.50), It is clearly described that each term depends on π^0 p_T. That is originally Q^2 dependence of PDF and FF, as well as p_T dependence of the partonic cross section. In Section 4.3, an interpretation from measured $A_{LL}^{\pi^0}$ into Δg is introduced using a simple model based on the relation of Equation (1.50).

The first experimental results of $A_{LL}^{\pi^0}$ was published in 1991 by E704 experiment at FNAL with proton-proton and proton-antiproton collisions at $\sqrt{s} = 19.4$ GeV [1]. However, uncertainty of the measurement was too large to constrain Δg. At the collider energy, the PHENIX experiment published the results of $A_{LL}^{\pi^0}$ in 2004 [2] and improved in 2006 [3]. Figure 1.12 displays the results. Two pQCD-based theoretical calculations with different Δg input are overlaid in the figure. GRSV-std is the case that uses Δg of the best fit in the global analysis with DIS data, while GRSV-max adopts maximally polarized Δg. The data disfavors GRSV-max, but it is hard to constrain Δg due to poor statistics. The statistics is much

improved in this thesis by a factor of about 25 in figure-of-merit.[16] It results in making statistical uncertainty small to be one-fifth and extending p_T range of the measurement up to 9.0 GeV/c.

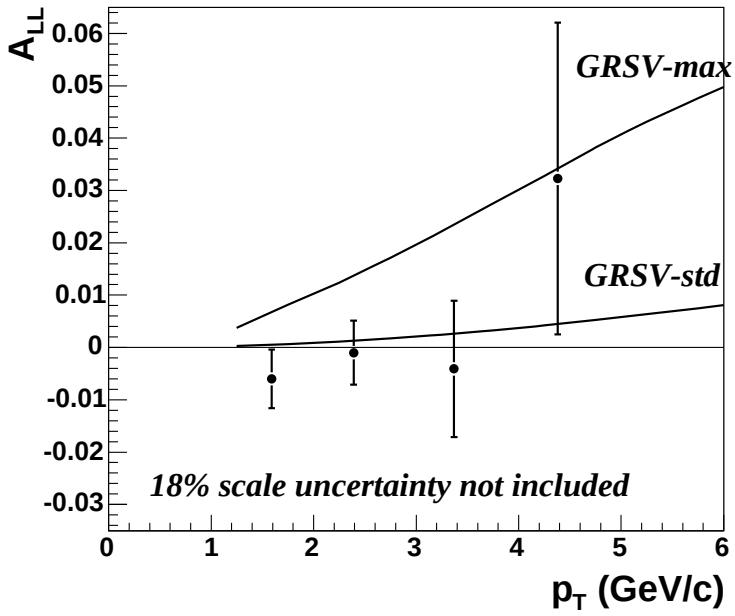

Figure 1.12: $A_{LL}^{\pi^0}$ as a function of p_T measured by the PHENIX experiment [3]. Two theoretical curve is calculated based on pQCD using unpolarized PDF by CTEQ [49], polarized PDF by GRSV [67] and FF by KKP [29]. GRSV-std uses Δg of the best fit in the global analysis with DIS data, while GRSV-max adopts maximally polarized Δg [84].

1.11 A_{LL} in terms of experimental observables

$A_{LL}^{\pi^0}$ is defined as Equation (1.47). From Equation (1.47), the helicity-dependent cross section is parameterized using A_{LL} as;[17]

$$\sigma_{h_1 h_2} = \sigma_0(1 + h_1 h_2 A_{LL}), \tag{1.51}$$

where σ_0 is the unpolarized cross section and obtained by averaging spin of the initial protons. h_1 and h_2 denote helicity of the initial protons and take $+1$ or -1 (simply $+$ or $-$ when appear as subscripts). In this equation, the cross section is constrained by relation;

$$\sigma_{++} = \sigma_{--}, \qquad \sigma_{+-} = \sigma_{-+}. \tag{1.52}$$

The constraints result from the parity conservation of the reaction since the parity-violating weak interaction is negligible at the energy scale of this experiment.

[16] Because statistical uncertainty of A_{LL} is described as Equation (1.56), figure-of-merit for A_{LL} can be written as $L(\bar{P}^a \bar{P}^b)^2$ and the statistical error is proportional to $\frac{1}{\bar{P}^a \bar{P}^b \sqrt{L}}$.

[17] In this equation, it should be deemed that the differential cross section $d\sigma$ is integrated over a certain kinematical range and A_{LL} is also average value in the range.

In the experiment, the polarized proton beams are collided for a certain period and yield of particles produced in the collisions, which is π^0 in this thesis, are measured. In general, the yield is proportional to the cross section, σ, and integrated luminosity, L. The integrated luminosity is decomposed into and proportional to intensities of two beams. The beam polarization P is defined as

$$P = \frac{I_+ - I_-}{I_+ + I_-}, \tag{1.53}$$

where I_+ (I_-) is population of the proton with positive (negative) helicity in the beam. Obviously, range of P is -1 to $+1$. In accordance with these, the yield can be written as

$$N_{P^a P^b} = L_{P^a P^b}\, \epsilon\, \sigma_0 (1 + P^a P^b A_{LL}), \tag{1.54}$$

where two beams are identified by a and b at superscript of P. ϵ indicates a factor from the experimental instruments, such as detector acceptance, detection efficiency and so on. More detail formalization is described in Section A.3.

In this experiment, up to 120 bunches of the polarized proton beam are stored in each RHIC ring and continuously collided. It is optional to assign positive or negative helicity to each bunch of the protons. We usually choose the assignment of the beam helicities so as to occur the collisions with all possible helicity states in a single store of the beams. Owing to this feature, the data from the collision with any helicity combinations are obtained practically at the same time. The measurement confirmed no bunch dependence of the beam polarization and no difference in the polarization between positive- and negative-helicity bunches. See Section 2.1 in more detail about the beam. The helicity combination of the beams in every collision is categorized into 4 pattern; $(+\bar{P}^a, +\bar{P}^b)$, $(+\bar{P}^a, -\bar{P}^b)$, $(-\bar{P}^a, +\bar{P}^b)$ and $(-\bar{P}^a, -\bar{P}^b)$. $\bar{P}$ is introduced as absolute value of the beam polarization. For simplicity, each combination is written as $+-$ for $(+\bar{P}^a, -\bar{P}^b)$ and $N_{+-} \equiv N_{+\bar{P}^a\ -\bar{P}^b}$, for example.

Based on Equation (1.54), A_{LL} and its statistical error ($\Delta A_{LL}|_{stat}$) is obtained from the measured variables as follows;

$$A_{LL} = \frac{1}{\bar{P}^a \bar{P}^b} \frac{(N_{++} + N_{--}) - (N_{+-} + N_{-+})R}{(N_{++} + N_{--}) + (N_{+-} + N_{-+})R}, \qquad R = \frac{L_{++} + L_{--}}{L_{+-} + L_{-+}} \tag{1.55}$$

$$\begin{aligned} \Delta A_{LL}|_{stat} &= \frac{1}{\bar{P}^a \bar{P}^b} \frac{(N_{++} + N_{--})(N_{+-} + N_{-+})(1+R)}{(N_{++} + N_{+-} + N_{-+} + N_{--})^2} \\ &\quad \times \left[\left(\frac{\Delta(N_{++} + N_{--})}{N_{++} + N_{--}} \right)^2 + \left(\frac{\Delta(N_{+-} + N_{-+})}{N_{+-} + N_{-+}} \right)^2 \right]^{\frac{1}{2}} \\ &\sim \frac{1}{\bar{P}^a \bar{P}^b} \frac{1}{\sqrt{N_{++} + N_{+-} + N_{-+} + N_{--}}}. \end{aligned} \tag{1.56}$$

Here ΔN indicates error of N. To obtain the last equation, $N_{++} + N_{--} = N_{+-} + N_{-+}$, $R = 1$ and $\Delta N = \sqrt{N}$ are assumed. However, the assumption of $\Delta N = \sqrt{N}$ is finally modified as described in Section 3.6.3. In Equation (1.56), ϵ and σ_0 in Equation (1.54) are canceled between the numerator and the denominator, and the systematic uncertainties from them don't affect the result of A_{LL}. R is called "relative luminosity". Since R is ratio of the helicity-dependent luminosities, it is not necessary to consider absolute scale of the luminosities, which is usually one of the major uncertainties in cross section measurements. Consequently one needs to measure the beam polarization $\bar{P}$, the yield N and the relative luminosity R to extract A_{LL}.

1.12 Other asymmetries measured

In addition to A_{LL}, two kinds of asymmetries are measured in this thesis. One is single helicity asymmetry A_L. A_L appears with one of the incident protons polarized longitudinally and spin of the other proton is averaged. A_L is defined as follows;

$$A_L \equiv \frac{(d\sigma_{-+} + d\sigma_{--}) - (d\sigma_{++} + d\sigma_{+-})}{(d\sigma_{-+} + d\sigma_{--}) + (d\sigma_{++} + d\sigma_{+-})} = \frac{(d\sigma_{+-} + d\sigma_{--}) - (d\sigma_{++} + d\sigma_{-+})}{(d\sigma_{+-} + d\sigma_{--}) + (d\sigma_{++} + d\sigma_{-+})}. \quad (1.57)$$

$d\sigma$ and its subscripts indicate the cross section and helicity state of the incident protons. In the middle of Equation (1.57), spin of the proton denoted at the second sign of the subscript is averaged, while the first sign is averaged in the right-hand side. In the reaction conserving the parity, A_L must be zero. This is equivalent to that substituting Equation (1.52) into Equation (1.57) results in $A_L = 0$. In terms of the experiment, confirmation of zero A_L is important to prove validity of the measurement because the contribution of the weak interaction is negligible at the energy scale of the experiment.

Another measured asymmetry is transverse double spin asymmetry A_{TT}. A_{TT} appears when both incident protons are polarized transversely. Definition of A_{TT} is similar to A_{LL};

$$A_{TT} \equiv \frac{d\sigma_{\uparrow\uparrow} - d\sigma_{\uparrow\downarrow} - d\sigma_{\downarrow\uparrow} + d\sigma_{\downarrow\downarrow}}{d\sigma_{\uparrow\uparrow} + d\sigma_{\uparrow\downarrow} + d\sigma_{\downarrow\uparrow} + d\sigma_{\downarrow\downarrow}}. \quad (1.58)$$

Two arrows at subscripts of $d\sigma$ correspond to spin state of two incident protons each. $\uparrow$ ($\downarrow$) indicates that the spin is (anti)parallel to a certain axis which is perpendicular to motion direction of the beam. One difference from A_{LL} is dependence on azimuthal angle in the particle production. In general, the measured asymmetry (A'_{TT}) depends on $-\cos(2\phi)$, where $\phi = 0$ or π is defined as direction parallel to the polarization [85]. In this experiment, the detector covers 33.75 to 123.75 and -123.75 to -33.75 degrees. The scale factor is

$$\frac{\int -\cos(2\phi) d\phi}{\int d\phi} \sim 0.588. \quad (1.59)$$

Therefore, A'_{TT} must be scaled by the factor to obtain A_{TT}; $A'_{TT} \sim 0.588 A_{TT}$.

In analogy with the factorization of A_{LL}, A_{TT} is described by the convolution of the transversity, the partonic cross section and FF. As described in Section 1.5.3, the proton does not have the gluon transversity. Therefore, there is no contributions to A_{TT} from processes with gluons at the initial state in the QCD subprocess. Because gluon-gluon scatterings and gluon-quark scatterings are dominant in the measured p_T range (see Figure 1.10), A_{TT} is assumed to be smaller than A_{LL}. In addition, A_{TT} is suppressed at the stage of the QCD subprocess. Figure 1.13 displays the transverse double spin asymmetry of the partonic cross section ($\hat{a}_{TT}$). Because π^0s are detected at the central rapidity in our measurement, $\cos\theta$ is roughly zero. $\hat{a}_{TT}$ with the gluon at the initial state is not shown in Figure 1.13. In RHIC, the contribution from quark-quark scatterings is larger than quark-antiquark scatterings due to the proton-proton collider. Therefore, $\hat{a}_{TT}$ is suppressed in RHIC compared to $\hat{a}_{LL}$ in Figure 1.11. For these reason, A_{TT} is expected to be much smaller than A_{LL}.

In this thesis, A_{TT} is mainly regarded as contamination in the A_{LL} measurement. In practice, spin direction of the polarized beam is not exactly longitudinal in the measurement of A_{LL}, where it is of course intended to make the polarization longitudinal, due to imperfection of the instrumental apparatus. Remaining transverse component of the beam polarization

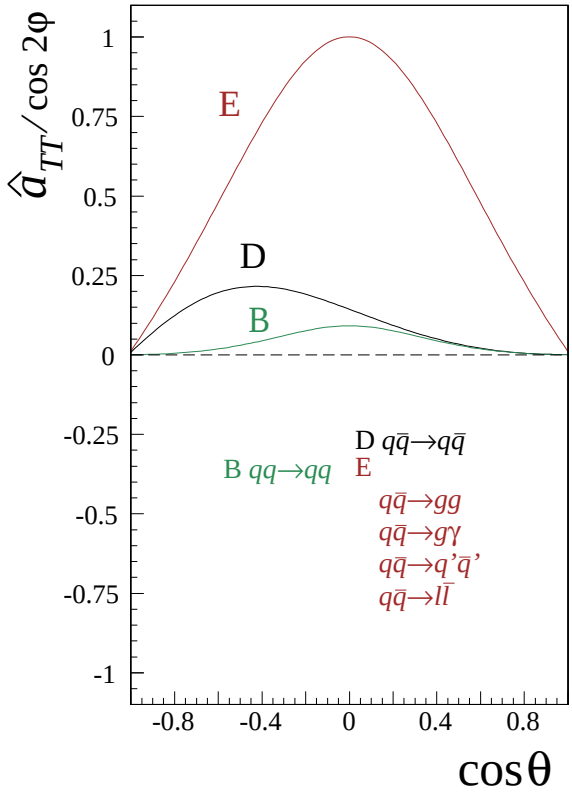

Figure 1.13: The transverse double spin asymmetry of the partonic cross section ($\hat{a}_{TT}$) as a function of the scattering angle on the partonic center-of-mass system. This is the leading order calculation. Our measurement covers central rapidity and it roughly corresponds to $\cos\theta \sim 0$. The azimuthal angle dependence of $\hat{a}_{TT}$, which is denoted as $\cos 2\phi$, is corrected in the figure.

causes contribution of A_{TT} to the measured asymmetry. In such a case, the relation between A_{LL} and measured quantity is modified as follows (see also Section A.3);

$$\frac{P_L^a}{\bar{P}^a}\frac{P_L^b}{\bar{P}^b}A_{LL} + \frac{P_T^a}{\bar{P}^a}\frac{P_T^b}{\bar{P}^b}A'_{TT} = \frac{1}{\bar{P}^a\bar{P}^b}\frac{(N_{++}+N_{--})-(N_{+-}+N_{-+})R}{(N_{++}+N_{--})+(N_{+-}+N_{-+})R}, \tag{1.60}$$

where P_L and P_T are longitudinal and transverse component, respectively, of the beam polarization and $\bar{P} = \sqrt{(P_L)^2 + (P_T)^2}$. Therefore, the measured asymmetry must be corrected by the term of A'_{TT} to extract A_{LL}.

Method to extract A_L and A_{TT} in the experiment is similar to Equation (1.56) for A_{LL}. To obtain A_{TT}, transversely polarized beam is used unlike the measurement of A_{LL}. See also Section A.3 for more detail.

Chapter 2

Experiment

The data for this thesis were taken by means of the PHENIX detector with polarized proton beam of RHIC (Relativistic Heavy Ion Collider) at Brookhaven National Laboratory (BNL) in the U.S. during the 2005 run.[1] The duration of the 2005 polarized proton run was about 10 weeks (April 17th – June 24th) mainly with the beam energy of 100 GeV, which corresponds to a center-of-mass energy ($\sqrt{s}$) of 200 GeV, and with the beam spin polarized longitudinally at the collision point of PHENIX.[2] The data taken in this period was used in the analysis. RHIC achieved a maximum luminosity of 10×10^{30} cm^{-2} sec^{-1} and an average luminosity of 6×10^{30} cm^{-2} sec^{-1}. PHENIX accumulated the integrated luminosity of 3.8 pb^{-1}. After various quality assurance selections for polarized beam, total amount of data used in this thesis is 2.4 pb^{-1}. The average polarization of the beams for this data set was about 50 %. Figure 2.1 displays the integrated luminosity and figure-of-merit for A_{LL} as a function of time. In this chapter, the experimental setup is explained.

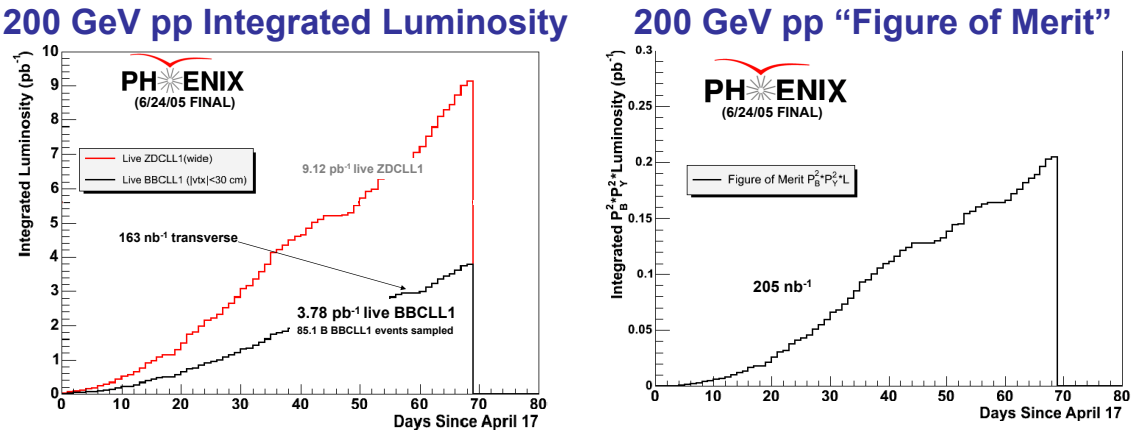

Figure 2.1: (Left) Integrated luminosity as a function of time. The black line is for BBCLL1 live trigger and the red line is for ZDCLL1-wide live trigger. Events with BBCLL1 is used in the usual analysis at PHENIX, as well as in this thesis. See Section 2.3.5 about the triggers. (Right) Figure-of-merit for A_{LL} as a function of time. The figure-of-merit is based on BBCLL1 live trigger. See Section 1.11 about the figure-of-merit.

[1] RHIC can also collide heavy ions up to $\sqrt{s}$ of 200 GeV per nucleon to search for quark gluon plasma.

[2] In the 2005 run, a short physics run with transverse polarization and a commissioning run with the beam energy of 205 GeV were also performed.

2.1 RHIC as a polarized proton collider

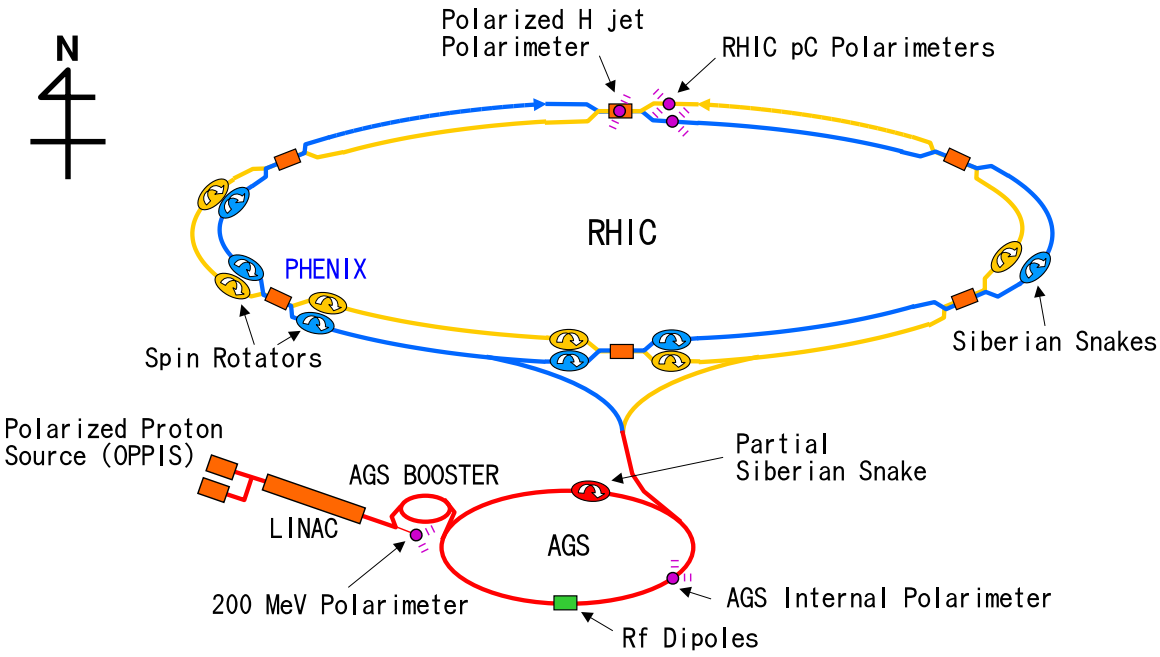

Figure 2.2: The accelerator complex of RHIC for the polarized proton run.

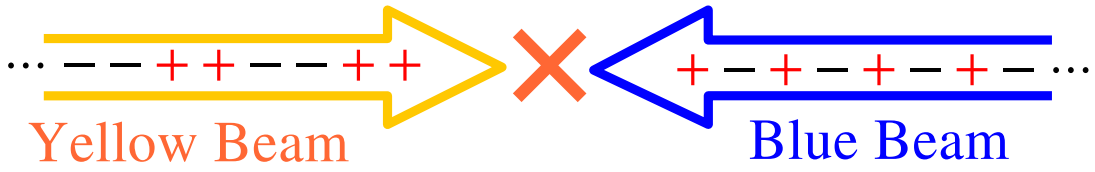

Figure 2.3: Example of the spin pattern of the beams. In this case, positive and negative helicities are assigned to the alternating successive bunches in the blue beam and the alternating successive pairs of bunches in the yellow beam. This spin pattern allows us to detect particles from the collision with any helicity combinations at the same time.

Figure 2.2 displays the accelerator complex to accelerate and collide the polarized proton beams. The polarized proton is provided at optically pumped polarized H^- source (OPPIS), where the DC beam of 0.5 – 1.5 mA H^- in a single 300 μsec pulse ($9 - 28 \times 10^{11}$ H^- ions) and the polarization of more than 80 % was reached [86]. A pulse of H^- is accelerated up to 200 MeV in kinetic energy by an RFQ (Radio Frequency Quadrupole) and the LINAC (Linear Accelerator) with an efficiency of ~50 %, then it is strip-injected and captured into a single bunch in the AGS (Alternating Gradient Synchrotron) booster. Bunched polarized protons are accelerated by the booster to kinetic energy of 1.5 GeV and transferred to AGS. Protons achieve the energy of 24.3 GeV in AGS and are injected through AGS-to-RHIC transfer line into two RHIC rings, which are referred to as blue (clockwise) and yellow (counter-clockwise) rings. RHIC can accelerate protons keeping polarization up to 250 GeV and collide them at

the 6 interaction points.[3]

RHIC can store up to 120 bunches of polarized proton beam in each ring and therefore the time interval of the bunches is 106 nsec considering the RHIC circumference of 3834 m. The process to boost the protons from the source and inject them into the RHIC ring is repeated bunch by bunch until all planned bunches are filled. After that, the bunches of the protons are accelerated up to the flat top energy in RHIC and then collided. The collisions continue with typical life time of 8 hours and then the beams are dumped. We define "fill" as a sequence of the flow from injection to dump of the beam. One of the remarkable features of RHIC is that the spin pattern of the bunches is optional by freely flipping the spin of the protons at OPPIS bunch by bunch. (see Figure 2.3) This feature makes it possible to collect the data of the collision with possible spin combination almost simultaneously. This is greatly helpful in the analysis, where one can cancel out any common systematic uncertainties between bunches, therefore between spin combinations, like that of detector acceptance. Only errors depending on the bunches have to be considered, for example, such as the correlation between bunch characteristic (intensity and shape) and spin because a certain bunch of the blue ring collides always with the same bunch of the yellow ring.[4]

RHIC is designed with ε_N (normalized emittance) of 20π mm·mrad and β^* (betatron amplitude function at an interaction point) at PHENIX of 1 m. The transverse size of the beam at the PHENIX collision point is calculable using these values to be $\sim$0.4 mm. This value is reasonable compared with the measurement, where the transverse beam profile is estimated from the collision rates with the beam positions continuously shifted each other. It must be also noted that the transverse position of the collision and the tilt of the beam travel from the designed circumference are negligible compared to other systematic uncertainties like a resolution or a misalignment of the detector (see Section 3.7.1). The spread of the actual collision position along the beam axis is typically 50 cm in root-mean-square (RMS), which is measured by the detector and the longitudinal offset from the ideal collision point is considered in the analysis.

The spin of the beam is oriented to the vertical direction, which is the stable direction during the acceleration in the normal synchrotron accelerator because the magnetic field to bend the beam is vertical. However, there are many depolarizing resonances at certain beam energies, depending on parameters of the accelerator. The important role to overcome the depolarization and maintain the beam polarization is played by the "Siberian Snake" magnets [87]. To avoid additional depolarizing resonance caused by installing the single Snake, Two Snakes are placed in each ring of RHIC and the location of one Snake is opposite side of the other (3 o'clock and 9 o'clock). Each Snake in RHIC consists of four superconducting helical dipole magnets of identical structure. The strength and the direction of the field are different between four magnets (-4 – $+4$ T), while they are independent of beam energy. By one Snake's reversing the spin direction of the beam without an orbit distortion at the entrance and the exit of the Snake, the resonance conditions are shifted and the depolarization is avoided. Similarly, one other type of the Snake magnet is placed in AGS. Unlike the Snake in RHIC, the AGS Snake is just one normal-conducting helical dipole magnet and rotates the direction of the beam spin by only 9 degrees, which is enough to maintain the polarization in the lower-energy synchrotrons, such as AGS, with weaker depolarizing resonances. This partial rotation forces to induce full spin flip at the beam energy on the depolarizing resonances,

[3]Comparing the RHIC rings to a clock face, each interaction point is named using number of its location, for example, as IP12 or 12 o'clock for the most north interaction point.

[4]Actually, a certain spin combination is usually assigned to more than 10 bunches in one fill, therefore the bunch characteristic is well averaged and the difference between spin combinations becomes small.

while it keeps spin direction unperturbed except for such a depolarizing conditions.

It is necessary to collide beams with polarized longitudinally to measure double helicity asymmetry to study gluon polarization in the proton. To realize this purpose, spin rotators are located before and after the interaction region of PHENIX in each ring; the former rotates the beam spin from the vertical to the longitudinal direction and the latter restores it to the vertical direction. It is also possible to collide beams with radial transverse polarization, but data with such a condition were not taken in the 2005 run. One spin rotator consists of four helical dipole magnets, whose structure is same as that for the Snake magnet except two of them have alternate handedness of helical magnet. They are powered independently to generate appropriate field needed for the spin rotation, which depends on the beam energy (-3 – $+3$ T at around 100 GeV).

2.2 Polarimeters

RHIC utilized two types of polarimeters to determine the absolute beam polarization; the proton-carbon polarimeter [88] and the polarized hydrogen gas jet polarimeter [89]. In addition to these, another polarimeter is located at the interaction region of PHENIX to monitor the direction of the beam polarization at the time of the collision. All of these polarimeters utilize the transverse single-spin asymmetry (A_N) which arises by the collision of the transversely polarized beam and the target (or another beam). Because the measured raw asymmetry (ϵ) is proportional to the beam polarization (P), if the size of the physics asymmetry A_N is known, one can obtain the beam polarization by dividing ϵ by A_N ($P = \epsilon/A_N$). The average beam polarization for the data set in this study was about 50 %. The error on the polarization behaves as the scale error on A_{LL}. The spin rotators were turned on during the data taking period for this study. The transverse component of the beam polarization at the collision point was measured to be less than 15 %, which corresponds to the longitudinal component of more than 98 %. See Section 3.3 and Table 3.1 in Section 3.2 about the polarization in this thesis.

2.2.1 Proton-carbon polarimeter (pC polarimeter)

The proton-carbon polarimeter (pC polarimeter) employs A_N in the elastic scattering between the polarized proton beam and the carbon target ($A_N^{p\mathrm{C}}$) at very forward region, 4-momentum transfer squared of $-t \sim 0.01 - 0.02$ GeV$^2/c^2$. It is desirable to collect high statistics within short measurement time to periodically monitor the polarization with satisfactory accuracy and without disturbing physics experiments. While the size of $A_N^{p\mathrm{C}}$ in this $-t$ region is small, about 1 %, the cross section is large. Moreover, the requirement is satisfied by using an ultra-thin carbon ribbon of 3 – 5 μg/cm^2 with a width of 10 μm as the target. It is inserted into the beam at the polarization measurement and slow recoil carbons are detected by the silicon detectors placed on both sides of the target. pC polarimeter collects $\sim 2 \times 10^7$ events per one measurement of $\sim$20 seconds on an average. It corresponds to the statistical error of the beam polarization of $\sim$2 %, which is comparable with fill-by-fill uncorrelated systematic uncertainty and smaller than global systematic uncertainty of $\sim$6 %. The measurements were performed about once an hour and it turned out that there is no significant depolarization during the fill. Owing to large event sample, it is possible to study the bunch-by-bunch variation and no bunch dependence in the polarization was confirmed within the uncertainty of the measurement. One difficulty of pC polarimeter was large systematic uncertainty due to the unknown $A_N^{p\mathrm{C}}$ at the beam energy of 100 GeV, which was extrapolated from the

measurement at 21.7 GeV on the basis of the theory. This systematic shift was calibrated by another polarimeter, the polarized hydrogen gas jet polarimeter.

2.2.2 Polarized hydrogen gas jet polarimeter (jet polarimeter)

The polarized hydrogen gas jet polarimeter (jet polarimeter) features the self-calibration system, which means that absolute beam polarization can be measured without any theoretical assumption by means of the scattering of identical particles with both polarized. Jet polarimeter utilizes A_N in the proton-proton elastic scattering (A_N^{pp}); the polarized proton beam and the polarized atomic hydrogen gas jet target.

Since both the beam and the target are polarized and periodically flip its spin direction, A_N^{pp} can be defined by using either the beam or the target polarization, and averaging the other polarization to reproduce the unpolarized condition; polarized beam with unpolarized target and unpolarized beam with polarized target. In either case, A_N^{pp} is same in the same kinematical region. The polarization of beam (P_{beam}) and target (P_{target}) are related as $A_N^{pp} = \epsilon_{beam}/P_{beam} = \epsilon_{target}/P_{target}$, where $\epsilon_{beam}(\epsilon_{target})$ is the measured raw asymmetry based on the beam (target) polarization. Therefore the beam polarization can be determined absolutely by the well-known P_{target} and the asymmetry measurement with sufficient precision.

The free atomic hydrogen gas jet crosses the RHIC beam from top to bottom at a speed of 1.6×10^3 m/sec. The areal density of the target is 10^{12} H atoms/sec. The direction of the target spin is vertical and reversed every 10 minutes. The target polarization is measured by a Breit-Rabi polarimeter, which is located below the interaction point with the beam, to be 0.924 ± 0.018 and no difference in the polarization is observed between spin up and down. The recoil protons are detected by silicon detectors located to the left and to the right of the target. The kinematical region of $0.001 < -t < 0.01$ GeV$^2/c^2$ in the proton-proton elastic scattering is used to determine the beam polarization. A_N^{pp} is around 4 % in this kinematical range and the order of 10^7 events is required in terms of the precision. However, because the event rate of jet polarimeter is very low, about 5 Hz, due to the gas target, it cannot be used for the periodical fast measurement, unlike pC polarimeter with high event rate using the solid target. On the other hand, the operation of jet polarimeter does not interrupt the physics measurements because of the low event rate. Jet polarimeter accumulated events continuously through the 2005 run and the average beam polarization over the run was extracted. The relative error of the beam polarization ($\Delta P/P$) was $\sim$6 % based on the measurement by jet polarimeter. To normalize pC polarimeter, pC polarimeter aggregated the data in the same period as when jet polarimeter operated and extracted $A_N^{p\mathrm{C}}$ using the beam polarization determined by jet polarimeter. The fill-by-fill and hourly beam polarization was in turn obtained based on measured $A_N^{p\mathrm{C}}$. In this sense, jet polarimeter is regarded as the calibrator for pC polarimeter.

2.2.3 PHENIX local polarimeter

It is necessary for the study of the polarized gluon distribution to collide the beam with longitudinally polarized. The function to rotate the beam spin from vertical to longitudinal direction is carried out by the spin rotator described in Section 2.1. In the interaction region of PHENIX, two polarimeters are located for the blue and the yellow beam to monitor the direction of the beam polarization at the collision point (local polarimeter). As hardware, local polarimeters are identical to zero degree calorimeters of PHENIX, which are placed at 1800 cm away from the collision point and between the blue and yellow beam pipes after DX magnet for the separation of two beams. The size of the acceptance is 13.6 cm high

and 10.0 cm wide. See Section 2.3.3 for more details about the detector. The single spin asymmetry with longitudinally polarized beam (A_L) is expected to be 0 (or quite small) in the proton-proton collision because it violates the parity conservation. Instead, local polarimeter uses A_N in the neutron production at the proton-proton collision. The size of the asymmetry is ∼10 % at $\sqrt{s}$ = 200 GeV and significant asymmetry is observed even at $\sqrt{s}$ =62 and 410 GeV. The asymmetry appears for the neutron generated in the forward region in view of the polarized beam, and therefore each local polarimeter watches the beam facing it. Local polarimeter confirms that the beam is polarized longitudinally at the collision point by measuring zero asymmetry because A_N can be observed with a transversely polarized beam. Moreover, it can also determine the residual transverse component of the beam polarization by comparing the size of the asymmetries measured with spin rotator on and off. One concern is whether the beam helicity is positive or negative with the rotator on because A_N is related to only transverse component of the beam spin and therefore local polarimeter can not determine its longitudinal direction. The concern is resolved by commissioning the rotator carefully. For example, by tuning the rotator, radial polarization is obtained as expected; it can be confirmed by local polarimeter.[5] The feature of local polarimeter is that its nondestructive measurement allows other physics measurements in parallel with it. It is important to remind that pC polarimeter observed $A_N^{p\mathrm{C}}$ with rotators on and with the asymmetry by local polarimeter zero. This means that spin rotators properly restore the beam polarization from the longitudinal to the vertical direction.

2.3 PHENIX detector

2.3.1 Overview

The location of the PHENIX detector is 8 o'clock of the RHIC ring. The photos of the PHENIX detector as well as the schematic view are displayed in Figure 2.4 and 2.5. For convenience, we define Cartesian coordinate system in PHENIX. The z-axis is taken along the beam axis and its direction is south to north at 8 o'clock. The y-axis is oriented from bottom to top and the x-axis is east to west. The origin is the planned collision point by RHIC and many detectors of PHENIX are constructed symmetrically about the origin. The variable often used in this thesis is also defined in Figure 2.6. Azimuthal angle (ϕ) of a vector is defined as the angle between the y-axis and the projection of the vector on the x-y plane. Polar angle (θ) of a vector is defined as the angle between the x-y plane and the vector. Therefore pseudorapidity (η) is defined as $\eta = \log\left[\frac{1+\tan(\theta/2)}{1-\tan(\theta/2)}\right]$. Based on this coordinate, the detectors of PHENIX are sometimes called with prefix of the direction, like east arm and north counter, for example.

The abbreviations of the detectors in Figure 2.5 are listed in Table 2.1. The PHENIX detector consists of global detectors and four spectrometers. Global detectors include beam-beam counters and zero degree calorimeters. They can provide information about characteristic of event and are frequently utilized in various analysis in PHENIX.

Two of spectrometers are constructed at the left and right side of the collision point to cover central region (central arms). Each central arm has the acceptance of -0.35 to $+0.35$ in pseudorapidity and 90 degrees (33.75 to 123.75 and -123.75 to -33.75 degrees) in azimuthal angle. To measure momentum of charged particles, the inside of the central arms are filled by

[5]The rotator is operated considering the effect of the DX magnet to bend the beam, which also rotates the beam spin. For this reason, even if the rotator is configured by mistake, it does not result in the opposite helicity to what is expected. This also assures that the the beam helicity is correct direction.

Figure 2.4: (Top) The photo of the PHENIX detector from beam view. Beams go up and down. The two spectrometers on the left and right side are the central arms. The blue detectors at the outermost are EMCal. The north muon arm was not installed at the time when the photo was taken. (Bottom) The side view of the PHENIX detector. Beams go left and right. The two spectrometers on the left and right are the muon arms. The structure labeled as PHENIX at the center is the magnet for the central arms. The east arm is moved in the bottom photo.

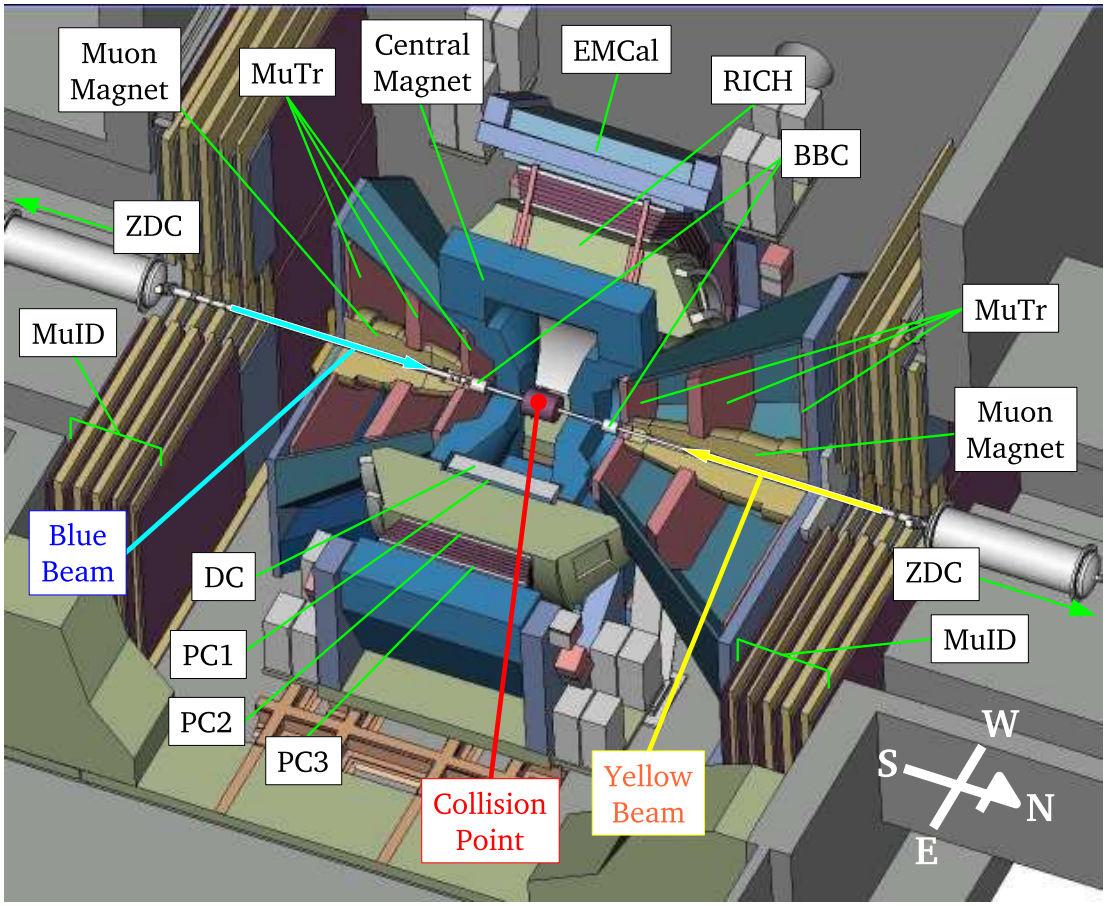

Figure 2.5: The cutaway figure of the PHENIX detector.

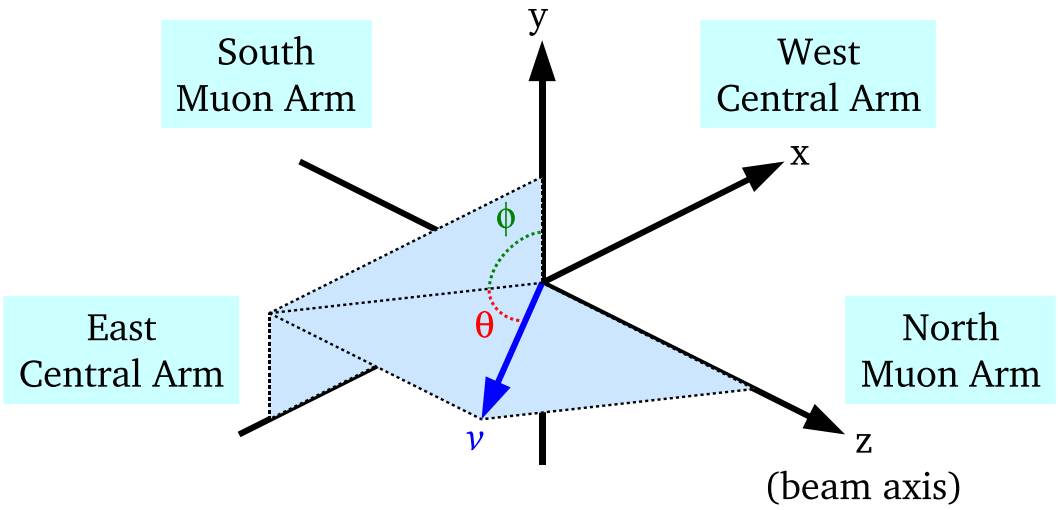

Figure 2.6: The coordinate at the PHENIX detector. The beams go on the z-axis. Azimuthal angle ϕ and Polar angle θ is defined for the reference vector v as shown in the figure.

Abbreviation	Detector name
BBC	beam-beam counters
ZDC	zero degree calorimeter
DC	drift chamber
PC1, 2, 3	pad chamber 1, 2, 3
RICH	ring image Cherenkov counter
TEC	time expansion chamber
ToF	time of flight detector
EMCal (PbSc)	electromagnetic calorimeter (lead scintillator)
(PbGl)	(lead glass)
MuTr	muon tracker
MuID	muon identifier

Table 2.1: The abbreviations of the detectors.

the magnetic field, which is oriented along the beam axis, and therefore charged particles are bent to the azimuthal direction. The magnet (the central magnet) is designed not to block the aperture of the central arms and to minimize the interaction with particles produced at the collision point. The central arms include chambers for tracking charged particles, RICH and ToF for particle identification, and EMCal to detect mainly electrons and photons. Figure 2.7 displays the beam view of the central arm.

Another two spectrometers specialize in the detection of muon (muon arms) and located at the forward and backward region. The coverage of the south (north) muon arm is $1.2 < |\eta| < 2.2$ (2.4) over full azimuth. Each muon arm consists of two detector systems; MuTr to measure momentum of muons and MuID to select muon events. To measure the momentum of the particles, MuTr is enclosed by the conical-shaped magnet which generates radial field. In addition to these detectors, a material of 5 interaction lengths is located between the collision point and the muon arm and it reduces the hadron background by a factor of $\sim$100. In this thesis, this arm is not used, however it plays the leading role in physics with W bosons, which are detected by hunting high-momentum muons, to study the contribution of sea quarks to the proton spin (see also Section 4.5).

The PHENIX detector is composed of many sub-detectors to cover a wide range of physics by detecting various kinds of particles including photons, electron, muons and identified hadrons. The goal of this work is to study the gluon polarization in the proton via the measurement of A_{LL} in the π^0 production. Hence, a part of the PHENIX detector related to the π^0 detection is mainly used in this thesis. The most important detector in this thesis is EMCal at the outermost of the central arm. Both the energy and the hit position of the photons from the decay of π^0s are detected by use of EMCal. EMCal generates trigger for high energy photon, which is described in Section 2.3.4. To support particle identification, PC3 in front of EMCal is used to remove charged particle. BBC and ZDC, which are used in the general analyses in PHENIX, are essential in addition to EMCal. They can measure the position the beams collide at. Because of the better resolution of BBC than ZDC, the measurement by BBC is usually adopted for the purpose. Moreover, the events triggered by BBC is adopted as the minimum bias trigger, which is also one of the requirements for the high-energy photon trigger, and the number of such events is used for both the absolute and the relative luminosity. See Section 2.3.5 about the trigger. ZDC has the role as local

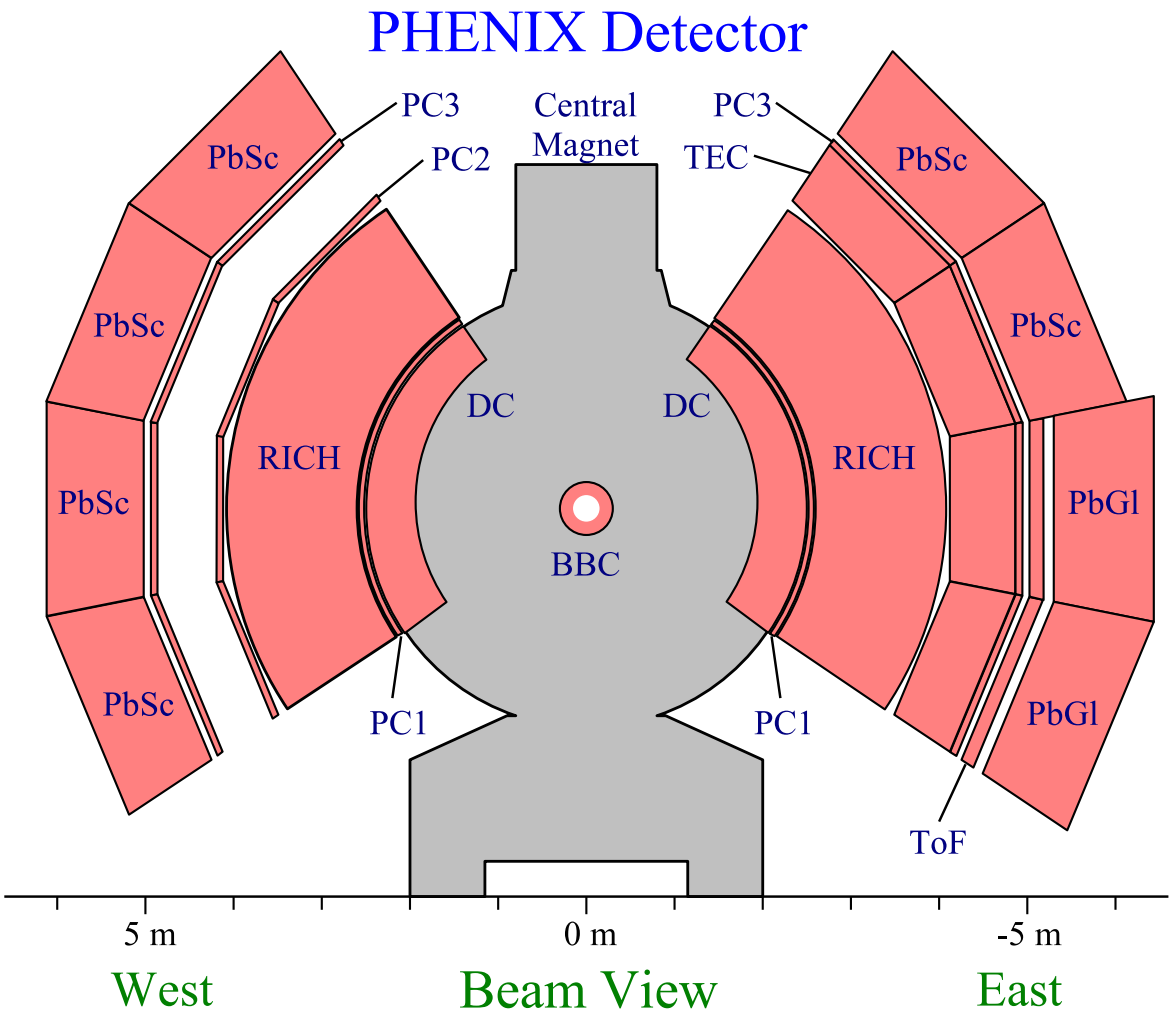

Figure 2.7: The beam view of the PHENIX detector. The beams pass the center of BBC.

polarimeter as described in Section 2.2.3. In addition, ZDC is reference detector to BBC to evaluate the uncertainty of the relative luminosity. In the following sections, detectors playing major role in this thesis, BBC, ZDC and EMCal, and data acquisition system (DAQ) are explained. Introduction for some other detectors are described in Section A.4.

In the following text, we concentrate on the system of PHENIX and the specific procedure for PHENIX. To explain things smoothly, we define some terminologies used in this thesis. We describe the origin of the PHENIX coordinate as "collision point" and actual position the beam protons collide at as "event vertex" to avoid confusing. As described in Section 3.7.1, the transverse component (offset in the x-y plane) of the event vertex and the direction of beam momentum momentum at the collision point are ignored in this thesis. What a bunch of the RHIC beam crosses the collision point is described as "beam crossing". RHIC is designed to collide a bunch of the blue beam always with a certain bunch of the yellow beam. Therefore the events taken at PHENIX are sorted by the crossings and the "crossing number", $0 - 119$, is assigned to each event. The dependence of measurements on the crossing is often discussed since some important variables such as the luminosity and the spin pattern are dependent on

the crossing. Technically the system of PHENIX like the electrical circuits is synchronized with 9.4 MHz clock called "RHIC beam clock", or simply RHIC clock, which is the periodic pulse generated every crossing timing of $\sim$ 106 nsec.

2.3.2 Beam-beam counters (BBC)

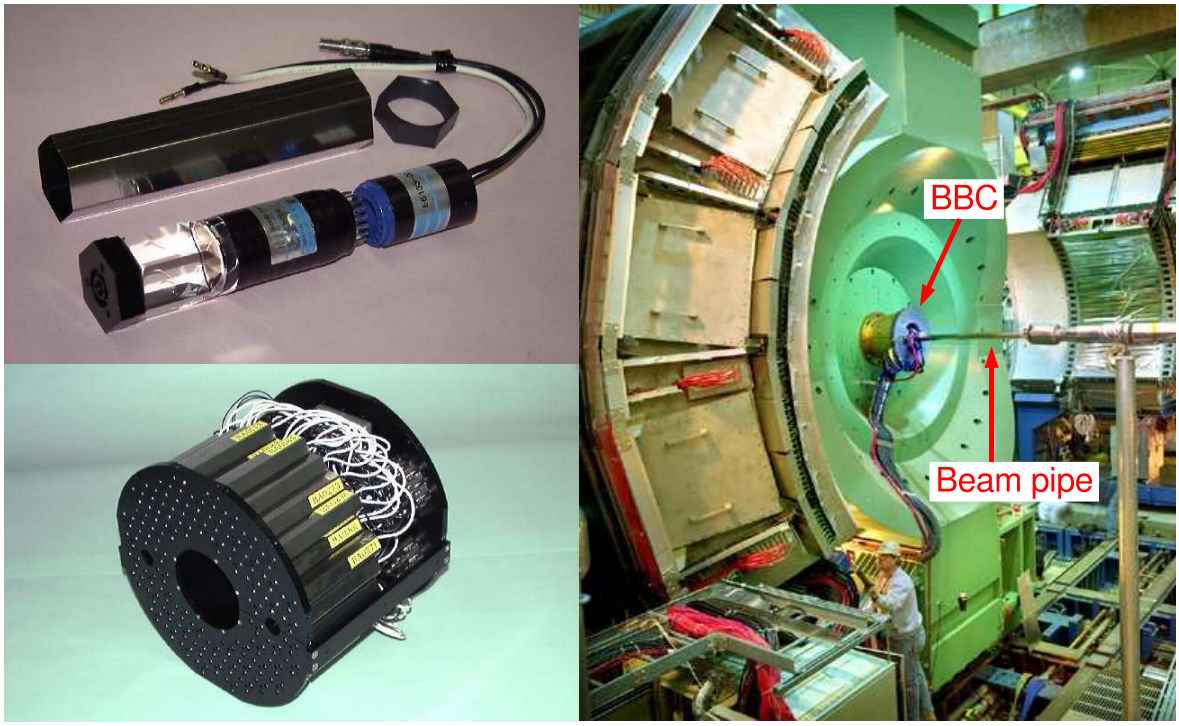

Figure 2.8: Photos of BBC. (Left top) The element of BBC. (Left bottom) The half piece of BBC which consists of 64 elements. (Right) BBC after installation. The collision point is the left of the picture and BBC is attached behind the magnet of the central arm.

Beam-beam counters (BBC) consist of two identical pieces installed across the beam interaction point and along the beam axis. Each counter surrounding the beam pipe is located at 144 cm from the collision point and has outer diameter of $\sim$30 cm and inner diameter of $\sim$10 cm. This corresponds to the acceptance of 3.0 – 3.9 in pseudorapidity (η) over full azimuth. Each counter is composed of 64 photomultiplier tubes (PMT) of 2.5 cm diameter attached to 3 cm-long quartz as a Cherenkov radiator, and therefore 128 elements are in whole BBC. The shape of quartz is hexagonal cylinder and they are assembled closely each other. The photos of BBC are displayed in Figure 2.8.

The important role of BBC is to determine the collision time and the event vertex. The former is used as the start time of the time-of-flight measurement and the latter is primary start point for the particle tracking. The width of the vertex along the beam axis is typically 50 cm. The collision time and the event vertex are obtained from the timing information of the hit in the counters. The collision time is related to the average time of the counters, $\frac{T_S+T_N}{2} - \frac{L}{c}$, where T_S (T_N) is the time of the particle hit in south (north) counter, L is the distance from the collision point to each counter (= 144 cm), and c is the speed of light. T_S and T_N are estimated by averaging the timing of the elements with particle hit in

each counter. The vertex is calculated from the time difference of the counters, $\frac{c(T_S - T_N)}{2}$. Therefore, the time resolution of BBC is important for both the efficient particle identification and the precise tracking. As described above, the event vertex is reconstructed online with degraded precision and utilized for the trigger of the data taking (see Section 2.3.5 about the trigger). In addition, the number of such triggered events is counted by a scaler and is used as the relative luminosity. The resolution of the event vertex is estimated to be ∼5 cm online. In the offline analysis, the precision is improved by applying corrections like a basic slewing correction as well as using the data without degradation. The collision time resolution (ΔT_S and ΔT_N) of better than 100 psec and the vertex resolution of 2 cm is achieved offline. In both offline and online, at least one hit is required in each counter to reconstruct the event vertex. The proton-proton cross section detected by BBC is ∼23 mb, which corresponds that the detection efficiency of BBC to the proton-proton collision is about 50 %. The most of the cross section measurements utilize the events triggered by BBC to normalize the yield by the luminosity.

2.3.3 Zero degree calorimeter (ZDC)

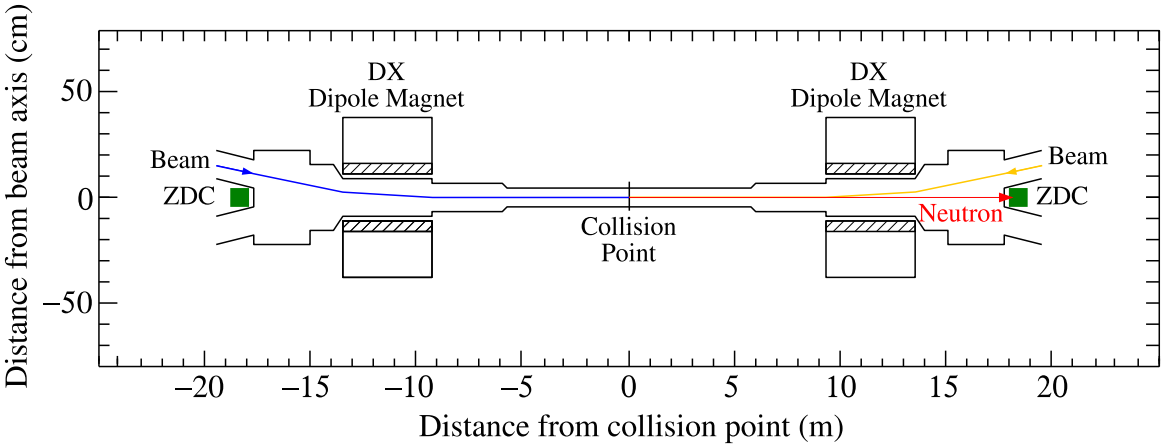

Figure 2.9: The top view of the ZDC location.

In PHENIX, 2 zero degree calorimeters (ZDC) are installed at the north and the south side of the collision point each as displayed in Figure 2.9. They are placed at 1800 cm away from the collision point between the blue and the yellow beam pipes on the extended line of the beam axis (on the z-axis) behind the DX magnet to bend the beam. The acceptance window is 10 cm wide and 13.6 cm high. The width of the detector is constrained by limited space. ZDC is a hadron calorimeter composed of three identical modules. The mechanical design of the module is displayed in Figure 2.10. Each module is made by an absorber of tungsten plates to generate hadronic shower and PMMA-based (polymethylmethacrylate-based) optical fibers to detect the Cherenkov radiation emitted by charged particles in the shower. The size of the tungsten plate is 10 cm wide, 18.7 cm high and 0.5 cm thick. The optical fibers with diameter of 0.5 mm and numerical aperture of 0.5 are arranged in plates and fixed by silicone rubber glue. In one module, 27 layers of tungsten plate and optical fibers are sandwiched each other with tilted by 45 degrees. This angle is defined to roughly accord with the direction of the Cherenkov radiation in the optical fibers with refractive

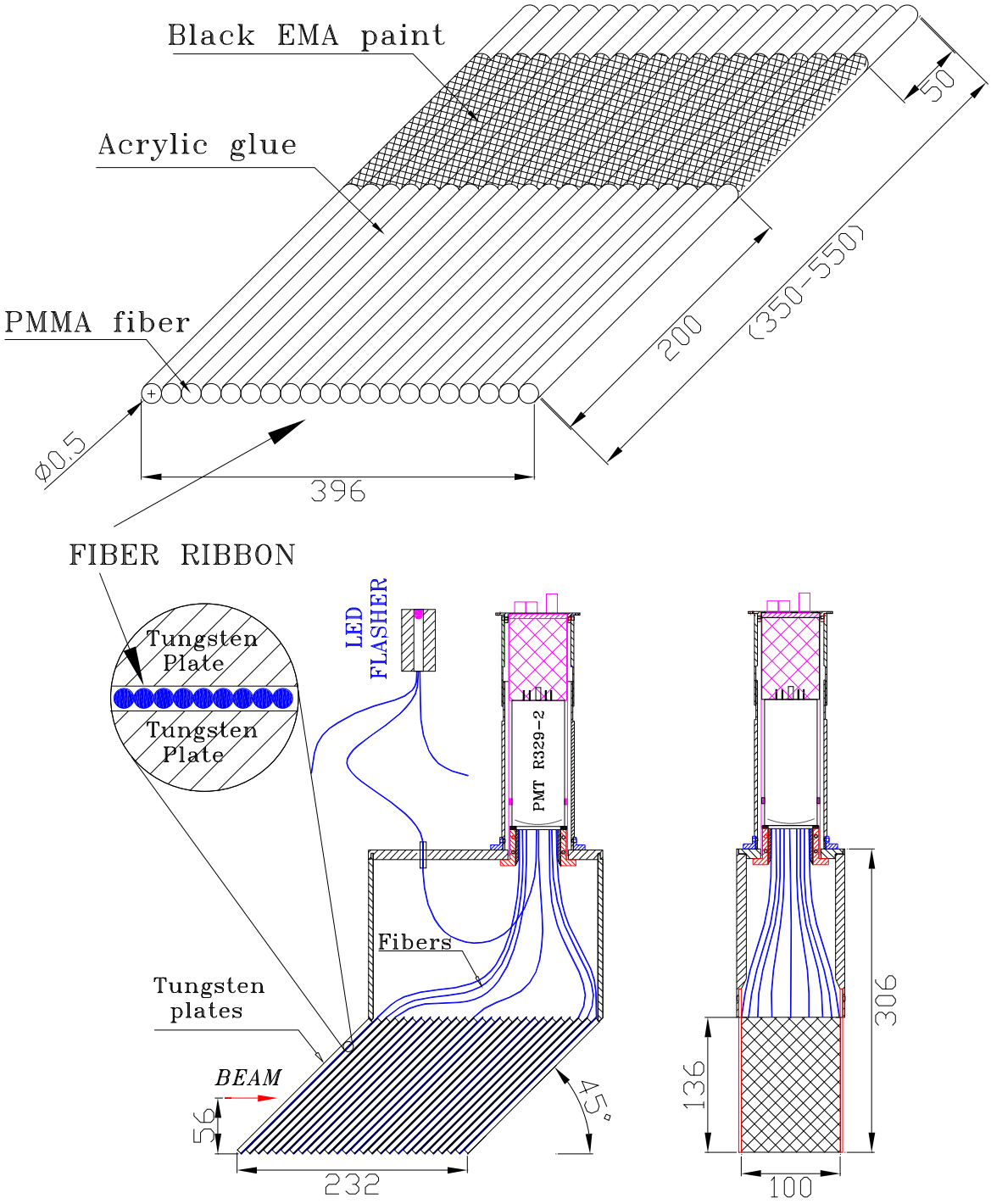

Figure 2.10: The mechanical design of ZDC. Dimensions shown are in millimeter. The side view and the beam view of one module is displayed in the bottom left and the bottom right, respectively. The top is one layer of the PMMA fibers.

index of ∼1.5. All optical fibers in one module are gathered and mounted on one PMT. After assembled, one module has length of 23.2 cm, interaction length of 1.7 and radiation length of 50. The performance of ZDC is evaluated using test beam and energy resolution of 19 % at 100 GeV proton beam was obtained. Because ZDC is located just behind the DX magnet, charged particles are swept away and neutral particles of long life, mainly photons and neutrons, can arrive at ZDC. The separation of photons and neutrons is done by looking at the energy deposit in the second module, which electromagnetic shower cannot reach due to long radiation length.

In order to measure 2-dimensional position of the particle hit, 2 layers of scintillator hodoscopes are installed between the first and second module of ZDC. Twenty-one scintillator slabs with size of $0.5 \times 0.5 \times 18$ cm^3 are oriented vertically and run along horizontal direction for the x-coordinate in one hodoscope and 3 neighboring slabs are read out by single channel of multi-anode PMT. The other hodoscope consists of 32 slabs which are oriented horizontally and run along vertical direction for the y-coordinate and 4 slabs group for single channel. Therefore 15 channels are read out in total for hodoscopes in each ZDC. The position of the particle hit is obtained by taking center of gravity weighted by the energy deposit in each scintillator. The position resolution for hadronic shower is still under discussion. Bad resolution causes dilution in A_N in terms of PHENIX local polarimeter described in Section 2.2.3. However, to know only longitudinal component of the beam polarization, such systematic uncertainty can be canceled by comparing the asymmetries with the spin rotator on and off.

In addition to the role of PHENIX local polarimeter, the event vertex is obtained using both north and south ZDC in the same way as BBC, though the resolution is worse than that of BBC. The vertex resolution by ZDC is ∼30 cm online and ∼10 cm offline. The coincidence of both ZDC hits with a certain vertex range selected is one of the trigger inputs in the data taking. The number of this trigger is recorded by a scaler as well and is important as the reference to that of BBC in the analysis of relative luminosity (see Section 3.4). The energy threshold applied for the trigger is ∼5 GeV for each ZDC, while it is 20 GeV for the local polarimeter to select neutron events.

2.3.4 Electromagnetic calorimeter (EMCal)

In the central arm, the outermost part from the collision point is covered by electromagnetic calorimeters (EMCal). The energy of photons and electrons can be measured by use of EMCal, while it is hard to determine that of hadrons due mainly to small nuclear interaction length (∼1). As well as the energy, the time-of-flight (ToF) of the particles between EMCal and the event vertex, which is used for the particle identification, is measured. As described in Section 2.3.2, the start time at the event vertex is determined by BBC. Moreover, because PHENIX EMCal is finely segmented both along the beam axis and along azimuthal direction, the position of the particle hit can be also obtained by estimating the center of the electromagnetic or hadronic shower from the energy distributed between adjacent segments. We call this segment "tower". Though the track of charged particles is determined by inner tracking chambers with better accuracy than EMCal, the matching between the track by the chambers and the hit position by EMCal is helpful to separate photons, electrons and charged hadrons. Technically, since the energy of the incident particle is distributed over several neighboring towers, it is necessary to reconstruct the cluster from the energy deposited in each tower. In this process, the profile of the shower is obtained and useful for the separation of the electromagnetic shower and the hadronic one. Such a procedure is described in Section 3.5.2.

EMCal is constructed for both central arms and its acceptance covers full arms; from

-0.35 to $+0.35$ in pseudorapidity and 90 degrees (33.75 – 123.75 degrees) in azimuthal angle in each arm. EMCal is divided into 4 sectors in each arm. Each sector covers 22.5 degrees in azimuthal angle and same pseudorapidity region as the central arm. In terms of the size of its surface, each sector has about 4 m along the beam axis and 2 m along the azimuthal direction. In this thesis, we name EMCal sectors in the west (east) arm W0, W1, W2, W3 (E0, E1, E2, E3) from bottom to top. Two kinds of electromagnetic calorimeters are used in PHENIX; lead-scintillator sampling calorimeter (PbSc) and lead-glass Cherenkov calorimeter (PbGl). PbSc is adopted for all sectors in west arm and upper 2 sectors in east arm (W0 – W3, E2 and E3), while rest 2 sectors (E0 and E1) is PbGl. The distance from the collision point to each sector is slightly different between PbSc and PbGl, 507 cm for PbSc and 540 cm for PbGl, because an additional detector for the ToF measurement [90] is installed in front of PbGl. The features of PbSc and PbGl are very different and summarized in Table 2.2. Total EMCal consists of 24768 towers (channels), and the deposit energy and the signal timing of each tower are read out using PMT and recorded. The energy measured by EMCal is utilized for a trigger to collect high energy photons, which are of interest to the study of the gluon polarization in the proton as well as the examination of QCD via the cross section measurements. Specific features of PbSc and PbGl, the readout electronics and trigger scheme are described in following sections.

Quantity	PbSc	PbGl
Radiation length (X_0)	2.1 cm	2.8 cm
Moliere radius	$\sim$3.0 cm	3.7 cm
Nuclear interaction length (λ_I)	44 cm	38 cm
Total η coverage	0.7	0.7
Total ϕ coverage	$90 + 45$ degrees	45 degrees
Number of sectors	6 (W0–W3, E2, E3)	2 (E0, E1)
Size of sector surface	2×4 m^2	2×4 m^2
Number of towers in one sector	36×72	48×96
Tower cross section	5.5×5.5 cm^2	4.0×4.0 cm^2
Tower $\eta \times \phi$ coverage	0.011×0.011	0.008×0.008
Tower depth	37.5 cm	40.0 cm
Tower depth in X_0	18	14
Tower depth in λ_I	0.85	1.05

Table 2.2: Design parameters of PbSc and PbGl.

Lead scintillator calorimeter (PbSc)

Each PbSc tower consists of 66 layers of alternating tiles of lead and plastic scintillator. The scintillator based on polystyrene contains 1.5% of p-Terphenyl and 0.01% of POPOP (p-bis[2-(5-phenyloxazolyl)]-benzene). The thicknesses of the lead and the scintillator are 0.15 cm and 0.4 cm, and the total active depth of the tower is 37.5 cm. The cross section of the tower, which corresponds to the size of the tiles, is 5.5 cm by 5.5 cm. Each tile has 36 tiny holes at the same position in all tiles and wavelength shifting fibers penetrate the tiles through the holes. The fibers are gathered at the rear of the tower and attached to a PMT. The light from the scintillators is propagated in the fibers and read out by the PMT. To alleviate

the effect of attenuation in the fibers, two fibers penetrating tiles are connected at the front of the tower. Therefore, though the scintillation light originates from a certain tower depth depending on the energy and species of the incident particle, it always travels through both long and short path in the fibers. Mechanically, 4 towers which are optically isolated form the basic structure of PbSc named "module". A cutaway figure of the PbSc module is displayed in Figure 2.11. Thirty six modules, 6 in width and 6 in height, are assembled into one rigid structure named "supermodule", which is the unit for the readout electronics. Finally, one sector consists of 18 supermodules, 6 along the beam axis and 3 along the azimuthal direction, and includes 2592 towers.

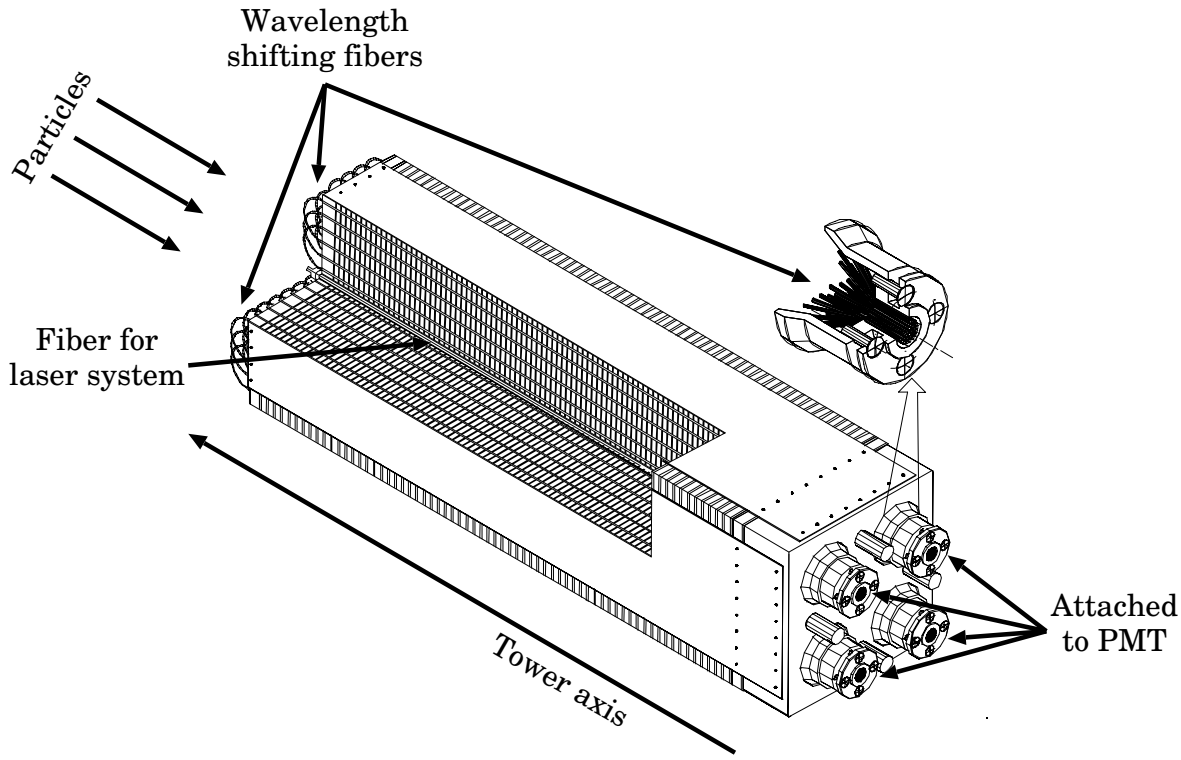

Figure 2.11: The module of PbSc. One module consists of 4 towers. The fiber for the laser system is inserted at the center of the module and along the tower axis.

A laser-based system is implemented for PbSc to monitor a possible shift of the gain from the signal voltage to the energy. This also contributes on determining the initial energy-gain coefficients at the experiment. A high power YAG (yttrium aluminum garnet) laser is used for this system. The light from the laser is propagated through fibers into each PbSc module after being split at three stages; the original laser to 6 sectors, each sector to 18 supermodules and each supermodule to 36 modules. On each stage splitting light, the light is additionally split and its amplitude is monitored by a PMT and photodiodes to calibrate the laser itself. At terminal, each fiber is inserted into the center of the module and penetrate the module along the tower axis. Hence, 4 towers in same module simultaneously detect the light via same fiber. The fibers in the modules are mechanically processed to simulate the real electromagnetic shower. The signals of the laser with various intensities and delays are continuously measured during the data taking period. The time dependence of the energy gain is corrected tower by tower assuming that the shift of the energy gain is reflected on

the deviation from the normal in the measured amplitude of the laser signal. The timing scale and offset is also determined by the signal with delay as well as the dependence of the timing on the signal amplitude using the laser with various intensities. The correction and the calibration are performed semi-online. The residual effect on the energy gain is corrected in the offline analysis and the detail is described in Section 3.5.6. We must note that the corrections of the timing offset and its amplitude dependence do not work well in the 2005 run. However, it is not a crucial issue in our analysis and the detail is described in Section 3.5.5.

To determine the initial energy-gain coefficients, following procedure was adopted. At first, the PbSc towers were placed with the tower axis horizontal and cosmic ray muons were measured at the same time as the laser signal. In this stage, the relation between the laser amplitude and the deposit energy by muons (∼38 MeV, unknown in this stage), which penetrate the tower almost orthogonally to the tower axis, was determined. The deposit energy of muons were in turn determined at a test experiment with electron beam, where the data of cosmic ray muons were taken simultaneously. Finally at the construction, 48 towers with similar energy-gain were grouped because the available high-voltage equipments provide common value over 48 channel. The fine-tuning for the energy-gain is applied by the variable gain amplifier on the readout electronics and its initial gain were determined using the laser system.

The performance of PbSc was evaluated by the test beam. The test experiments were performed using electron beam at AGS in BNL and SPS (Super Proton Synchrotron) in CERN. The linearity in the energy was guaranteed 2 – 80 GeV within 1% order and the small deviation is well understood in terms of the effect from the fiber attenuation and the mechanical structure of the tower. The measured energy resolution (ΔE) is displayed in Figure 2.12. As displayed as red curve in Figure 2.12, the energy resolution is well described by

$$\frac{\Delta E}{E} = \frac{8.1\ \%}{\sqrt{E(\mathrm{GeV})}} \oplus 2.1\ \%, \tag{2.1}$$

where E is energy in GeV and $\oplus$ means quadratic sum. A fit to a function with simple sum, instead of quadratic sum, is also performed and shown as blue curve in the figure, but it slightly disagrees with data at the low energy region. The position resolution (Δx) depends on the incident angle of the beam due to the fluctuation of the shower depth. It is expressed as

$$\Delta x = \Delta x_0 \oplus L \sin\theta, \qquad \Delta x_0 = 1.55\ \mathrm{mm} \oplus \frac{5.7\ \mathrm{mm}}{\sqrt{E(\mathrm{GeV})}}, \tag{2.2}$$

where $L \sim X_0 (= 21\ \mathrm{mm})$ and θ is the angle between the PbSc tower axis and the direction of the incident particle. These results are well reproduced by GEANT simulation. At the same beam time, the response to the proton and charged pions with momentum of a few GeV/c was studied. Only a part of the total energy is deposited in PbSc because of the small nuclear interaction length of 0.85. MIP (minimum ionizing particle) energy for the charged hadrons penetrating the tower is measured to be 270 MeV. Figure 2.13 displays the resolution of the ToF measurement for electrons, pions and protons. The resolution at more than 0.5 GeV in the deposit energy is almost constant, ∼270 psec for pions and ∼120 psec for electrons and protons. The difference of pions and the others is mainly from the shower fluctuation. The fluctuation of energy deposit for pions with 1 GeV/c is large; sometimes MIP and sometimes totally deposit. This results in the worse time resolution because light generated near PMT is faster than that generated at the surface of EMCal by ∼200 psec. Meanwhile protons nearly deposit total energy at 1 GeV/c.

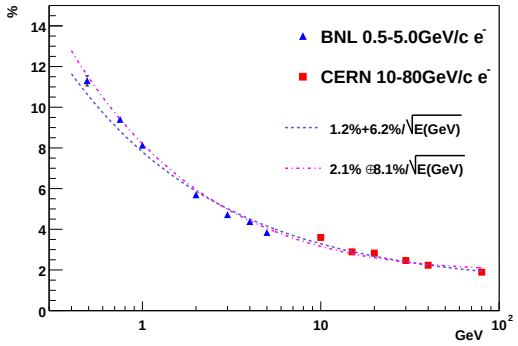

Figure 2.12: The energy resolution of PbSc for the electromagnetic shower as a function of the incident energy. The vertical axis indicates $\Delta E/E$.

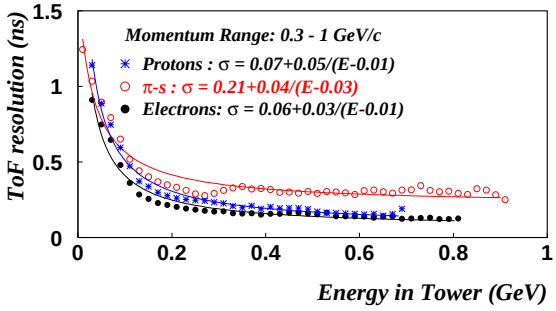

Figure 2.13: ToF resolution of PbSc as a function of the deposit energy in the tower.

Lead glass calorimeter (PbGl)

Two of 8 EMCal sectors, E0 and E1 are occupied by lead glass calorimeter (PbGl), which was previously used in WA98 experiment at CERN [91]. PbGl utilizes the Cherenkov radiation, which is emitted in the lead glass block and detected by a PMT. The PMT is attached for each tower and energized individually. The lead glass contains 51% of lead oxide and has a refraction index of 1.648 and a density of 3.85 g/cm^3. The size of the block for each tower is $4.0 \times 4.0 \times 40.0$ cm^3, and the depth corresponds to 14 radiation length and 1.05 nuclear interaction length. Individual lead glass is wrapped with aluminized mylar and shrink-tube. An array of 6×4 towers forms a mechanical unit, named "supermodule". One PbGl sector consists of an array of 16×12 supermodules, which is therefore 96 towers along the beam axis and 48 towers along the azimuthal direction. In the same way as PbSc, an array of 12×12 towers, which is 2×3 supermodules, are read out by a single electronic module, which is described later in this section.

Towers in the same supermodule share a system for the calibration and the monitoring using LED (light-emitting diode). Figure 2.14 displays the structure of the supermodule with the LED system. An aluminized plastic mirror-foil and polystyrene reflective cover are attached on the front of the supermodules and the LED board is enclosed in the reflective cover. The light from the LED enters each tower through the hole on the mirror-foil and the wrap of the tower. The intensity of the LED light is monitored by the photodiode with preamplifier, which is attached to the reflective cover. The basic idea for the calibration and monitoring system is same as PbSc. The LED signal detected by the PMT is normalized by the photodiode and the gain of the PMT is corrected based on the fluctuation of the normalized amplitude. Three kinds of LED are implemented in this system. One is the yellow LED with a fixed amplitude and it simulates the shape of the real electromagnetic shower. Other two is yellow and blue, which allows various amplitudes. The initial absolute calibration was adjusted using 10 GeV electrons at the CERN X1 beam line in Fall 1993 and Spring 1994, where the amplitude of the LED signal was related to the energy equivalent. In the experiment at PHENIX, the corrections by the LED system were applied semi-online and further calibration was performed offline. See Section 3.5.6 about the offline calibration

and the final performance of EMCal for this thesis.

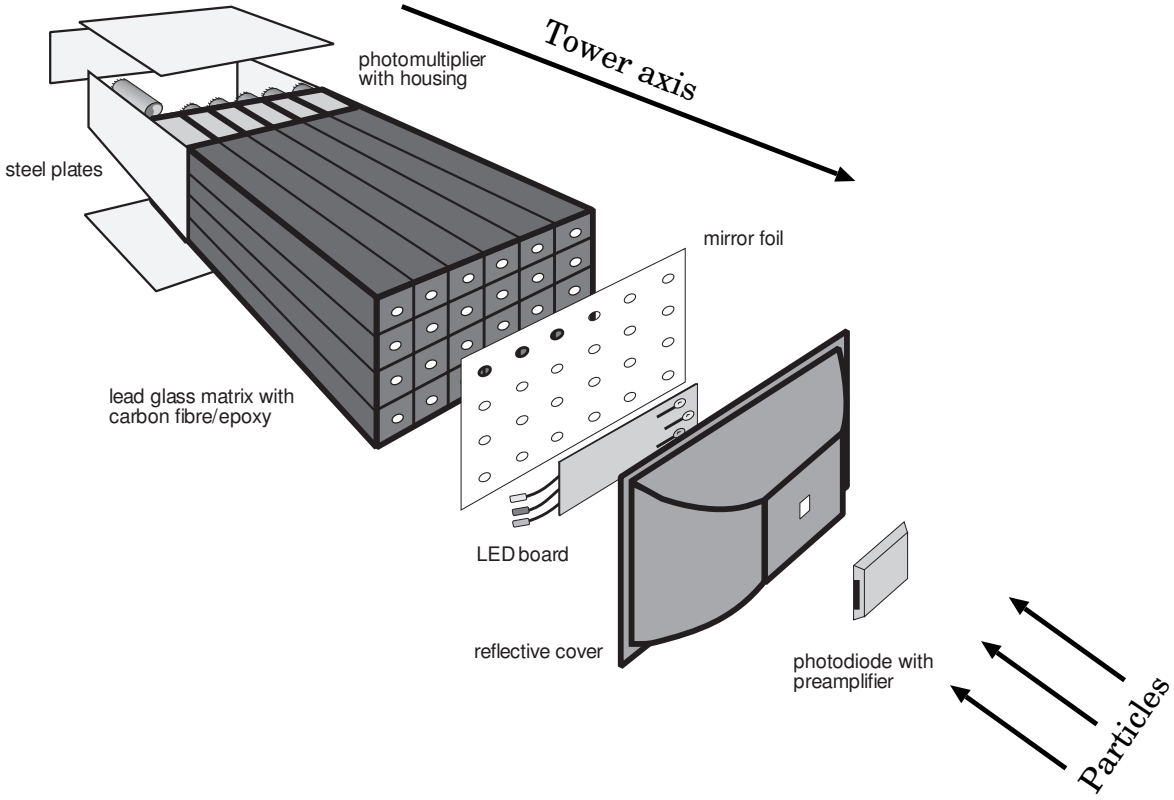

Figure 2.14: The schematic view of the supermodule of PbGl including the LED system for the calibration. The supermodule consists of 24 towers.

The intrinsic performance of PbGl was evaluated with the test beams of AGS at BNL as well as SPS at CERN. The obtained energy resolution for the electromagnetic shower is displayed in Figure 2.15. No significant dependence on the incident angle was observed and the energy resolution is well described as a function of the incident energy as

$$\frac{\Delta E}{E} = \frac{5.9\ \%}{\sqrt{E(\mathrm{GeV})}} \oplus 0.8\ \%. \tag{2.3}$$

The position resolution for electromagnetic shower was also measured and parameterized as

$$\Delta x = \frac{8.4\ \mathrm{mm}}{\sqrt{E(\mathrm{GeV})}} \oplus 0.2\ \mathrm{mm}. \tag{2.4}$$

The resolution of ToF is estimated for the positron as well as the pion. and is displayed in Figure 2.16. The resolution is described as a function of the deposit energy and there is small difference between positrons and pions. In the region of the deposit energy more than 1 GeV, the resolution is below 200 psec. One complicated issue of ToF is that ToF for hadrons is faster than that for the electromagnetic shower by about 800 psec, because the hadronic shower typically arises at the deep area of the PbGl tower due to the small nuclear interaction-length. In this thesis, however, due to the mis-calibration in ToF of PbSc as remarked in the section of PbSc, a loose cut is applied even for ToF of PbGl to uniform the condition of the analysis. The detail is described in Section 3.5.4.

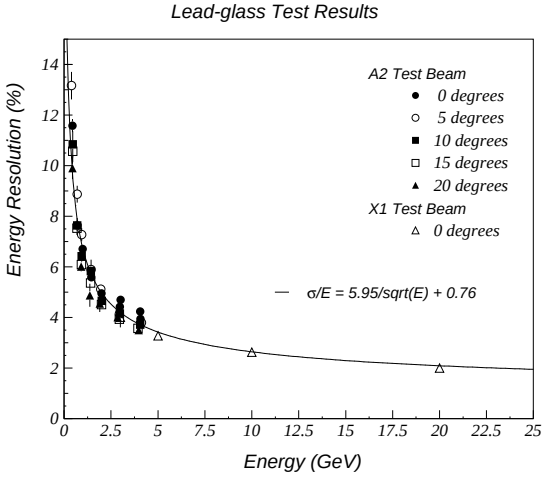

Figure 2.15: The energy resolution of PbGl for the electromagnetic shower as a function of the incident energy. The vertical axis indicates $\Delta E/E$.

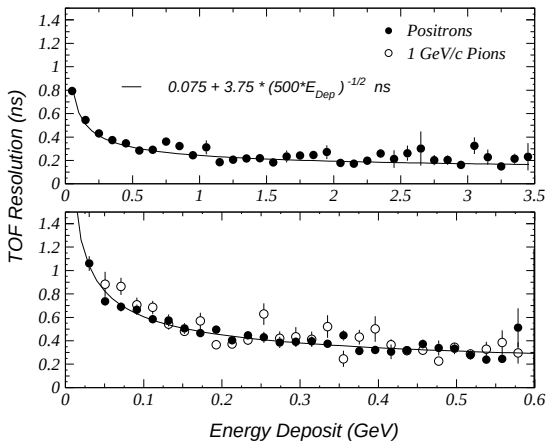

Figure 2.16: The ToF resolution of PbGl as a function of the energy deposit.

One of the features of PbGl is the difference of the response to electrons/photons and that to hadrons, which is based on the fact that PbGl is the Cherenkov detector. In addition to the small nuclear interaction-length of PbGl, the deposit energy is suppressed for hadrons due to its high Cherenkov threshold; 715 MeV/c for protons and 106 MeV/c for pions, as well as 81 MeV/c for muons. The response to hadrons were also examined with test beams. For example, the deposit energies of protons and pions with 1 GeV/c are ∼80 MeV and ∼460 MeV, and those with 4 GeV/c are ∼540 MeV both, where the energy scale is normalized for electrons.

EMCal front end electronics (FEE)

Signals from each PMTs are processed on the front end electronics (FEE) and finally converted into the energy and ToF, as well as the flag for the high-energy photon trigger. Figure 2.17 displays the schematic of the analog part of FEE. The most part to process the analog signal is executed by ASIC (application specific integrated circuit) chip with the input voltages at the point A and B in Figure 2.17. The single ASIC chip deals with signals from 4 adjacent towers forming 2×2 block, which is the minimum unit to provide the trigger. The output of the analog part is then digitized at the next step, which consists of AMU (analog memory unit) and ADC (analog-to-digital converter). A series of these processes is performed individually for 12×12 towers by a front end module (FEM), which includes boards for the controller and the trigger in addition to several boards for the actual processes.

At the input of the signal, a 93 Ω register and 500 pF capacitor are coupled serially, and +4 V bias voltage is applied with a large register to allow the negative current from the PMT. Therefore, the voltage profile at the point A simply follows the current profile from the PMT, whose rise time is less than 5 nsec, and is insensitive to the base shift. This fast voltage pulse is used for ToF measurement. The pulse is discriminated, where the threshold voltage is remotely assigned via ARCNet (attached resource computer network), and then

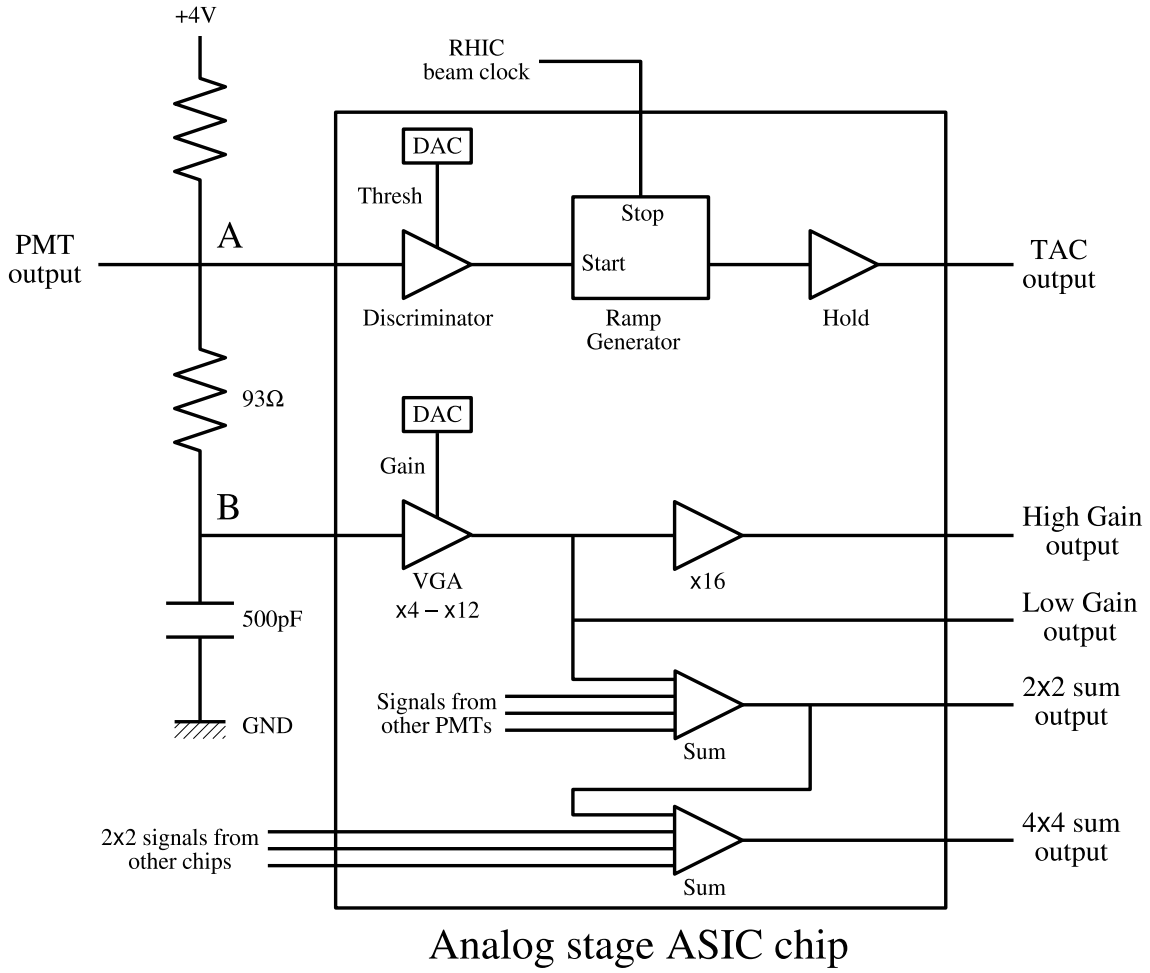

Figure 2.17: The diagram of the analog part of FEE. One ASIC chip deals with 4 signals from PMTs of 2×2 towers. In the figure, only the process for one PMT is displayed.

starts the ramp generator. The constant current from the ramp generator is stored into a capacitor until it is turned off by the RHIC beam clock. Hence, this stored charge provides TAC (time-to-amplitude converter) with the common stop mode. Since the time interval between a particle hit on the EMCal and the RHIC clock is measured in the EMCal FEE, the difference of the RHIC clock and the actual collision time, which is obtained by use of BBC, is subtracted from the value of EMCal afterward in the offline analysis.

At the point B which is the input for the energy measurement, the voltage follows the charge stored in the 500 pF capacitor. Due to the long discharge time at the capacitor, the voltage profile at B is almost a step function with the amplitude proportional to the deposit energy, rise time of $\sim$100 nsec and decay time of the order of 10 μsec. This signal is amplified by a VGA (variable gain amplifier), where the gain can be remotely assigned with the factor of 4 – 12 and the resolution of 5 bits. It is important to uniform the gain of the voltage to the energy at this stage to obtain the efficient performance of the high-energy photon trigger. The amplified signal after the VGA is then replicated into 3 identical signals. One is again amplified by a factor of 16 and used for the energy measurement with "high gain" (HG).

Another copy is also used without amplification for the energy measurement with "low gain" (LG). This feature is necessary to cover the wide energy range of 20 MeV – 30 GeV with satisfactory resolution for the purpose of the spin physics as well as the heavy ion physics. The boundary of the valid range between HG and LG corresponds to about 1 GeV. The last copy of the VGA output is used for the high-energy photon trigger. The outputs from 4 PMTs in the ASIC chip are summed within the chip and provide the energy sum for 2×2 towers. More detail about the trigger is described later in this section.

The analog outputs of TAC, the LG voltage and the HG voltage are kept without digitization to wait for the decision of the global trigger. This role is played by AMUs which is the array of capacitors. Each AMU with 64 cells for the storage is assigned to each of TAC, the LG and the HG voltage of each PMT. The AMU samples the voltage every RHIC clock and stores the charge in each cell circularly. Therefore, each cell is overwritten every 64 RHIC clocks or the AMU can keep the signal for 64 clocks, which is $\sim$7 μsec and enough longer than the time of 4 μsec needed for the trigger decision. Once the triggering is decided, the value in the corresponding cell is read out and converted into ADC value. These ADC values are sent to the PHENIX DCM (data collection module). See Section 2.3.5 about the PHENIX DAQ.

High energy photon trigger

Because the event rate at RHIC is too high to take and record every event at PHENIX, the trigger to efficiently collect special and rare events is necessary. EMCal provides signals of events with high energy particles, which include photons, neutral mesons and electrons from heavy flavor decays. Basic idea of this trigger is quite simple; select events with a deposit energy on EMCal over a certain threshold. However, since the shower generated by a particle hit usually spreads over several towers, it is needed for the efficient trigger to sum the energy deposits on the neighboring towers. Typically, the energy deposit in one tower is $\sim$20% when a particle hits the corner of the tower, while it is $\sim$80% with a hit at the center. The conceptual diagram of the actual procedure to select the events is displayed in Figure 2.18.

As described in the previous section, the energies of 2×2 towers are summed at first by ASIC chip. On this stage, towers do not overlap and hence 36 energy sums of 2×2 towers are produced per one FEM (12×12 towers). To eliminate the inefficiency in case of a particle hit at the border of the 2×2 block, the energy sum of 4×4 towers is formed from four 2×2 energy sum, allowing the overlap of 2×2 regions. This enables to collect more than 90 % of the energy of a particle hit in at least one of the 4×4 regions. Technically, the signal from a 2×2 region is transmitted to three ASIC chips for the adjoining 2×2 regions. Therefore, one energy sum of 4×4 towers are generated in each ASIC chip using 2×2 energy sums from three adjacent regions with own sum. This communication between ASIC chips is relayed over FEMs and the trigger organization is seamless over the EMCal sector. Finally, 36 signals of 4×4 energy sum is obtained for one FEM. Each 4×4 energy sum, as well as the 2×2 energy sum, is compared to a certain threshold to make a flag for the trigger. To avoid the effect of noisy towers, which always provide a large signal due to the electrical noise, the trigger can be masked with a unit of the FEM.

In the experiment, three thresholds are applied for the 4×4 energy sum. The values of the thresholds are summarized in Table 2.3 with that for the 2×2 energy sum. The triggers are named "ERT4x4a", "ERT4x4b", "ERT4x4c" and "ERT2x2".[6] The first three triggers

[6] "ERT" is initial letters of EMCal RICH trigger since the overall circuit has an option to require the RICH signal for the electron detection. However, triggers with RICH is not used in this thesis.

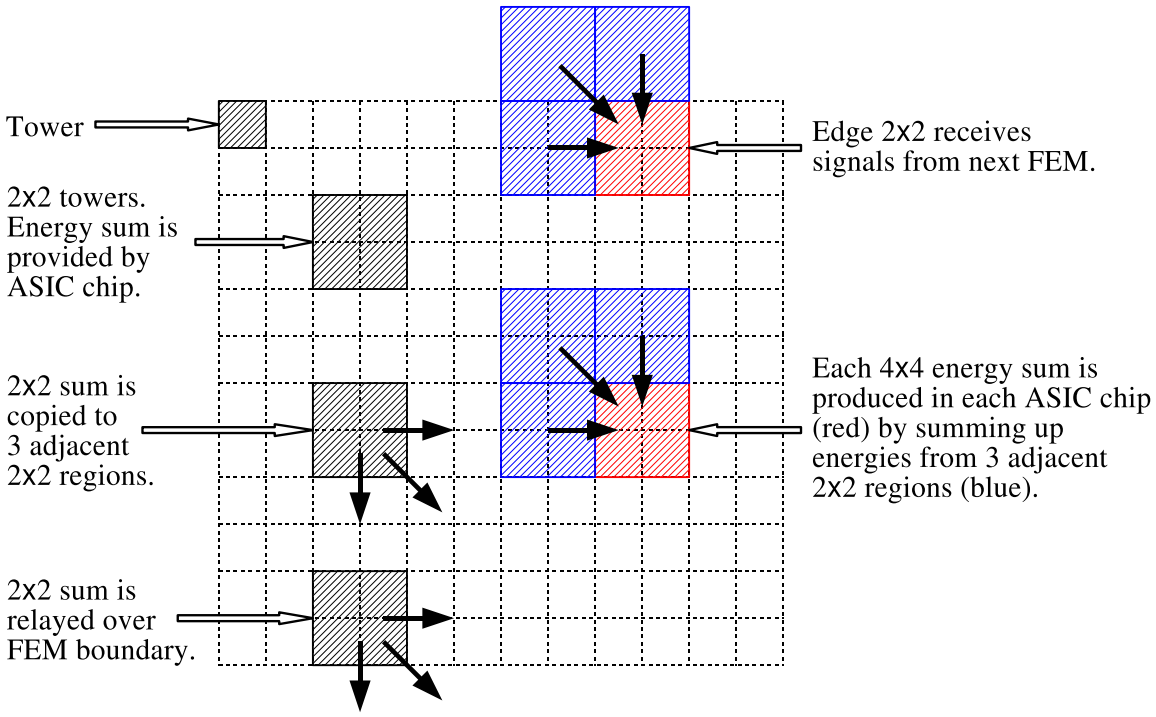

Figure 2.18: The method to produce the signal for the EMCal trigger. The region of 12×12 towers displayed in the figure are processed by one FEM. Signals of 2×2 energy sum are relayed across the boundary of 12×12 region.

are for the 4×4 energy sum and the last one is for the 2×2 sum. These triggers are often combined with other triggers, for example, the minimum bias trigger by BBC to require the event vertex within 30 cm from the collision point. In the analysis, the trigger of ERT4x4c with BBC is used. See Section 2.3.5 for more detail about the trigger.

	ERT4x4a	ERT4x4b	ERT4x4c	ERT2x2
Threshold	2.1 GeV	2.8 GeV	1.4 GeV	0.8 GeV

Table 2.3: The energy threshold for the EMCal trigger. The threshold is compared to the energy sum of the 4×4 towers or 2×2 towers.

It is important to note a feature of the trigger circuit. In practice, two identical integrating units to generate the 2×2 energy sum are implemented in one ASIC chip, for a set of 2×2 towers stated another way. During the data taking, alternating circuit is active with synchronized with the RHIC beam clock to attain the circuit with no dead time. However, this feature causes the trigger efficiency which depends on the beam crossing due to the slight difference of the alternating integrating unit. Concretely speaking, the efficiency of high-energy photon trigger is different between even-numbered and odd-numbered beam crossings. Because the crossing number is directly related to the spin assignment, this slightly different efficiency affects the extraction of the spin dependent asymmetry. In the analysis, the data

are processed independently between even and odd crossings.

2.3.5 Data acquisition system (DAQ)

The flow of the data taking

The data acquisition (DAQ) system of PHENIX is designed to adjust to two very different environments of the proton-proton collisions and the heavy ion collisions. The event rate for the minimum bias trigger at the design luminosity of RHIC varies from 500 kHz at the former to a few kHz at the latter. In respect of the occupancy in the detectors, the number of generated particles is several at the former and more than 5000, which derives hits in 10 % of all detector channels, at the latter. This difficulty is overcome through the deadtimeless front-end module (FEM) of the detectors and the triggering system.

The flow of PHENIX DAQ is displayed in Figure 2.19. The system of the triggering and FEMs are synchronized with RHIC clock, which must be exactly same as the frequency of the beam and is sent from RHIC to all experiments including PHENIX. MTM (master timing module) receives the original RHIC clock and distributes it to GL1 (global level-1 trigger) module and GTMs (granule timing module). The GL1 module manages the level-1 trigger system. The signals of LL1s (local level-1 trigger), which is the requests of accepting the event from individual subsystems such as BBC, ZDC, EMCal etc., are sent to the GL1 module. After verifying no busy signals from GTMs, the GL1 module sent the accept signal to FEMs via GTMs. Many kinds of the triggers are provided by subsystems and some of them used in this thesis is described later. To "prescale" triggers, which is one of the important features of DAQ, is also executed by the GL1 module. "Prescale" means scaling down triggers of high rate to favor rare triggers of interest. The interchange between the GL1 module and FEMs is performed by GTMs, each of which is assigned to a certain unit of detectors (granule), for example the east DC. In addition to the trigger signal, GTMs send the mode bits to control FEMs and the RHIC clock as well as its own clock for the data taking without beams. Another role of GTMs is to convey the busy signals from DCMs (data collection module) to the GL1 module.

As described in Section 2.3.4 for EMCal, the task of FEM is to process raw signals, which includes amplification, shaping and digitization, and buffer either analog or digital signals until the decision of the trigger. The judgment of triggering is decided within 40 RHIC clock, which is $\sim$4 μsec. FEMs are free from the dead time owing to this function of the event buffering. Once a trigger is fired, the data are digitized if analog and sent to DCMs. The specific treatment for the detector ends at FEMs and the common modules in detectors are available for DCMs. DCMs receive the digitized signals from FEMs and perform zero-suppression, error checking and data formatting, where zero-suppression is to compress data by suppressing the channels with its value less than the threshold. The partitioner collects the data of the event from DCMs and sends them with parallel streams to EvB (event builder) composed of SEBs (sub-event buffer) and ATPs (assembly/trigger processor) for further assembly. The busy signal of DCMs are also combined by the partitioner and sent to GTMs. SEBs temporarily store the data of the event fragments from DCMs. The EvB controller commands ATPs to fetch the data after the controller is noticed by SEB for GL1 module. The data is transported from SEBs to ATPs through a 96-port gigabit switch (ATM, asynchronous transfer mode). Upon fetching the event fragments, ATPs concatenate them into the complete event. ATPs also provide the environment for the level-2 trigger where events are selected based on the reconstructed events not to exceed the limit of the data recording. However, the level-2 trigger is not needed because of relatively low event rate

compared to the DAQ performance and therefore is not used in the 2005 run. The events assembled in ATPs are monitored online and sent to the buffer boxes for the storage, which the end users can access via the LINUX terminal. The data in the buffer boxes are finally recorded in the tape storage (HPSS, high performance storage system) periodically to keep room for further data taking.

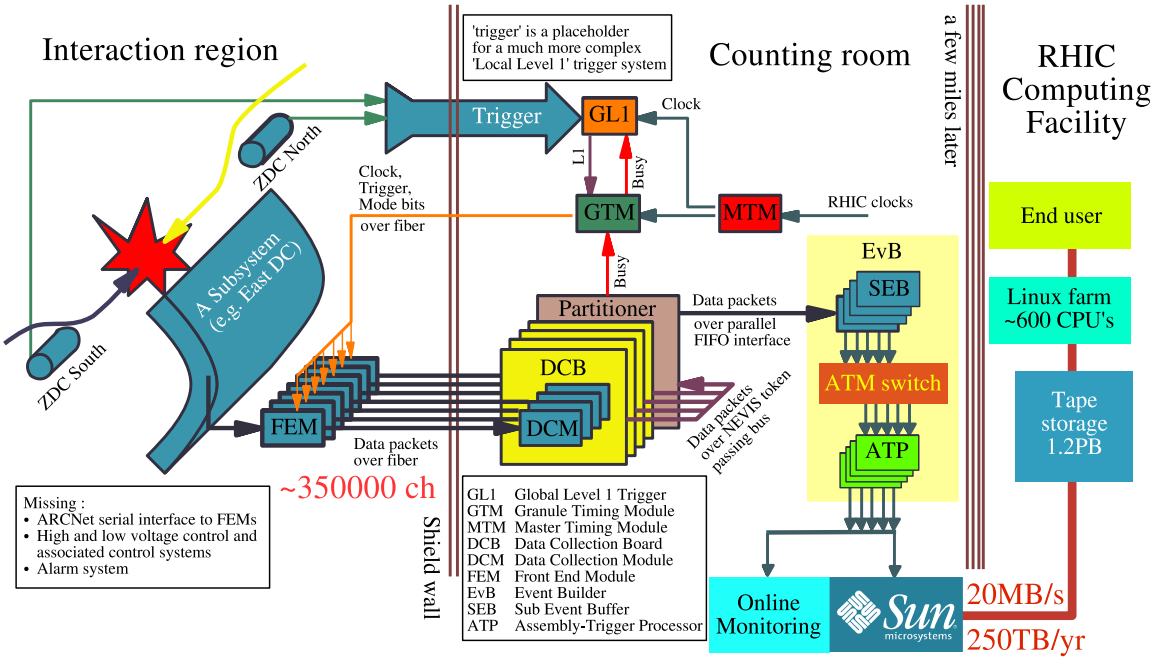

Figure 2.19: The schematic diagram of PHENIX DAQ.

Level-1 trigger

The PHENIX detector is composed of many subsystems and many physics observables are suggested, and hence many kinds of triggers are prepared at PHENIX. In the mechanism of the data taking at PHENIX, three kinds of the level-1 triggers are defined; raw trigger, live trigger and scaled trigger. The raw trigger is one which is primarily fired by the detector. Assuming that FEMs have the feature of no dead time, the raw trigger is same as what is sent to the GL1 module. The raw trigger is discarded when the GL1 module receives the busy signals from GTMs, which originate in busy DCMs. The trigger surviving this stage is the live trigger. The live time of DAQ is defined as the ratio of the number of live triggers to the number of the raw triggers and the dead time is 1− live time. The live time was kept around 90 % in the most of the data taking period as displayed in Figure 3.4 in Section 3.2. The live trigger is moreover prescaled to suppress the events of less interest. The trigger prescaled is the scaled trigger and is actually sent to FEMs to convert the raw signals and reconstruct the event. The rate of prescaling is expressed by the prescale factor. The prescale factor N results in processing the events every $N+1$ live triggers. In fact, the events are collected with many kinds of triggers at the same time. Therefore, at least one of the scaled triggers must be fired in the recorded events. In this section, triggers used in this thesis are explained.

- BBCLL1 (MB)
  In most cases, whether the event is generated by the collision of the beams is confirmed

by measuring the event vertex. As described in Section 2.3.2, BBC provides the event vertex along the beam axis. Meanwhile the displacement in the plane perpendicular to the beam axis can be ignored (see Section 3.7.1). The events with the BBC vertex within a certain region are triggered and the trigger is described as BBCLL1. The cut for the vertex is optional and ±30 cm, which is same as the offline cut, was applied in most of the period in the 2005 run. We decided the cut of ±30 cm base on the measurement that the detection efficiency of BBC is sufficiently flat over the vertex region within ±30 cm around the collision point as displayed in Figure 2.20. This fact is especially important in the measurement of the cross section to evaluate the absolute luminosity, while the effect of BBC efficiency is canceled in the measurement of A_{LL} in principle. In the measurements of the asymmetries, BBCLL1 is utilized as the measure of the relative luminosity introduced in Section 1.11. The resolution of the vertex measurement by BBC is estimated to be ∼5 cm online for the trigger, while it is improved to 2 cm in the offline analysis. The prescale factor was set to ∼500 at most depending on the luminosity. This trigger is the most basic one and the minimum bias trigger (MB) is defined as BBCLL1 in PHENIX.

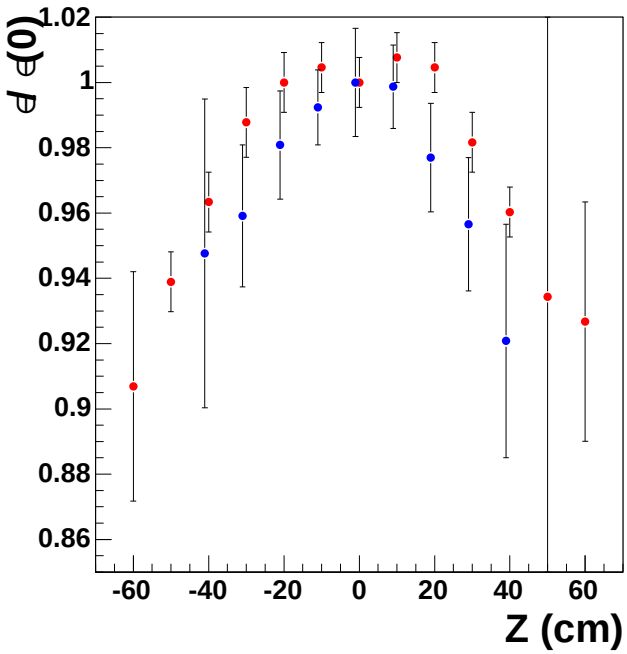

Figure 2.20: The event vertex (z) dependence of the detection efficiency of BBC $\epsilon(z)$. Red points are for the BBC efficiency to the proton-proton collision (probability to reconstruct the vertex by BBC when protons are collided). Blue points shows the BBC efficiency to π^0 observed by EMCal (probability to reconstruct the vertex by BBC when π^0 is observed by EMCal). Both red and blue points are normalized to 1.0 at $z = 0$ cm. The blue points drop out at $|z| > 40$ cm because the acceptance of EMCal is masked by the material of the central magnet.

- ZDCLL1-narrow and ZDCLL1-wide

The event vertex can be also measured by ZDC and the events with the ZDC vertex within a certain cut are triggered. The value of the cut is optional and two cuts, $\pm$30 cm and $\pm$150 cm, were adopted for the triggers in the 2005 run. The trigger with narrow cut is named ZDCLL1-narrow and that with wide cut is named ZDCLL1-wide. The resolution of the vertex by ZDC is $\sim$30 cm online and $\sim$10 cm offline. These triggers by ZDC is used for the evaluation of the uncertainty in the relative luminosity measurement. The uncertainty is estimated by comparing the number of BBCLL1 with that of ZDCLL1-narrow and therefore the same cut of 30 cm as BBCLL1 is applied for ZDCLL1-narrow. ZDCLL1-wide is used for the correction of ZDCLL1-narrow and helps to reduce the uncertainty. See Section 3.4 for more detail about the analysis of the relative luminosity. The trigger rate is lower than BBCLL1 due to smaller acceptance. The prescale factor was about 10 for ZDCLL1-wide and fixed at 900 for ZDCLL1-narrow.

- ERT4x4c&BBCLL1 (ERT)
  The trigger to collect high energy photons is implemented in EMCal as described in Section 2.3.4. In practice, the coincidence of BBCLL1 and the EMCal triggers (ERT4x4a, ERT4x4b, ERT4x4c and ERT2x2) is the main triggers in photon analyses to assure that the events are generated by the beam-beam collisions.[7] In the 2005 run, it was not needed to prescale the triggers of ERT4x4's with BBCLL1 owing to the progress in DAQ, while the large prescale factor was assigned to ERT2x2 with BBCLL1 due to its high rate. For these reasons, only ERT4x4c, to which the lowest energy threshold of 1.4 GeV in ERT4x4's is applied, is utilized out of all EMCal triggers in this thesis. The trigger of ERT4x4c with BBCLL1 is described as ERT4x4c&BBCLL1, or simply ERT unless otherwise noted. ERT4x4c&BBCLL1 is mainly used to extract A_{LL} in π^0 production. Because more statistics for the region of low π^0 p_T were accumulated with BBCLL1 than that with the EMCal triggers, BBCLL1 is also analyzed as complement to ERT as well as the confirmation of no bias in the EMCal trigger.

GL1P scaler

To obtain enough statistics for the measurement of the relative luminosity, the number of live triggers for BBC and ZDC are counted by scalers without prescaling. The scaler is named the GL1P scaler because its design is similar to the GL1 module. Four scaler inputs were available and the triggers of BBCLL1, ZDC-narrow and ZDC-wide were input in the 2005 run. Another channel is assigned for a few kinds of triggers which are not used in this analysis. Each channel counts the number of the triggers crossing by crossing of the beams. Consequently, 480 numbers (4 channels $\times$ 120 crossings) are available and 360 numbers of the total are used in this thesis.

The counts of the GL1P scalers are recorded in 2 ways. In both ways, DAQ read out and record the scaler data event by event and only counts for the corresponding crossing number to the event are recorded. Hence, 4 scaler counts are recorded event by event. The difference of the 2 ways of recording is whether the counts are summed up or not. One is named "GL1Psum", where the counts accumulated from the start of the data taking by DAQ are recorded. The other is named "GL1Pres", where the counts accumulated from the previous readout for the corresponding crossing (or the start of DAQ) are recorded, in

[7] In addition, the EMCal triggers without BBCLL1 is used in the analysis of the cross section to extract the efficiency of BBCLL1 to the particle detection in EMCal.

other words, the scaler counts in GL1Pres are reset at the time when they are read out. In addition to these, the scaler counts accumulated from the last event to the stop of DAQ are also recorded for all channels and added in the analysis. In the ideal case, the GL1Psum count for a crossing is reproduced by summing up the GL1Pres counts from the first event to the last event. However, they sometimes do not agree since a part of the events are lost when the raw data are processed through the analysis codes. The crossing dependence of the difference between GL1Psum and accumulated GL1Pres is examined and nothing over the statistical fluctuation is found (see Section A.12). In the extraction of the relative luminosity, the accumulated GL1Pres counts are adopted because the data of other detectors are also lost simultaneously with the data of the GL1P scaler.

Chapter 3

Analysis

3.1 Outline

In this chapter, detail procedure of the analysis to extract $A_{LL}^{\pi^0}$ is described. The relation of $A_{LL}^{\pi^0}$ and the experimental observables is described in Section 1.11. Equation (1.56) is reintroduced below;

$$A_{LL} = \frac{1}{\bar{P}^B \bar{P}^Y} \frac{(N_{++} + N_{--}) - (N_{+-} + N_{-+})R}{(N_{++} + N_{--}) + (N_{+-} + N_{-+})R}, \qquad R = \frac{L_{++} + L_{--}}{L_{+-} + L_{-+}}. \tag{3.1}$$

$\bar{P}^B$ and $\bar{P}^Y$ are the beam polarizations. N is the yield of π^0 and L is the luminosity. Subscripts of N and L denote helicities of the beams. R is the relative luminosity. Therefore, what are needed to extract $A_{LL}^{\pi^0}$ are the beam polarizations, the relative luminosity and helicity-dependent yield of π^0.

In the analysis, data set used in this thesis is determined based on several criteria at first. It is described in Section 3.2. In Section 3.3, results of the beam polarization measured by three polarimeters, which are described in Section 2.2, are summarized. Section 3.4 is devoted to the relative luminosity. In the section, how to evaluate the relative luminosity and its uncertainty, and results of the analysis are written. Subsequently, analysis related to EMCal, which is most important detector for this thesis, is described in Section 3.5. It includes quality assurance, reconstruction of π^0 and calibration of energy gain and ToF. At the last of this chapter, in Section 3.6 and Section 3.7, asymmetries in π^0 production are calculated and the systematic uncertainty is evaluated.

3.2 Data selection

In the data taking, DAQ is stopped after about 1 hour from the start of DAQ. We define this unit as "run" and the number assigned to each run as "run number".[1] The whole data-taking period in 2005 is always referred to as the "2005 run" to avoid a confusion. Similarly "fill number" is assigned to each fill[2] (the fill is defined in Section 2.1). This is for the convenience in the analysis. Empirically, an hour for one run is reasonable for stable operation of the detector, while it is not so inefficient to restart DAQ every hour. Hence, the quality assurance of the detector is performed run by run, for example. On the other hand,

[1] The run number is assigned serially from the first year of the RHIC running. Therefore, the run number in the 2005 run is from about 168000 to 180000.

[2] Similarly to the run number, the fill number in the 2005 run is from about 6900 to 7400.

the asymmetries are calculated fill by fill, because the characteristic of the beam bunches, which is the possible source of the systematic uncertainty, are correlated between runs in the same fill. See Section 3.6.1 about the calculation of the asymmetries. Runs with some problem in the data taking are discarded in the analysis. The criteria are as follows;

- Runs with too short data taking period are discarded because some problem is expected in the runs.
- Runs in fills with no polarization measurement are discarded because they are unavailable to calculate asymmetries.
- Runs where something is wrong with the detector, such as wrong high voltage assigned to EMCal and the GL1P scaler not working properly, are discarded.
- Runs in fills where local polarimeter observes finite transverse polarization in longitudinal beam setting are discarded.

It is possible for PHENIX DAQ to collect events with multiple triggers. As described in Section 2.3.5, two kinds of triggers are utilized in the measurement of π^0; MB and ERT. One of the remarks in the analysis using the ERT sample is that the calculation of the asymmetries is performed with the even and odd crossing numbers separately due to the slightly different performance of the EMCal trigger. See Section 2.3.4 about the EMCal trigger. Figure 3.1 displays the number of the crossings as a function of the run number. Only even bunches are filled by the beam at the beginning of the 2005 run and both even and odd bunches are filled at the end. Figure 3.2 displays the raw trigger rate of MB as a function of the run number. Since the cross section detected by BBC is about 23 mb, the luminosity is evaluated to be about 3 cm^{-2} sec^{-1} in the 2005 run. The inset in Figure 3.2 is the closeup of a certain period. A series of the points is from the runs in the same fill and it indicates that the luminosity decreases during the beam store by a factor of $\sim$2. It also turns out that the luminosity is not proportional to the number of crossings collided and the accelerator still has the capability for the development. It is impossible to record every triggered event and the events are thinned out due to the limited DAQ bandwidth. Figure 3.3 displays the event rate actually recorded by DAQ. The PHENIX DAQ achieves the recorded event rate of more than 5 kHz. The typical live time of DAQ is more than 90 % as displayed in Figure 3.4.

At the online data taking, both MB and ERT require the event vertex within $\pm$30 cm window around the collision point, where the detection efficiency of EMCal is flat. In addition, the vertex cut of $\pm$30 cm is again applied using the offline vertex with more accurate resolution. The efficiency of the offline vertex cut is $\sim$16 %. The number of recorded events finally used in this thesis and the integrated luminosity corresponding to the events, as well as the average beam polarization weighted by the integrated luminosity, are summarized in Table 3.1. The integrated luminosity used in the analysis is slightly different between ERT and MB. The difference is about 10 %.

3.3 Beam polarization

As described in Section 2.2, the beam polarization is measured by pC polarimeter and jet polarimeter. The former measures the polarization typically once an hour. Based on the fact that significant depolarization is not observed during one fill, measurements in one fill are averaged to obtain the fill-by-fill polarization. The latter polarimeter is used to calibrate

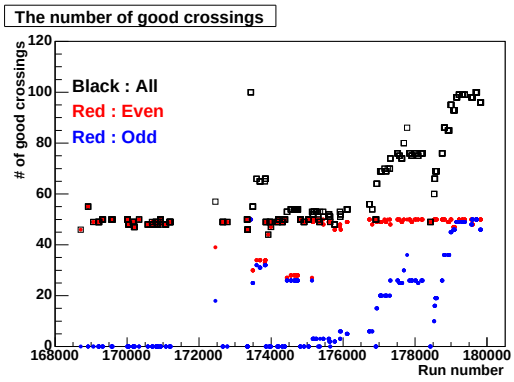

Figure 3.1: The number of the beam crossings as a function of the run number. The red points are the number for only even crossings and the blue points are for only odd crossings. The black points indicates the number of all crossings.

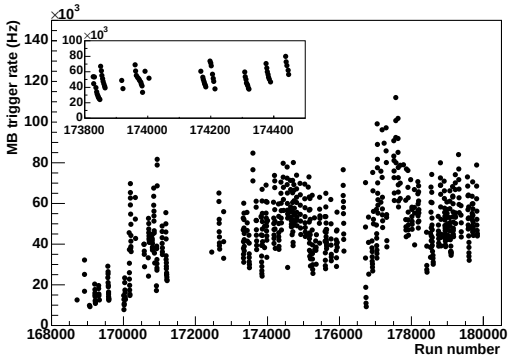

Figure 3.2: The raw trigger rate of MB as a function of the run number. The inset displays the closeup of a certain period.

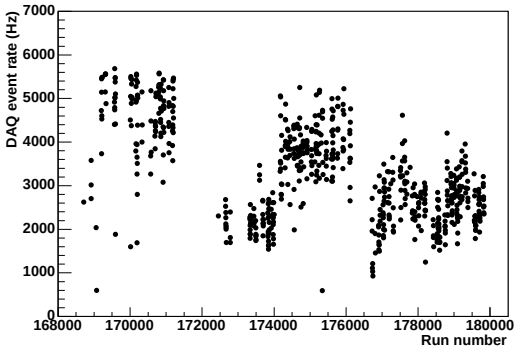

Figure 3.3: The rate of the events recorded by DAQ. The rate is adjusted to keep high live time.

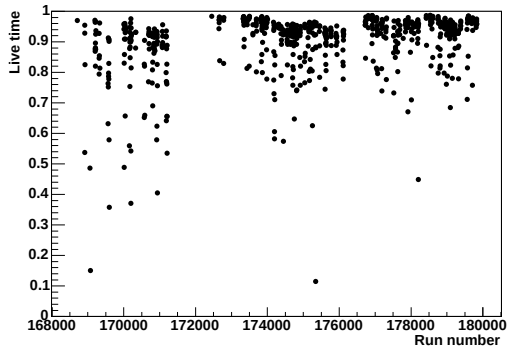

Figure 3.4: The live time of DAQ as a function of the run number.

	Int. lum.	MB events	ERT events	$\langle P_B \rangle$	$\langle P_Y \rangle$
A_{LL}	2.3 pb^{-1}	1.21×10^9	1.01×10^9	50.3 %	48.5 %
A_{TT}	0.13 pb^{-1}	1.14×10^7	4.28×10^7	47.2 %	51.3 %

Table 3.1: The integrated luminosity (int. lum.), the number of MB and ERT events, and the average beam polarization ($\langle P_B \rangle$ for the blue beam and $\langle P_Y \rangle$ for the yellow beam). The integrated luminosity in the table is for the ERT sample and that for the MB sample is about 10 % smaller than ERT. The average beam polarizations are calculated by weighting the polarization in each fill by the integrated luminosity for the fill. The difference between ERT and MB sample in the polarization is negligible.

the measurement by pC polarimeter, using whole data throughout 2005 run. In addition to these two polarimeters, PHENIX local polarimeter determines the longitudinal and transverse component of the polarization at the collision point.

Figure 3.5 displays the fill-by-fill polarization of the blue and yellow beam. Major contribution to the systematic uncertainty comes from the position dependence of the polarization in the beam profile; low polarization at the noncentral region of the beam. Because the polarization profile is more significant in the yellow beam than the blue beam, larger systematic uncertainty is assigned to the fill-by-fill polarization of the yellow beam than the blue beam. The average beam polarizations, P_B for the blue beam and P_Y for the yellow beam, over all fills weighted by the integrated luminosity accumulated by PHENIX are

$$P_B = 0.503 \times (1 \pm 0.006 \pm 0.051 \pm 0.029) = 0.503 \times (1 \pm 0.059) \quad (3.2)$$
$$P_Y = 0.485 \times (1 \pm 0.008 \pm 0.054 \pm 0.029) = 0.485 \times (1 \pm 0.062) \quad (3.3)$$

for the data set with longitudinal beam polarization and

$$P_B = 0.472 \times (1 \pm 0.030 \pm 0.051 \pm 0.029) = 0.472 \times (1 \pm 0.066) \quad (3.4)$$
$$P_Y = 0.513 \times (1 \pm 0.041 \pm 0.054 \pm 0.029) = 0.513 \times (1 \pm 0.074) \quad (3.5)$$

for the transverse polarization. The difference between ERT and MB sample in the polarization is negligible. The first uncertainty in the middle of the formula is calculated from the fill-to-fill uncorrelated errors, while the second and the third error is the global uncertainty for every measurement. The second one is uncorrelated between the blue and yellow beam and the third one is fully correlated. The global uncertainty uncorrelated in the blue and the yellow is again mainly from the polarization profile of the beam and statistical error of jet polarimeter. The blue-yellow correlated global error is caused by the systematic uncertainty on the jet polarimeter measurement. Considering the correlated error between the blue and yellow beam, the product of the beam polarization and the uncertainty are

$$P_B P_Y = 0.244 \times (1 \pm 0.095) \quad (3.6)$$

for the longitudinal polarization data and

$$P_B P_Y = 0.242 \times (1 \pm 0.107) \quad (3.7)$$

for the transverse polarization data.

The residual transverse component of the beam polarization during the data taking with the polarization directed longitudinally is monitored by PHENIX local polarimeter. The results are

$$\frac{P_{B,T}}{P_B} = 0.100 \pm 0.010 \qquad \frac{P_{Y,T}}{P_Y} = 0.146 \pm 0.011, \quad (3.8)$$

where the direction of the polarization is 53 degree for the blue beam and -73 degree for the yellow beam in ϕ (see Figure 2.6 for the definition of ϕ). In terms of the longitudinal component,

$$\frac{P_{B,L}}{P_B} = 0.995 \pm 0.001 \qquad \frac{P_{Y,L}}{P_Y} = 0.989 \pm 0.002. \quad (3.9)$$

$P_{B,T}$ and $P_{B,L}$ are the transverse and longitudinal polarization, respectively, for the blue beam, and related by $P_B = \sqrt{P_{B,T}^2 + P_{B,L}^2}$. This is same for the yellow polarization.

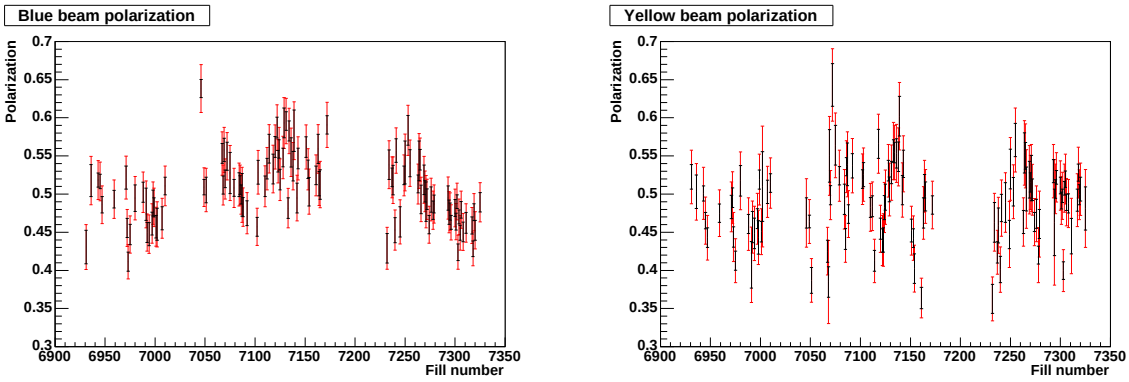

Figure 3.5: The beam polarization as a function of the fill number. The left is for the blue beam and the right is for the yellow beam. The error bars with black indicate the statistical uncertainty and those colored by red are quadratic sum of the statistical and systematic uncertainties.

3.4 Relative luminosity

In this section, we describe the relative luminosity and its uncertainty. In this thesis, A_{LL} in the π^0 production is extracted using both ERT trigger and MB trigger, and the data sets for them are slightly different. Moreover, π^0 A_{TT} is also calculated using the data set with beam spin polarized transversely, where the relative luminosity is again necessary. Therefore the relative luminosity also depends on which data set to use. The plots in this section are produced using the ERT data set for A_{LL}. The same procedure is applied for every data set and the results are summarized in Table 3.3.

3.4.1 Basic idea

The relative luminosity is defined as $R = \frac{L_{++}}{L_{+-}}$ in Equation (1.56), where L_{++} (L_{+-}) is the integrated luminosity for the collisions with like (unlike) helicity beams. In principle, measured counts by any detectors are available for R as far as they are proportional to the integrated luminosity. However, it is preferable to satisfy the requirements,

- Less background,
- No spin dependent asymmetry observed in the acceptance of the detector,
- Appropriate acceptance; not too small to accumulate sufficient statistics and not too large to be insensitive to multiple collisions in the single intersection of the beams,

Based on these requirements, the number of the minimum bias trigger (MB or BBCLL1) is chosen for R (See Section 2.3.5 about the trigger);

$$R = \frac{\sum_{i=\text{like-helicity crossings}} n_i^{\text{BBCLL1}}}{\sum_{i=\text{unlike-helicity crossings}} n_i^{\text{BBCLL1}}}, \tag{3.10}$$

where n^{BBCLL1} is GL1P scaler counts for BBCLL1 and i indicates the beam crossing number. The uncertainty of A_{LL} which originates in the relative luminosity is calculated using

Equation (1.56) to be

$$\Delta A_{LL}|_{R.L.} = \frac{2(N_{++}+N_{--})(N_{+-}+N_{-+})R}{P_B P_Y\left[(N_{++}+N_{--})+(N_{+-}+N_{-+})R\right]^2}\left(\frac{\Delta R}{R}\right) \sim \frac{1}{2P_B P_Y}\left(\frac{\Delta R}{R}\right), \quad (3.11)$$

where $N_{h_B h_Y}$ is the yield by the collisions with helicity states of h_B for the blue beam and h_Y for the yellow beam. P_B and P_Y are the polarization of the blue and yellow beams, respectively, instead of $\bar{P}_1$ and $\bar{P}_2$ in Equation (1.56). The approximations of $(N_{++}+N_{--}) \sim (N_{+-}+N_{-+})$ and $(L_{++}+L_{--}) \sim (L_{+-}+L_{-+})$ are used at the step from the middle to the right side in Equation (3.11).

The uncertainty of R is evaluated by comparing the number of BBCLL1 with that of ZDCLL1. Because BBCLL1, as well as ZDCLL1, requires coincidence of the north and south detector, background in both BBCLL1 and ZDCLL1 is tiny and therefore the accumulated numbers of the triggers are proportional to the integrated luminosity. In addition, the acceptance for ZDCLL1 is very small and the effect of multiple collisions is negligible in the current luminosity. Hence, the effect of multiple collisions in the relative luminosity can be examined by comparing BBCLL1 with ZDCLL1. In view of physics, since BBCLL1 and ZDCLL1 cover much different acceptance, possible spin-dependent asymmetry in the relative luminosity is expected to be observed and the correction is applied to the asymmetries of π^0 in the case. Therefore, when c_i is defined as the ratio of ZDCLL1 count to BBCLL1 count for i-th beam crossing, non-constant in c_i over the beam crossings indicates the systematic uncertainties in the measurement. Mathematically, the uncertainty of R is related to the average of c_i over the crossings (C) as

$$\frac{\Delta R}{R} \sim \frac{2\Delta C}{C}. \quad (3.12)$$

See Section A.5 for more detail calculation.

In this analysis, three kinds of triggers (BBCLL1, ZDCLL1-narrow and ZDCLL1-wide) which are counted by the GL1P scaler are used (see Section 2.3.5 about the GL1P scaler). Because the events of ZDCLL1-wide and ZDCLL1-narrow are overlapped, following variables are defined to make statistics independent.

$$n_i^{\mathrm{BBC-in}} = n_i^{\mathrm{BBCLL1}}, \quad (3.13)$$

$$n_i^{\mathrm{ZDC-in}} = n_i^{\mathrm{ZDCLL1-narrow}}, \quad (3.14)$$

$$n_i^{\mathrm{ZDC-out}} = n_i^{\mathrm{ZDCLL1-wide}} - n_i^{\mathrm{ZDCLL1-narrow}}, \quad (3.15)$$

where n^A indicates the number of the trigger A and the subscript i denotes the beam crossing number. The crossing-by-crossing ratio of BBCLL1 and ZDCLL1 to evaluate ΔR is defined as

$$c_i = \frac{n_i^{\mathrm{ZDC-in}}}{n_i^{\mathrm{BBC-in}}}. \quad (3.16)$$

Note that the cut of the event vertex is ± 30 cm in both BBC-in and ZDC-in though the detectors have a finite resolution. Therefore these 2 triggers measure same events. In practice, the possible spin-dependent asymmetry is assumed and the "bunch fitting" method is utilized to check the uniformity of c_i, instead of fitting c_i to a constant. The bunch fitting is to fit data to the function of the crossing number i;

$$f_i = C[1 + \epsilon_{LL} h_{Bi} h_{Yi}], \quad (3.17)$$

where h_{Bi} and h_{Yi} is the helicity of the blue and yellow beam for the i-th crossing. C and ϵ_{LL} are the fit parameters. Obviously, ϵ_{LL} represents the raw double-helicity asymmetry of

the ratio of BBCLL1 and ZDCLL1. When ϵ_{LL} is fixed to 0, the bunch fitting is same as the constant fitting. C obtained by fitting c_i to f_i corresponds to the average of c_i and to that in Equation (3.12). Since the errors of C and ϵ_{LL} in the bunch fitting are roughly related as $\Delta\epsilon_{LL} \sim \frac{\Delta C}{C}$ (see Section A.6), ΔR can be estimated from Equation (3.12) as follows;

$$\frac{\Delta R}{R} \sim 2\Delta\epsilon_{LL}. \tag{3.18}$$

The analysis is processed fill by fill, because the characteristic of beam bunches is common between runs in the same fill and its variation causes the systematic uncertainty of the relative luminosity. Figure 3.6 displays the correlation of the vertex center and width between the first run and the last run in the same fill. The correlation in the center of the event vertex is not so clear, while the vertex widths are correlated between these two runs but become wider and wider.

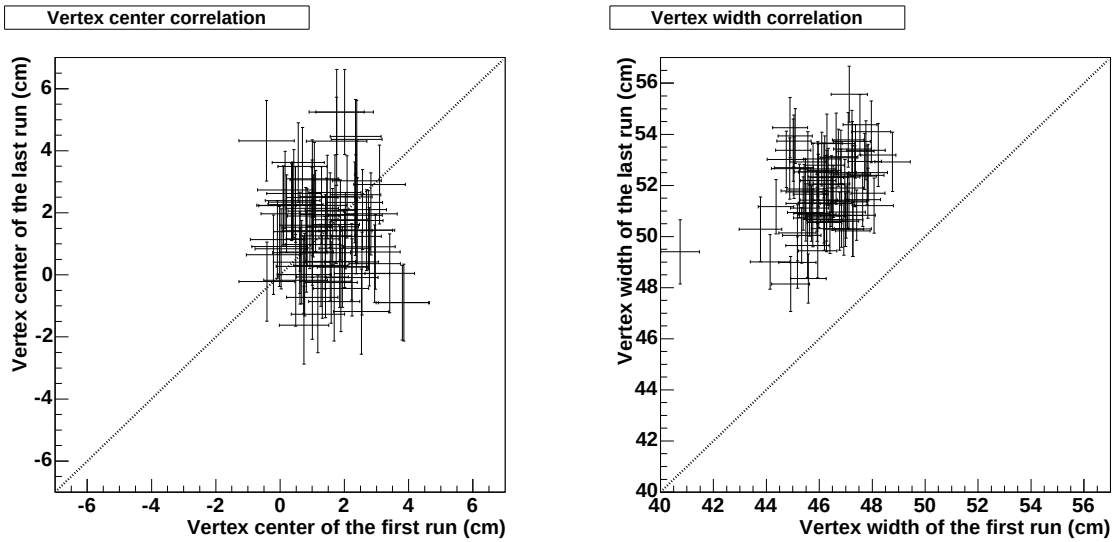

Figure 3.6: The correlation in the center (left) and the width (right) of the event vertex between the first run and the last run in a certain fill. Lines in the figures shows $y = x$.

3.4.2 Bunch selection

In the analysis, some crossings are discarded as bad crossings. One of the bunches in each blue and yellow beam is always used for the tuning of the beam. Because the population of such a bunch is usually very small compared with other bunches, they are removed. In addition, bunches with small population which are likely to have strange vertex distribution are removed. The threshold is set to 1/10 of the average and applied fill by fill. One other criterion is that bunches which are far from the correlation in Figure 3.8 are discarded, since such property implies the bunches with strange vertex distribution. The correlation in Figure 3.8 is explained in the following section.

3.4.3 Vertex width correction

One of the sources of the nonuniformity in c_i is caused by the combination of the variation of the event vertex width and the resolution in the vertex measurement. This dependence

on the vertex width is corrected to evaluate uncertainty of R properly. However, the vertex width is not directly used in this analysis because of the following reason. In the typical analysis in PHENIX, the event vertex is cut at ± 30 cm to obtain the detection efficiency of BBC which is independent of the vertex position. Therefore, the ± 30 cm cut is also applied to many of the triggers for the physics measurements to use the DAQ bandwidth efficiently. For this reason, the events with the vertex out of the cut are limited and it is difficult to determine the vertex width with good accuracy. Instead of using the vertex width obtained by BBC, which is the most accurate way in PHENIX, w_i is used for the correction in the analysis for the relative luminosity, where w_i is defined as

$$w_i = \frac{n_i^{\mathrm{ZDC-out}}}{n_i^{\mathrm{ZDC-in}}}. \tag{3.19}$$

Figure 3.7 displays the scatter plot of w_i and the vertex width measured by BBC. The clear correlation is seen between them and it assures to use w_i for the vertex width.

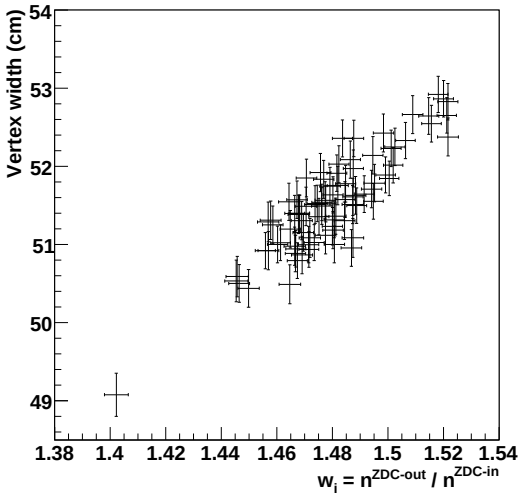

Figure 3.7: The correlation between w_i and the event vertex width. The vertex width is proportional to w_i.

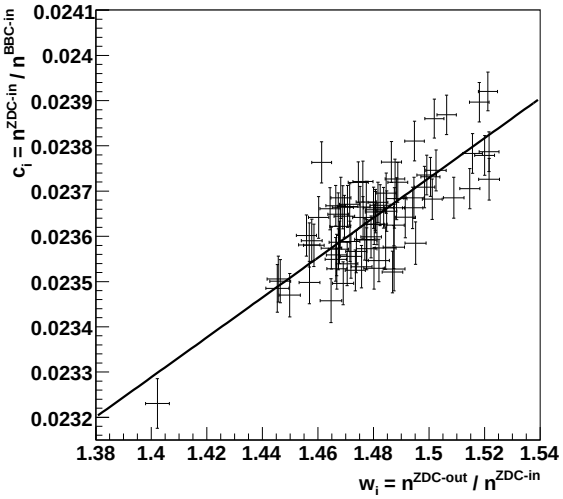

Figure 3.8: The correlation between c_i and w_i. c_i is proportional to w_i. The line shows the result of fit and is used for the correction to c_i.

As described above, c_i depends on w_i, which is displayed in Figure 3.8. This phenomenon is mainly due to the resolution of ZDC and can be explained as follows. The vertex distribution is roughly Gaussian with a width of $\sim$50 cm. When the ± 30 cm cut is applied for the event vertex, some amount of the events come and go at the edge of the cut, because the measured vertex position is smeared by the detector resolution. As the vertex width becomes narrower and the slope becomes steeper at the edge of the cut, more events go outside the accepted region of ± 30 cm compared with the events coming into the region. Figure 3.9 displays schematic view of the effect. This phenomenon is more serious in detectors with worse resolution. Hence the effect by ZDC is larger than that by BBC, where the resolution in the vertex measurement online is $\sim$30 cm with ZDC and $\sim$5 cm with BBC. Consequently, $n^{\mathrm{ZDC-in}}$ becomes smaller as the vertex width becomes narrower and it results in c_i being proportional to w_i.

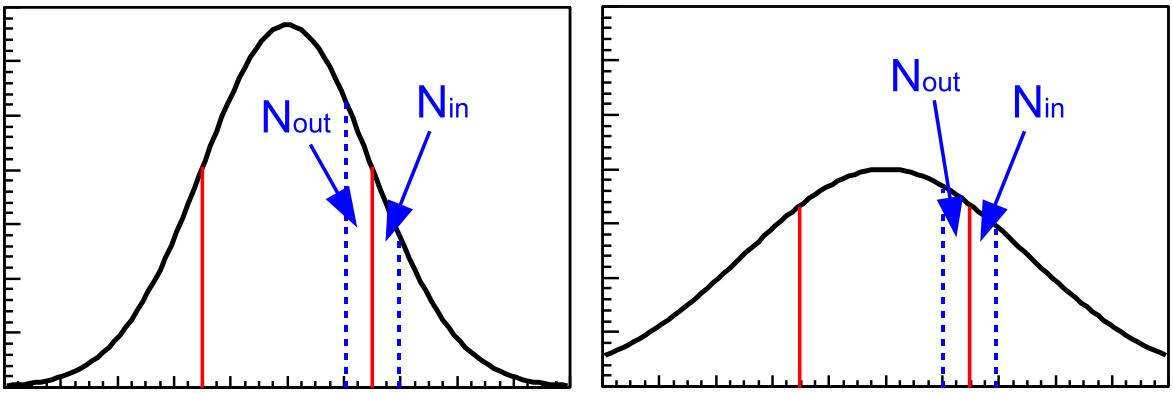

Figure 3.9: Schematic view to explain the phenomenon that c_i depends on w_i. When a certain vertex cut is applied (red line), events around the cut are smeared due to the detector resolution ($N_{\rm in}$ and $N_{\rm out}$). Amount of the events escaping from the window by the cut are roughly proportional to $N_{\rm out} - N_{\rm in}$ and therefore depends on the vertex width. Obviously, the effect is larger for a detector with worse resolution.

The line in Figure 3.8 is the result of the fit with the linear function and c_i is corrected based on the function. In the correction, we do not add the error of the function to c_i. By looking at the chi-square of the bunch fitting, where only statistical error is assigned to the points, it turns out whether the vertex width correction is effective or not. Figure 3.10 displays the reduced chi-square of the bunch fitting before (black) and after (red) the correction. The fitting is performed fill by fill and therefore the each entry of the red and black histogram corresponds to the number of fills in whole 2005 run. It is seen that the reduced chi-square becomes smaller after the correction, though it is still larger than unity. The larger chi-square indicates the existence of unknown systematic error. Figure 3.11 displays the scatter plot of the reduced chi-square and the statistical error of ϵ_{LL} by the bunch fitting. As expected, the reduced chi-square of the fitting is larger as the statistics is higher and any strange behaviors are not found. Finally, the residual nonuniformity of c_i is included in the systematic uncertainty of the relative luminosity R.

The dependence of c_i described here mainly originates in the resolution of ZDC. Hence, it is not necessary to correct $n^{\rm BBC-in}$, which is used as the relative luminosity in the calculation of π^0 A_{LL}. However the same effect should occur in the part of BBC though it is smaller than ZDC because of the better resolution of BBC. The size of the effect on BBC is estimated based on the simple model calculation, where the distribution of the event vertex and the vertex resolution of BBC and ZDC are assumed to be Gaussian. It turns out that the effect by BBC is small and it is fully absorbed by the systematic uncertainty of R.

3.4.4 Result of the relative luminosity analysis

After the correction using w_i, ϵ_{LL} for c_i is calculated fill by fill. Figure 3.12 displays ϵ_{LL} as a function of the fill number. Since the uncertainties of R are thought to be uncorrelated between fills, following Equation (3.18), ΔR for whole 2005 run is estimated by fitting Figure 3.12 to a constant. As described above, the reduced chi-square of the bunch fitting is still larger than unity after the vertex width correction. However, even though the large chi-square is taken into account, the uncertainty of the relative luminosity is enough smaller than

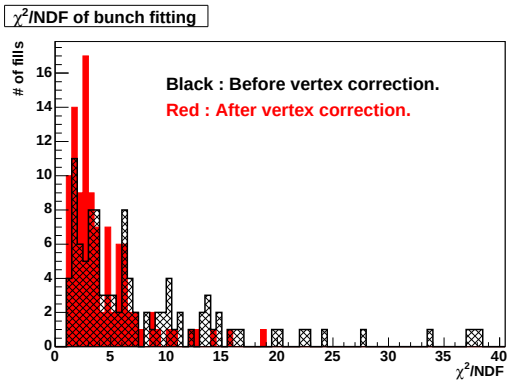

Figure 3.10: The reduced chi-square of the bunch fitting before (black) and after (red) the correction by the event vertex width. Only statistical error is assigned at the fitting. The chi-square is clearly smaller after the correction.

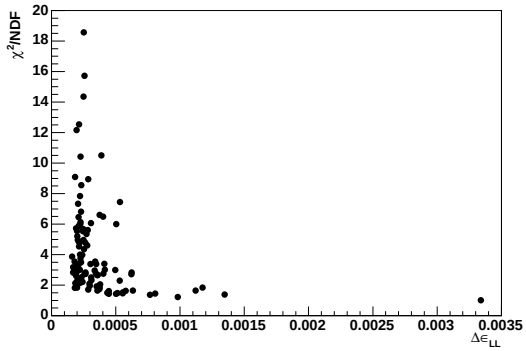

Figure 3.11: The scatter plot between the reduced chi-square and the statistical error of ϵ_{LL} of the bunch fitting. The larger chi-square is with the larger statistics as expected.

the statistical uncertainty of π^0 A_{LL}. Therefore, we don't make further efforts to investigate the source of the systematic uncertainty. To evaluate ΔR conservatively, point-to-point error for c_i are enlarged so that the reduced chi-square of the bunch fitting in each fill becomes unity. The red (black) points in Figure 3.12 are after (before) the correction of the chi-square. The results of fitting the fill dependence of ϵ_{LL} to a constant are also written in the figure. The reduced chi-square after the fill-by-fill chi-square correction is almost unity and no fill dependence is observed. The result of ϵ_{LL} has finite value even though the significance is only 2 sigma. ΔR is evaluated conservatively using ϵ_{LL} instead of $\Delta\epsilon_{LL}$ to be 1.83×10^{-4}, which is translated into 3.8×10^{-4} in terms of the uncertainty of π^0 A_{LL} assuming the beam polarizations of 50 % and 48 %. This result is enough small compared to the statistical uncertainty of π^0 A_{LL}. The comparison of with and without the vertex width correction is summarized in Table 3.2.

	$\epsilon_{LL}(10^{-5})$	χ^2/NDF
w/o vertex corr.	2.46±2.57	599.7/103
w/o vertex corr. (χ^2 corr.)	3.10±5.94	97.0/103
w/ vertex corr.	8.94±2.57	401.5/103
w/ vertex corr. (χ^2 corr.)	9.17±4.79	99.2/103

Table 3.2: ϵ_{LL} and the reduced chi-square (χ^2/NDF) by the constant fitting over the fills. The reduced chi-squares become almost unity after the fill-by-fill chi-square correction.

Since the data set used in the analysis is slightly different between ERT and MB, the result of ΔR is also different. Table 3.3 lists the results of $\Delta R/R$ for the ERT and MB sample with longitudinal and transverse beam polarization. Figure 3.13 and 3.14 display R as a function of the fill number. The line in the figures is $R = 1$. R in Figure 3.13 is calculated using all beam crossings except for the bad bunches described in Section 3.4.2. On the other hand, R in Figure 3.14 is obtained using only crossings of either even (red) or odd

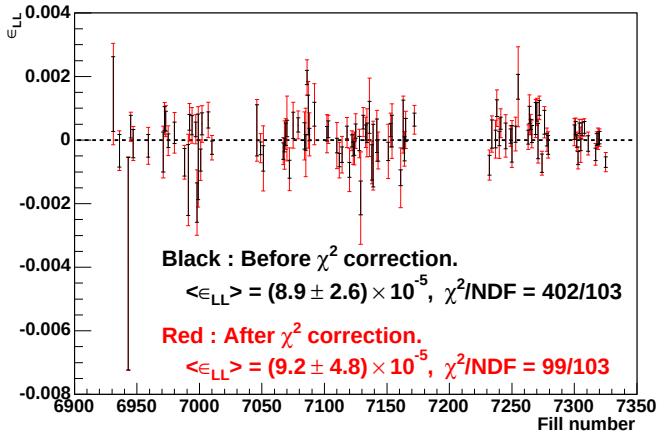

Figure 3.12: ϵ_{LL} as a function of the fill number. The points are obtained after the vertex width correction. The error bars of the black points are only statistical, while those of the red are enlarged to make the reduced chi-square of the bunch fitting unity in each fill. The line indicates $\epsilon_{LL} = 0$.

(blue) crossing numbers, for the calculation of A_{LL} is performed with the even and the odd crossing numbers separately for the ERT data set because of the specification of ERT (see Section 2.3.4 about the EMCal trigger).

	$\epsilon_{LL}(10^{-5})$	χ^2/NDF	$\frac{\Delta R}{R}(10^{-4})$
MB longitudinal	9.67±4.96	94.2/100	1.93
MB transverse	58.1±21.7	2.01/3	11.62
ERT longitudinal	9.17±4.79	99.2/103	1.83
ERT transverse	56.3±20.9	2.08/3	11.26

Table 3.3: ϵ_{LL}, the reduced chi-square (χ^2/NDF) and $\Delta R/R$ for the data sets used in this thesis. ϵ_{LL} instead of $\Delta\epsilon_{LL}$ is used to evaluate $\Delta R/R$.

Some of the reasons of the residual nonuniformity in c_i are considered. The candidates are the resolution of BBC as well as ZDC, more complicated shape of the event vertex distribution, time dependence of the event vertex and the multiple collisions in a single intersection of the beam bunches. Though the effects from these are included in ΔR, we describe about the estimation of the multiple collisions at the end of this section.

Considering that the high intensity in a single bunch of beam is likely to cause the multiple collisions, the problem occurs in the fill with the small number of crossings and high trigger rate. As displayed in Figure 3.1 and 3.2, the serious case is ∼80 kHz of MB in the fill with ∼50 crossings. Roughly assuming the BBC detector acceptance of 50 % and the efficiency of the ±30 cm vertex cut of 50 %, the actual collision rate is ∼320 kHz. While a single bunch intersects a bunch of the other beam at the collision point with 78.2 kHz using the RHIC circumstance of 3834 m. Therefore, the probability of the collisions per a single intersection of beams is $\frac{320\text{k}}{78.2\text{k}\times 50} = 8.2$ %. This probability of 8.2 % includes both the signle collision and the multiple collisions because BBC cannot separate them. When the multiplicity of the collision

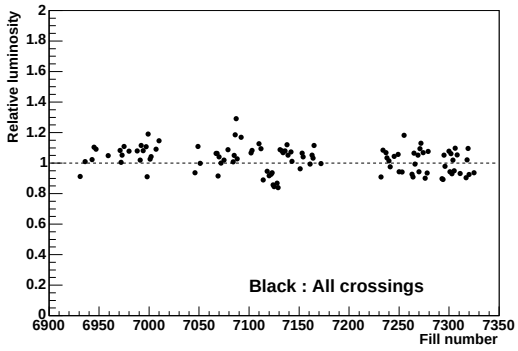

Figure 3.13: The relative luminosity as a function of the fill number. All crossings are used for the extraction. The error bars are smaller than the size of the points.

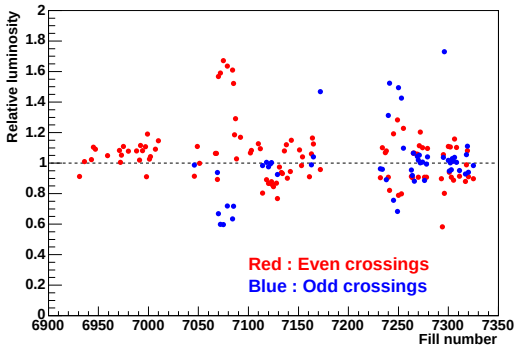

Figure 3.14: The relative luminosity as a function of the fill number. The values are extracted with even (red) and odd (blue) crossings separately. The error bars are smaller than the size of the points.

follows the Poisson distribution, the probability of the multiple collisions is calculated to be 0.34 % per a signle intersection, which is 4.2 % of all events with collisions. See Section A.7 about the detail calculation.

If this effect contributes to the false asymmetry maximally, the size is $\frac{4.2\ \%}{P_B P_Y}$ where P_B (P_Y) is the blue (yellow) beam polarization. However, if the rates of the multiple collisions are same in all crossings, they do nothing in the π^0 A_{LL} calculation. For example, even if the rate is different by 20 % between the crossings for like- and unlike-helicity collisions, the size of the false asymmetry becomes smaller by a factor of 10. In fact, the rate is higher in like-helicity crossings at times and in unlike-helicity crossings at other times. Consequently, the bias of the collision rate is well randomized over the whole 2005 run. Moreover, it must be emphasized that the uncertainty of R is evaluated by comparing with ZDCLL1. Due to the much smaller acceptance of ZDC than BBC, the luminosity measurement by ZDC is less affected by the multiple collisions. Since the trigger rate of ZDCLL1-narrow is 2 kHz at most and it means that ZDC detects only 1.25 %(= 2 kHz/160 kHz) of the collisions within $\pm$30 cm vertex cut, while BBC detects $\sim$50 %. In the same calculation as BBCLL1, the probability of the multiple collision for ZDCLL1 is 0.026 % per all events with the collisions. The effect caused by this level of the multiple collisions is negligible compared to the present precision of π^0 A_{LL}. Eventually, the effect of the multiple collisions to the relative luminosity is absorbed in ΔR by requiring the uniformity in c_i.

3.5 Performance of EMCal

3.5.1 Performance of ERT

This analysis utilizes two triggers; MB and ERT. ERT collects the events when the energy measured by EMCal is more than a threshold of 1.4 GeV. In addition, ERT also requires MB fired. The extraction of the asymmetries is not affected by the performance of the trigger because the performance should be independent of the physical state of the beam helicity. As an exception, one thing to be careful is the specific feature of the electrical circuit for ERT,

where alternative circuit is assigned to every other beam crossings. Due to this feature, the asymmetry using ERT must be calculated for the even and the odd beam crossings separately. See Section 2.3.4 and 2.3.5 about ERT. Though the detail study of the trigger performance is not needed in this thesis, a brief review of ERT is useful and is described in this section.

The performance of ERT is evaluated by monitoring the rejection power. The rejection power for ERT is defined as $N_{\mathrm{MB}}/N_{\mathrm{ERT}}$, where N_{MB} and N_{ERT} are the number of MB and ERT events, respectively, without prescaling. The ratio must be calculated using the data taken in the same period. Figure 3.15 displays the rejection power as a function of the run number. Since ERT requires MB, the rejection power of ERT indicates how much events are suppressed by the EMCal trigger (ERT4x4c). The average of the rejection power is about 60, which means that the events are reduced by a factor of $\sim$60. The fluctuation of the rejection power is mainly from the electrical noise of EMCal. Because the towers with terribly frequent noise always fire ERT and decrease the rejection power, the regions including such towers are masked in the trigger during the data taking period. However, the remaining towers, which is not so noisy and can be discarded in the offline analysis, cause the time dependence in the rejection power. Other reason of the fluctuation of the rejection power is related to the cleanness of the beam. The beam gas background tends to be larger when the number of beam crossings is larger. Therefore the rejection power of ERT is correlated to the number of the crossings (see also Figure 3.1).

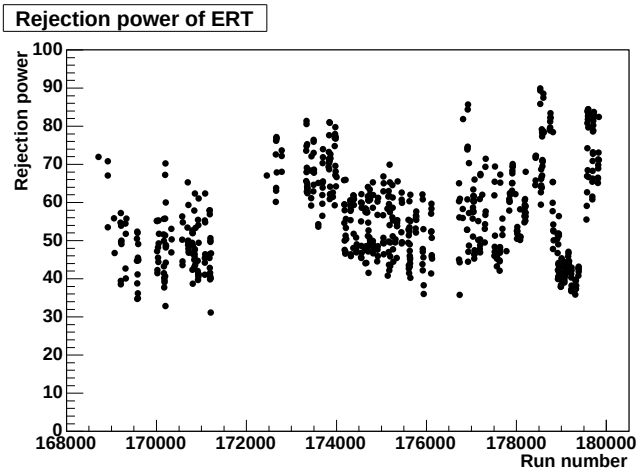

Figure 3.15: The rejection power of ERT as a function of the run number.

The efficiency of ERT as a function of the cluster energy on EMCal is displayed in Figure 3.16 for PbSc and PbGl separately. See Section 3.5.2 about the clustering. The efficiency in Figure 3.16 is defined as the fraction of the clusters which fire ERT in all clusters. The slope where the trigger is turned on is understood by the variation of the tower-by-tower pedestals and gains in the energy measurement. The efficiency flats and becomes about 90% at more than 3 GeV in both PbSc and PbGl. The inefficiency at the flat region results from the region in which ERT is disabled due to the electrical noise. Figure 3.17 displays the ERT efficiency for the π^0 detection as a function of π^0 p_T. The efficiency in Figure 3.17 is defined as the fraction of π^0s whose decay photon with higher energy fires ERT in all π^0s measured by use of EMCal. The efficiency becomes constant at more than 4 GeV/c. The efficiencies for π^0s at the flat is consistent with those for the single clusters in Figure 3.16 within an

uncertainty of 1 %.

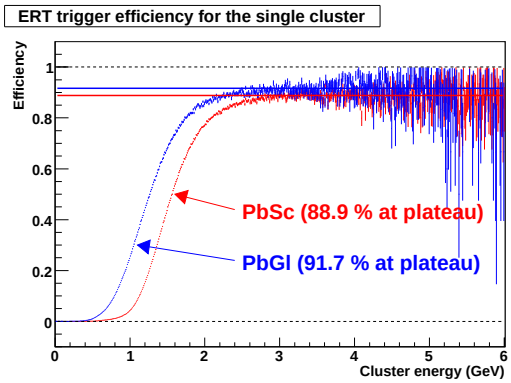

Figure 3.16: The ERT efficiency as a function of the cluster energy. The red one is for PbSc and the blue one is for PbGl. The error bars on the points show only the statistical uncertainty. The points are fitted to a constant using the energy range more than 3 GeV and the results are displayed as the red and blue line.

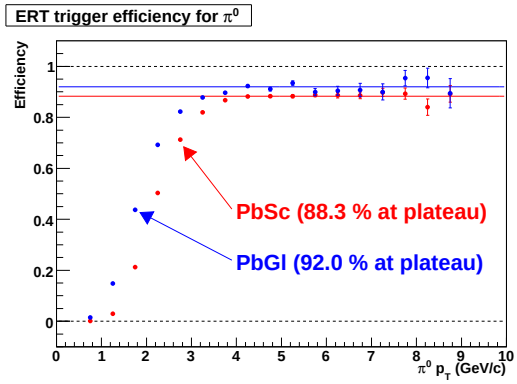

Figure 3.17: The ERT efficiency as a function of π^0 p_T. The red one is for PbSc and the blue one is for PbGl. The error bars on the points show only the statistical uncertainty. The points are fitted to a constant using the p_T range more than 4 GeV/c and the results are displayed as the red and blue line.

3.5.2 Clustering on EMCal

As described in Section 2.3.4, EMCal is segmented into towers. The energy deposited by a particle hitting EMCal is distributed over several neighboring towers. Therefore, it is necessary to reconstruct the energy of the incident particle from the energies in the towers. At the same time, the position of the particle hit is also obtained from the distribution of the energies in the towers.

At the beginning to reconstruct energy and hit position of the incident particle, towers with the energy deposit more than a certain threshold are picked up. The threshold was set to ∼0.010 GeV for PbSc and ∼0.014 GeV for PbGl. The higher threshold for PbGl than PbSc is due to larger noise in PbGl than PbSc. In 2005 run, the noise of EMCal was about 0.007 GeV for PbSc and 0.010 GeV for PbGl in RMS. After applying energy threshold to every tower, the regions of geometrically continuous towers with energy deposit are formed. Assuming the possible case that more than 2 particles hit near positions on EMCal, when n towers in the single region locally have a energy peak, the region is divided into n pieces. Such regions, which have been split if necessary, are named "cluster"s. Therefore the cluster has only one peak energy tower.

Figure 3.18 displays the multiplicity of the hit towers in the clusters. In this figure, the photon-like clusters are selected using the photon probability as described below. As expected, the multiplicity increases as the cluster energy becomes higher. The long tail in the high multiplicity region in the low energy clusters is assumed to be caused by hadrons whose shower spreads widely than the electromagnetic shower. For this reason, the tail is significant in PbSc while such a component is small in PbGl which is insensitive to hadrons (see Section 2.3.4 about EMCal). The multiplicity of PbSc is slightly higher than PbGl because the energy threshold to each tower is slightly higher in PbGl.

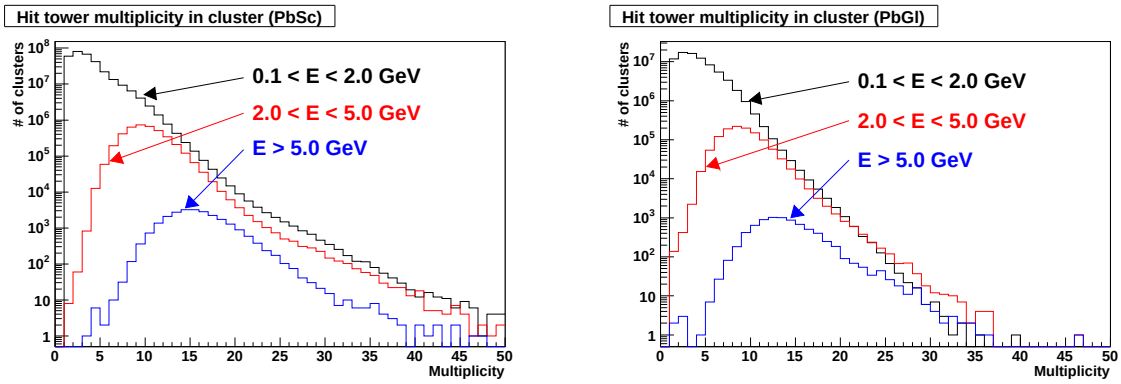

Figure 3.18: The multiplicity of the hit towers in the clusters. The left figure is for PbSc and the right is for PbGl. Black, red and blue histograms are for 0.1 – 2.0 GeV, 2.0 – 5.0 GeV and more than 5 GeV in the cluster energy.

The process to reconstruct the energy of the cluster is different in PbSc and PbGl. In PbGl, all energies in the cluster are simply summed and the total energy is corrected for the dependence on the impact angle of the incident particle. On the other hand, the energies in the core towers are summed in PbSc. The core towers are defined as those in which the incident particle is estimated to deposit the energy more than 2 % of the total. This estimation is based on the ideal electromagnetic shower profile, which is parameterized in the test beam experiment. Roughly, more than 90 % of the total energy is observed in the core towers. The energy summed over the core towers is corrected for the impact angle dependence as in PbGl. In addition, the energy loss by the attenuation in the fibers to propagate the scintillation light is corrected in PbSc. In both PbSc and PbGl, the energy between the incident photon and the reconstructed cluster is not linear in the low energy region due to the energy threshold to towers. The non-linearity is evaluated in the offline analysis and corrected. See Section 3.5.6 about the non-linearity correction.

The position of the particle hit is obtained as follows. At first, the cluster position is simply obtained as the center-of-gravity of the tower position weighted by the energy in each tower. However, following the profile of the electromagnetic shower in EMCal, the position calculated by the center-of-gravity is systematically shifted from the real position. Therefore the shift is corrected in the next step. Then, the dependence on the impact angle of the particle is corrected. The way to extract the position is almost same in both PbSc and PbGl, but the parameters in the calculation is different due to the different detector.

The timing information is also recorded in EMCal and it is used for the particle identification. In this analysis, the timing of the tower with the maximum energy deposit is used as the timing of the particle hit.

One of the important values in this analysis is the photon probability. It is the probability that the cluster is produced by the photon and obtained by comparing the ideal shower profile and the actual energy sharing in the cluster. In practice, the chi-square between the distribution of the energies and the ideal profile is calculated and translated into the probability using the number of the towers in the cluster as the degree of freedom. Ideally, the cut at the probability p for the cluster results in the efficiency of p for the photon and this is independent of the cluster size, energy and position.

3.5.3 Quality assurance of the EMCal towers

EMCal consists of many towers and a certain amount of them acts unordinary behavior. Such towers are roughly categorized into 3 groups. One is the dead towers, whose response is too poor and almost no signals are observed from them. Other one is the noisy towers, which send meaningless signals of the electronic noise with high frequency. The last one is the not-calibrated towers, for which the tower-by-tower offline calibration using π^0 peak is failed. Most of them have the problem of the electronics or the broken PMT. Some of them have the software problem, such as the improper gain coefficient assigned, and fake the noisy or dead towers. These unavailable towers are named "bad tower". In consideration of the shower spreading over several towers, the region of the bad towers and 3×3 towers around the bad towers are named "warn towers". In addition to these, towers with successful calibration but with not good π^0 spectrum are included in the warn towers, but towers around them are not included. The warn towers are masked and not used in this analysis. As well as the warn towers, towers at the most edge of the EMCal sectors ("edge towers") are masked too, because the shower leaks out of EMCal and a part of the energy is lost. In this section, the process to find the warn towers is described for first 2 categories; the dead towers and the noisy towers. The last one about the not-calibrated towers is described in Section 3.5.6.

To determine the dead and noisy towers, the tower-by-tower frequency to find the cluster hitting the tower is examined. Towers with too low or too high frequency are assigned as the dead or noisy tower. The determination of the dead tower is simple and the tower with the frequency less than 10 over all the 2005 run are labeled as the dead tower. The number of the dead towers is 9. On the other hand, finding the noisy towers is a little bit different. At first, the distribution of the frequency is produced sector by sector of EMCal, for the energy windows with 1 GeV step, and for the ERT and MB samples each. The minimal threshold of 0.1 GeV, which is same value at the final asymmetry calculation, for the cluster energy is applied. It is also required that ToF is in valid range (not an overflow) for the clusters with active ToF module, where EMCal towers whose electric circuit is broken for ToF while is working correctly for the energy measurement are considered. Figure 3.19 displays the example of the distributions, which is for sector W0 and the energy range of 2.0 – 3.0 GeV using ERT sample. Then, the frequency distribution is fitted to Gaussian and towers which are far from the mean value by more than a certain sigmas are labeled as the noisy tower. The threshold is applied depending on the cluster energy. It is 10 sigmas in the energy region more than 1 GeV while 20 sigmas at less than 1 GeV to keep the statistics. In the low energy region, electric noise have a large effect and the tower-by-tower fluctuation of the ERT threshold is effective for the ERT sample in addition to the noise. Finally, the towers once tagged as the noisy tower in any energy range and any trigger samples are assigned as the noisy tower. Therefore, we adopt only one noisy/dead tower map for any data samples. It's to be noted that the threshold in this analysis is relatively loose compared with other study like direct photon measurement because π^0 is clearly identified by the reconstruction of the invariant mass.

In practice, finding the noisy towers is performed twice. The first is done before the energy calibration of EMCal because the noisy towers must be excluded to reconstruct π^0 for the calibration. The second is after the calibration because some towers are masked at the first step due to the mis-calibration as described above. Figure 3.20 displays the results of the warn and edge towers in this analysis. The number of the warn and edge towers are summarized in Table 3.4. The percentage of the masked towers in whole EMCal is 15.8 %. About half of the masked towers are the edge towers and the rest is the warn towers. The

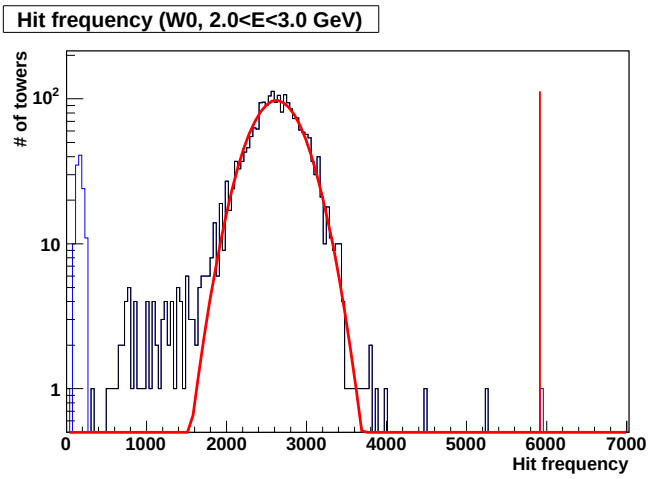

Figure 3.19: The tower-by-tower hit frequency for W0 sector and 2 – 3 GeV in the cluster energy using the ERT sample. The entries of the blue histogram consist of all towers in the sector. The peak around 0 of the blue one is from the 12×12 towers where ERT is disabled due to the noisy towers. The black histogram is produced excluding the towers in the ERT-disabled region and is used for the fitting to Gaussian (red curve). The threshold to determine the noisy towers is 10 sigma in this sample and is indicated by the red line around 6000. The tower for the highest entry in the blue histogram is masked as the warn tower.

bad towers are about 2.5 % of total. This means that about 70 % of the warn towers are not actually bad but excluded because their neighbors are bad towers.

3.5.4 Reconstruction of π^0

π^0 is the signal for this study. Moreover, its measured peak position and width in the mass spectrum are utilized for the calibration and the quality assurance of EMCal. π^0s are measured by detecting two photons from its decay by use of EMCal. In the analysis, any pairs of the clusters on EMCal are selected and the invariant mass of them is calculated using measured energy and hit position. The 4-momentum square for every cluster is regarded as zero in the calculation. Then, the peak of π^0 is observed on the continuous background in the invariant mass spectrum. Several criteria are applied to the clusters or the pairs mainly to reduce background and make clear peak. The criteria are listed as follows.

- Minimal energy threshold
  Because the clusters with too low energy are affected by the electrical noise, the minimal energy threshold is applied to the clusters. The threshold for the cluster energy is 0.1 GeV for both PbSc and PbGl. In addition, the tower-by-tower threshold of $\sim$0.010 GeV for PbSc and $\sim$0.014 GeV for PbGl is applied in the clustering as described in Section 3.5.2. The tower-by-tower threshold causes the non-linearity between the incident energy and the reconstructed energy. This non-linearity is corrected as described in Section 3.5.6.

- Warn and edge towers
  Clusters which hit on the warn or edge towers are discarded. In the case of the cluster

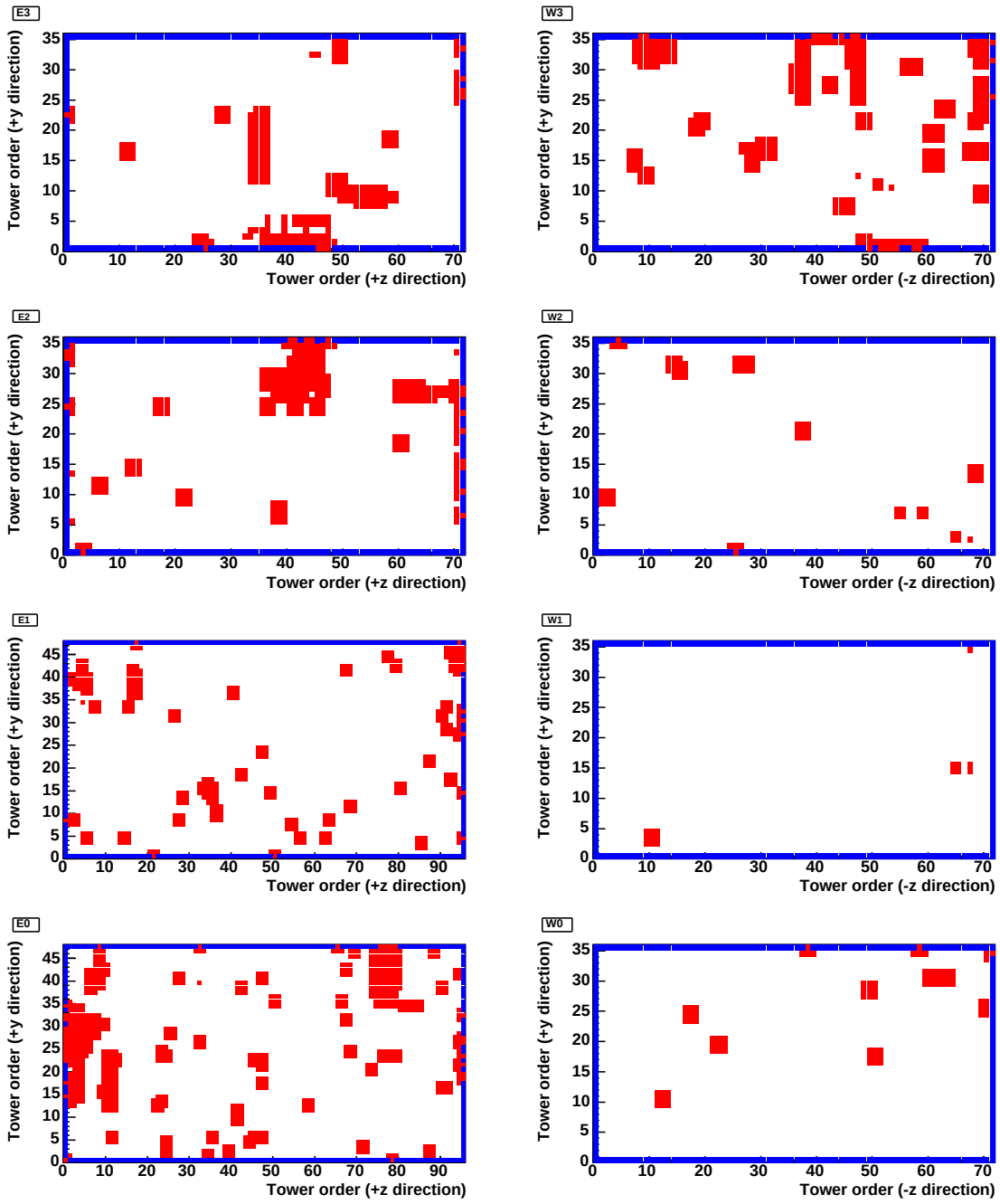

Figure 3.20: The masked towers. Eight histograms correspond to EMCal sectors. The horizontal axis is the order of the tower parallel (antiparallel) to the beam axis in the east (west) arm. The vertical axis is the order of the tower along the y-axis. The red towers correspond to the warn towers and blue towers are edge towers. Both red and blue towers are masked in the analysis.

sector	bad towers	warn towers	edge towers	masked towers	total
W0	14 (0.5 %)	77 (3.0 %)	212 (8.2 %)	289 (11.1 %)	2592
W1	8 (0.3 %)	16 (0.6 %)	212 (8.2 %)	228 (8.8 %)	2592
W2	22 (0.8 %)	72 (2.8 %)	212 (8.2 %)	284 (11.0 %)	2592
W3	100 (3.9 %)	357 (13.8 %)	212 (8.2 %)	569 (22.0 %)	2592
E0	192 (4.2 %)	702 (15.2 %)	284 (6.2 %)	986 (21.4 %)	4608
E1	81 (1.8 %)	393 (8.5 %)	284 (6.2 %)	677 (14.7 %)	4608
E2	87 (3.4 %)	251 (9.7 %)	212 (8.2 %)	463 (17.9 %)	2592
E3	115 (4.4 %)	214 (8.3 %)	212 (8.2 %)	426 (16.4 %)	2592
PbSc	346 (2.2 %)	987 (6.3 %)	1272 (8.2 %)	2259 (14.5 %)	15552
PbGl	273 (3.0 %)	1095 (11.9 %)	568 (6.2 %)	1663 (18.0 %)	9216
Total	619 (2.5 %)	2082 (8.4 %)	1840 (7.4 %)	3922 (15.8 %)	24768

Table 3.4: The number of the bad towers, the warn towers and the edge towers. The bad towers are included in the warn or edge towers. The masked towers are the sum of the warn and edge towers and they are masked in the analysis. The numbers in the parenthesis are the percentages to the total.

pair, both clusters of the pair must be located on the non-warn and non-edge region. The definition of the warn and edge towers are described in Section 3.5.3.

- ERT check
  The ERT check is only for the ERT sample and requires that the higher energy cluster in the pair fires ERT. This is to eliminate the event bias in particular in the sample of low p_T π^0s. π^0s obtained by the ERT data sample are categorized into 2 groups. π^0 in the first group is the origin to fire ERT. π^0 in the second group does not fire ERT and other source such as high energy particles or noise in the same event fires ERT. When π^0s in the second group are included in the analysis, π^0s with another high energy particle in the same event are favored and, on the other hand, π^0s with only lower energy particles in the same event are disfavored. Therefore, non application of the ERT check causes the bias in the event structure.

- Photon probability cut
  The photon probability is calculated by comparing the ideal shape of the electromagnetic shower with the measured shower shape in EMCal. See section 3.5.2 about the photon probability. The clusters with the photon probability less than 0.02 are discarded in the analysis. This threshold results in the efficiency of 0.98 in the photon detection in the ideal condition. In the case of the cluster pairs, both clusters are required to satisfy the cut of 0.02.

- Charged particle veto
  Charged particles, which are mainly charged pions, kaons and protons, introduce the background. They are rejected by the cut in the association between the hit position on EMCal and that on PC3, which is located just in front of EMCal and responds to only charged particles. See Section A.4.2 about PC3. The variable used for the cut in the actual analysis is the angle δ which is displayed in Figure 3.21. δ is defined as the angle between the vector from the event vertex to the EMCal hit position and the vector from the event vertex to the PC3 hit position nearest to the EMCal hit position.

Figure 3.22 displays the distribution of δ obtained in the experiment. Clusters with small δ are likely to be the charged particles. However, they include the electron position pairs from the photon conversion near EMCal. Such pairs do not separate each other and produce single clusters like photon with same energy and hit position as the initial photon, and can form π^0 with another cluster. To keep the statistics, the conversion pairs are used in the analysis. The separation of the conversion pairs from charged hadrons is roughly possible because the position resolution of EMCal is worse for the hadronic shower than that for the electromagnetic shower. Therefore, δ is larger for the charged hadrons than the electron positron pairs. This statement is illustrated in Figure 3.22. Finally, the region of the charged hadrons are removed in the analysis. The cut value in δ depends on the cluster energy and is optimized to minimize the error of the asymmetries. Figure 3.23 displays the cut value for PbSc and PbGl as a function of the cluster energy. The region surrounded by two lines are discarded. The cut disappears for the higher energy clusters since the loss of π^0 by the cut becomes serious. The energy at the disappearance of the cut is lower in PbGl than PbSc because of the insensitivity to the hadronic interaction in PbGl. The detail method of the optimization is described in Section A.8.

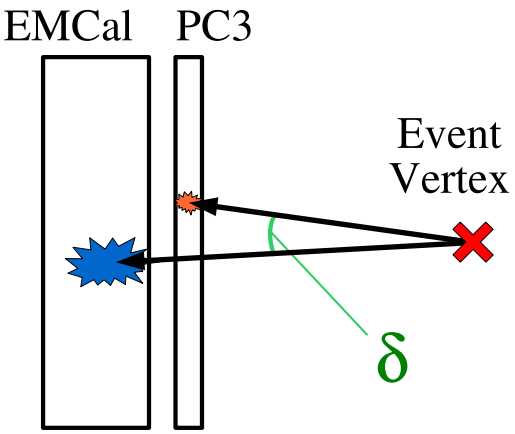

Figure 3.21: The definition of the angle δ. The hit position on PC3 which is nearest to the cluster on EMCal is used in the calculation of δ.

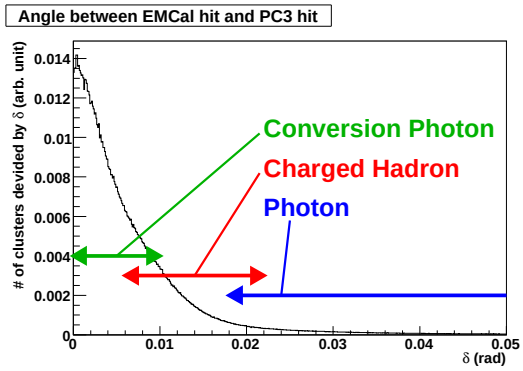

Figure 3.22: The distribution of δ. Entry in each bin is divided by δ. The distribution is roughly divided into 3 regions as displayed in the figure. The region of charged hadrons is discarded in the analysis.

- ToF cut
  ToF measured by EMCal is another tool for the particle identification. However, the resolution of ToF is worse than the expected value because the energy dependence of ToF is not corrected properly. For this reason, the loose cut with ToF is applied in this thesis. In addition to the requirement that clusters must have valid ToF value, only clusters with ToF $< t_\gamma + 5$ nsec are accepted in the calculation of the asymmetries, where t_γ is ToF of photon. This loose cut is rather to remove abnormal cluster than to purify the photon sample.[3] As described in Section 3.5.3, ToF cut is not applied

[3]It is expected that optimized ToF cut with proper calibration does not significantly improve the particle

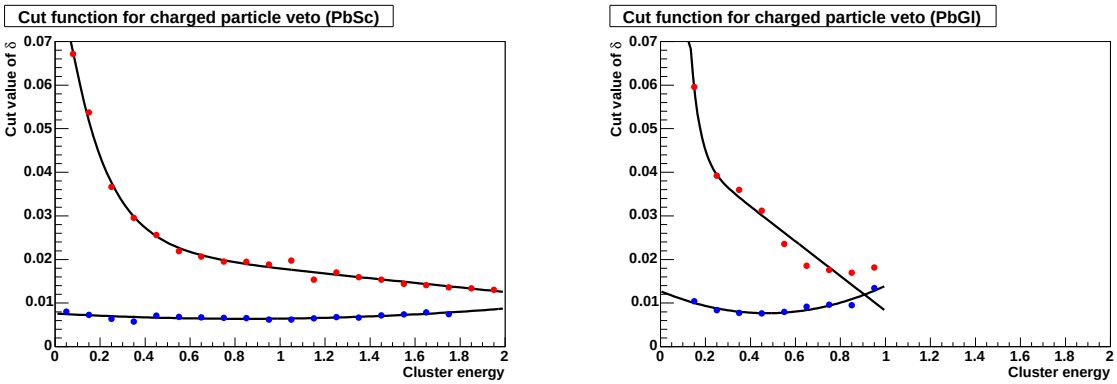

Figure 3.23: The cut value for the charged particle veto. The left is for PbSc and the right is for PbGl. The cut value is dependent on the cluster energy and extracted using data (red and blue points). The line is the fit function and the region surrounded by the two lines are discarded in the cut.

to EMCal towers with ToF module broken. The offset calibration of EMCal ToF is described in Section 3.5.5.

The performance of the photon probability cut and the charged-particle veto cut for π^0 is evaluated by comparing the number of π^0 with and without these two cuts. Other selections above except for the photon probability and the charged particle veto are applied in this evaluation. The efficiency of the cut and the purity of π^0 are calculated using ERT sample and summarized in Table 3.5. The efficiency is defined as the percentage of π^0s surviving the cuts. The purity is defined as the percentage of π^0 in the all cluster pairs. In the calculation of the purity, the cluster pairs in the "signal window" is considered. The signal window is fixed in all measured p_T bins to 0.111 – 0.161 GeV/c^2 in the mass spectrum and same as used in the calculation of the asymmetries. See Section 3.6.1 about how to calculate the asymmetries. The efficiency is independent of the mass window chosen within the uncertainty of 1%. The uncertainty of the purity is about a few % which is evaluated as in Section 3.6.2. It introduces the error on the efficiency of ∼10 % for the lowest p_T bin and ∼0.1 % for higher p_T region. The cuts for the particle identification is effective for π^0 with lower p_T because EMCal is insensitive to hadrons and all energy from hadrons is not absorbed in EMCal. The results from MB data are also extracted and no significant discrepancy between MB and ERT is observed except for the lowest p_T bin, 0.5 – 1.0 GeV/c, where the efficiency is worse. In the lower p_T region, π^0s of MB sample consist of clusters with nearly equal low energy, while ERT π^0s consist of the high and low energy clusters due to the requirement of ERT. Since the charged-particle veto cut is tight for the low energy clusters, the efficiency of π^0 is roughly twice worse in MB than ERT.

The invariant mass spectra after applying all cuts above are displayed in Figure 3.24 and 3.25 using ERT and MB sample, respectively. The spectra are displayed for each p_T bin which is same as the used in the calculation of the asymmetries. The main contribution to the background is the combinatorial background, which is the pairs of clusters which are not from the common π^0. Hence, the background reduces in the higher p_T region where the

identification because it must correlate with other cuts. Based on the data in the past years, the optimized ToF cut would raise the purity by ∼5 % and reduce the efficiency by ∼2 % in low p_T region, and would not change them in high p_T.

	PbSc		PbGl	
p_T (GeV/c)	Efficiency (%)	Purity (%)	Efficiency (%)	Purity (%)
0.5 – 1.0	100	36 (17)	95	52 (42)
1.0 – 2.0	94	67 (48)	94	75 (68)
2.0 – 3.0	95	84 (75)	93	88 (84)
3.0 – 4.0	95	91 (86)	93	92 (90)
4.0 – 5.0	96	93 (89)	94	93 (91)
5.0 – 6.0	96	93 (89)	95	94 (92)
6.0 – 7.0	96	93 (90)	95	94 (91)
7.0 – 8.0	96	94 (90)	96	94 (91)
8.0 – 9.0	97	94 (90)	97	95 (91)

Table 3.5: The performance of the photon probability cut and the charged-particle veto cut. Numbers without parenthesis in the column of the purity are the purities after the cuts and the purities before the cuts are shown in the parentheses. ERT sample is used in the evaluation.

multiplicity of π^0 and other high momentum particles is small. The suppression of the lower energy pairs in ERT sample generates the difference in the background shape in the lower p_T bins between ERT and MB. The peak near 0 in the low p_T region is produced by the single hadrons. Their primary and secondary interaction points in EMCal often separate due to the long nuclear-interaction length and it provides two adjacent clusters forming pairs with mass of $\sim$0.

Finally, the statistics of π^0 after the background subtraction are summarized in Table 3.6. π^0s in the signal window is counted for the table. See Section 3.6.2 about the evaluation of the background fraction.

p_T (GeV/c)	MB A_{LL} ($\times 10^3$)	ERT A_{LL} ($\times 10^3$)	MB A_{TT} ($\times 10^3$)	ERT A_{TT} ($\times 10^3$)
0.5 – 0.75	13248	446	129	20.0
0.75 – 1.0	8072	2163	78.5	101
1.0 – 1.5	6627	12982	64.2	671
1.5 – 2.0	1862	19179	17.8	1028
2.0 – 2.5	571	12993	5.61	705
2.5 – 3.0	193	6152	1.83	337
3.0 – 3.5	72.2	2633	0.70	145
3.5 – 4.0	29.3	1120	0.29	61.9
4.0 – 5.0		733		40.8
5.0 – 6.0		180		10.1
6.0 – 7.0		54.8		3.01
7.0 – 9.0		28.6		1.53

Table 3.6: The statistics of π^0 used in the calculation of the asymmetries.

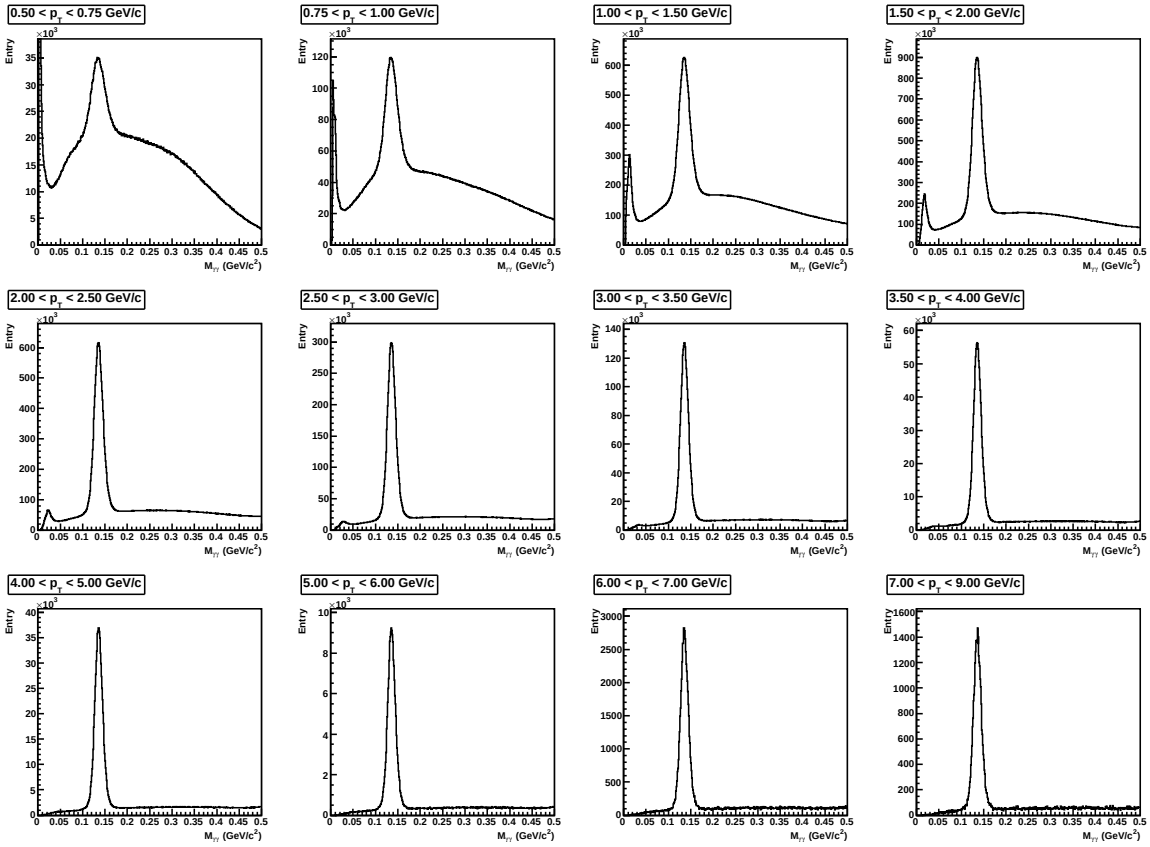

Figure 3.24: The invariant mass spectra using ERT data sample. The p_T binning is same as that in the calculation of the asymmetries. Both PbSc and PbGl are used.

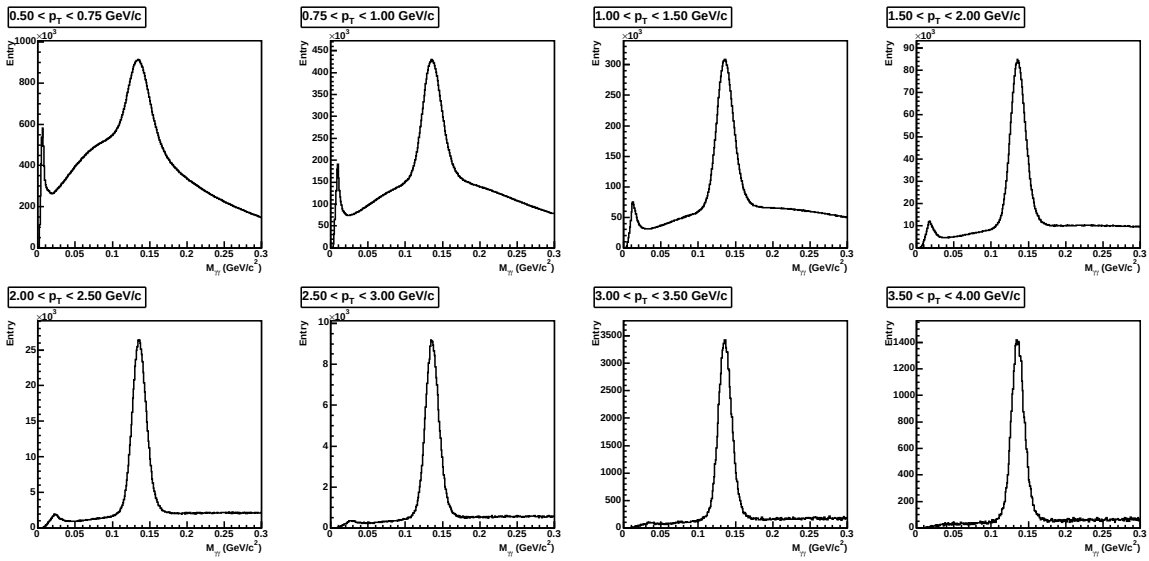

Figure 3.25: The invariant mass spectra using MB data sample. The p_T binning is same as that in the calculation of the asymmetries. Both PbSc and PbGl are used.

3.5.5 ToF calibration of EMCal

The calibration of offset and gain of EMCal ToF is initially performed semi-online based on the laser system. See Section 2.3.4 about the detector. However, the energy dependence in PbSc and the offset in both PbSc and PbGl are not calibrated properly semi-online in the 2005 run. In this section, the calibration of the offset is described. The energy dependence of PbSc ToF is left in this analysis because of the technical issue and this results in the loose ToF cut for the particle identification. See Section 3.5.4 about the particle identification and the reconstruction of π^0.

Two kinds of the offset calibrations are applied in this analysis. One is the EMCal tower-by-tower calibration and the other is the run-by-run calibration. In the tower-by-tower calibration, all events in the 2005 run are accumulated to obtain enough statistics for each tower. On the other hand, in the run-by-run calibration, the offset is extracted EMCal sector by sector by combining data of all towers in each sector in each run. Therefore, the iteration of these two calibrations are needed in principle, but the resolution of PbSc ToF is not best due to a limited correction for the energy dependence and more than a set of calibrations does not provide the improvement. No iteration is also needed for PbGl because the same loose cut as PbSc is adopted.

Both tower-by-tower and run-by-run calibrations are carried out using a peak in the ToF distribution. Mainly photons which has the large statistics and the constant velocity form the peak. The corrections of the start timing by BBC and the distance from the event vertex to the hit position on EMCal are applied before the calibration. Then, the peak of every tower or every run is set to 0 nsec in the offset calibration. Figure 3.26 displays the ToF distribution after the offset calibration. The tail on the right side of the peak indicates slower particles like hadrons than photon. The tail on the left side in PbSc is caused by the wrong calibration for the energy dependence of ToF. For this reason, the cut for the particle identification is applied only for the slower particles and the particles with faster ToF than photon are accepted in the analysis. The ToF offset becomes shifted as the time goes and the shift is about 1 nsec between the first and the last of the 2005 run. Figure A.4 in Section A.9 displays the sector-by-sector ToF offset as a function of the run number.

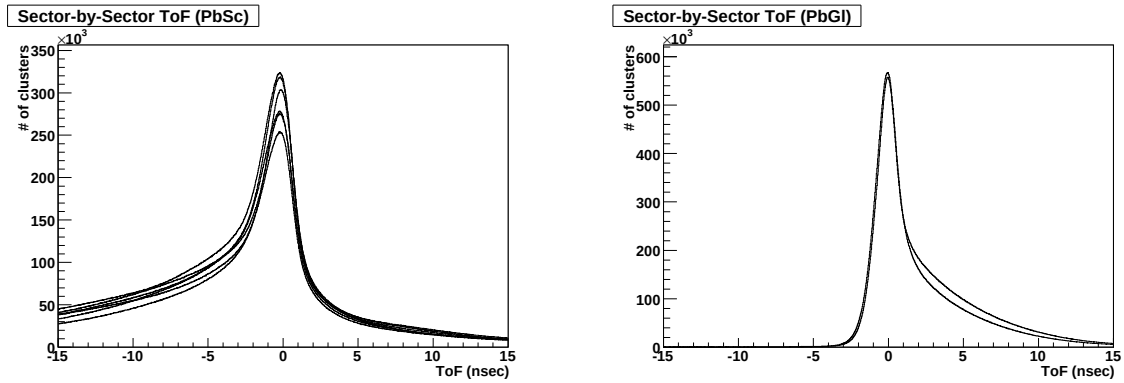

Figure 3.26: The sector-by-sector ToF distribution after the offset calibration. The left is for PbSc and the right is for PbGl. The difference of the statistics comes from the sector-by-sector variation of the ERT efficiency and the warn towers.

In the tower-by-tower calibration, some towers indicate unavailable ToF value. For ex-

ample, two peaks are found in the ToF distribution, or ToF value spreads very widely. It is assumed that the electric circuit to process ToF is broken for these towers, however the energy measurement by these towers are often performed properly. Since the ToF cut for these towers causes more inefficiency than other usual towers, in this thesis, the cut is not applied to the towers and all clusters hitting the towers pass the cut.

3.5.6 Energy calibration of EMCal

Initially the time dependence of the energy gain is corrected tower by tower using the laser system for both PbSc and PbGl. This semi-online calibration corrects only tower-by-tower relative time-shift. Therefore, the gain ununiformity between towers remains. See Section 2.3.4 about the laser system. In the offline analysis, additional energy calibration is carried out utilizing the measured π^0 peak, which is the physics signal and therefore most reliable. The offline calibration is divided into 3 steps; run dependence (time dependence), tower-by-tower calibration and calibration for the absolute scale. The first two calibrations need the iteration each other in principle because the events in whole 2005 run are accumulated in the tower-by-tower calibration and the correction of the run dependence is done sector by sector. However, the satisfactory resolution is achieved by a set of the calibrations and no further iterations are performed. The non-linearity in the energy measurement due to the threshold to each tower is also evaluated in the step for the calibration of the absolute scale. See also Section 3.5.2 about the clustering. Since the measured π^0 peak is used in these steps, the invariant mass of π^0 is need to be reconstructed from the EMCal cluster pairs. To remove the warn towers, the quality assurance of the towers described in Section 3.5.3 is once executed before the energy calibration. After the calibration is finished, the warn tower finding is performed again because the mis-calibration fakes noisy towers. In the following sections, detail description about the offline calibration appears.

Run dependence of energy gain

The time dependence of the EMCal energy gain is initially corrected using the laser system for both PbSc and PbGl. This correction is executed semi-online. In this step, the residual time dependence is calibrated using the measured π^0 peak. π^0s are reconstructed sector-by-sector in every run and the spectra are fitted to the combination of Gaussian and polynomial. The shift of the π^0 peak from the normal position is assumed to be the shift of the energy gain and additional factor is applied to the gain in the analysis. The normal position of the π^0 peak is not same as the mass of π^0, 0.135 GeV/c^2, because of the resolution of the detector. In this step, the observed π^0 peak is set to a certain value near 0.135 GeV/c^2. Finally the absolute scale is calibrated in the last step of the energy calibration. The energy gain turns to become shifted by $\sim$3 %. The position of the π^0 peak as a function of the run number is displayed in Figure A.5 in Section A.10

Tower-by-tower energy gain

The tower-by-tower energy calibration also utilizes the peak position of π^0 in the invariant mass spectrum of the cluster pairs. The deviation of the π^0 peak in the tower-by-tower spectrum from the normal position is assumed to reflect the gain shift. The mass spectrum for a certain tower (the target tower) consists of the cluster pairs which include the cluster located at the target tower. Figure 3.27 displays the concept schematically. On the other hand, probably, the other cluster of such a pair is formed in other place on EMCal. In this

step, it is assumed that the shift of the π^0 peak for the target tower is caused by the gain shift of the target tower and the effects from other towers are averaged and negligible. However, to achieve better calibration, this step is iterated several times. Figure 3.28 displays the comparison of the π^0 peak width before and after the tower-by-tower energy calibration. The width becomes significantly narrower by the calibration. In both cases, the contribution to make the width wider at low p_T is dominated by the energy resolution of EMCal, while that at high p_T is by the position resolution.

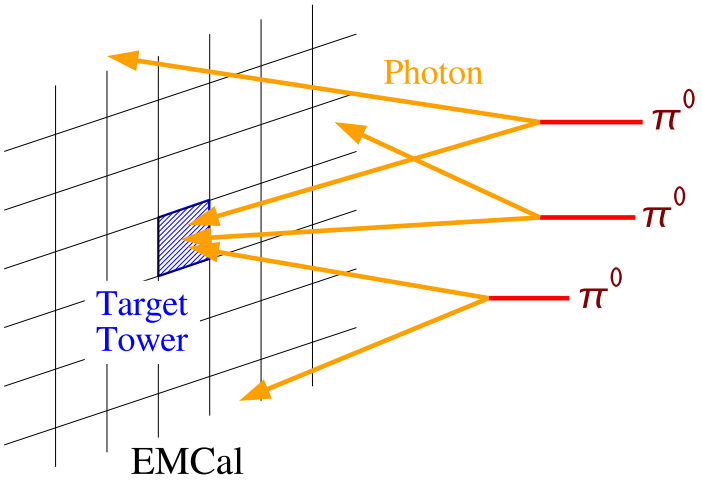

Figure 3.27: The conceptual drawing for the tower-by-tower energy calibration. π^0s whose photon hits the target tower are collected to make the tower-by-tower spectrum.

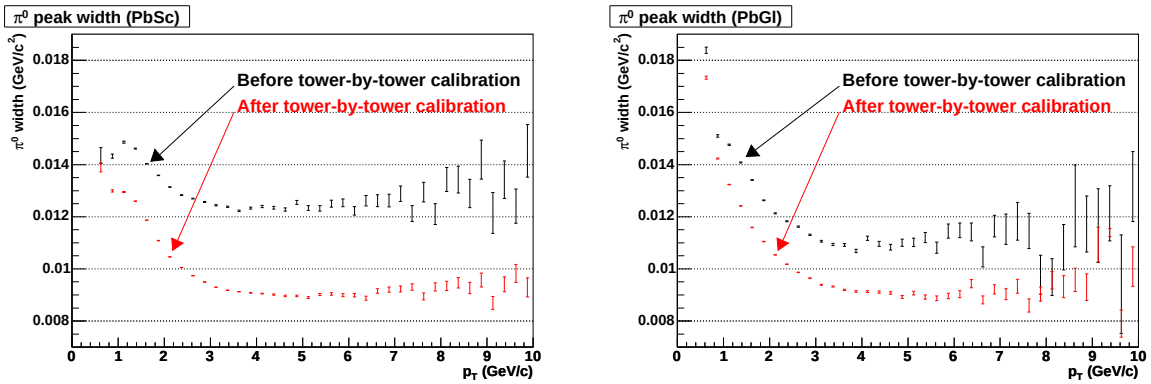

Figure 3.28: The π^0 peak width as a function of π^0 p_T. The left is for PbSc and the right is for PbGl. Less statistics are used for the points before the calibration than those after the calibration because it is sufficient for the comparison.

In this step, the calibration is tried for all towers in EMCal, including even towers with problem in the electrical circuit and the towers located at the edge of the EMCal sector. Then, towers which cannot be calibrated are included in the warn tower described in Section 3.5.3. The reason of the failure in the calibration is mainly due to the electrical noise which covers the π^0 peak. In addition, the behavior of the electrical circuit is strange in some towers,

where two π^0 peaks are observed for example. The incident particle hitting the edge of the EMCal sector does not deposit all energy in EMCal due to the shower leakage. However π^0s are successfully reconstructed using the clusters hitting the edge towers because the most of the energy is detected by the tower the particle hits, though the peak position of π^0 is slightly lower than the normal position. In this calibration, the π^0 peak position for the edge towers is set to the same position as other inner towers since the edge towers are masked in the extraction of the asymmetries. The effect of the slight mis-calibration in the edge towers to the towers near the edge tower is expected to be negligible compared with the accuracy of the calibration. Moreover, the warn tower includes the suspicious towers in which the calibration works but the mass spectrum has bad shape, such as the broad π^0 peak, too much background and so on.

Absolute energy gain

The absolute scale of the energy is calibrated by comparing the π^0 peak and the fast Monte Carlo simulation (FastMC) using both the ERT and MB sample. FastMC is the simple numerical simulation unlike GEANT and utilizes the measured cross section of π^0 as the particle generator. The produced π^0s decay into two photons isotropically in the rest frame of π^0. In the generation of π^0, the spread of the event vertex is simulated based on Gaussian with a width of 30 cm, which is a little narrower than the measured width but the difference does not change the results. Then, FastMC simulate the photons from π^0 with the following setup.

- Energy and position resolution
  The initial energy and position is fluctuated following Gaussian distribution. The resolutions are evaluated by the test beam. See Section 2.3.4 about the performance of EMCal. In this simulation, the additional factor is applied to fit the real data.

- Electromagnetic shower profile
  The profile of the electromagnetic shower is simulated and tower-by-tower energy threshold ($\sim$0.01 GeV) is applied based on the profile. Selection of the core towers in the PbSc clustering is also simulated. See Section 3.5.2 about the clustering.

- Warn and edge towers
  Masked region of EMCal due to the warn or edge towers is simulated. See Section 3.5.3 about the warn and edge towers.

- Trigger efficiency of ERT
  The trigger efficiency of ERT is applied for the single photon. This is disabled for the MB data sample. See Section 3.5.1 about the ERT performance.

Because the charged-particle veto cut and ToF cut is difficult to simulate, they are not applied in the comparison between the data and FastMC.

As well as the energy scale, the resolutions of the energy and position are also reflected by the peak position and width of π^0, which is measured using the data. Therefore, the energy and position resolution in the simulation must be tuned to fit the real data and the energy scale is in turn determined properly.

There are two reasons why not only the width but also the position of the π^0 peak are modified. One is the energy threshold for the EMCal tower, $\sim$0.01 GeV, and it causes that the energy of the reconstructed clusters is lower than the incident energy. The percentage of the

energy loss is larger for the lower energy clusters. The correction of this energy non-linearity is corrected for every cluster based on FastMC. The other effect to modify the peak position of π^0 is caused by the combination of the steep slope of the p_T spectrum of π^0 and the energy resolution of EMCal. In the experiment, when a certain p_T window is selected, the events in the window include not only events with original p_T in the window but also those from the neighbor window because of the smearing effect by the detector resolution. In the case that the p_T spectrum is downside, more events leak into the target window from the initially low p_T window than those from the high p_T window. Since the measured p_T of such events from the lower (higher) p_T window is higher (lower) than the original p_T, the reconstructed π^0 mass is also higher (lower) than the original and universal value of 0.135 GeV/c^2. Consequently, the measured peak position of π^0 becomes higher in the case of the downside p_T distribution and lower for the soaring distribution.

The π^0 peak position becomes additionally lower due to the unusual π^0s. One of the sources of such π^0s is the case that photons from the decay of π^0 convert into the electron positron pairs. π^0 is well reconstructed using such electron positron pairs, when they do not separate each other to form the single clusters. See also Section 3.5.4 about the photons which convert into electron positron pairs. π^0s from the decay of other hadrons like K^0_s and η is another source. One other is π^0s generated in the secondary interaction with the beam pipe or detectors. The invariant mass of all of these unusual π^0s has lower peak position than the usual π^0s reconstructed by the pure photons. The size of the shift due to this effect is evaluated by means of the GEANT simulation to be -1 ± 1 MeV/c^2. Because FastMC cannot simulate this effect, the peak position of π^0 is simply lowered by 1 MeV/c^2. The error of this effect, 1 MeV/c^2, is included in the uncertainty of the energy calibration.

The energy non-linearity determined in this calibration is a function of the cluster energy and described as

$$\begin{aligned} E_{\rm incident} &= E_{\rm cluster}\left[1.0 + \frac{A}{(E_{\rm cluster} - B)^n}\right]^{-1}, \\ \text{where} \quad & A = -101,\ B = -1.91,\ n = 10.0 \text{ for PbSc}, \\ & A = -0.0403,\ B = -0.121,\ n = 0.846 \text{ for PbGl}. \end{aligned} \tag{3.20}$$

$E_{\rm incident}$ and $E_{\rm cluster}$ in the equation is the incident energy and the cluster energy, respectively. The non-linearity correction is normalized to 1 at $E_{\rm incident} \to \infty$. Following this relation, the measured energy of the cluster is corrected. The ratio of the cluster energy and the incident energy obtained by FastMC is displayed in Figure 3.29 as a function of the cluster energy. The difference between PbSc and PbGl is from the method of the clustering. Because only the core towers are used to extract the cluster energy in PbSc, the energy loss due to the tower-by-tower threshold, which is usually caused by the non-core towers, is automatically corrected.

Figure 3.30 and 3.31 displays the comparison between the data and FastMC in the position and the width of the π^0 peak using the ERT data sample. The energy non-linearity is already corrected in these figures. In the tuning of FastMC, additional factor of 6 – 7 % and 2 – 3 mm is added quadratically to the constant term of the energy resolution and the position resolution, respectively. FastMC reproduces the data well at more than 1 GeV/c^2. The discrepancy between the data and FastMC at the lower p_T region is expected to be due to the large background and the difficulty in the extraction of π^0 by the fitting. But the energy scale is determined by the higher p_T region and it is not necessary to fit FastMC to the data at the lower p_T. The figures of the comparison between the data and FastMC for other data sets are summarized in Section A.11.

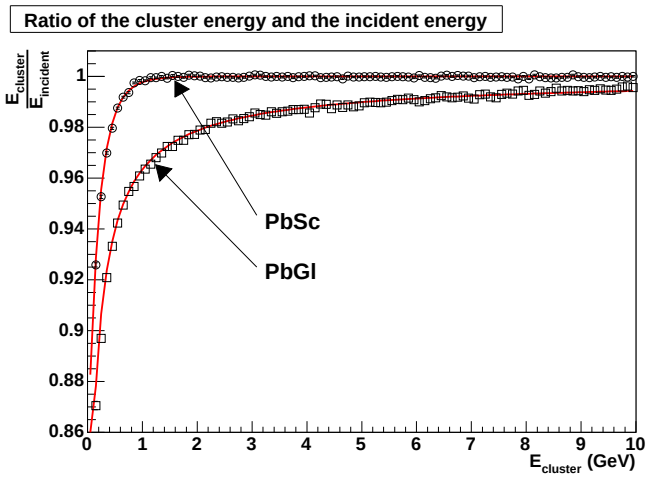

Figure 3.29: The ratio of the cluster energy and the incident energy. The points are obtained by FastMC and the lines show the fit function.

Owing to the enough statistics, FastMC is well tuned with the accuracy of 0.2 MeV/c^2. The uncertainty of 1 MeV/c^2 by the unusual π^0s described above is translated into the uncertainty of 0.7 % in terms of the energy scale. In addition, the slight difference of the π^0 peak position between sectors of EMCal is observed and is expected to be from the mis-alignment of EMCal. The error from the mis-alignment is conservatively evaluated to be 2 % in the energy scale. Finally, the systematic uncertainty of the energy scale is calculated by the quadratic sum to be 2.1 %. As described in Section 3.7.5 in detail, the contribution of this error to that of the asymmetries is negligibly small because the p_T dependence of the observed asymmetries are nearly flat.

3.5.7 Stability of EMCal

The purity of π^0 is utilized to examine the stability of EMCal and the quality of the data. The purity is defined as $\frac{N_{\pi^0}}{N_{\pi^0}+N_{BG}}$, where N_{π^0} and N_{BG} is the number of π^0 and the background under the π^0 peak. In this analysis, N_{π^0} and N_{BG} are counted within the signal window of 0.111 – 0.161 GeV/c^2 for the calculation of the asymmetries. See Section 3.6.1 about the window. Figure 3.32 displays the sector-by-sector π^0 purity as a function of the run number. In the runs with low purity and high background, it is assumed that some additional tower of EMCal is electrically noisy or the beam background is large. The beam background is generated by the interaction of the beam and the material around the collision point such as the beam pipe and the air. Therefore, such runs are discarded in the analysis. The criterion in the rejection is that the deviation from the average is more than 4 sigma in the run-by-run fluctuation. The stability of the position and the width of the π^0 peak are also examined. The information of the peak position is used for the energy calibration as described in Section 3.5.6. The width of the peak is stable over whole 2005 run as displayed in Figure A.6 and no run is discarded by these criteria.

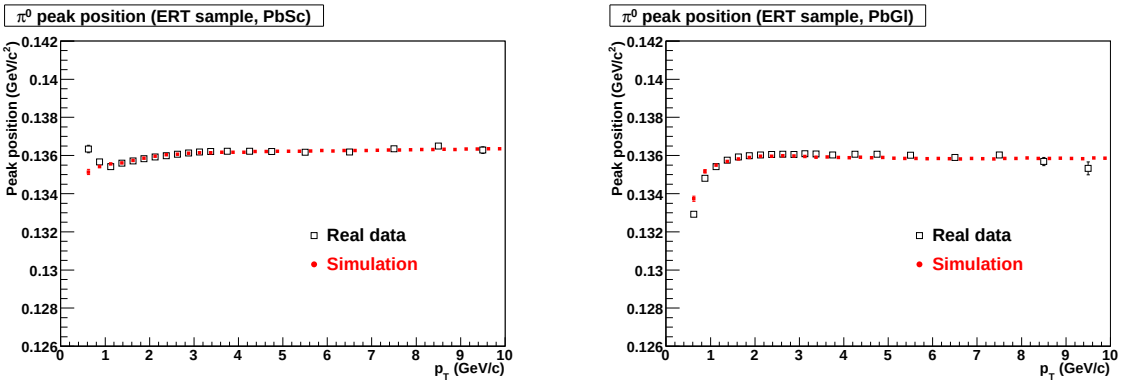

Figure 3.30: The π^0 peak position as a function of p_T after the energy calibration and the energy non-linearity correction. The left is for PbSc and the right is for PbGl. The ERT data sample is used in these figures. The black boxes are obtained by the real data and the red points are the simulation.

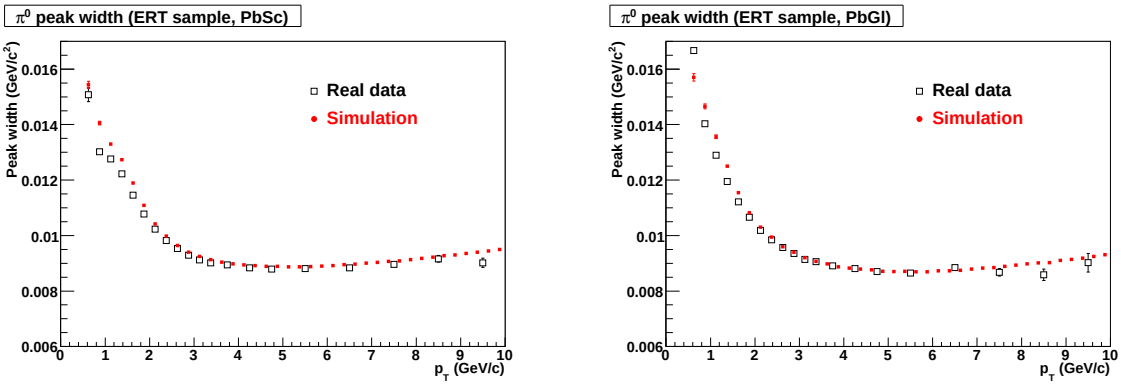

Figure 3.31: The π^0 peak width as a function of p_T after the energy calibration and the energy non-linearity correction. The left is for PbSc and the right is for PbGl. The ERT data sample is used in these figures. The black boxes are obtained by the real data and the red points are the simulation.

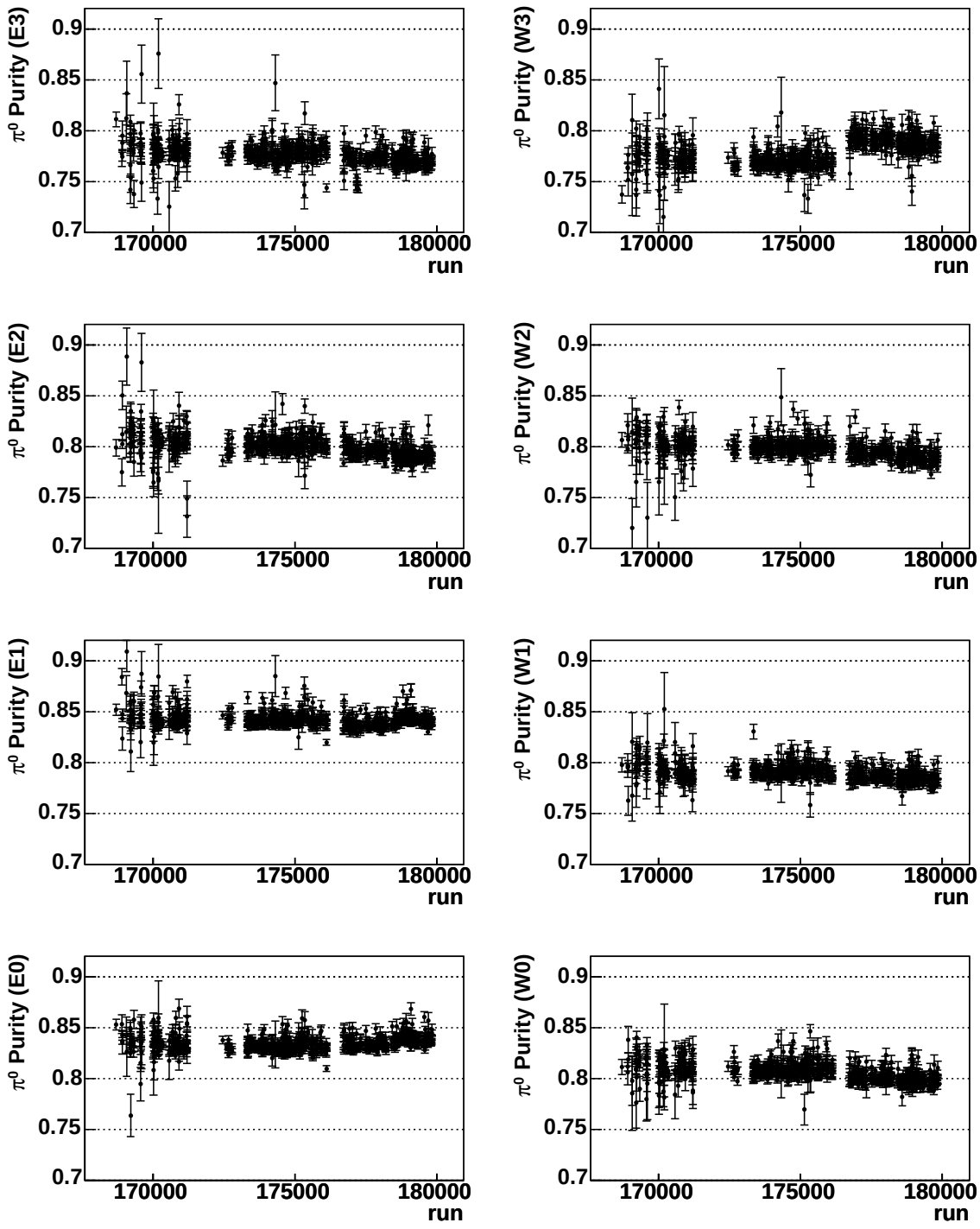

Figure 3.32: The sector-by-sector purity of π^0 as a function of the run number. There is a gap around run 176000, when the number of the beam crossings is increased and the successive bunches are filled by the beam. Therefore, the threshold of ERT is slightly changed at that time. See Section 2.3.4 about the specification of the EMCal trigger.

3.6 Calculation of asymmetries

3.6.1 Process to extract the asymmetries

Since the process is common for A_{LL}, A_{TT} and A_L, the case of A_{LL} is described in this section as an example. The extraction of A_{LL} is performed as follows. Instead of directly extracting the yield of π^0 by the subtraction of the background under the π^0 peak, the contribution of the background is subtracted in terms of A_{LL}. This is the effort to minimize the number of fitting the mass spectrum because it is difficult to evaluate the uncertainty in the fitting.

Figure 3.33 displays the invariant mass spectrum of the cluster pairs in a certain kinematic region and the peak around 0.135 GeV/c^2 on the continuous background is the signal of π^0. The goal is the extraction of A_{LL} for the red region in Figure 3.33. At the first step, A_{LL} is calculated for the sum of π^0 and the background under the π^0 peak in a certain mass window, which is defined as the "signal window" (the sum of the red and yellow region). In the same way, A_{LL} for the background on the both sides of the peak, which is defined as the "background window" (the blue region), is calculated. These two A_{LL}'s are calculated fill by fill and averaged over all fills in the 2005 run. The asymmetries obtained by the average are described as A_{LL}^{sig} for the signal window and $A_{LL}^{BG(side)}$ for the background window. Similarly, $A_{LL}^{\pi^0}$ and $A_{LL}^{BG(under)}$ are defined as the asymmetry for the red and yellow region, respectively, though they cannot be obtained directly. At the second step, the purity of π^0 (p) is evaluated by use of fitting the mass spectrum. The π^0 purity is defined as the percentage of the red region in the signal window. The detail about the evaluation of the purity is described in Section 3.6.2. At the last step, the contribution of $A_{LL}^{BG(under)}$ is subtracted from A_{LL}^{sig}. Based on Equation (1.56), the relation between $A_{LL}^{\pi^0}$, A_{LL}^{sig} and $A_{LL}^{BG(under)}$ is written as

$$\begin{aligned} A_{LL}^{sig} &= \frac{1}{\bar{P_B}\bar{P_Y}}\frac{N_{++}^{sig}-N_{+-}^{sig}R}{N_{++}^{sig}+N_{+-}^{sig}R} \\ &= p\frac{1}{\bar{P_B}\bar{P_Y}}\frac{N_{++}^{\pi^0}-N_{+-}^{\pi^0}R}{N_{++}^{\pi^0}+N_{+-}^{\pi^0}R} + (1-p)\frac{1}{\bar{P_B}\bar{P_Y}}\frac{N_{++}^{BG(under)}-N_{+-}^{BG(under)}R}{N_{++}^{BG(under)}+N_{+-}^{BG(under)}R} \\ &= pA_{LL}^{\pi^0} + (1-p)A_{LL}^{BG(under)}. \end{aligned} \tag{3.21}$$

$\bar{P_B}$ and $\bar{P_Y}$ is the blue and yellow beam polarization, respectively. N is the yield and the superscript indicates the mass window as for A_{LL} and the subscript indicates the helicity combination of the collision. R is the relative luminosity. Therefore $A_{LL}^{\pi^0}$ and its uncertainty is obtained by

$$A_{LL}^{\pi^0} = \frac{1}{p}A_{LL}^{sig} - \frac{1-p}{p}A_{LL}^{BG(under)}, \tag{3.22}$$

$$\Delta A_{LL}^{\pi^0} = \frac{1}{p}\Delta A_{LL}^{sig} \oplus \frac{1-p}{p}\Delta A_{LL}^{BG(under)} \oplus \frac{A_{LL}^{sig}-A_{LL}^{BG(under)}}{p}\frac{\Delta p}{p}. \tag{3.23}$$

However, because $A_{LL}^{BG(under)}$ cannot be extracted directly, it is evaluated by $A_{LL}^{BG(side)}$ assuming $A_{LL}^{BG(under)}$ and $A_{LL}^{BG(side)}$ are the same value. In the following text, $A_{LL}^{BG(side)}$ is simply described as A_{LL}^{BG}. In the actual calculation, range of $M_{center} - 0.025$ GeV/c^2 to $M_{center} + 0.025$ GeV/c^2 is adopted for the signal window, and range of $M_{center} - 0.08$ GeV/c^2 to $M_{center} - 0.05$ GeV/c^2 and $M_{center} + 0.05$ GeV/c^2 to $M_{center} + 0.08$ GeV/c^2 are for the background window. M_{center} is determined to be 0.136 GeV/c^2. The range and position of

the windows are fixed in all measured p_T bins. As displayed in Figure 3.30, M_{center} is nearly the center of the measured π^0 peak and the deviation is 0.003 GeV/c^2 at most. The signal window covers more or less 2-sigma in the width of the π^0 peak as compared to Figure 3.31.

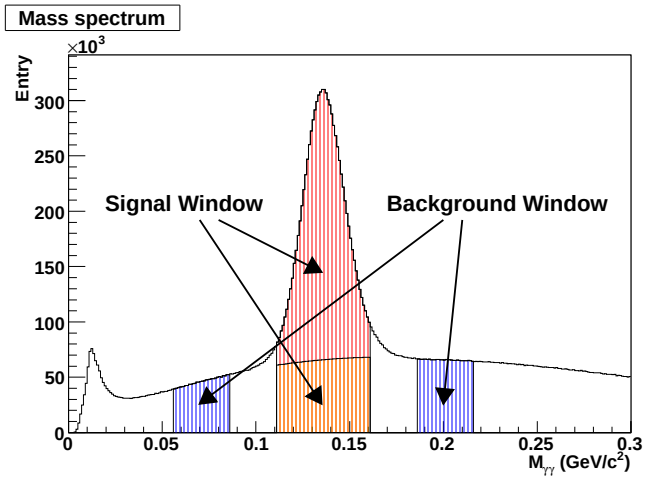

Figure 3.33: The mass window for the asymmetry calculation. To extract the asymmetry of π^0 (red), the contribution of the background under the peak (yellow) is evaluated using the background on the sides of the peak (blue).

The validity of this process to subtract the background is supported utilizing FastMC described in Section 3.5.6. Figure 3.34 and 3.35 display the energy asymmetry distribution for π^0 and compare the data with FastMC. The energy asymmetry is defined as $\frac{|E_1-E_2|}{E_1+E_2}$, where E_1 and E_2 are the energy of each cluster of the cluster pair. The red points are obtained from the data and the histogram filled with gray is produced by FastMC. As in the case to calculate the asymmetry, the extraction of the energy asymmetry distribution for pure π^0s is executed by subtracting the contribution of the background under the π^0 peak by use of the background on the sides of the peak. On the other hand, the distribution is for pure π^0 in FastMC.

The energy threshold for the cluster of 0.1 GeV makes the steep drop on the right side of the figures. The asymmetric decay favored in the ERT sample is caused by the EMCal trigger which require that at least one of the clusters in the pair is over the threshold in energy. Therefore, the distribution becomes more flat for π^0s with high p_T. FastMC reproduces the data well except for the lowest p_T bin, where the background shape in the mass distribution is asymmetric around the π^0 peak and the energy asymmetry distribution of the background is a little different between the lower and the higher mass window. The agreement between the data and FastMC implies both that FastMC is well tuned and that the background on the sides of the peak well represents the background under the peak.

Similarly, the mean p_T value corresponding to each p_T bin is evaluated. In terms of the equation, p_T for pure π^0s is described as

$$\langle {p_T}^{\pi^0} \rangle = \frac{1}{p} \langle {p_T}^{sig} \rangle - \frac{1-p}{p} \langle {p_T}^{BG} \rangle, \tag{3.24}$$

where the superscript of p_T indicates the mass window and $\langle p_T \rangle$ means taking an average value of p_T in the corresponding mass window. The mean values are listed in Table 3.7.

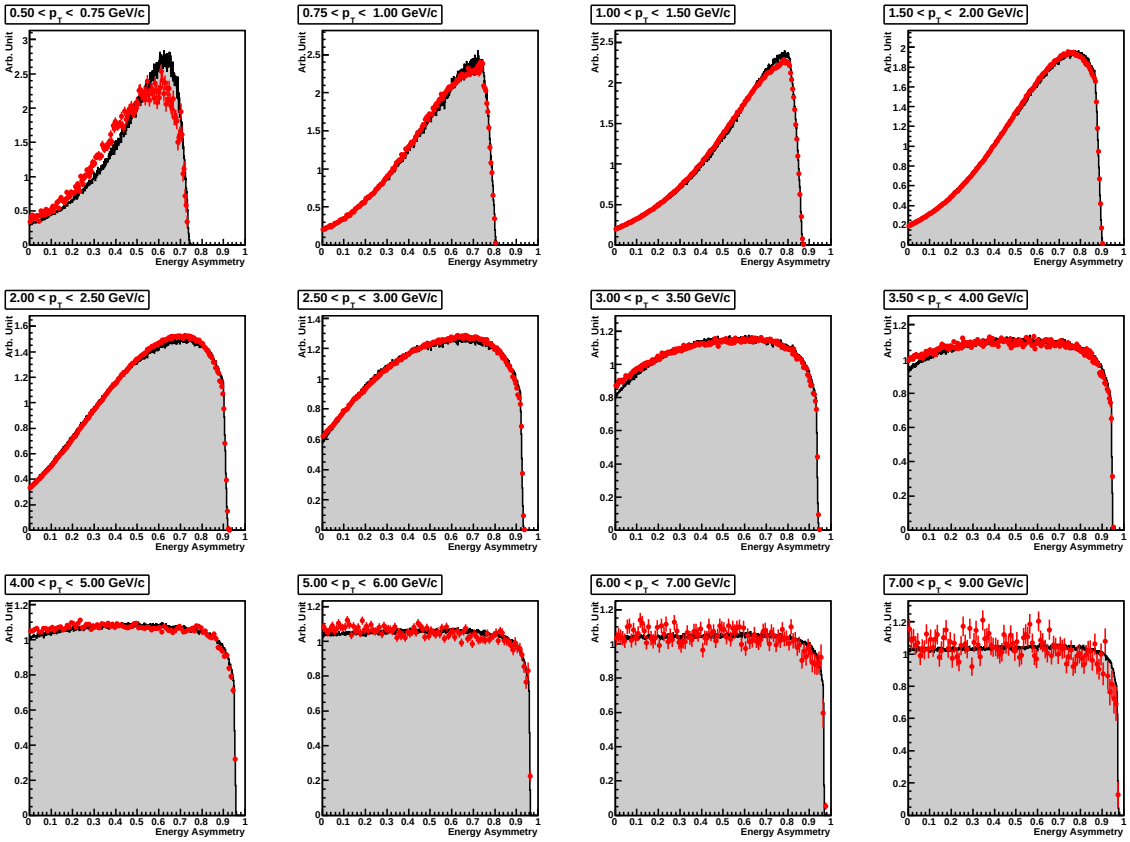

Figure 3.34: The energy asymmetry distribution using the ERT data sample. The red points is obtained from the data and the histogram filled with gray is produced by FastMC.

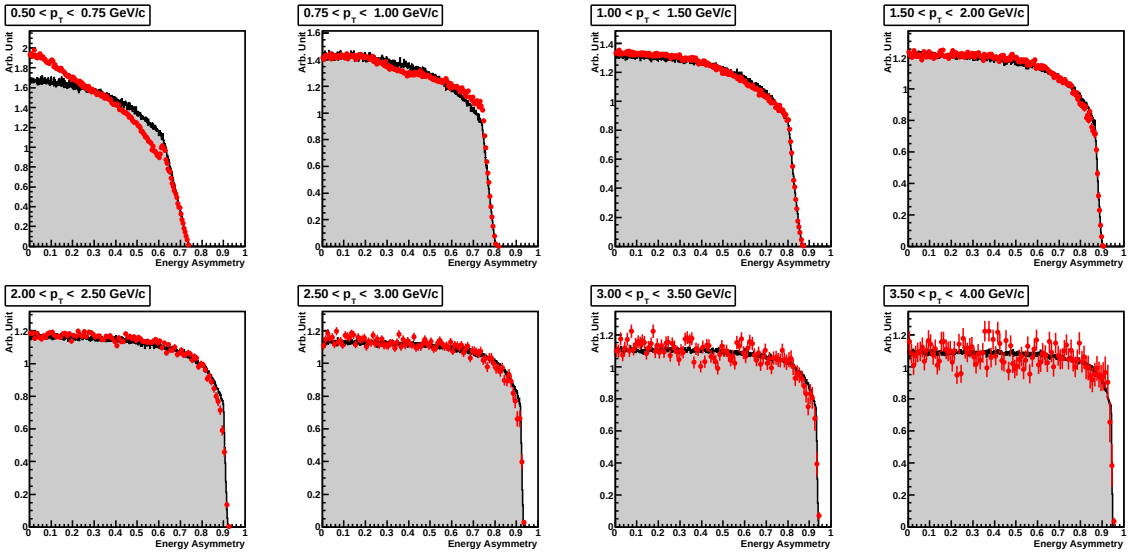

Figure 3.35: The energy asymmetry distribution using the MB data sample. The red points is obtained from the data and the histogram filled with gray is produced by FastMC.

The mean p_T for pure π^0 is also calculated using the background on the only lower side or higher side of the peak. The discrepancy more than the statistical uncertainty between them is assigned as the systematic error. The error on the mean p_T is 2.4 % at a maximum at the lowest p_T bin for the MB data sample and contributes to the negligible uncertainty in terms of the asymmetries. It is evaluated in the same way as that from the uncertainty of the energy scale. See Section 3.7.5 for more detail.

p_T range (GeV/c)	Mean p_T (MB) (GeV/c)	Mean p_T (ERT) (GeV/c)
0.5 – 0.75	$0.62 \pm 0.000 \pm 0.015$	$0.67 \pm 0.000 \pm 0.004$
0.75 – 1.0	$0.86 \pm 0.000 \pm 0.003$	$0.90 \pm 0.000 \pm 0.001$
1.0 – 1.5	$1.20 \pm 0.000 \pm 0.002$	$1.29 \pm 0.000 \pm 0.002$
1.5 – 2.0	$1.70 \pm 0.000 \pm 0.000$	$1.75 \pm 0.000 \pm 0.000$
2.0 – 2.5	$2.20 \pm 0.000 \pm 0.000$	$2.22 \pm 0.000 \pm 0.000$
2.5 – 3.0	$2.71 \pm 0.000 \pm 0.000$	$2.72 \pm 0.000 \pm 0.000$
3.0 – 3.5	$3.21 \pm 0.001 \pm 0.000$	$3.21 \pm 0.000 \pm 0.000$
3.5 – 4.0	$3.71 \pm 0.001 \pm 0.000$	$3.72 \pm 0.000 \pm 0.000$
4.0 – 5.0		$4.38 \pm 0.000 \pm 0.000$
5.0 – 6.0		$5.40 \pm 0.001 \pm 0.000$
6.0 – 7.0		$6.41 \pm 0.001 \pm 0.000$
7.0 – 9.0		$7.72 \pm 0.003 \pm 0.000$

Table 3.7: The mean value of p_T for pure π^0 after the background subtraction. The first error shows the statistical one and the second is systematic.

3.6.2 π^0 purity

As described in Section 3.6.1, it is necessary to know the purity of π^0 to finally extract the asymmetries for pure π^0. The purity is defined as the percentage of the π^0 yield in a certain mass window including the π^0 peak. The purity is obtained by fitting the mass spectrum and Figure 3.36 displays the explanation drawing for that. Instead of fitting the π^0 peak directly, only the background region on the sides of the peak (two blue window) are fitted to the polynomial (green line) to evaluate the yield of the background under the peak (the yellow region). The background yield is simply calculated by integrating the fit function over the mass window for the asymmetry extraction (the red window), which is defined as the signal window as described in Section 3.6.1. Then the yield of π^0 is obtained by subtracting the background yield from the total yield in the signal window.

The reason not to fit the peak is that the π^0 peak is not the simple Gaussian distribution and the fitting to Gaussian results in the huge chi-square (the reduced chi-square is the order of 100). This tendency of the peak shape is reproduced by FastMC described in Section 3.5.6. On the other hand, only the background around the peak is well expressed by the polynomial function (the reduced chi-square of the fitting is a few). The function to fit the background region is from the quadratic polynomial for the higher p_T bin to the 5th degree polynomial for the lowest p_T bin.

The basic windows for the fitting to evaluate the background yield (the blue window) are $(M_{center} - 0.08)$ – $(M_{center} - 0.05)$ GeV/c^2 and $(M_{censer} + 0.05)$ – $(M_{center} + 0.15)$ GeV/c^2, which is wider than the background window used for the calculation of the asymmetries.

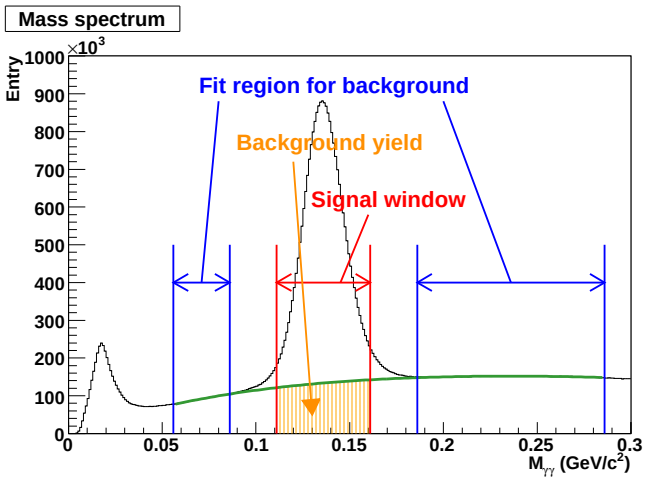

Figure 3.36: The drawing to explain how to evaluate the purity of π^0. The green curve is the function fitted to the background region displayed as the blue windows.

The signal window is ± 0.025 GeV/c^2 around M_{center}. For all p_T range, M_{center} is set to 0.136 GeV/c^2, which is roughly the center of the π^0 peak as displayed in Figure 3.30.

The uncertainty of the purity is evaluated considering as follows.

- Statistical error of the yield.
- Uncertainty from the fit function.
  In the integral of the fit function to evaluate the background yield, the uncertainty from the fit parameters is calculated. Since it should include the statistical error of the background yield, the contribution of the statistics are subtracted.
- Fluctuation of the fittings.
  The fitting is performed 9 times with mass range changed. In addition, the degree of the polynomial is increased by one at the fitting. Totally 18 patterns of the fitting are proved and the maximal deviation from the value with the basic window is assigned to the final uncertainty of the purity.

Table 3.8 summarize the purities and its error for the data with the longitudinal polarization. The results are consistent with the purities for the transverse polarization data within the uncertainties. The systematic uncertainty is dominant compared with the statistical one. The major contribution to the systematic error in the lower p_T region is the fluctuation of the fitting by changing the fit window and the function (the third item in the above itemization). While the error from the each fitting is main in the higher p_T region (the second item in the above itemization) and it implies that the poor statistics and the fit function with relatively large degree-of-freedom produce the ambiguity in the fitting. The error of the purity is propagated into the error of the asymmetries. However, it is considerably small following Equation (3.23). See Section 3.7.6 about the systematic error on the asymmetries.

3.6.3 Statistical error evaluation for the asymmetries

Instead of the square root of the statistics, the statistical error of the yield is estimated more properly in this analysis. The basic idea is that what follows the Poisson distribution is not

p_T (GeV/c)	MB purity (%)	ERT purity (%)
0.5 – 0.75	$34.8 \pm 0.01 \pm 1.70$	$30.9 \pm 0.04 \pm 1.15$
0.75 – 1.0	$51.0 \pm 0.01 \pm 1.40$	$48.7 \pm 0.02 \pm 3.53$
1.0 – 1.5	$67.6 \pm 0.01 \pm 0.75$	$63.7 \pm 0.01 \pm 1.76$
1.5 – 2.0	$80.4 \pm 0.03 \pm 0.69$	$74.6 \pm 0.01 \pm 1.49$
2.0 – 2.5	$86.2 \pm 0.04 \pm 0.50$	$83.2 \pm 0.01 \pm 0.18$
2.5 – 3.0	$89.1 \pm 0.07 \pm 0.48$	$88.2 \pm 0.01 \pm 0.15$
3.0 – 3.5	$91.4 \pm 0.10 \pm 1.82$	$90.8 \pm 0.02 \pm 0.40$
3.5 – 4.0	$92.4 \pm 0.15 \pm 2.03$	$92.0 \pm 0.02 \pm 0.34$
4.0 – 5.0		$92.7 \pm 0.03 \pm 0.34$
5.0 – 6.0		$93.1 \pm 0.06 \pm 0.53$
6.0 – 7.0		$93.4 \pm 0.10 \pm 1.23$
7.0 – 9.0		$93.7 \pm 0.14 \pm 1.27$

Table 3.8: The purity of π^0 for the ERT and MB sample with longitudinal polarization. The first and second error indicates the statistical and systematic error, respectively.

the statistics of π^0 but the number of the collisions. This statement is easily understood if always two particles are generated in the single collision. In this case, the number of the generated particles is $2n$ when n collisions occur. Therefore, the statistical error of the generated particles should be $2\sqrt{n}$, not $\sqrt{2n}$.

For more realistic case, the situation that k particles are observed in N_k^{col} collisions out of N^{col} collisions in a certain kinematical range is considered. N^{col} and the total number of the particles (N^{part}) in N^{col} collisions are written as

$$N^{col} = \sum_{k=0}^{\infty} N_k^{col}, \qquad N^{part} = \sum_{k=0}^{\infty} k N_k^{col}. \tag{3.25}$$

As described above, when N^{col} follows the Poisson distribution ($\Delta N_k^{col} = \sqrt{N_k^{col}}$), the error of N^{part} is calculated as follows.

$$\begin{aligned} \Delta N^{part} &= \sqrt{\sum k^2 N_k^{col}} \\ &= k^{enhance} \sqrt{N^{part}}, \end{aligned} \tag{3.26}$$

where

$$k^{enhance} = \sqrt{\frac{\mu_k^2 + \sigma_k^2}{\mu_k}}, \qquad \mu_k = \frac{\sum k N_k^{col}}{\sum N_k^{col}}, \qquad \sigma_k = \frac{\sum (k-\mu_k)^2 N_k^{col}}{\sum N_k^{col}}. \tag{3.27}$$

The range of k for the summation is abbreviated. $k^{enhance}$ indicates the enhancement of the statistical error from the simple square root. In the case of the example above, obviously $\mu_k = 2$ and $\sigma_k = 0$. Then, the enhancement factor of $\sqrt{2}$ is reproduced. In terms of A_{LL}, the uncertainty is multiplied by a factor of $k^{enhance}$ from Equation (1.56).

In this analysis, N^{part} corresponds to the statistics of the cluster pairs in a certain mass window and kinematical region. Table 3.9 collects $k^{enhance}$'s for the yield in the signal window and the background window defined in Section 3.6.1. Because the multiplicity of the cluster pairs is larger in the lower p_T region for the MB data sample, $k^{enhance}$ is larger in the lower p_T bin. On the other hand, $k^{enhance}$ is smaller for the ERT sample than that for MB since the low energy clusters are suppressed by the EMCal trigger.

p_T (GeV/c^2)	MB	ERT
0.5 – 0.75	1.16 (1.14)	1.05 (1.05)
0.75 – 1.0	1.09 (1.08)	1.05 (1.04)
1.0 – 1.5	1.08 (1.08)	1.06 (1.06)
1.5 – 2.0	1.04 (1.05)	1.05 (1.05)
2.0 – 2.5	1.03 (1.04)	1.03 (1.04)
2.5 – 3.0	1.02 (1.04)	1.02 (1.04)
3.0 – 3.5	1.02 (1.03)	1.02 (1.04)
3.5 – 4.0	1.01 (1.03)	1.01 (1.03)
4.0 – 5.0		1.02 (1.04)
5.0 – 6.0		1.02 (1.04)
6.0 – 7.0		1.01 (1.04)
7.0 – 9.0		1.02 (1.05)

Table 3.9: $k^{enhance}$ for the yield in the signal window. $k^{enhance}$ for the background window is in the parenthesis. These values are extracted using whole EMCal sectors. The data with p_T more than 4.0 GeV/c are not analyzed for the MB sample due to the small statistics.

3.6.4 Asymmetries

A_{LL}, A_{TT} and A_L are calculated following the process described in Section 3.6.1. Figure 3.37 displays an example of A_{LL} for the signal window, 0.111 – 0.161 GeV/c^2 in the mass spectrum, as a function of the fill number. Then, the points of fill-by-fill A_{LL} are fitted to constant. The obtained average value is defined as A_{LL}^{sig} in Equation (3.23). Similarly, A_{LL}^{BG} is calculated using the background window. Reduced chi-squares of fitting the fill-by-fill asymmetries are in the range of 0.65 – 1.48 for A_{LL}, 0.002 – 5.97 for A_{TT} and 0.66 – 1.76 for A_L. Small and large reduced chi-squares for A_{TT} are simply due to small number of fills. Evaluation of the chi-squares are carried out by bunch shuffle as explained in Section 3.7.8. It is concluded by

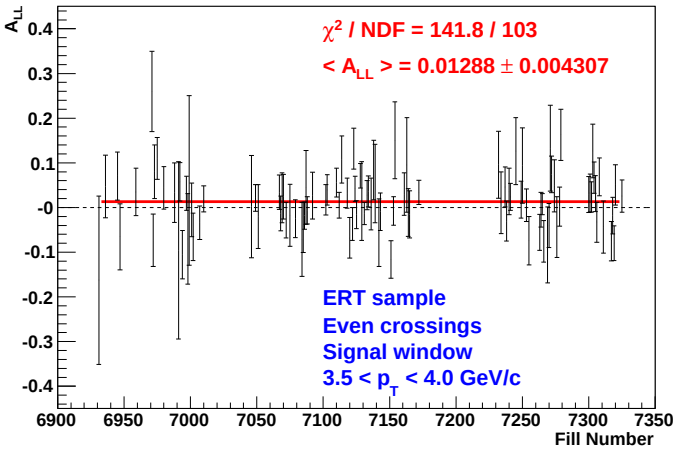

Figure 3.37: A_{LL} for the signal window as a function of the fill number. The even beam crossing of the ERT data sample are used for this figure. p_T range selected is 3.5 – 4.0 GeV/c as an example. The dashed line indicates $A_{LL} = 0$. The red line is the result of fitting to constant.

the bunch shuffle that the chi-squares are within statistical fluctuation except for the lower p_T bin of A_{LL} with MB sample. Finally, $A_{LL}^{\pi^0}$ is obtained by subtracting the contribution of A_{LL}^{BG} from A_{LL}^{sig} following Equation (3.23), where the purity in Table 3.8 is used. In the calculation of the asymmetries for ERT sample, the data is divided into even and odd number crossings due to the trigger specification. See Section 2.3.4 about the ERT trigger.

Figure 3.38 displays A_{LL}^{sig} and A_{LL}^{BG} for the ERT sample with even and odd crossings, and the MB sample as a function of p_T. $A_{LL}^{\pi^0}$ after the background correction is displayed in Figure 3.39. The results of $A_{LL}^{\pi^0}$ are consistent between the ERT and MB data. The results from the even and odd crossings of the ERT sample are averaged to obtain the final results, which is described in Section 4.1. For these and following figures of the asymmetries in this section, the mean value of p_T described in Table 3.7 is not applied but just a center of each bin is used.

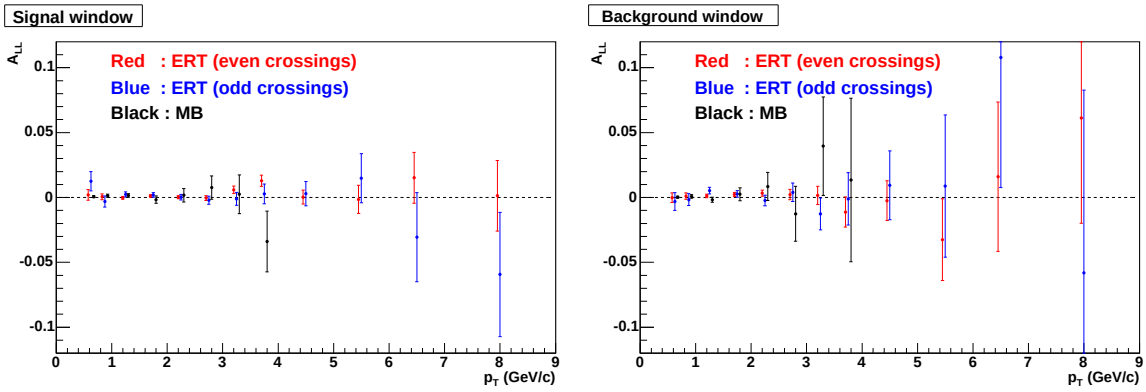

Figure 3.38: A_{LL} as a function of p_T for the signal window (left) and the background window (right). The red, blue and black points are produced using the ERT even crossings, the ERT odd crossings and the MB data, respectively. p_T for each black point is just a center of the bin, and those for blue and red points are shifted by ± 0.05 GeV/c from the center.

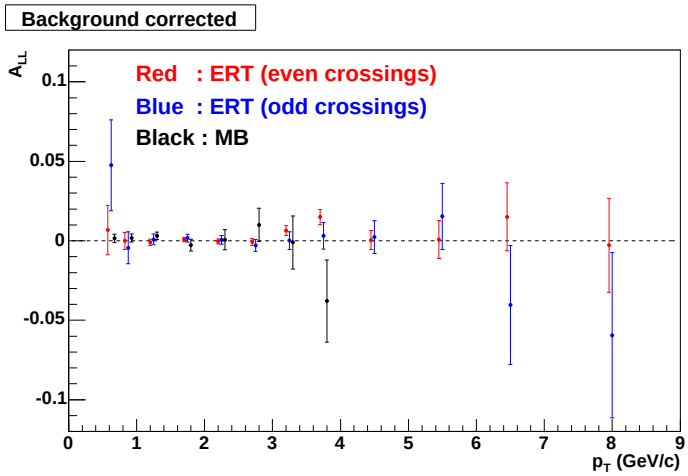

Figure 3.39: π^0 A_{LL} as a function of p_T. The red, blue and black points are produced using the ERT even crossings, the ERT odd crossings and the MB data, respectively. p_T for each point is just a center of the bin, and those for blue and red points are shifted by ± 0.05 GeV/c from the center.

In the same way, π^0 A_{TT} is extracted using the data with the beam polarized transversely. In practice, the measured asymmetry A'_{TT} should have azimuthal angle dependence as described in Section 1.12. However, the data is integrated over whole detector coverage in the analysis. Because A'_{TT} is proportional to $-\cos(2\phi)$ (see Section 2.3.1 for definition of ϕ), it is necessary to correct A'_{TT} by a factor of $\sim$0.588 to obtain A_{TT}. (see Section 2.3.1 about the detector coverage). In Figure 3.40, $A'^{\pi^0}_{TT}$ is displayed. In terms of the A_{LL} measurement, A_{TT} causes a systematic uncertainty and the contribution is evaluated in Section 3.7.3.

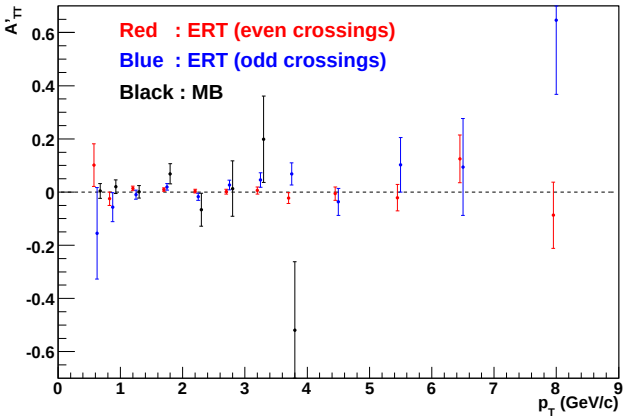

Figure 3.40: π^0 A'_{TT} as a function of p_T. The red, blue and black points are produced using the ERT even crossings, the ERT odd crossings and the MB data, respectively. p_T for each point is just a center of the bin, and those for blue and red points are shifted by ± 0.05 GeV/c from the center.

In addition, the single spin asymmetry A_L is also calculated using the longitudinal polarization data. Since both the blue and yellow beam are polarized, A_L can be extracted using the blue and yellow beam, respectively. Figure 3.41 displays $A_L^{\pi^0}$ as a function of p_T. It is expected that the contribution of the weak interaction is negligibly small in this energy scale and A_L results in zero. As expected, the measured A_L is consistent with zero within the statistical error.

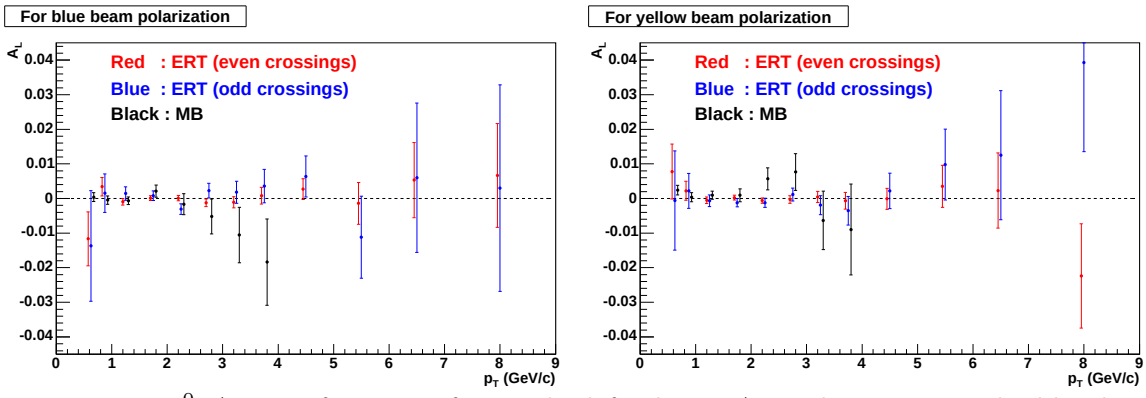

Figure 3.41: π^0 A_L as a function of p_T. The left plot is A_L with respect to the blue beam polarization and the right is for the yellow beam polarization. The red, blue and black points are produced using the ERT even crossings, the ERT odd crossings and the MB data, respectively. p_T for each point is just a center of the bin, and those for blue and red points are shifted by ± 0.05 GeV/c from the center.

3.7 Systematic uncertainty evaluation

The several sources of the systematic uncertainty are considered in this analysis. They are listed in the following subsections and the summary of the systematic uncertainty for π^0 A_{LL} is put in Section 3.7.9. The summary for A_{TT} and A_L is written in Section A.16.

3.7.1 Beam shift and tilt at the collision point

As described in Section 2.1, the beam has a finite size on the x-y plane and may tilt from the ideal trajectory. The contribution from such effects to the uncertainty in the results are evaluated in this section. Three cases (a), (b) and (c) are assumed as displayed in Figure 3.42.

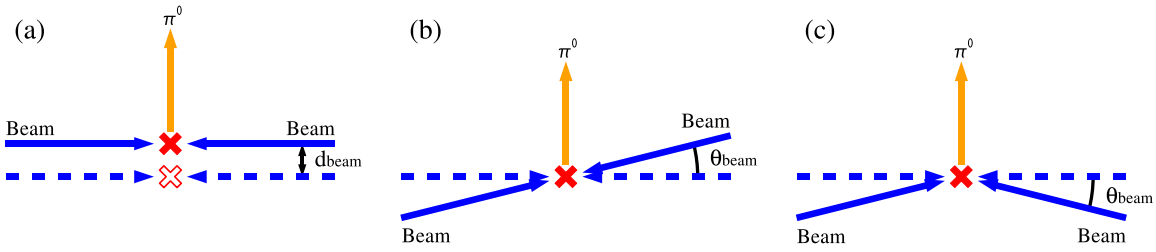

Figure 3.42: Three cases of the systematic uncertainty related to the initial beam direction. The dashed arrows are the planned beam direction and the solid arrows indicate the assumption for the evaluation of the error.

(a) Shift of the event vertex.
RHIC beam is designed to have the transverse size of $\sim$ 0.4 mm. In addition, the analysis on the charged particle using the central arm reveals that the beam position at the collision point is shifted by about 3 mm along the y-axis from the planned position. Since the measured π^0 mass is inversely proportional to the distance from the event vertex to EMCal, the shift of 3 mm, d_{beam} in Figure 3.42.(a), results in the shift of the measured mass of $\sim \frac{3}{5000} = 0.06$ %, where 5000 mm is the typical distance of the collision point to EMCal. Though the systematic shift of the measured π^0 peak has possibility to affect the energy calibration, the shift of 0.06 % is negligible compared to the assigned uncertainty of the energy scale of 2.1 %. See Section 3.5.6 about the energy scale.

(b) Tilt of the beam direction.
In this case, the blue and yellow beam are parallel each other but tilted by θ_{beam} as displayed in Figure 3.42.(b). This effect results in the shift in the rapidity η of π^0. For the evaluation, the angle of the beam tilt of $\theta_{beam} = 0.002$ is assumed.[4] This introduces the shift of $\sim$0.002 in η, which is negligible in our measurement where the data are accumulated over the measured η region.

[4]This assumption corresponds to 3.6 cm shift on the x-y plane at 1800 cm from the collision point, where ZDC is located. Therefore, it is supposed to be an overestimation since A_N (a left-right asymmetry by the beam transversely polarized) is properly measured by a 10 cm-width ZDC. See Section 2.2.3 about PHENIX local polarimeter.

(c) Boost by the beam tilt.
When the beams are tilted as displayed in Figure 3.42.(c), generated particles are boosted. Assuming the angle of the beam tilt of 0.002 in the same way as the previous item, the discrepancy between the measured momentum and the momentum in the rest frame of the initial collision system is calculated to be ∼0.2 %. This systematic shift is negligible compared to the uncertainty of the energy scale of 2.1 % as described in Section 3.5.6.

3.7.2 Beam polarization

Uncertainty of A_{LL} is evaluated based on Equation (1.56);

$$\Delta A_{LL}|_{pol.} = A_{LL}\frac{\Delta(P_B P_Y)}{P_B P_Y}, \tag{3.28}$$

where residual transverse component of the polarization is ignored. As obtained above, the uncertainty from the beam polarization is fully correlated over all p_T bin and behaves as a scale. This is same for A_{TT}. Similarly, the uncertainty from the polarization becomes approximately scale error for A_L as explained in Section A.15. Using values described in Section 3.3, the error from the beam polarization is summarized in Table 3.10. Following

	A_{LL}	A_{TT}	A_L
$\frac{\Delta A}{A}$	0.095	0.107	0.047

Table 3.10: Systematic uncertainty of A_{LL}, A_{TT} and A_L from the error of the beam polarization. The uncertainty is correlated over all p_T bin.

a general manner, such a scale uncertainty is treated separately from other uncorrelated systematic uncertainties in this thesis.

3.7.3 Local polarimeter

PHENIX local polarimeter detects the residual transverse component of the beam polarization during the data taking with the polarization directed longitudinally. The relation between A_{LL}, A_{TT} and the measured asymmetry A_{meas} normalized by the beam polarization is described as follows;

$$A_{LL} = \frac{P_B}{P_{B,L}}\frac{P_Y}{P_{Y,L}}A_{meas} - \frac{P_{B,T}}{P_{B,L}}\frac{P_{Y,T}}{P_{Y,L}}A'_{TT}, \tag{3.29}$$

where P is the beam polarization. B (Y) at the subscript indicates the blue (yellow) beam and L (T) indicates the longitudinal (transverse) polarization. P with neither L or T is the size of the polarization; $P = \sqrt{P_L^2 + P_T^2}$. See Section 1.12 and A.3 about this equation. Because A_{TT} is predicted to have $-\cos(2\phi)$ dependence as mentioned in Section 1.12, the measured asymmetry A'_{TT} instead of A_{TT} itself is used in Equation (3.29). From Equation (3.29), the finite transverse polarization observed introduces the contamination of A'_{TT} in A_{LL} measurement, as well as the need to correct by P/P_L. The results of local polarimeter are described in Section 3.3.

- Contamination of A'_{TT}
  Though A_{TT} appears when the beam polarizations are parallel, it is ignored and the error is evaluated conservatively. Instead of correcting A_{meas} by measured A'_{TT}, the size of $\frac{P_{B,T}}{P_{B,L}}\frac{P_{Y,T}}{P_{Y,L}}A'_{TT}$ is assigned as the error of A_{LL}. Though the measured A'_{TT} is consistent with 0 within the statistical error, the contamination of A'_{TT} is evaluated assuming the absolute value of real A'_{TT} is in the range from 0 to the maximum one σ edge of the statistical error. The error is summarized in Section 3.7.9.

- Uncertainty from P/P_L
  Similarly to the previous section, A_{meas} is not corrected by $\frac{P_B}{P_{B,L}}$ and $\frac{P_Y}{P_{Y,L}}$. Instead, the error is evaluated as follows. The first term of Equation (3.29) is approximated by

$$\frac{P_B}{P_{B,L}}\frac{P_Y}{P_{Y,L}}A_{meas} \sim A_{meas} + (\Delta_B + \Delta_Y)A_{meas}, \tag{3.30}$$

  where $\Delta_{B(Y)}$ is $1 - \frac{P_{L,B(Y)}}{P_{B(Y)}}$ and the approximation is executed assuming $\Delta_{B(Y)} \ll 1$. The second term of Equation (3.30) is assigned as the systematic uncertainty of A_{LL}. The evaluated uncertainty is summarized in Summary 3.7.9.

3.7.4 Relative luminosity

The uncertainty of the relative luminosity ΔR is described in Section 3.4. ΔR is translated into the uncertainty of A_{LL} following Equation (3.11). The uncertainty is evaluated for whole 2005 run using the average beam polarization listed in Table 3.1. The results are summarized in Section 3.7.9.

3.7.5 Energy calibration

For the uncertainty of the energy calibration, 2.1 % from the energy scale, the error for each p_T bin summarized in Table 3.7 and the smearing effect for the p_T binning caused by the finite energy resolution are considered. As easily expected, when an observed asymmetry has no dependence on p_T, the uncertainties above do not affect the final results of the asymmetry. On the other hand, steep p_T dependence causes a large systematic uncertainty on the asymmetry. Although currently the observed asymmetries do not show a significant p_T dependence, the uncertainty from the energy calibration is evaluated assuming the case that $A_{LL} = \pm 0.005\times$ [p_T in GeV/c], which is displayed as green lines in Figure 3.43. Similarly, the gradients of 0.0025 and 0.03 are used in the evaluation for A_L and A'_{TT}, respectively.

Obviously, the error for p_T, Δp_T, introduces the product of the gradient and Δp_T as an error for the asymmetries. While the smearing effect is evaluated utilizing FastMC which is described in Section 3.5.6. Figure 3.44 expresses the smearing effect for p_T. Three peaks indicate the original p_T distribution for π^0s in the bins of 1.0 – 1.5, 3.0 – 3.5 and 7.0 – 9.0 GeV/c, respectively, in the measured p_T. ERT is simulated for Figure 3.44. Because the fluctuation of the energy measurement is larger for higher energy clusters, the smearing effect also becomes larger in higher p_T bin. Usually the smearing is larger at the lower p_T edge than the higher edge since the p_T distribution is steeply downside. However, in the case of the ERT sample, it is opposite due to the EMCal trigger as displayed as the red peak in Figure 3.44. Finally, the systematic uncertainties on the asymmetries are summarized in Section 3.7.9 for the error from the energy calibration as well as the smearing effect.

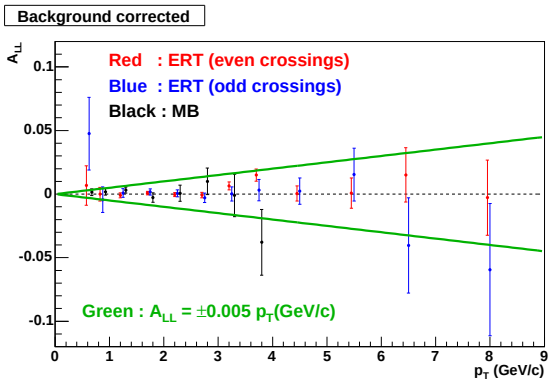

Figure 3.43: The measured asymmetries and the line (green) which is used to evaluate the error of A_{LL} from the uncertainty of the energy calibration. Data points are same as displayed in Figure 3.39. The line is $A_{LL} = \pm 0.005 \times p_T$ in GeV/c.

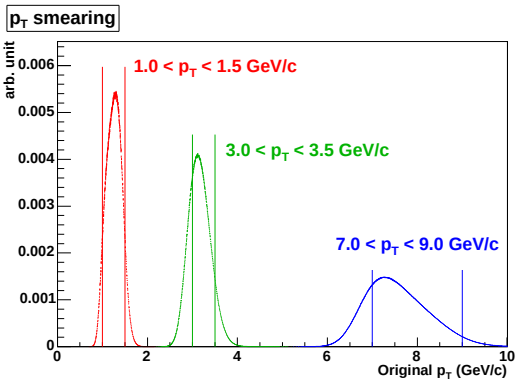

Figure 3.44: Original p_T distribution for a certain window of the measured p_T; 1.0 – 1.5, 3.0 – 3.5 and 7.0 – 9.0 GeV/c. This figure is produced based on FastMC.

3.7.6 Purity of π^0

The uncertainty of π^0 purity is listed in Table 3.8. It is propagated to the uncertainty of the asymmetries following Equation (3.23). The results are summarized in Table 3.7.9.

3.7.7 Background asymmetries

To extract the asymmetries for pure π^0, the contribution from the background under the π^0 peak is corrected using the background on the both sides of the peak. See Section 3.6.1 about the calculation of the asymmetries. This procedure is based on the idea that the asymmetries of the background under the peak and on sides of the peak are identical. Assuming the asymmetry under the peak is between that of the lower and higher side of the peak, the discrepancy of the asymmetry between the lower and higher one is assigned as the systematic uncertainty of the background asymmetry. Since the statistical error of the background asymmetry is separately propagated to the final results, the discrepancy over the statistical fluctuation is assigned as the systematic error. Therefore, when the asymmetries of the lower and higher background are consistent within the statistical error, no systematic error is assigned. Though obtained error is assumed to be statistical fluctuation because resulting errors have no significant tendency nor dependence on p_T, it is conservatively assigned to the systematic error. The contribution to the final asymmetries is summarized in Section 3.7.9.

3.7.8 Bunch shuffle

The bunch shuffle is a powerful technique to evaluate the uncertainty for the fill-by-fill and crossing-by-crossing yield. The validity of the error assignment to the measured yield is examined by looking at the chi-square of the fitting in Figure 3.37. However, the chi-square means the probability and only one measurement cannot prove the validity. The bunch shuffle technique can mimic the many measurement and make it possible to evaluate the chi-square of the fit statistically. In one shuffle, a helicity combination of each beam crossing in each fill

are randomly assigned. Then, the same process to extract the asymmetries for the signal and background window is performed. Therefore, one shuffle provides a set of the asymmetries and the chi-squares, and many shuffles can produce the distributions of the asymmetries and the chi-squares. By comparing the chi-square distribution obtained by the bunch shuffle with the expected ideal distribution, it is examined whether the assigned error to the yield is proper or not.

Instead of the chi-square distribution, the distribution of A_{LL} by the bunch shuffle, which is for the signal or background window, is utilized in this analysis. Other asymmetries such as A_L is also available but the results do not and should not change. A_{LL} by the bunch shuffle should fluctuate following the Gaussian distribution with a width of the real error of A_{LL}. In other words, if the error is correctly assigned to A_{LL}, it should be consistent with the width of the A_{LL} distribution obtained by the bunch shuffle. Figure 3.45 displays the A_{LL} distribution for the signal window and $0.75 < p_T < 1.0$ GeV/c using MB sample. The red curve is the Gaussian with a width of the statistical error for A_{LL} and the blue one is the result of the fit. The larger width of the blue one than the red one implies the additional uncertainty to the statistical fluctuation in A_{LL}. The red points in Figure 3.46 displays the ratio of the width by the fitting to the width from the statistics; the blue width divided by the red width in Figure 3.45. The points more than one implies the systematic uncertainty over the statistical one.

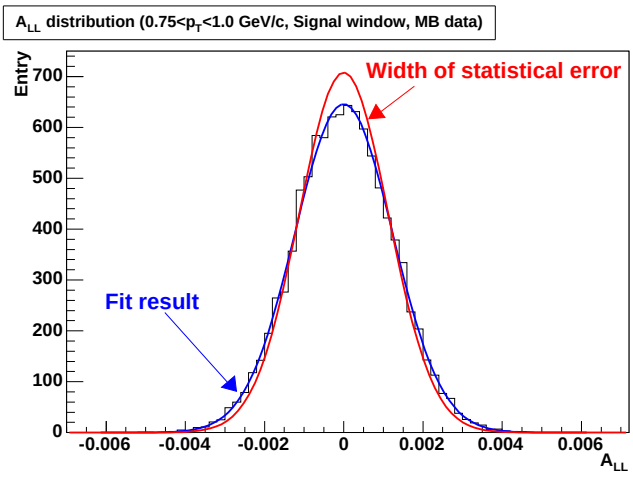

Figure 3.45: The A_{LL} distribution by the bunch shuffle. This figure is for 0.75 – 1.0 GeV/c and for the signal window using MB data. The red curve shows the Gaussian distribution with a width of the statistical error of A_{LL} for the corresponding p_T bin. The blue curve is the result of the Gaussian fit.

Generally, when the statistics become higher, the systematic error becomes significant. However, the width of A_{LL} distribution is wider than the statistical error in the higher p_T bins, where statistics is much poorer than that in the lower p_T bins, as displayed in Figure 3.46. This phenomenon is due to too small statistics in each crossing to apply the Poisson distribution for the error of the yield and is reproduced by the numerical simulation. For the confirmation, the bunch shuffle is executed for A_{LL} calculated with fills merged (fill-merging A_{LL}) instead of usual A_{LL} calculated fill by fill. Unlike the procedure described in Section 3.6.1, fill-merging A_{LL} is extracted as; (1) the yield and the integrated luminosity are accumulated over all fills in the 2005 run, (2) A_{LL} is calculated following Equation (1.56)

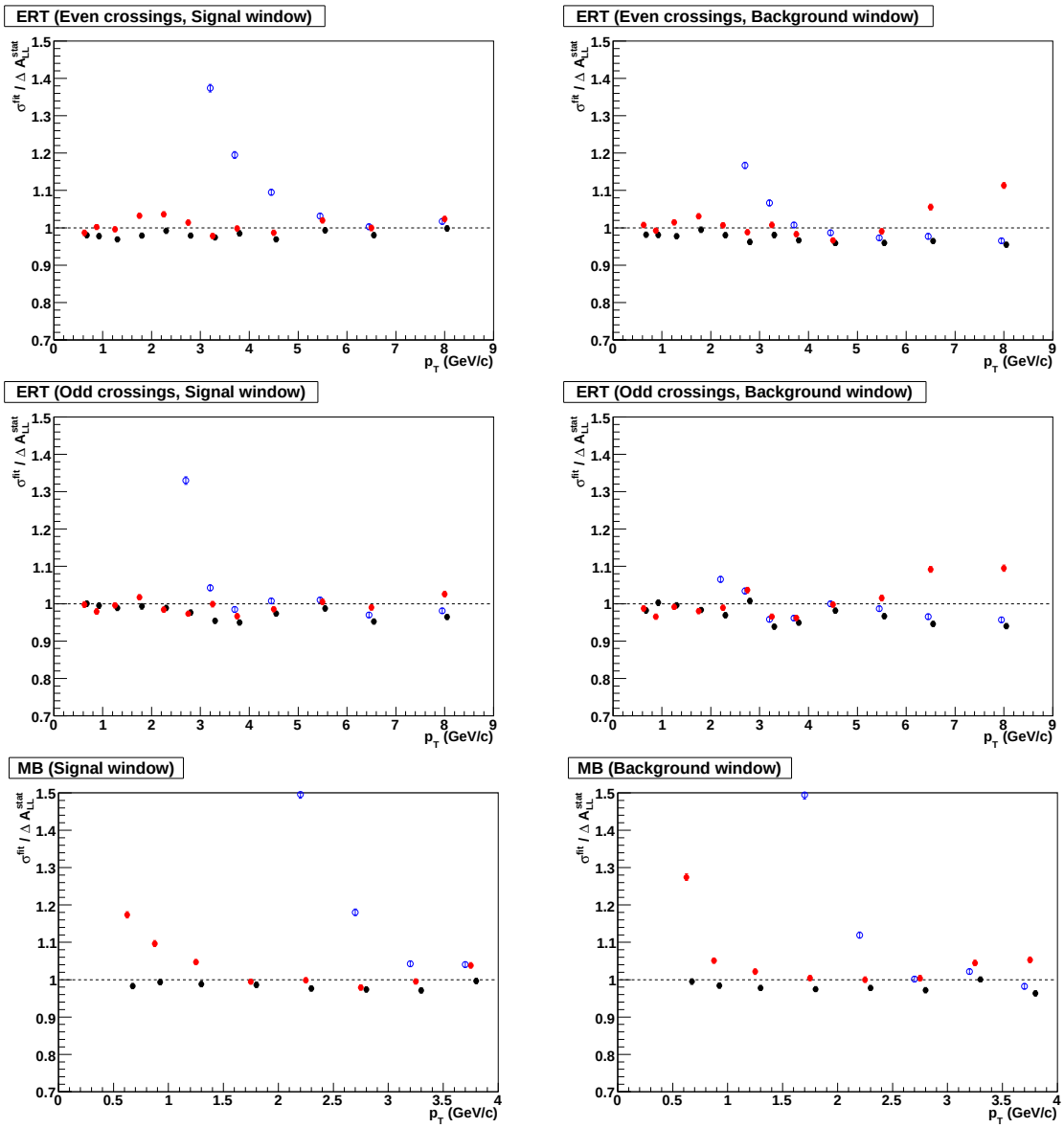

Figure 3.46: The ratio of the width of the A_{LL} distribution (σ^{fit}) to the error of A_{LL} (ΔA_{LL}) as a function of p_T. The plots on the left side is for the signal window and the right is for the background window. The top, middle and bottom plots are obtained using the ERT even crossings, the ERT odd crossings and the MB sample, respectively. The red points are for A_{LL} calculated fill by fill and then averaged over all fills. The blue points are for A_{LL} obtained with the helicity dependent yield merged over all fills before the calculation of the asymmetry. The statistical error is assigned as ΔA_{LL} for the red and blue points. The black points are calculated in the same way as the blue points but the correction for the systematic fluctuation of the background level is applied for ΔA_{LL} in addition to the statistical error (see Section A.14). The blue points in the low p_T region are much larger than 1 and out of the range of these figures.

using the accumulated yield and the luminosity. By merging fills, the yield is sufficient to calculate its error following the Poisson distribution. The results of the bunch shuffle using fill-merging A_{LL} are displayed as blue points in Figure 3.46. The ratio is around one in the higher p_T bins. On the other hand, the blue points are much larger than one in the lower p_T bins. This is well understood by the fill-by-fill fluctuation of the background level and the results after the correction of the background fluctuation are displayed as the black points in Figure 3.46. The detail about the fill-merging A_{LL} and the correction of the background level are described in Section A.14.

When there is a finite asymmetry, the width of A_{LL} distribution by the bunch shuffle additionally broadens. Its contribution is proportional to the observed asymmetry and can be calculated using data to be less than $0.03 \times A_{LL}$. This is much smaller than the error of A_{LL}, i.e. the width of the A_{LL} distribution. The detail is described in Section A.13.

As the results of the bunch shuffle, the additional systematic uncertainty is assigned for only p_T bins less than 2.0 GeV/c for the MB data sample, where the ratio of the width of the A_{LL} distribution to the statistical error is significantly larger than one as displayed by the red points in Figure 3.46. The source of the additional error is supposed to be the fluctuation of the background because the black points well sit around one. The assigned systematic uncertainty is summarized in Section 3.7.9.

3.7.9 Summary of the systematic uncertainty

The systematic errors described in the previous subsections are tabulated in Table 3.11 and 3.12 for A_{LL} with the MB sample and the ERT sample, respectively. Each source of the uncertainty is labeled as follows.

A. Contamination of A_{TT}. (Section 3.7.3)

B. P/P_L from the measurement by the local polarimeter. (Section 3.7.3)

C. Relative luminosity. (Section 3.7.4)

D. Absolute scale of the energy calibration. (Section 3.7.5)

E. Mean p_T. (Section 3.7.5)

F. Smearing effect for p_T bin. (Section 3.7.5)

G. Purity of π^0. (Section 3.7.6)

H. Background asymmetry. (Section 3.7.7)

I. Bunch shuffle. (Section 3.7.8)

In addition to these items, there is the scale uncertainty from the beam polarization. See Section 3.7.2 about the error from the beam polarization. Errors for A_{TT} and A_L is similarly summarized in Section A.16.

p_T (GeV/c)	A	B	C	D	E	F	G	H	I	total (10^{-5})
	(10^{-5})									
0.5 – 0.75	47	2	40	11	7	1	7	0	181	192
0.75 – 1.0	69	3	40	11	1	5	3	0	107	134
1.0 – 1.5	37	5	40	11	1	8	5	0	68	88
1.5 – 2.0	159	4	40	11	0	13	4	118	11	203
2.0 – 2.5	192	1	40	11	0	17	5	0	0	197
2.5 – 3.0	175	16	40	11	0	22	12	0	0	182
3.0 – 3.5	540	2	40	11	0	27	81	0	0	548
3.5 – 4.0	1160	60	40	11	0	32	113	1207	0	1680

Table 3.11: The summary of the systematic errors for π^0 A_{LL} with MB sample. The unit for the numbers is 10^{-5}. The quadratic sum of the systematic errors is put in the last column as the total systematic error. The scale uncertainty from the beam polarization of 9.5 % is not included in the table.

p_T (GeV/c)	A	B	C	D	E	F	G	H	I	total (10^{-5})
	(10^{-5})									
0.5 – 0.75	191	25	38	11	2	3	63	0	0	207
0.75 – 1.0	80	2	38	11	1	6	11	0	0	90
1.0 – 1.5	25	1	38	11	1	10	7	134	0	142
1.5 – 2.0	25	2	38	11	0	14	3	0	0	49
2.0 – 2.5	10	0	38	11	0	18	0	0	0	45
2.5 – 3.0	22	2	38	11	0	23	1	0	0	51
3.0 – 3.5	38	8	38	11	0	27	3	42	0	75
3.5 – 4.0	35	19	38	11	0	32	8	0	0	65
4.0 – 5.0	51	2	38	11	0	38	0	0	0	75
5.0 – 6.0	70	7	38	11	0	48	15	0	0	95
6.0 – 7.0	298	2	38	11	1	59	49	0	0	310
7.0 – 9.0	221	26	38	11	2	72	65	860	0	894

Table 3.12: The summary of the systematic errors for π^0 A_{LL} with ERT sample. The unit for the numbers is 10^{-5}. The quadratic sum of the systematic errors is put in the last column as the total systematic error. The scale uncertainty from the beam polarization of 9.5 % is not included in the table.

Chapter 4

Results and discussion

Results of this experiment and discussion on them are described in this chapter. The results of measured $A_{LL}^{\pi^0}$ are displayed in Section 4.1 and comparison between the data and theory is described. Subsequently, measured cross section in π^0 production is referred in Section 4.2. In Section 4.3, naive interpretation from measured $A_{LL}^{\pi^0}$ to Δg is explained. The extraction of Δg by some global-analysis groups including the present results is introduced in Section 4.4. Finally, further prospects are described in Section 4.5.

4.1 Results

Results of A_{LL} in π^0 production are displayed in Figure 4.1. Corresponding values are summarized in Table 4.1. For the points in Figure 4.1, MB data sample is used at less than 1.0 GeV/c and ERT sample is used at more than 1.0 GeV/c to keep high statistics. For ERT sample, the data for even and odd bunch crossings are averaged. Band at the bottom of Figure 4.1 indicates size of total systematic uncertainty except for normalization uncertainty of 9.5 % from the beam polarization measurement. See Section 3.7.2 about the uncertainty from the beam polarization. Four theory curves based on NLO pQCD calculation are also drawn in Figure 4.1. These calculations are performed following Equation (1.48) with the factorization scale set to p_T of π^0.[1] Difference of the calculations is the Δg input [84, 92]. GRSV-std is calculated with Δg of the best fit in the global analysis by GRSV group [67], where only polarized DIS data are used. $\Delta g = +g$, $\Delta g = -g$ and $\Delta g = 0$ indicate the case that $\Delta g(x)$ is equal to $g(x)$, $-g(x)$ and 0, respectively, at the input scale of $Q^2 = 0.4$ GeV^2.[2] Unpolarized PDF by CTEQ group [49] and FF by KKP group [29] are adopted in common in these calculations.

To compare the data and the theoretical calculation, chi-square between the data and the theoretical calculations, as well as the case of $A_{LL} = 0$, and probability are calculated and summarized in Table 4.2. Considering validity of pQCD calculation, the chi-square is computed for two p_T range; $p_T > 1$ GeV/c and $p_T > 2$ GeV/c. The soft QCD component at low p_T is discussed in Section 4.2 based on the measured cross section. The case of the gluon polarized maximally, $\Delta g = +g$ and $\Delta g = -g$, is rejected by the measurement. Other models are still consistent with the data. To extract shape of Δg as a function of Bjorken

[1] There are three scales are involved in the calculation. One is the scale of PDF, μ_F, which is described as $\sqrt{Q^2}$ in this thesis. The second is the scale of FF, μ'_F. The other is the renormalization scale, μ_R. In the calculation, these are set to same value; $\mu \equiv \mu_F = \mu'_F = \mu_R$.

[2] Δg at the scale of $Q^2 = p_T^2$ is quite different from that at the input scale of $Q^2 = 0.4$ GeV^2 in p_T range of our measurement. As explained in Section 1.5.4, it is because PDF at low Q^2 evolves rapidly as Q^2 increases.

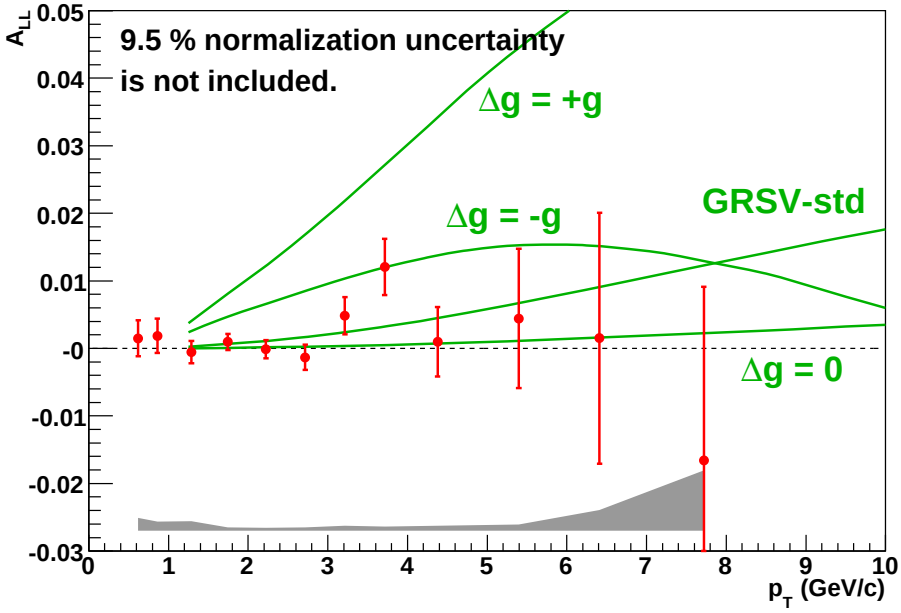

Figure 4.1: $A_{LL}^{\pi^0}$ as a function of p_T. Error bars for the points are only statistical. Bottom gray band indicates systematic uncertainties, which do not include 9.5 % normalization uncertainty from the beam polarization. Four theoretical calculations with different Δg input are superposed [84, 93]. They employ CTEQ PDF [49] and KKP FF [29] in the calculation. Factorization scale is set to p_T of π^0 in the theories. Δg of the best fit in the global analysis by GRSV group [67] is applied for GRSV-std. $\Delta g = +g$, $-g$ and 0 correspond to the case of positively largest Δg, negatively largest Δg and unpolarized Δg at the input scale of $Q^2 = 0.4$ GeV^2. The theoretical calculations are unavailable at low p_T region due to inapplicable domain of pQCD.

p_T range (GeV/c)	Mean p_T (GeV/c)	$A_{LL}^{\pi^0}$ (10^{-2})
0.5 – 0.75	0.62	$0.15 \pm 0.27 \pm 0.19$
0.75 – 1.0	0.86	$0.19 \pm 0.25 \pm 0.13$
1.0 – 1.5	1.29	$-0.05 \pm 0.17 \pm 0.14$
1.5 – 2.0	1.75	$0.10 \pm 0.12 \pm 0.05$
2.0 – 2.5	2.22	$-0.01 \pm 0.13 \pm 0.04$
2.5 – 3.0	2.72	$-0.13 \pm 0.18 \pm 0.05$
3.0 – 3.5	3.21	$0.49 \pm 0.27 \pm 0.07$
3.5 – 4.0	3.72	$1.21 \pm 0.42 \pm 0.07$
4.0 – 5.0	4.38	$0.10 \pm 0.51 \pm 0.07$
5.0 – 6.0	5.40	$0.44 \pm 1.03 \pm 0.10$
6.0 – 7.0	6.41	$0.15 \pm 1.86 \pm 0.31$
7.0 – 9.0	7.72	$-1.66 \pm 2.57 \pm 0.89$

Table 4.1: Values of $A_{LL}^{\pi^0}$. The first uncertainty in the third column is statistical and the second one is systematic. Normalization uncertainty of 9.5 % from the beam polarization is not included in the systematic uncertainty.

x, an interpretation from $A_{LL}^{\pi^0}$ to Δg is discussed with a simple model in Section 4.3. More detail and proper extraction of Δg is executed by orthodox global analysis. The results and comments by some global analysis group are introduced in Section 4.4.

Model	χ^2 (Probability (%))			
	$p_T > 1$ GeV/c (NDF = 10)		$p_T > 2$ GeV/c (NDF = 8)	
$A_{LL} = 0$	12.8	(23.5)	12.2	(14.3)
GRSV-std	10.2 – 10.7	(42.0 – 38.5)	10.0 – 10.5	(26.3 – 23.4)
$\Delta g = +g$	264 – 395	($< 10^{-18}$)	236 – 352	($< 10^{-18}$)
$\Delta g = 0$	11.9 – 11.7	(29.1 – 30.3)	11.4 – 11.2	(18.1 – 18.9)
$\Delta g = -g$	59.3 – 87.4	($< 10^{-6}$)	51.1 – 74.5	($< 10^{-5}$)

Table 4.2: chi-square (χ^2) and probability between the data and theoretical calculations, as well as $A_{LL} = 0$. For the calculation, quadratic sum of the statistical and systematic uncertainty except for the normalization uncertainty is used. The range of chi-square and probability is from the normalization uncertainty of 9.5 % from the beam polarization. Note that normalization uncertainty does not change significance of the data from 0.

In Figure 4.2, $A_{LL}^{\pi^0}$ reported in this paper are compared with the measurement in 2003 and 2004 by the PHENIX collaboration. Error bars in the figure indicate statistical uncertainty only. Systematic uncertainties of 2003 – 2004 data are negligible compared to the statistical uncertainty. Normalization uncertainties from the beam polarization are 18 % for 2003 – 2004 data and 9.5 % for the data of this experiment, but they are not fully uncorrelated. To examine consistency between these data, chi-square between them is calculated to be 3.07 with NDF of 4, where only statistical error is considered. At the comparison, points of this experiment in the corresponding bin of 2003 – 2004 data point are combined. Mean p_T for the combined bins of this experiment is almost same as those of 2003 – 2004 data. The obtained chi-square corresponds to probability of 54.6 % and we conclude that these data are consistent.

Figure 4.3 displays A_{TT} in π^0 production and Table 4.3 shows the values. In the same way as the case of A_{LL}, MB sample is used for p_T less than 1.0 GeV/c and ERT sample for p_T more than 1.0 GeV/c. A_{TT} is obtained from measured asymmetry A'_{TT}, which is displayed in Figure 3.40, by correcting the azimuthal angle dependence of A_{TT}. The correction is applied by simply dividing A'_{TT} by the factor of 0.588 which is calculated based on the detector acceptance in the measurement assuming that the azimuthal angle dependence is $\cos(2\phi)$. See Section 1.12 about the factor. Chi-square between the data points and $A_{TT} = 0$ is 9.29, which is probability of 67.8 % with NDF of 12, and we conclude that the data of $A_{TT}^{\pi^0}$ is consistent with 0 within uncertainty of the measurement. In the calculation, full p_T range measured is used and both statistical and systematic errors are considered. Measurement of $A_{TT}^{\pi^0}$ has possibility to probe transversity distribution in the proton. However, pQCD-based calculation [94] predicts that size of $A_{TT}^{\pi^0}$ is smaller than 0.001 in p_T range of our measurement. The reason of small A_{LL} predicted is that gluons does not contribute to A_{TT} and the asymmetry of the QCD subprocess is small. More details are in Section 1.5.3. In the calculation, $\delta q(x)$ is assumed to be positive and on the bound of the inequality of Equation (1.29) because of no information about the transversity. Based on the calculation, it is quite difficult to constrain transversity by the precision of the data. In PHENIX, the

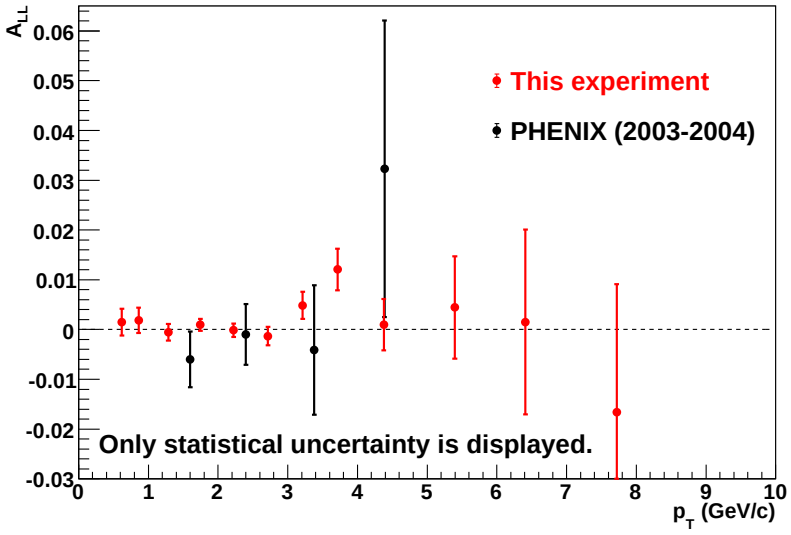

Figure 4.2: Comparison of $A_{LL}^{\pi^0}$ between this experiment and the data measured by PHENIX in 2003 – 2004. Error bars indicate only statistical uncertainty.

single transverse-spin asymmetry is also measured and published [95] as well.

Figure 4.4 displays A_L in π^0 production and Table 4.4 lists the values. The points at p_T less than 1.0 GeV/c are from MB sample and those at p_T more than 1.0 GeV/c are ERT sample. In ERT data sample, results from even and odd crossings are combined. Chi-square/NDF and corresponding probability between the data and $A_L = 0$ are evaluated to be 5.08/12 and 95.5 %, respectively, where both statistical and systematic errors are used. If A_L has finite value, it indicates the parity violation. Because the weak interaction which violate the parity is expected to be negligible at the energy scale in this experiment, A_L in π^0 production is also expected to be zero. That is satisfied in our measurement.

4.2 Cross section

As introduced in Chapter 1, the framework to interpret experimental data is based on pQCD. Therefore, it is important to evaluate validity of pQCD in the kinematical region of our measurement. One of the tests of pQCD is whether pQCD can reproduce measured cross section. As well as asymmetries, the PHENIX experiment published the results of cross sections of inclusive π^0 and charged pions. π^0 is detected using EMCal explained in Section 2.3.4 and charged pions are measured at the same kinematical region using tracking chamber described in Section 2.3.1. Hence the comparison of these cross sections between data and theory are useful to evaluate the pQCD validity for the π^0 production at given p_T range.

Figure 4.5 displays cross sections for inclusive π^0 production at $\sqrt{s} = 200$ GeV and pseudorapidity of -0.35 to 0.35 [96]. Lines on the figure are NLO pQCD calculation [84, 93] with CTEQ PDF [49] and KKP FF [29]. Empirically, the energy scale of factorization μ is set to p_T of π^0 (solid line).[3] To evaluate systematic uncertainty of the calculation, the

[3]There are three scales are involved in the calculation. One is the scale of PDF, μ_F, which is described as $\sqrt{Q^2}$ in Section 1.5.4. The second is the scale of FF, μ'_F. The other is the renormalization scale, μ_R. In the calculation, these are set to same value; $\mu \equiv \mu_F = \mu'_F = \mu_R$.

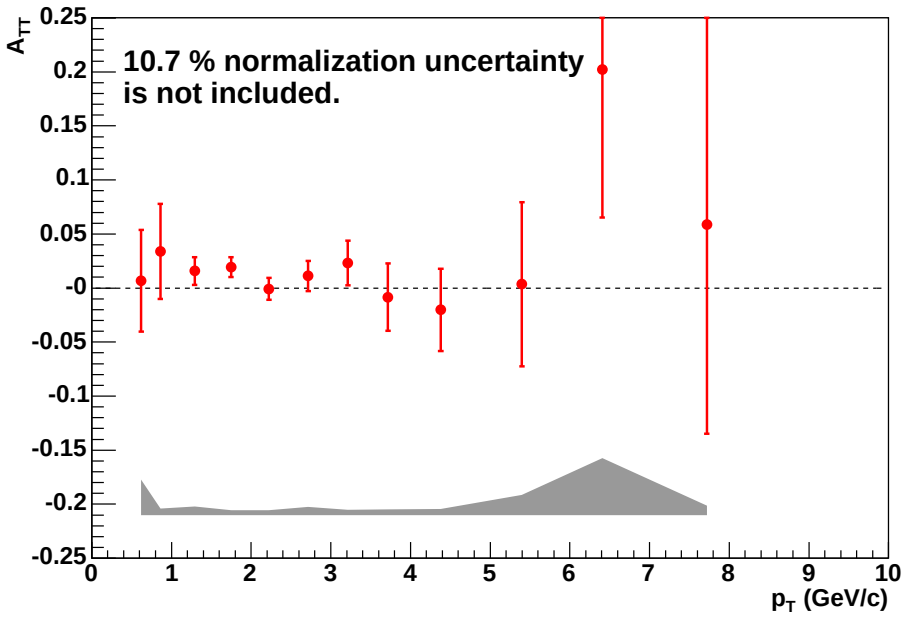

Figure 4.3: $A_{TT}^{\pi^0}$ as a function of p_T. Error bars for the points are only statistical. Bottom gray band indicates systematic uncertainties, which do not include 10.7 % normalization uncertainty from the beam polarization.

p_T range (GeV/c)	Mean p_T (GeV/c)	$A_{TT}^{\pi^0}$ (10^{-2})
0.5 – 0.75	0.62	$0.68 \pm 4.71 \pm 3.29$
0.75 – 1.0	0.86	$3.40 \pm 4.41 \pm 0.60$
1.0 – 1.5	1.29	$1.57 \pm 1.29 \pm 0.79$
1.5 – 2.0	1.75	$1.93 \pm 0.92 \pm 0.43$
2.0 – 2.5	2.22	$-0.09 \pm 1.01 \pm 0.45$
2.5 – 3.0	2.72	$1.12 \pm 1.39 \pm 0.74$
3.0 – 3.5	3.21	$2.31 \pm 2.06 \pm 0.50$
3.5 – 4.0	3.72	$-0.84 \pm 3.11 \pm 0.52$
4.0 – 5.0	4.38	$-2.02 \pm 3.80 \pm 0.57$
5.0 – 6.0	5.40	$0.36 \pm 7.59 \pm 1.85$
6.0 – 7.0	6.41	$20.22 \pm 13.68 \pm 5.26$
7.0 – 9.0	7.72	$5.86 \pm 19.35 \pm 0.85$

Table 4.3: Values of $A_{TT}^{\pi^0}$. The first uncertainty in the third column is statistical and the second one is systematic. Normalization uncertainty of 10.7 % from the beam polarization is not included in the systematic uncertainty.

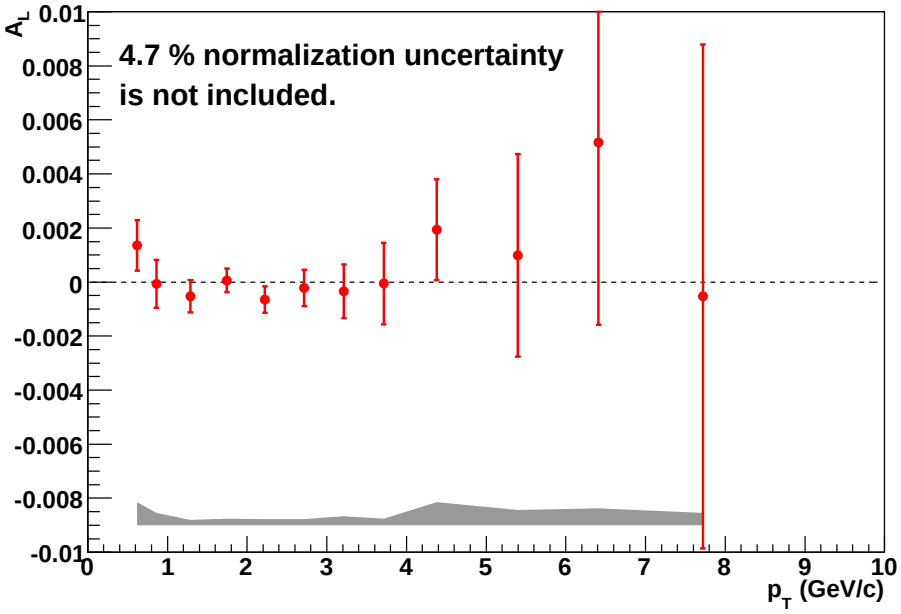

Figure 4.4: $A_L^{\pi^0}$ as a function of p_T. Error bars for the points are only statistical. Bottom gray band indicates systematic uncertainties, which do not include 4.7 % normalization uncertainty from the beam polarization.

p_T range (GeV/c)	Mean p_T (GeV/c)	$A_L^{\pi^0}$ (10^{-2})
0.5 – 0.75	0.62	$0.135 \pm 0.094 \pm 0.085$
0.75 – 1.0	0.86	$-0.006 \pm 0.089 \pm 0.046$
1.0 – 1.5	1.29	$-0.052 \pm 0.060 \pm 0.020$
1.5 – 2.0	1.75	$0.006 \pm 0.044 \pm 0.025$
2.0 – 2.5	2.22	$-0.065 \pm 0.049 \pm 0.022$
2.5 – 3.0	2.72	$-0.022 \pm 0.067 \pm 0.023$
3.0 – 3.5	3.21	$-0.034 \pm 0.100 \pm 0.033$
3.5 – 4.0	3.72	$-0.006 \pm 0.151 \pm 0.025$
4.0 – 5.0	4.38	$0.193 \pm 0.187 \pm 0.086$
5.0 – 6.0	5.40	$0.099 \pm 0.375 \pm 0.057$
6.0 – 7.0	6.41	$0.516 \pm 0.674 \pm 0.063$
7.0 – 9.0	7.72	$-0.053 \pm 0.933 \pm 0.045$

Table 4.4: Values of $A_L^{\pi^0}$. The first uncertainty in the third column is statistical and the second one is systematic. Normalization uncertainty of 4.7 % from the beam polarization is not included in the systematic uncertainty.

cross section is calculated with different energy scale, $\mu = \frac{p_T}{2}$ (dotted line) and $\mu = 2p_T$ (dashed line). At the bottom of Figure 4.5, difference between the data and the calculation is displayed. The pQCD calculation reproduces the data well over 1 – 20 GeV/c in p_T and this result supports the validity of pQCD-based framework in the evaluation of $A_{LL}^{\pi^0}$.

One of the concerns is the contribution of soft QCD process at low p_T region, which cannot be calculated by perturbation theory. The contribution was estimated using the data of charged pions. Inset of Figure 4.5 displays measured cross section of charged pions superposed on that of π^0. We assumed that the cross section at $p_T < 0.8$ GeV/c is dominated by soft QCD and the soft QCD component is represented by an exponential function. By fitting the cross section of charged pions at the p_T range to the exponential function (dashed line in the inset), the fraction of the soft QCD component is estimated to be less than 10 % at p_T of 2.0 – 2.5 GeV/c. On the basis of this study, we applied an interpretation from $A_{LL}^{\pi^0}$ to Δg using the data more than 2.0 GeV/c in p_T in Section 4.3.

4.3 Interpretation from $A_{LL}^{\pi^0}$ to Δg

In Section 4.1, our $A_{LL}^{\pi^0}$ results and theoretical calculations are compared. In this section, x dependence of Δg is extracted based on the calculations. To establish relation between $A_{LL}^{\pi^0}$ and Δg, we adopt the approximation of Equation (1.50). Then, dependence of $A_{LL}^{\pi^0}$ on Δg is parameterized based on theoretical calculations. Finally, function form of Δg is assumed and the measured $A_{LL}^{\pi^0}$ is fitted with the shape of Δg as free parameters. As well as the uncertainty of the measurement, the model itself would have uncertainty. However, we don't evaluate the uncertainty of the model and only brief and qualitative discussion about the obtained Δg is made in this section. In Section 4.4, Δg extracted by AAC global analysis [70] is introduced and discussed in more detail.

In this section, a following equation is used instead of Equation (1.50) just for a technical reason;

$$A_{LL}^{\pi^0}(p_T) = \left(C_2(p_T) \left[\frac{\Delta g(\xi)}{g(\xi)} \right] + C_1(p_T) \right)^2 + C_0(p_T). \\ \xi \equiv \langle x_1 \rangle = \langle x_2 \rangle, \quad \text{depends on } p_T. \tag{4.1}$$

$C_{0,1,2}$ include contributions from FF, the partonic cross sections and PDF except for Δg. x_1 and x_2 indicate Bjorken x of partons in the initial two proton beams. In the approximation, x_1 and x_2 are represented by its mean value and the mean values are same. It is written as ξ. ξ should depend on p_T of π^0. It is notable that each component in the right hand side of the equation depends on p_T. In the equation, $\Delta g(\xi)$ appears as a ratio to $g(\xi)$. That is also convenient to alleviate Q^2 dependence of PDF. Figure 4.6 displays the variation of $\frac{\Delta g(x)}{g(x)}$ for various Q^2. The fluctuation of $\frac{\Delta g(x)}{g(x)}$ at a certain Bjorken x is roughly within 0.1.

In this analysis, we don't care about contents of $C_{0,1,2}$ and regard them as parameters. If more than three relations between A_{LL} and $\frac{\Delta g}{g}$ are known, $C_{0,1,2}$ can be written by the known values of A_{LL} and $\frac{\Delta g}{g}$ by solving Equation (4.1). For example, when one obtains three theoretical models of A_{LL} and corresponding $\frac{\Delta g}{g}$ labeled as *mod.A*, *mod.B* and *mod.C*, $P_{0,1,2}$

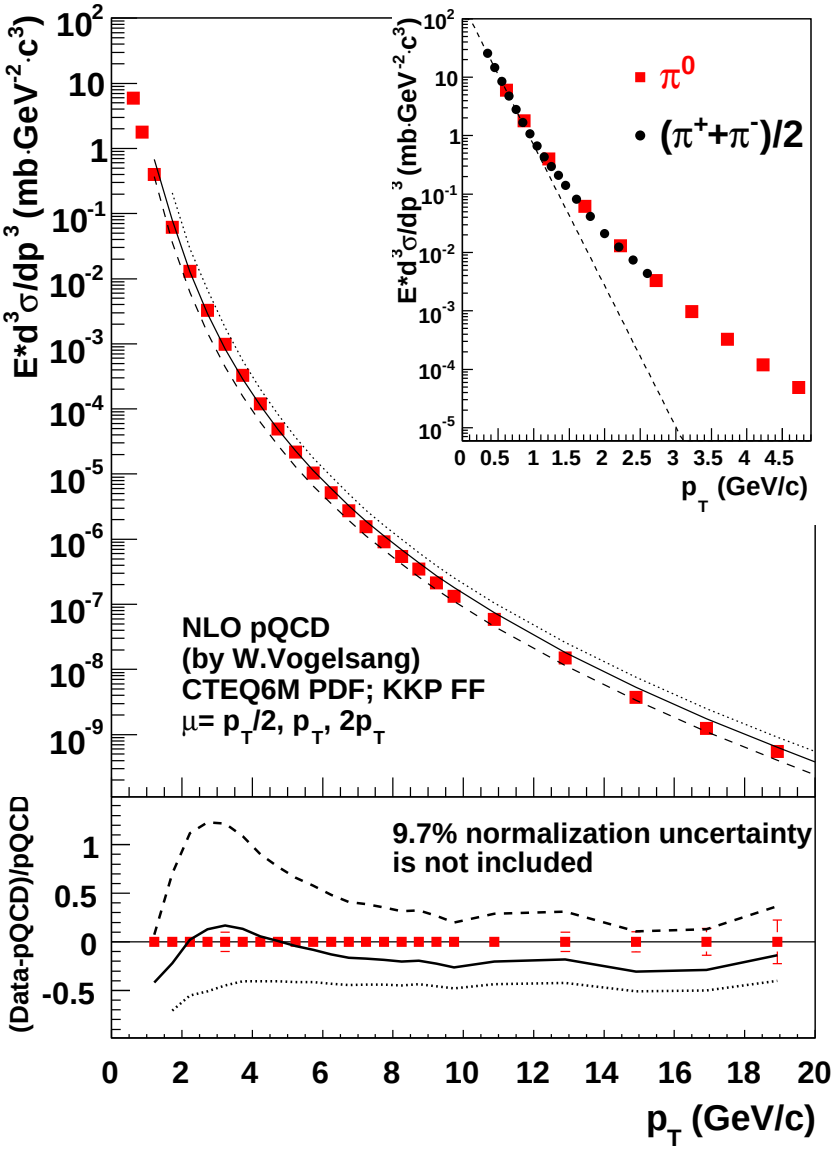

Figure 4.5: Cross sections in inclusive π^0 production in pp collision at $\sqrt{s} = 200$ GeV (red points). Error bars, which are smaller than the points, are quadratic sum of statistical uncertainty and experimental systematic uncertainty except for normalization uncertainty of 9.7 %. The normalization uncertainty is from the luminosity measurement. Theoretical curves using CTEQ PDF [49] and KKP FF [29] are superposed in the figure [84, 93]. Factorization scale of $\mu = \frac{p_T}{2}$, p_T and $2p_T$ is adopted for dotted, solid and dashed line, respectively. The Bottom figure displays difference between the data and the theory. Cross section of inclusive charged pions are drawn as black points in the inset of the figure. Dashed line in the inset is obtained by fitting the cross section of charged pions at $p_T < 0.8$ GeV/c to an exponential function for estimation of the soft QCD component. In both cross sections, measured coverage in pseudorapidity is -0.35 to 0.35.

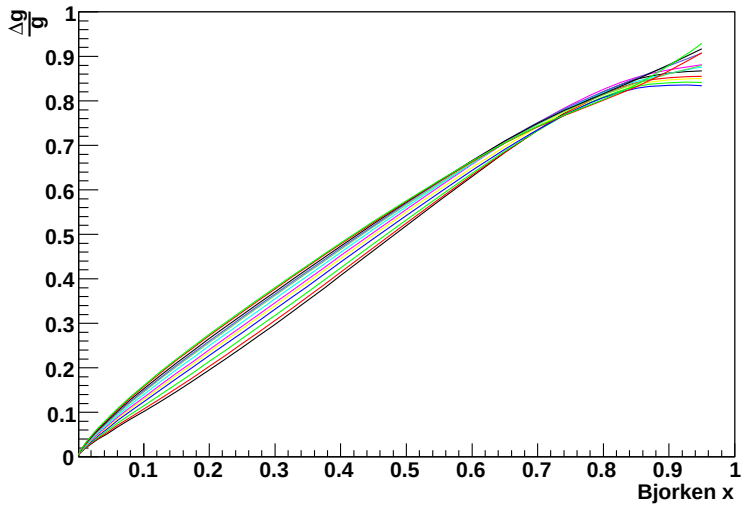

Figure 4.6: $\frac{\Delta g}{g}$ for GRSV-std model as a function of Bjorken x. Each curve is for a certain Q^2 in a range of 1 –100 GeV^2. Unpolarized PDF by GRV group [50] is used instead of CTEQ group [49] because initial Q^2 in global analysis by CTEQ is $(1.3)^2$ GeV^2 and PDF at smaller Q^2 than the value is not published.

can be extracted by calculating

$$\begin{pmatrix} P_0(p_T) \\ P_1(p_T) \\ P_2(p_T) \end{pmatrix} = \begin{pmatrix} 1 & \frac{\Delta g^{mod.A}(\xi)}{g(\xi)} & \left(\frac{\Delta g^{mod.A}(\xi)}{g(\xi)}\right)^2 \\ 1 & \frac{\Delta g^{mod.B}(\xi)}{g(\xi)} & \left(\frac{\Delta g^{mod.B}(\xi)}{g(\xi)}\right)^2 \\ 1 & \frac{\Delta g^{mod.C}(\xi)}{g(\xi)} & \left(\frac{\Delta g^{mod.C}(\xi)}{g(\xi)}\right)^2 \end{pmatrix}^{-1} \begin{pmatrix} A_{LL}^{mod.A}(p_T) \\ A_{LL}^{mod.B}(p_T) \\ A_{LL}^{mod.C}(p_T) \end{pmatrix}. \tag{4.2}$$

It is important to remember that relation of ξ and p_T is needed to obtain $P_{0,1,2}$ or $C_{0,1,2}$ as a function of p_T. In this thesis, four theoretical curves displayed in Figure 4.1 were adopted; GRSV-std, $\Delta g = +g$, $\Delta g = 0$ and $\Delta g = -g$. For each model, we obtained Δg as a function of Bjorken x, its Q^2 evolution and corresponding $A_{LL}^{\pi^0}$ through cooperation with theorists [97]. In this case, because four models are available, $C_{0,1,2}$ are obtained by fitting scatter plot of A_{LL} and $\frac{\Delta g}{g}$ to Equation (4.1), as displayed in Figure 4.7, instead of using Equation (4.2). Scale of Q^2 for $\frac{\Delta g}{g}$ is set to p_T^2 as usually adopted by literature.

At the same time, the relation between ξ and p_T is determined. p_T of measured π^0 is approximately related to ξ as following equation.

$$p_T \sim \xi\zeta P_{beam}, \qquad \zeta = \langle z \rangle, \tag{4.3}$$

where z is for FF and ζ indicates mean value of z. P_{beam} is the beam momentum, which is 100 GeV/c in this thesis. The longitudinal component of momentum of π^0 is ignored in this equation because the detector is located at the central region. ζ is regarded as a parameter and determined so that the fitting in extracting $C_{0,1,2}$ is optimized. Figure 4.7 displays a sample of the fitting at $p_T = 4.25$ GeV/c and $\zeta = 0.5$. Points are well on a quadratic function. The fitting is performed at many p_T points in 1.25 – 13.25 GeV/c for a certain value of ζ and most appropriate ζ is estimated by minimizing combined chi-square of the fittings over

all p_T range. Figure 4.8 displays combined chi-square of the fittings as a function of ζ. Error of each point in figures like Figure 4.7 is set to a constant in all fittings. The chi-square has a minimum around $\zeta = 0.5$, and therefore we fixed ζ at 0.5 in this analysis. $C_{0,1,2}$ obtained with $\zeta = 0.5$ is displayed as a function of p_T in Figure 4.9. $C_{0,1,2}$ are parameterized by fitting them to a suitable function as in Figure 4.9.

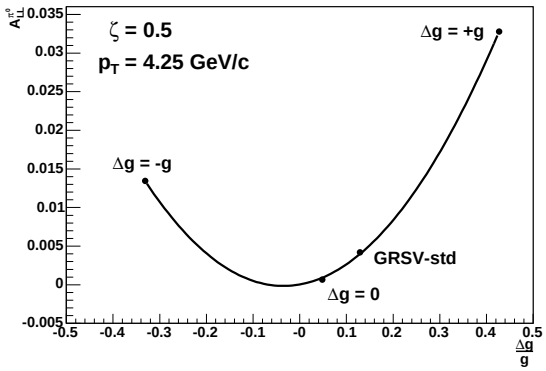

Figure 4.7: $\frac{\Delta g}{g}$ input and corresponding $A_{LL}^{\pi^0}$. This figure is produced at $p_T = 4.25$ GeV/c and the case of $\zeta = 0.5$. Curve on the figure indicates the fit result to quadratic function.

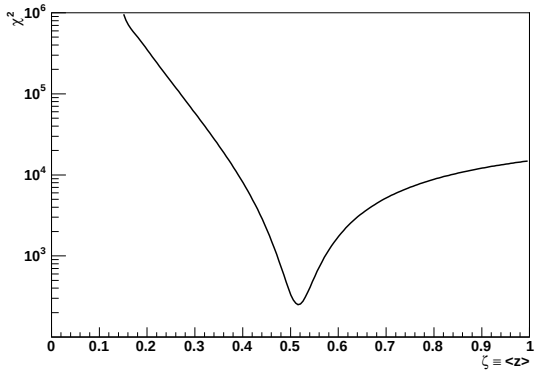

Figure 4.8: Combined chi-square in fitting $A_{LL}^{\pi^0}$ to quadratic function of $\frac{\Delta g}{g}$ over all p_T region. The chi-square is displayed as a function of ζ.

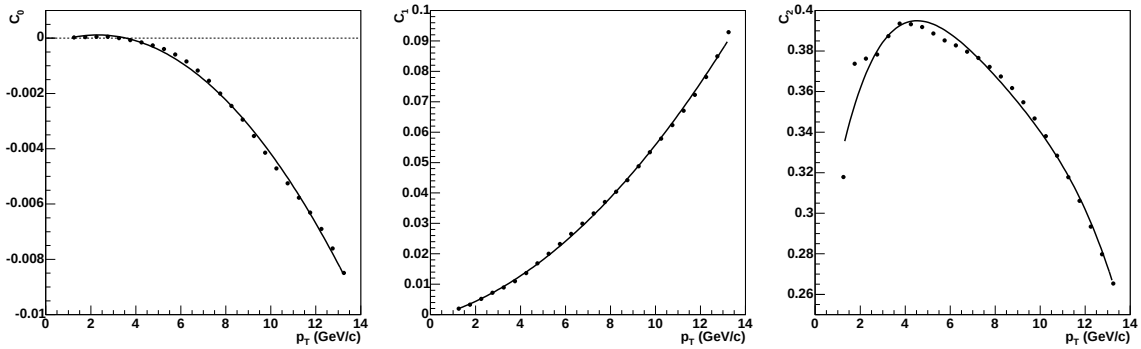

Figure 4.9: C_0 (left), C_1 (middle) and C_2 (right) extracted by fitting $A_{LL}^{\pi^0}$ to quadratic function of $\frac{\Delta g}{g}$. They are displayed as a function of p_T of π^0. The points are fitted to suitable polynomial function and the fit results are shown as solid curve.

To apply the model developed here to measured $A_{LL}^{\pi^0}$, it is necessary to assume a function form of Δg. We assumed

$$\frac{\Delta g(\xi, Q^2 = p_T^2)}{g(\xi, Q^2 = p_T^2)} = K_1\xi + K_2\xi^2, \tag{4.4}$$

where K_1 and K_2 are free parameters in the fitting to data. In Equation (4.4), PDF is clearly described as a function of Bjorken x and Q^2, and they can be written by p_T in this model. Therefore, as shown by Equation (4.1), $A_{LL}^{\pi^0}$ is written as a function of p_T with parameters of K_1 and K_2, and Δg can be extracted by fitting measured $A_{LL}^{\pi^0}$ to Equation (4.1). To obtain

Δg at a certain Q^2, evolution by Q^2 is needed because $\frac{\Delta g}{g}$ in Equation (4.1) is a value at $Q^2 = p_T^2$. The evolution was performed by interpolation following the known Δg calculation. Figure 4.10 displays scatter plot of Δg with Bjorken x of 0.1 at $Q^2 = 1$ GeV^2 and 25 GeV^2. Four points are from theoretical calculations used to build the model and curve is obtained by spline approximation. For example, the Q^2 evolution from 25 GeV^2 to 1 GeV^2 for arbitrary Δg with $x = 0.1$ was performed using the curve in Figure 4.10.

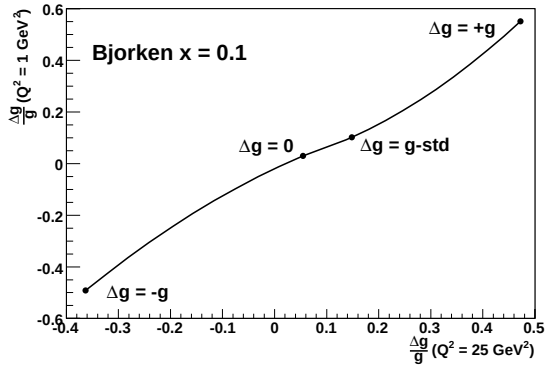

Figure 4.10: Comparison of $\frac{\Delta g}{g}$ with Bjorken x of 0.1 at $Q^2 = 25$ GeV^2 and that at $Q^2 = 1$ GeV^2. Curve is obtained by spline approximation.

To test the model developed in this section, reproducibility of four theoretical calculations, GRSV-std, $\Delta g = +g$, $\Delta g = 0$ and $\Delta g = -g$, is examined. The left panel of Figure 4.11 displays $A_{LL}^{\pi^0}$ as a function of p_T of the theories. Each set of points indicates the original calculation and the curves on the points are results of the fitting to Equation (4.1). Right of Figure 4.11 displays $\frac{\Delta g}{g}$ as a function of Bjorken x ($= \xi$) at $Q^2 = 1$ GeV^2. Dashed lines are original theoretical calculations and solid lines are extracted $\frac{\Delta g}{g}$ by the fitting. As displayed in Figure 4.11, the model reproduces the original values of $\frac{\Delta g}{g}$ well.

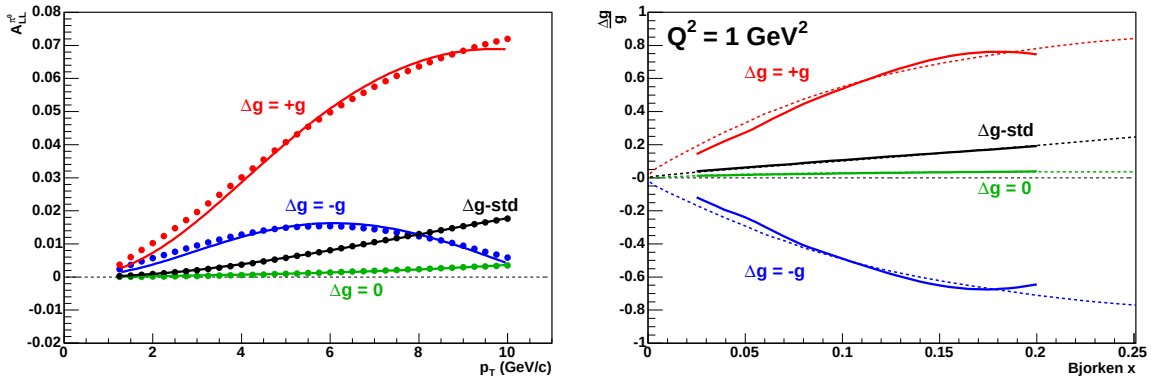

Figure 4.11: (Left) $A_{LL}^{\pi^0}$ as a function of p_T for theoretical calculations by GRSV group [67]. Points are the original calculations and lines are results of the fitting to Equation (4.1). (Right) $\frac{\Delta g}{g}$ as a function of Bjorken x at $Q^2 = 1$ GeV^2 for GRSV calculations. Dashed lines are original and solid lines are obtained by the fitting.

Then, the model was applied to measured data. As described in Section 4.2, data at low p_T region have possibility to include effect of soft QCD. For this reason, we limited p_T range used in the fitting to more than 2 GeV/c. Figure 4.12 displays results of the fitting to the data. Because $A_{LL}^{\pi^0}$ is approximately written by a quadratic function of Δg, it is possible that two solutions of Δg are derived from single $A_{LL}^{\pi^0}$ measurement. As expected from tendency of the theoretical curves, predicted $A_{LL}^{\pi^0}$ of $\Delta g = -g$ model becomes smaller than the line of $\Delta g = 0$ and therefore this duality is likely to be disentangled at higher p_T region, more than $\sim$15 GeV/c. However, the data in this thesis do not cover so high p_T region. For this reason, two results from the fitting are obtained as displayed in left of Figure 4.12 for the result of positive Δg and right for negative Δg.

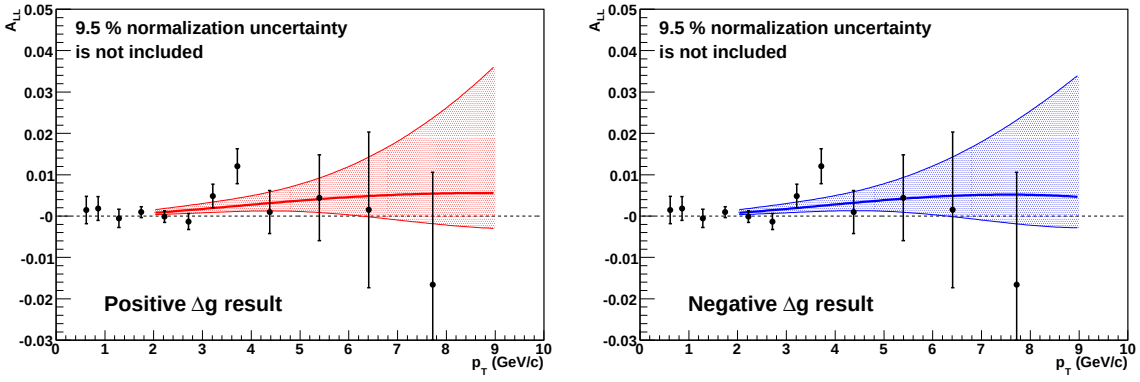

Figure 4.12: $A_{LL}^{\pi^0}$ as a function of p_T. Data points are from this experiment. Error bars of the points are quadratic sum of the statistical and systematic uncertainty, except for 9.5 % normalization uncertainty from the beam polarization. Lines are results of the fitting to Equation (4.1) and bands indicate the uncertainty of the fitting. Left figure is for solution of positive Δg and right figure is for negative Δg. Chi-squares of the fitting are 9.83 and 9.77 for the positive and negative Δg solution, respectively, with NDF of 6.

Obtained results of the fitting can be converted into Δg as a function of Bjorken x, which is represented by ξ. Figure 4.13 displays $x\Delta g$ as a function of Bjorken x at $Q^2 = 1$ GeV^2. As well as four theory curve by GRSV group, Δg extracted by global analysis of AAC group in 2004 [72] is also on the figure. As explained above, two Δg solutions are obtained from this experiment. For the results in this figure, normalization uncertainty of 9.5 % from beam polarization is considered. To evaluate the uncertainty, the fitting was performed with three cases of the beam polarization; P, $P + \Delta P$ and $P - \Delta P$, where P is the mean value and ΔP is the uncertainty of the beam polarization. Then, the uncertainty for Δg is assigned so as to cover any cases of the fittings. Contribution from the uncertainty of the beam polarization enlarges the size of the error of Δg by less than 10 %. Other uncertainties such as those from unpolarized PDF and FF are not considered in the results.

Though it is hard to derive conclusive statement from Δg extracted here because of difficulty in estimation of uncertainty of the naive model, some knowledge are obtained. One is the capability of our data to significantly reduce the uncertainty of Δg. This statement is supported by the recently published literature [69, 70]. The second is that, however, the measurement in this thesis provides the information of Δg at limited x range. To cover wider x, the measurement at larger p_T or with different $\sqrt{s}$ is necessary. The other is two solution of the positive and negative Δg. This problem is caused by the relation of the quadratic

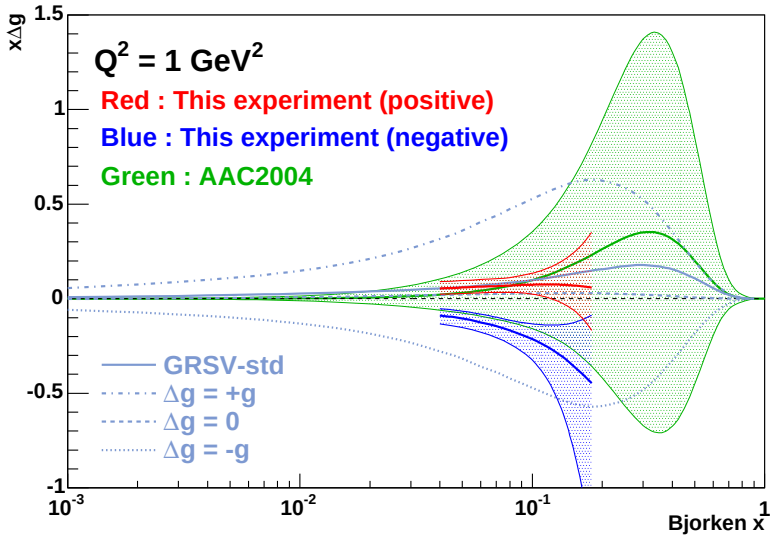

Figure 4.13: $x\Delta g$ as a function of Bjorken x at $Q^2 = 1$ GeV^2. Red and blue band represent Δg extracted from the data of this experiment. Δg and its uncertainty extracted by AAC group in 2004 [72], as well as four theoretical calculations by GRSV group [67], are superposed in the figure.

function between $A_{LL}^{\pi^0}$ and Δg, like Equation (4.1). It is difficult to disentangle the duality by the measurement of π^0. Therefore, other probes are needed to determine the sign of Δg. It must be noted that the analysis of AAC in 2004 did not consider negative Δg and they also referred to it in a paper published recently [70]. These issues presented here are discussed in more detail in Section 4.4 and 4.5.

4.4 Results and comments by global analysis

Currently, polarized PDFs are extracted from many experimental data by global analysis [66–71] described in Section 1.8.2. For polarized PDF, most data points are obtained by polarized DIS experiments. The first measurement of $A_{LL}^{\pi^0}$ by the PHENIX experiment was published in 2004 [2] and improved in [3]. However, they cannot constrain Δg very much due to large uncertainty as described in Section 1.11. Statistics of new measurement in this thesis is larger than [3] by a factor of $\sim$25 in terms of figure-of-merit and the uncertainty of $A_{LL}^{\pi^0}$ becomes smaller by a factor of $\sim$5. Moreover, larger statistics make it possible to extend the measured p_T range up to 9.0 GeV/c. In this background, the new result is expected to contribute to gain further knowledge on Δg.

In fact, AAC group has already performed global analysis [70] with our preliminary results [98]. Figure 4.14 displays polarized gluon PDF by AAC at $Q^2 = 1$ GeV^2, as well as experimental results using SIDIS. Three types of AAC results are displayed in Figure 4.14. One is the result with only DIS data (Type 2). Other two types incorporate $A_{LL}^{\pi^0}$ in addition to DIS data (Type 1 and 3). Difference of Type 1 and 3 corresponds to positive and negative Δg solution. Δg of Type 1 (Type 3) is obtained by fitting data with initial function form of Δg positive (negative). No practical difference in chi-square of the fit results between Type 1 and 3. No significant change is also observed in the quark and the antiquark distributions.

The resulting Δg's of Type 1 and 3 are much different at small x ($x < 0.1$), while they are similar at large x. At large x, both Δg is positive. The reason is analyzed in [70] and is understood as requirement by DIS measurements with deuteron target. On the other hand, Δg of Type 3 is negative at small x as expected, but much larger uncertainty is assigned than the result of Type 1. This is due to the functional form of Δg. It is emphasized in [70] that the direct constraint in Δg by measurements is only at large x and the constraint at small x is only from Q^2 evolution of DIS data and requirement of smoothness of functional form. It implies that Type-1 Δg has possibility to carry similar size of uncertainty to Type 3, too. In addition to DIS and $A_{LL}^{\pi^0}$, Δg is extracted by SIDIS with high-p_T hadron production. SMC [73], HERMES [74] and COMPASS [75] collaborations reported their results. Their results have moderate size of uncertainty and are consistent with the results by AAC as displayed in Figure 4.14. The integral over x of polarized PDF by AAC group is tabulated in Table 4.5. Based on Equation (1.24), the proton spin can currently be explained by contributions only from quarks, antiquarks and gluon spin, though still large uncertainty is assigned to Δg.

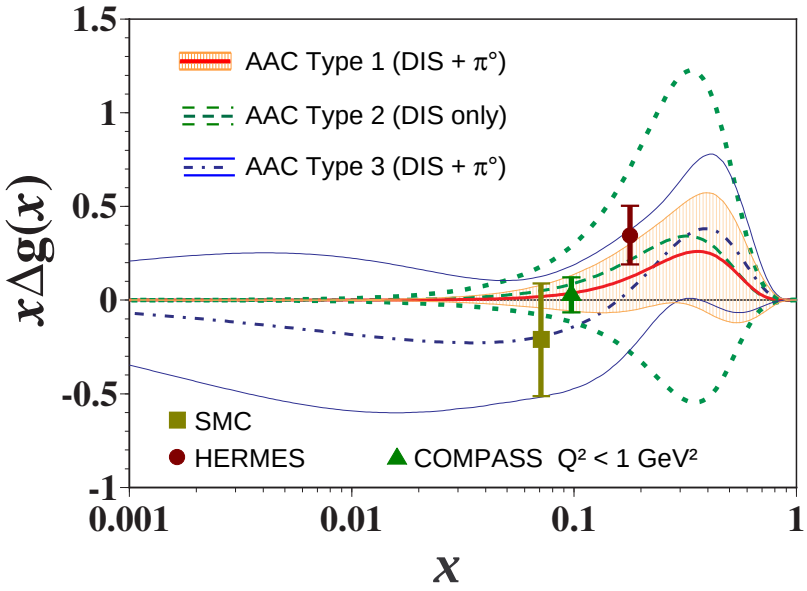

Figure 4.14: $x\Delta g(x)$ as a function of Bjorken x obtained by AAC group [70] with experimental results using SIDIS by SMC [73], HERMES [74] and COMPASS [75]. Result of Type 2 is obtained by only DIS data. Type 1 and 3 are extracted incorporating our preliminary $A_{LL}^{\pi^0}$ data in addition to DIS data. Initial functional form of Δg is positive in Type 1 and negative in Type 3. Because SMC, HERMES and COMPASS reported $\frac{\Delta g(x)}{g(x)}$, $g(x)$ by GRV group [50] is used to obtain $\Delta g(x)$ for the comparison.

In global analysis by DNS group [69], $A_{LL}^{\pi^0}$ is not used in their analysis but they discussed capability of $A_{LL}^{\pi^0}$ measurement. Figure 4.15 displays prediction of $A_{LL}^{\pi^0}$ by DNS group with estimation of measurements by the PHENIX experiment. Comparing the estimation for this thesis (tagged as Run 5) to the range of dashed-dotted line denoting uncertainty from PDF, it is indicated that our data has potential to constrain polarized PDF.

	$\Delta\Sigma$	Δg	$\Delta\bar{q}$
Type 1 (DIS $+A_{LL}^{\pi^0}$, positive Δg)	0.27 ± 0.07	0.31 ± 0.32	-0.05 ± 0.01
Type 2 (DIS only)	0.25 ± 0.10	0.47 ± 1.08	-0.06 ± 0.02
Type 3 (DIS $+A_{LL}^{\pi^0}$, negative Δg)		-0.56 ± 2.16	

Table 4.5: Integral of polarized PDF over Bjorken x at $Q^2 = 1$ GeV^2 by AAC [70]. $\Delta\Sigma$ indicates sum of both quarks and antiquarks; $\Delta\Sigma(x) = \sum_q [q(x) + \bar{q}(x)]$. AAC group assumes symmetric sea quark distribution; $\Delta\bar{q}(x) \equiv \Delta\bar{u}(x) = \Delta\bar{d}(x) = \Delta\bar{s}(x) = \Delta s(x)$. Integral of quarks and antiquarks PDF for Type 3 is not described in [70], though they mention that no significant difference between Type 1 and 3 are observed for quarks and antiquarks.

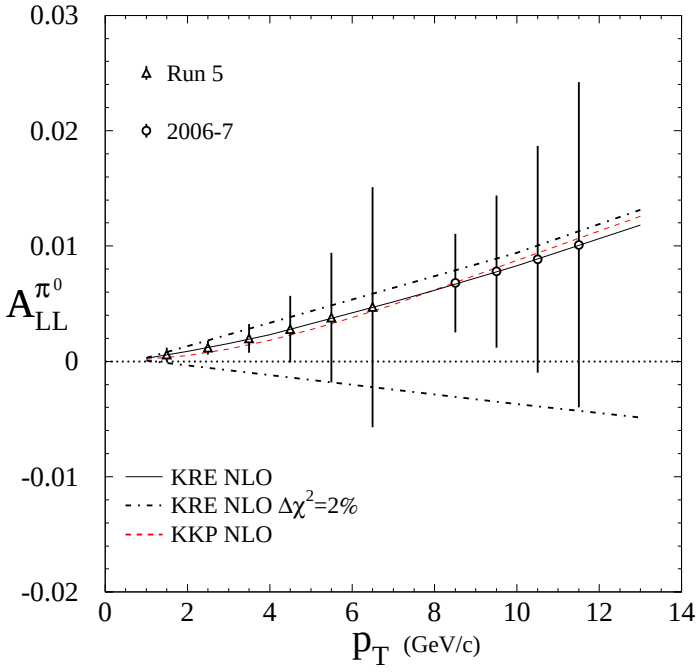

Figure 4.15: NLO pQCD-based prediction of $A_{LL}^{\pi^0}$ using polarized PDF obtained by DNS group [69]. Solid line and red dashed line denote expected value with KRE [28] and KKP [29] fragmentation function, respectively. Dashed-dotted line indicates the uncertainty which is derived from uncertainty of PDFs. DNS group assigns the uncertainty as the range where chi-square of the global analysis increases by 2 %. Error bars of the points on the solid line (KRE NLO) represent expected uncertainty of the measurement by the PHENIX experiment. The points tagged as Run 5 corresponds to the data taken in 2005 and those tagged as 2006-7 is for 2006 and 2007. (The figure is as it is in the reference. Therefore, though the points of Run 5 correspond to the data in this thesis, they are not exactly same.)

4.5 For further knowledge on polarized PDF

As described in Section 4.3 and 4.4, our data will significantly reduce uncertainty of Δg. However, the uncertainty is still large and there are still some concerns. One is duality of sign of Δg. At large Bjorken x, the sign turns out to be positive by DIS measurement with deuteron target. However, both positive and negative Δg is acceptable at small x region. As explained in Section 4.3 and 4.4, it is difficult to disentangle the duality of Δg sign by measurement of $A_{LL}^{\pi^0}$, especially at small x ($x <\sim 0.2$), where gluon-gluon scattering at QCD sub-process is dominant in π^0 production. One of the favorable method to determine the sign of Δg is A_{LL} in prompt photon production at pp collision. Prompt photon is produced directly at QCD sub-process as displayed in Figure 4.16. At the leading order, prompt photon is produced only via quark-antiquark or gluon-quark scattering, and there is no contribution from gluon-gluon scattering. For this reason, prompt-photon A_{LL} is approximated to be linear function of Δg and can disentangle the sign of Δg. Currently from PHENIX, only cross section is published for prompt photon [99] because statistics of prompt photon is much smaller than π^0. In the near future, the measurement of prompt photon A_{LL} in PHENIX is expected to achieve sufficient accuracy to constrain Δg as introduced in Section 4.6.

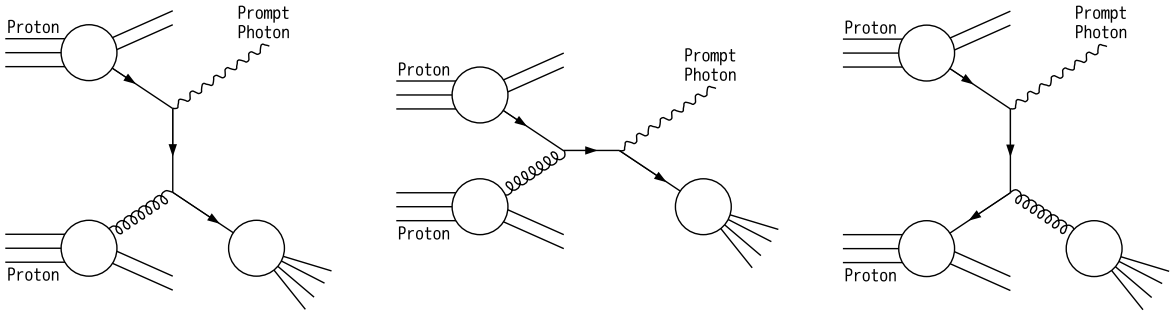

Figure 4.16: Diagrams of prompt photon production for QCD sub-process of the leading order.

Another concern on Δg is coverage of Bjorken x by measurements and it is deeply related to the first concern described above. As pointed out in Section 4.4, direct constraint by experiments is only at large x region ($x >\sim 0.1$). This introduces large uncertainty and ambiguity of sign of Δg at small x. It must be noted that Type 1, as well as Type 3, in Figure 4.14 potentially has large uncertainty at small x. To determine small-x PDF, RHIC is planning to collide protons at center-of-mass energy of 500 GeV. It will probe relatively smaller x region, up to ~ 0.01 in the case of π^0 production, for example. Though there is no distinct programs for polarized experiments, it is important to remember that DIS experiments in large Q^2 range constrain gluon distribution at small x in the case of unpolarized PDF. On the other hand, experiments at JLab intend to reach toward large x region close to 0.8 with polarized electron beam and various fixed target including proton, deuteron and nucleus [100].

Recently, uncertainty of FF is discussed in [32] and it influences uncertainty of global analysis for PDF. Needless to say about importance of constraining FF by experiment, reactions which do not require FF, such as prompt photon and jet, are also available to exclude the ambiguity of FF. However, they also have disadvantage, small statistics in prompt photon production and large uncertainty in momentum measurement for jet. For these reasons, it is also important to utilize various kinds of probes including meson and baryon production in addition to π^0 of this thesis. A_{LL}'s in jet-like multi-particles, charged pions, η and

J/ψ production are presented from the PHENIX experiment, and jet and π^0 from the STAR experiment at RHIC. However, uncertainty is presently large mainly due to short of statistics.

In AAC group [70] and some other groups [66, 68, 71], symmetric polarized sea-quark distribution is assumed because experimental data is poor for decomposition of quark flavor. Some groups [67, 69] attempt to discard flavor-SU(3) symmetry in global analysis. For the purpose, only SIDIS data is currently available. However, uncertainties on sea quarks are large as presumed. In particular, separation between $\bar{u}$ and $\bar{d}$ quark is more difficult than that of s quark because s quark in the proton can be identified by detecting hadrons containing s quark such as K meson while u and d quarks is easy to be produced by pair creation. HERMES collaboration mentions based on SIDIS measurement that no significant observation of breaking flavor-SU(3) sea distribution is observed within error of the measurement [101]. At PHENIX, the separation of $\bar{u}$ and $\bar{d}$ quark will be performed through measurement of W boson taking advantage that W selects quark flavor; W^+ produced by annihilation of u and $\bar{d}$ quark and W^- from $\bar{u}$ and d. For s quark PDF, SIDIS experiments will be continued, for example, at JLab. Another promising tool is DIS with neutrino beam utilizing weak current which selects quark flavor. Such neutrino DIS will be feasible at J-PARC in near future.

The last unknown contribution to the proton spin is orbital angular momentum of partons, L. Until now, we have almost no knowledge about L. To extract L, Deeply virtual Compton scattering (DVCS), $ep \to e'p'\gamma$ where γ is photon, is suggested. HERMES collaboration published various kinds of asymmetries in DVCS [102, 103]. DVCS is also measured at JLab [104]. However, the relation of DVCS and L is not established and no explicit statement about L is obtained.

4.6 Future measurement in PHENIX

Following the 2005 run, RHIC ran polarized pp experiment in 2006 and PHENIX accumulated data of 10.7 pb^{-1} at $\sqrt{s} = 200$ GeV. Average beam polarization was about 60 % during the data taking period. Currently, preliminary results of $A_{LL}^{\pi^0}$ have already been presented [105]. Owing to higher statistics and polarization than the 2005 run, the accuracy of the data become nearly twice better. The 2006 data is more staying around zero and prefer GRSV $\Delta g = 0$ than GRSV-std. In [105], other possibility is also discussed. It is an assumption of Δg with node around $x = 0.1$ (GSC-NLO) [66] as displayed in Figure 4.17. The first moment of GSC-NLO is $\sim$1.0. Meanwhile, because the integral of Δg over x region for the measurement is small, $A_{LL}^{\pi^0}$ with the GSC-NLO input becomes nearly zero. The suggestion also implies the importance of the measurement over wide Bjorken x and with detail x dependence. As well as 200 GeV, the data of 0.1 pb^{-1} with $\sqrt{s} = 62.4$ GeV were obtained in 2006 and the preliminary $A_{LL}^{\pi^0}$ were presented [106]. Because of lower energy than our data, the data at 62.4 GeV corresponds to relatively higher Bjorken x than our data. However, because the integrated luminosity is smaller than our data and the cross section of π^0 is also small about twice at the same p_T compared to 200 GeV [105], the precision of the data is moderate. Nevertheless, the data disfavor large Δg and consistent with our results at 200 GeV.

Presently, the polarized pp run at RHIC is planed for years. In 2008, another run will be performed at $\sqrt{s} = 200$ GeV. The goal of the 2008 run is integrated luminosity of 71 pb^{-1} with average bean polarization of 65 %. It is about 90 times larger statistics than our data in the 2005 run in terms of figure-of-merit for A_{LL}. At this stage, much better accuracy will be achieved in $A_{LL}^{\pi^0}$. Moreover, p_T range of the measurement will be extended and that is directly related to the wider Bjorken x region. As well as $A_{LL}^{\pi^0}$, the measurement of A_{LL} in

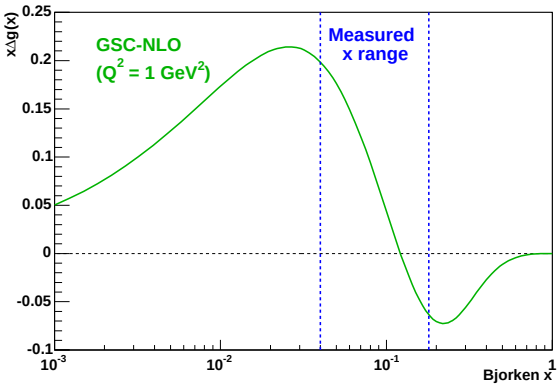

Figure 4.17: $x\Delta g$ of GSC-NLO model as a function of Bjorken x. The x range for our data is indicated by the blue window.

prompt photon production will start to constrain Δg. Figure 4.18 displays A_{LL} in π^0 and prompt photon production with similar statistics in the 2008 run (integrated luminosity of 65 pb^{-1} and polarization of 70 %). Prompt photon A_{LL} is expected to determine the sign of Δg, which is one of the difficulty in our results via π^0. In addition, measurements with other probes such as jet-like multi-particles, charged pions, η, J/ψ and single electrons, will be more significant with large statistics.

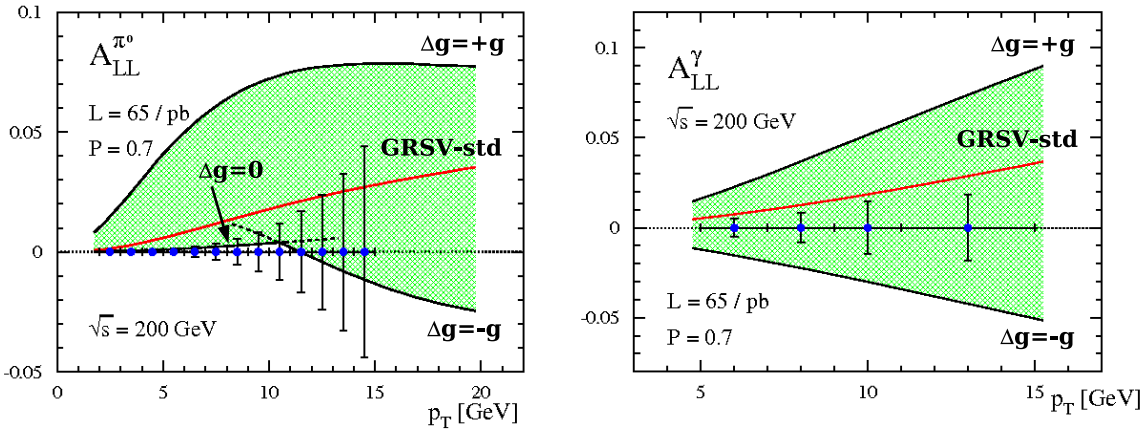

Figure 4.18: The expected accuracy of the measurement at PHENIX with integrated luminosity of 65 pb^{-1} and polarization of 70 %. The left is for π^0 A_{LL} and the right is for prompt photon A_{LL}. The green band indicates theoretical uncertainty depending on the Δg input. The theoretical calculation is based on Δg of GRSV group [67], which is same as in Figure 4.1. In the plot for prompt photon A_{LL}, upper and lower edges correspond to $\Delta g = +g$ and $\Delta g = -g$, respectively. The red curve is for GRSV-std.

From 2009, RHIC will start to operate polarized pp run with $\sqrt{s} = 500$ GeV. The goal at 500 GeV is the integrated luminosity of 800 pb^{-1} and the average beam polarization of 70 %. The measurements of A_{LL} at 500 GeV result in probing Δg at lower Bjorken x than 200 GeV. It is important to extend the coverage of Bjorken x because that is one of the concerns to determine Δg as described in Section 4.4. Another important research at $\sqrt{s} = 500$ GeV is to separate the contributions from $\bar{u}$ and $\bar{d}$ quarks to the proton spin. This will be achieved via measurement of A_L in W boson production. Finally, 8000 W^+s and 8000 W^-s are expected to be accumulated during the 500 GeV operation.

Chapter 5

Conclusion

We have measured double helicity asymmetry A_{LL} in π^0 production in pp collision with $\sqrt{s} = 200$ GeV. Kinematical coverage of the measurement was 0.5 to 9.0 GeV/c in p_T and -0.35 to 0.35 in η. The measurement of $A_{LL}^{\pi^0}$ is considered as a promising method to probe Δg, which is gluon polarization in the proton and large uncertainty was previously assigned to. As well as $A_{LL}^{\pi^0}$, single helicity asymmetry $A_L^{\pi^0}$ and double transverse spin asymmetry $A_{TT}^{\pi^0}$ were also measured in this thesis.

The polarized proton beams with energy of 100 GeV were provided and collided by RHIC at BNL in the U.S. The measurements were performed with the PHENIX detector in 2005. Integrated luminosity accumulated by PHENIX in the data-taking period was 3.8 pb^{-1}, and 2.4 pb^{-1} was used in this thesis after data quality selection. Averaged beam polarization was about 50 % for the selected data sample. Photons produced at the collision were detected by EMCal located at central region and π^0s were identified by selecting the invariant mass which was reconstructed from photons. The π^0 mass was also used for energy calibration of EMCal. For the particle identification, various cuts were applied utilizing ToF between EMCal and event vertex, shower profile and charged particle veto by use of tracking chambers in front of EMCal. High-energy photon trigger implemented in EMCal was utilized for the data taking to effectively collect photons in wide p_T range. The result of A_{LL} was consistent with zero within the measurement uncertainty. The statistical uncertainty of measured A_{LL} was 0.0017 at 1.0 – 1.5 GeV/c and 0.0257 at 7.0 – 9.0 GeV/c in p_T. The uncertainty from the beam polarization, which appears as normalization uncertainty for A_{LL}, was evaluated to be $\frac{\Delta A_{LL}}{A_{LL}} = 9.5$ %. The systematic uncertainty except for that from the beam polarization varied from 0.0005 to 0.0089 depending on p_T. Major source of the systematic uncertainty at small p_T was assumed to be due to fill-by-fill and crossing-by-crossing fluctuation of background, while that at large p_T was dominated by contamination from $A_{TT}^{\pi^0}$ and A_{LL} of background. However, the statistical uncertainty is currently dominant compared with the systematic one over all p_T region measured.

Our result of $A_{LL}^{\pi^0}$ is compared with theoretical calculations with various Δg inputs and clearly rejects the case of $\Delta g = +g$ and $\Delta g = -g$. In addition, based on an approximate relation between $A_{LL}^{\pi^0}$ and Δg, an interpretation of $A_{LL}^{\pi^0}$ into Δg with a simple model was introduced in this thesis. In the interpretation, it turned out that our data would significantly constrain the allowed region of Δg. This is consistent with the result of a global analysis which included our preliminary data. However, for more precise determination of Δg, it is important to employ various probes and extend a range of Bjorken x in measurements. In 2008, PHENIX will accumulate integrated luminosity of 71 pb^{-1} with beam polarizations of 65 % at $\sqrt{s} = 200$ GeV. From 2009, the operation with $\sqrt{s} = 500$ GeV is planned at RHIC. In total, 800 pb^{-1} with 70 % polarization will be accumulated at 500 GeV. It is expected that further knowledge on the structure of the proton spin will be obtained in the near future.

Acknowledgments

I would like to acknowledge Prof. Ken'ichi Imai, who is the leader of the experimental nuclear and hadronic physics laboratory. He has been my supervisor and gave me shrewd advises. The laboratory provided the place for the academic activity.

I'm grateful to Prof. Naohito Saito. He read my thesis carefully and made interactive discussion. As well as completing my thesis, a wide range of talks on physics stimulate my interests and they were beneficial time for me.

I'm obliged to the PHENIX collaborator and the staff of Collider-Accelerator Department at BNL. It was impossible to successfully operate the experiment without their help. In particular, I would like to convey the gratitude to Dr. Alexander Bazilevsky, Mr. Kieran Boyle, Dr. Gerry Bunce, Prof. Abhay Deshpande, Dr. Yuji Goto and Prof. Naohito Saito. They are members of the working group for π^0 A_{LL} measurement. With their supports, I could polish the analysis and finish my thesis.

I would like to thank Dr. Werner Vogelsang and Dr. Marco Stratmann who are experts in the theory of pQCD. The discussion with them was a great help to understand the experimental results of $A_{LL}^{\pi^0}$ with the theoretical knowledge. In terms of extracting Δg from the measured $A_{LL}^{\pi^0}$, Dr. Shunzo Kumano and Dr. Masanori Hirai, who are experts of the global analysis, gave me kind advisement.

I would like to express special thanks to the radiation laboratory and BNL research center in RIKEN for the research activity as well as financial supports. Especially, Dr. Hideto En'yo, who is the chief scientist of the radiation laboratory, often advised me about the research plan.

I would like to thank Dr. Kouji Miwa, Mr. Terunao Nakura, Dr. Hiromi Okada, Mr. Shinsuke Ota, Mr. Satoru Terashima and Mr. Manabu Togawa. They are in the same grade in the university and inspired interests in physics each other. Dr. Hiromi Okada read throughout my thesis and made useful comments.

Finally, I have to express an appreciation to my father, mother and brothers. My interests in science have been developed in the day-to-day communication with them. They have totally supported my work and have watched me with great patience.

Bibliography

[1] FNAL E581/704 Collaboration, Phys. Lett. B261, 197 (1991).

[2] PHENIX Collaboration, Phys. Rev. Lett. 93, 202002 (2004).

[3] PHENIX Collaboration, Phys. Rev. D73, 091102 (2006).

[4] Particle Data Group, J. Phys. G33, 1 (2006).

[5] CTEQ Collaboration, Rev. Mod. Phys. 67, 157 (1995).

[6] M. Anselmino, A. Efremov, and E. Leader, Phys. Rept. 261, 1 (1995).

[7] S. B. Bass, Rev. Mod. Phys. 77, 1257 (2005).

[8] E. W. Hughes and R. Voss, Ann. Rev. Nucl. Part. Sci. 49, 303 (1999).

[9] B. W. Fillipone and X. Ji, Adv. Nucl. Phys. 26, 1 (2001).

[10] R. L. Jaffe, hep-ph/9602236 (1996).

[11] B. Lampe and E. Reya, Phys. Rept. 332, 1 (2000).

[12] E. Leader, A. V. Sidorov, and D. B. Stamenov, JHEP 0506, 033 (2005).

[13] A. Pich, hep-ph/9505231 (1995).

[14] V. Barone, A. Drago, and P. G. Ratcliffe, Phys. Rept. 359, 1 (2002).

[15] J. C. Collins, Nucl. Phys. B396, 161 (1993).

[16] J. C. Collins, S. F. Heppelmann, and G. A. Ladinsky, Nucl. Phys. B420, 565 (1994).

[17] J. Soffer, Phys. Rev. Lett. 74, 1292 (1995).

[18] G. Altarelli and G. Parisi, Nucl. Phys. B126, 298 (1977).

[19] Yu. L. Dokshitzer, Sov. Phys. JETP 46, 641 (1977).

[20] V. N. Gribov and L.N. Lipatov, Sov. J. Nucl. Phys. 15, 438 (1972).

[21] S. Moch, J. A. M. Vermaseren, and A. Vogt, Nucl. Phys. B688, 101 (2004).

[22] A. Vogt, S. Moch, and J. A. M. Vermaseren, Nucl. Phys. B691, 129 (2004).

[23] R. Metrig and W. L. van Neerven, Z. Phys. C70, 637 (1996).

[24] W. Vogelsang, Phys. Rev. D54, 2023 (1996).

[25] P. J. Rijken and W. L. van Neerven, Phys. Lett. B386, 422 (1996).

[26] P. J. Rijken and W. L. van Neerven, Nucl. Phys. B487, 233 (1997).

[27] P. J. Rijken and W. L. van Neerven, Phys. Lett. B392, 207 (1997).

[28] S. Kretzer, Phys. Rev. D62, 054001 (2000).

[29] B. A. Kniehl, G. Kramer, and B. Pötter, Nucl. Phys. B582, 514 (2000).

[30] L. Bourhis et al., Eur. Phys. J. C19, 89 (2001).

[31] S. Albino, B. A. Kniehl, and G. Kramer, Nucl. Phys. B725, 181 (2005).

[32] M. Hirai et al., Phys. Rev. D75, 094009 (2007).

[33] H1 and ZEUS Collaborations, hep-ex/0406036; *Proceedings of 39th Rencontres de Moriond on Electroweak Interactions and Unified Theories, La Thuile, Aosta Valley, Italy* (2004).

[34] H1 Collaboration, Eur. Phys. J. C30, 1 (2003).

[35] ZEUS Collaboration, Eur. Phys. J. C42, 1 (2005).

[36] CCFR/NuTeV Collaboration, Phys. Rev. Lett. 86, 2742 (2001).

[37] CDF Collaboration, Phys. Rev. Lett. 81, 5754 (1998).

[38] European Muon Collaboration, Nucl. Phys. B213, 31 (1983).

[39] ZEUS Collaboration, Phys. Rev. D69, 012004 (2004).

[40] H1 Collaboration, Phys. Lett. B528, 199 (2002).

[41] H1 Collaboration, Eur. Phys. J. C40, 349 (2005).

[42] H1 Collaboration, Eur. Phys. J. C45, 23 (2006).

[43] NA51 Collaboration, Phys. Lett. B332, 244 (1994).

[44] FNAL E866/NuSea Collaboration, Phys. Rev. D64, 052002 (2001).

[45] CDF Collaboration, Phys. Rev. D64, 032001 (2001).

[46] CDF Collaboration, Phys. Rev. Lett. 96, 122001 (2006).

[47] CDF Collaboration, Phys. Rev. D74, 071103 (2006).

[48] D0 Collaboration, Phys. Rev. D64, 032003 (2001).

[49] CTEQ Collaboration, JHEP 0207, 012 (2002).

[50] M. Glück, E. Reya, and A. Vogt, Eur. Phys. J. C5, 461 (1998).

[51] A. D. Martin, W. J. Stirling, and R. S. Thorne, Phys. Lett. B636, 259 (2006).

[52] S. Alekhin, K. Melnikov, and F. Petriello, Phys. Rev. D74, 054033 (2006).

[53] J. D. Bjorken, Phys. Rev. 148, 1467 (1966).

[54] J. D. Bjorken, Phys. Rev. D1, 1376 (1970).

[55] E155 Collaboration, Phys. Lett. B493, 19 (2000).

[56] HERMES Collaboration, Phys. Rev. D75, 012007 (2007).

[57] F. E. Close and R. G. Roberts, Phys. Rev. Lett. 60, 1471 (1988).

[58] F. E. Close and R. G. Roberts, Phys. Lett. B316, 165 (1993).

[59] E143 Collaboration, Phys. Lett. B452, 194 (1999).

[60] M. J. Alguard et al., Phys. Rev. Lett. 37, 1261 (1976).

[61] M. J. Alguard et al., Phys. Rev. Lett. 41, 70 (1978).

[62] G. Baum et al., Phys. Rev. Lett. 45, 2000 (1980).

[63] G. Baum et al., Phys. Rev. Lett. 51, 1135 (1983).

[64] European Muon Collaboration, Phys. Lett. B206, 364 (1988).

[65] European Muon Collaboration, Nucl. Phys. B328, 1 (1989).

[66] T. Gehrmann and W. J. Stirling, Phys. Rev. D53, 6100 (1996).

[67] M. Glück et al., Phys. Rev. D63, 094005 (2001).

[68] J. Blümlein and Böttcher, Nucl. Phys. B636, 225 (2002).

[69] D. de Florian, G. A. Navarro, and R. Sassot, Phys. Rev. D71, 094018 (2005).

[70] Asymmetry Analysis Collaboration, Phys. Rev. D74, 014015 (2006).

[71] E. Leader, A. V. Sidorov, and D. B. Stamenov, Phys. Rev. D73, 034023 (2006).

[72] Asymmetry Analysis Collaboration, Phys. Rev. D69, 054021 (2004).

[73] Spin Muon Collaboration, Phys. Rev. D70, 012002 (2004).

[74] HERMES Collaboration, Phys. Rev. Lett. 84, 2584 (2000).

[75] COMPASS Collaboration, Phys. Lett. B633, 25 (2006).

[76] STAR Collaboration, Phys. Rev. Lett. 97, 252001 (2006).

[77] L. Mankiewicz, G. Piller, and A. Saalfeld, Phys. Lett. B395, 318 (1997).

[78] I. Balitsky and X. Ji, Phys. Rev. Lett. 79, 1225 (1997).

[79] S. J. Brodsky, M. Burkardt, and I. Schmidt, Nucl. Phys. B441, 197 (1995).

[80] V. Barone, T. Calarco, and A. Drago, Phys. Lett. B431, 405 (1998).

[81] H. J. Lee et al., Phys. Lett. B491, 257 (2000).

[82] P. Chen and X. Ji, hep-ph/0612174 (2006).

[83] J. E. Mandula, Phys. Rev. Lett. 65, 1403 (1990).

[84] B. Jäger et al., Phys. Rev. D67, 054005 (2003).

[85] J. P. Ralston and D. E. Soper, Nucl. Phys. B152, 109 (1979).

[86] A. Zelenski et al., Rev. Sci. Instrum. 75, 1535 (2004).

[87] Ya. S. Derbenev et al., Part. Accel. 8, 115 (1978).

[88] A. Bravar et al., Nucl. Phys. Proc. Suppl. 146, 77 (2005).

[89] H. Okada et al., Phys. Lett. B638, 450 (2006).

[90] PHENIX Collaboration, Nucl. Instrum. Meth. A499, 508 (2003).

[91] WA98 Collaboration, CERN-SPSLC-91-17 (1991).

[92] W. Vogelsang, hep-ph/0503036; *Proceedings of 16th International Spin Physics Symposium (SPIN 2004), Trieste, Italy.* (2004).

[93] F. Aversa et al., Nucl. Phys. B327, 105 (1989).

[94] A. Mukherjee, M. Stratmann, and W. Vogelsang, Phys. Rev. D72, 034011 (2005).

[95] PHENIX Collaboration, Phys. Rev. Lett. 95, 202001 (2005).

[96] PHENIX Collaboration, arXiv:0704.3599 [hep-ex]; To be published in Phys. Rev. D.

[97] Private communication with W. Vogelsang and M. Stratmann.

[98] PHENIX Collaboration, hep-ph/0606008; *Proceedings of 17th Particles and Nuclei International Conference (PANIC05), Santa Fe, New Mexico, US.* (2005).

[99] PHENIX Collaboration, Phys. Rev. Lett. 98, 012002 (2007).

[100] K. de Jager, nucl-ex/0612025; *Proceedings of 17th International Spin Physics Symposium (SPIN 2006), Kyoto, Japan* (2006).

[101] HERMES Collaboration, Phys. Rev. D71, 012003 (2005).

[102] HERMES Collaboration, Phys. Rev. D75, 011103 (2007).

[103] HERMES Collaboration, AIP Conf. Proc. 792, 424 (2005).

[104] F. Sabatie, nucl-ex/0612023; *Proceedings of 17th International Spin Physics Symposium (SPIN 2006), Kyoto, Japan* (2006).

[105] PHENIX Collaboration, *Talk by K. Boyle at RHIC & AGS Annual Users' Meeting in 2007* (2007).

[106] PHENIX Collaboration, arXiv:0704.1369; *Proceedings of 17th International Spin Physics Symposium (SPIN 2006), Kyoto, Japan* (2006).

[107] E. Iarocci, Nucl. Instrum. Meth. 217, 30 (1983).

[108] PHENIX Collaboration, Nucl. Instrum. Meth. A499, 489 (2003).

Appendix A

A.1 Splitting functions for QCD evolution of PDF

The splitting function is expanded by an order of the coupling constant of the strong interaction, α_s, like Equation (1.31). For this section, the leading order of the splitting function is summarized.

$$P_{qq}^{(0)}(z) = \frac{4}{3}\left(\frac{2}{[1-z]_+} - 1 - z\right) + 2\delta(1-z), \tag{A.1}$$

$$P_{qg}^{(0)}(z) = \frac{1}{2}\left(z^2 + (1-z)^2\right), \tag{A.2}$$

$$P_{gq}^{(0)}(z) = \frac{4}{3}\frac{1+(1-z)^2}{z}, \tag{A.3}$$

$$P_{gg}^{(0)}(z) = 6\left(\frac{1-z}{z} + \frac{z}{[1-z]_+} + z(1-z)\right) + \left(\frac{11}{2} - \frac{n_f}{3}\right)\delta(1-z). \tag{A.4}$$

$$\Delta P_{qq}^{(0)}(z) = \frac{4}{3}\left(\frac{2}{[1-z]_+} - 1 - z\right) + 2\delta(1-z), \tag{A.5}$$

$$\Delta P_{qg}^{(0)}(z) = \frac{1}{2}\left(z^2 - (1-z)^2\right), \tag{A.6}$$

$$\Delta P_{qg}^{(0)}(z) = \frac{4}{3}\frac{1-(1-z)^2}{z}, \tag{A.7}$$

$$\Delta P_{gg}^{(0)}(z) = 6\left(\frac{1}{[1-z]_+} - 2z + 1\right) + \left(\frac{11}{2} - \frac{n_f}{3}\right)\delta(1-z). \tag{A.8}$$

n_f in these formulae is the number of the quark flavor. Usually, only u, d and s quarks are considered. Therefore $n_f = 3$ in the case. $\frac{1}{[1-z]_+}$ is introduced to regulate singularity of $P_{ij}(z)$ at $z = 1$ and defined as

$$\int_0^1 \frac{f(z)}{[1-z]_+}dz \equiv \int_0^1 \frac{f(z)-f(1)}{1-z}dz. \tag{A.9}$$

A.2 Longitudinal double spin asymmetry by polarized DIS

To extract spin-dependent structure function g_1, longitudinal double spin asymmetry $A_{||}$ is frequently measured by polarized DIS experiments. $A_{||}$ is defined in Equation (1.45) and relation of $A_{||}$ and the structure functions becomes apparent by substituting Equation (1.13)

and (1.14) into Equation (1.45). Finally, $A_{||}$ is described by two terms on perspective of the interaction between the proton and virtual photon emitted by the incident electron.

$$A_{||} = D(A_1 + \eta A_2), \tag{A.10}$$

where variables in this equation are

$$A_1 \equiv \frac{\sigma_{\frac{1}{2}} - \sigma_{\frac{3}{2}}}{\sigma_{\frac{1}{2}} + \sigma_{\frac{3}{2}}} = \frac{g_1 - \gamma^2 g_2}{F_1}, \quad A_2 \equiv \frac{2\sigma_{TL}}{\sigma_{\frac{1}{2}} + \sigma_{\frac{3}{2}}} = \gamma \frac{g_1 + g_2}{F_1}, \quad \gamma^2 \equiv \frac{Q^2}{\nu^2} = \frac{2Mx}{\nu} \tag{A.11}$$

$$D \equiv \frac{E - \epsilon E'}{E(1 + \epsilon R)}, \qquad \eta \equiv \frac{\epsilon\gamma(E - E')}{E - \epsilon E'}, \qquad \frac{1}{\epsilon} \equiv 1 + 2\left(1 + \frac{1}{\gamma^2}\right)\tan^2\frac{\theta}{2} \tag{A.12}$$

$$R(x, Q^2) \equiv \frac{\sigma_L}{\sigma_T} = \frac{F_2(x, Q^2)}{2xF_1(x, Q^2)}(1 + \gamma^2) - 1. \tag{A.13}$$

$\sigma_{\frac{1}{2}}$ and $\sigma_{\frac{3}{2}}$ are cross sections of virtual photon absorption with transversely polarized[1] by polarized proton. $\sigma_{\frac{1}{2}}$ ($\sigma_{\frac{3}{2}}$) is the case that the helicity of the photon and the spin of the proton is antiparallel (parallel). σ_T (σ_L) is cross sections with unpolarized proton and virtual photon polarized transversely (longitudinally). σ_{TL} is result from an interference between transversely-polarized virtual photon and longitudinally-polarized one. γ is determined by the kinematics and becomes 0 at the Bjorken limit. Hence, A_1 is simply the ratio of g_1 and F_1 at the limit and A_2 is expected to be smaller than A_1. Moreover, η which is proportional to γ is also suppressed. D is named depolarization factor and represents the polarization of the virtual photon. R is ratio of σ_T and σ_L. R also relates F_1 and F_2. Because $F_1 = \frac{F_2}{2x}$ at the Bjorken limit as shown in Equation (1.21), R is equal to 0 in the simple parton model. If one neglects the second term of Equation (A.10) and puts $\gamma^2 = 0$, Equation (1.46) is obtained;

$$A_{||} \sim D\frac{g_1}{F_1} \sim D\frac{g_1}{F_2}2x(1 + R). \tag{A.14}$$

A.3 Yield from the collisions of the polarized beam

To begin with the calculation, a spin $\frac{1}{2}$ particle is considered. The spin of the particle is assumed to be on the x-z plane and oriented to have the angle α between the z-axis and the spin direction as displayed in Figure A.1 as the particle a. The operators for the spin $\frac{1}{2}$ for the particle a are defined as

$$\hat{S}_x^a = \frac{1}{2}\Big\{|a_+\rangle\langle a_-| + |a_-\rangle\langle a_+|\Big\}, \tag{A.15}$$

$$\hat{S}_y^a = \frac{i}{2}\Big\{-|a_+\rangle\langle a_-| + |a_-\rangle\langle a_+|\Big\}, \tag{A.16}$$

$$\hat{S}_z^a = \frac{1}{2}\Big\{|a_+\rangle\langle a_+| - |a_-\rangle\langle a_-|\Big\}, \tag{A.17}$$

where $\hat{S}_z^a$, $\hat{S}_y^a$ and $\hat{S}_z^a$ are the operators for the x, y and z-component of the spin. $|a_+\rangle$ and $|a_-\rangle$ are the eigenstate of $\hat{S}_z^a$; $\hat{S}_z^a|a_+\rangle = \frac{1}{2}|a_+\rangle$ and $\hat{S}_z^a|a_-\rangle = -\frac{1}{2}|a_-\rangle$. Based on the definition, the state of the particle a in Figure A.1 is described as follows;

$$|a\rangle = \sqrt{\frac{1 + \cos\alpha}{2}}|a_+\rangle + \sqrt{\frac{1 - \cos\alpha}{2}}|a_-\rangle. \tag{A.18}$$

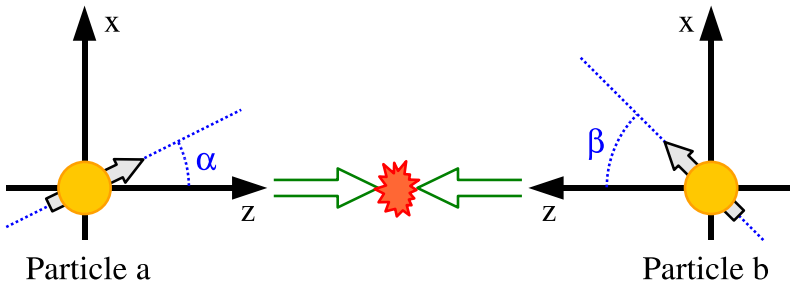

Figure A.1: The definition of the spin direction in the collision of the polarized protons. The z-axes for the particle a and b are set to the direction of movement of each particle.

Obviously, $\langle a|\hat{S}^a_x|a\rangle = \frac{1}{2}\sin\alpha$, $\langle a|\hat{S}^a_y|a\rangle = 0$ and $\langle a|\hat{S}^a_z|a\rangle = \frac{1}{2}\cos\alpha$.

In addition to the particle a, particle b is similarly defined as $|b\rangle$ to consider the double spin asymmetry.

$$|b\rangle = \sqrt{\frac{1+\cos\beta}{2}}|b_+\rangle + \sqrt{\frac{1-\cos\beta}{2}}|b_-\rangle. \tag{A.19}$$

Naively, the cross section of a certain process is represented by the operator $\hat{\sigma}$. The cross section by the collision of the state $|a\rangle$ and $|b\rangle$ is therefore written as;

$$\begin{aligned}
\langle ab|\hat{\sigma}|ab\rangle = {} & \frac{1}{4}\left[\sigma_{++}+\sigma_{+-}+\sigma_{-+}+\sigma_{--}\right] \\
& + \frac{1}{4}\cos\alpha\left[\sigma_{++}+\sigma_{+-}-\sigma_{-+}-\sigma_{--}\right] + \frac{1}{4}\cos\beta\left[\sigma_{++}-\sigma_{+-}+\sigma_{-+}-\sigma_{--}\right] \\
& + \frac{1}{4}\sin\alpha\left[\sigma_{\uparrow+}+\sigma_{\uparrow-}-\sigma_{\downarrow+}-\sigma_{\downarrow-}\right] + \frac{1}{4}\sin\beta\left[\sigma_{+\uparrow}-\sigma_{+\downarrow}+\sigma_{-\uparrow}-\sigma_{-\downarrow}\right] \\
& + \frac{1}{4}\cos\alpha\cos\beta\left[\sigma_{++}-\sigma_{+-}-\sigma_{-+}+\sigma_{--}\right] + \frac{1}{4}\sin\alpha\sin\beta\left[\sigma_{\uparrow\uparrow}-\sigma_{\uparrow\downarrow}-\sigma_{\downarrow\uparrow}+\sigma_{\downarrow\downarrow}\right] \\
& + \frac{1}{4}\cos\alpha\sin\beta\left[\sigma_{+\uparrow}-\sigma_{+\downarrow}-\sigma_{-\uparrow}+\sigma_{-\downarrow}\right] + \frac{1}{4}\sin\alpha\cos\beta\left[\sigma_{\uparrow+}-\sigma_{\uparrow-}-\sigma_{\downarrow+}+\sigma_{\downarrow-}\right],
\end{aligned} \tag{A.20}$$

where $\sigma_{s_a s_b}$ in the right side of the equation is equal to $\langle a_{s_a} b_{s_b}|\hat{\sigma}|a_{s_a} b_{s_b}\rangle$. s_a and s_b take $+$, $-$, $\uparrow$ or $\downarrow$. As described above, $+$ and $-$ indicate the eigenstates of $\hat{S}_z$. Meanwhile, $\uparrow$ and $\downarrow$ indicate those of $\hat{S}_x$ and they can be converted using $|+\rangle$ and $|-\rangle$ into

$$|\uparrow\rangle = \frac{1}{\sqrt{2}}\Big\{|+\rangle + |-\rangle\Big\} \tag{A.21}$$

$$|\downarrow\rangle = \frac{1}{\sqrt{2}}\Big\{|+\rangle - |-\rangle\Big\}. \tag{A.22}$$

Therefore, $\hat{S}_x|\uparrow\rangle = \frac{1}{2}|\uparrow\rangle$ and $\hat{S}_x|\downarrow\rangle = -\frac{1}{2}|\downarrow\rangle$ are satisfied.

For the further calculation, the z-axis for the spin of the particle a and b is set to the RHIC beam axis at PHENIX and $|+\rangle$ ($|-\rangle$) correspond to the positive (negative) helicity state. The x and y-axis for the spin direction are arbitrary. However, it is assumed that the

[1] Transverse polarization of the photon is eigen state of helicity $= \pm 1$ (circular polarization) and longitudinal polarization of the (virtual) photon has helicity $= 0$.

x-axes for the particle a and b are parallel. With this assumption, the cross section $\sigma_{s_a s_b}$ for the initial states which are the eigenstates of $\hat{S}_x$ or $\hat{S}_z$ is simply described as

$$\sigma_{s_a s_b} = \sigma_0 \left[1 + (h_{s_a} + h_{s_b})A_L + h_{s_a} h_{s_b} A_{LL} + (t_{s_a} + t_{s_b})A_N + t_{s_a} t_{s_b} A_{TT}\right], \tag{A.23}$$

where $h_+ = 1$, $h_- = -1$ and otherwise $h_s = 0$, and $t_\uparrow = 1$, $t_\downarrow = -1$ and otherwise $t_s = 0$. σ_0 is the spin-averaged cross section. A_L and A_N are the longitudinal and transverse single-spin asymmetry, and A_{LL} and A_{TT} are the longitudinal and transverse double-spin asymmetry. σ_0 and asymmetries depend on the kinematical region of measured particles. In the case of the single spin asymmetry A_L and A_N, they are generated by the spin of either particle a or b. In the measurement of π^0 by use of the PHENIX central arms, the kinematical range for A_L (or A_N) in the view of the particle a is same as that for b because the detector is symmetrically constructed on the both sides of the beam axis. Hence the contributions to A_L (or A_N) from the particle a and b are combined in Equation (A.23). See Section 2.3.1 about the overview of the PHENIX detector. Substituting Equation (A.23), Equation (A.20) is rewritten as

$$\begin{aligned}
\langle ab|\hat{\sigma}|ab\rangle &= \sigma_0\Big[1 + (\cos\alpha + \cos\beta)A_L + (\sin\alpha + \sin\beta)A_N \\
&\quad + (\cos\alpha\cos\beta)A_{LL} + (\sin\alpha\sin\beta)A_{TT}\Big] \\
&\equiv \sigma(\alpha, \beta).
\end{aligned} \tag{A.24}$$

To calculate the yield by the collisions of the polarized beams, the integrated luminosity can be written as

$$L = cI^a I^b = c(I^a_+ + I^a_-)(I^b_+ + I^b_-), \tag{A.25}$$

where I^a and I^b indicate the beam intensity for a and b, and c is the coefficient to relate I and L. I^a_+ is defined as the fraction of the particles with an angle of α to determine its spin direction. On the other hand, I^a_- is the fraction for an angle of $\alpha + \pi$. This is same for b. Therefore, $I = I_+ + I_-$ is satisfied for the particle a and b each. The beam polarization for the beam a (P^a) and b (P^b) is defined as

$$P = \frac{I_+ - I_-}{I_+ + I_-}, \tag{A.26}$$

which is equivalent to $I_\pm = \frac{1}{2} I(1 \pm P)$. The superscript a or b is abbreviated in this equation. Finally, the yield for the process represented by Equation (A.23) and for the luminosity defined by Equation (A.25) is obtained as follows;

$$\begin{aligned}
N &= cI^a_+ I^b_+ \sigma(\alpha, \beta) + cI^a_+ I^b_- \sigma(\alpha, \beta + \pi) \\
&\quad + cI^a_- I^b_+ \sigma(\alpha + \pi, \beta) + cI^a_- I^b_- \sigma(\alpha + \pi, \beta + \pi) \\
&= \frac{1}{4} cIJ\Big[\sigma(\alpha, \beta) + \sigma(\alpha, \beta + \pi) + \sigma(\alpha + \pi, \beta) + \sigma(\alpha + \pi, \beta + \pi)\Big] \\
&\quad + \frac{1}{4} cIJP^a\Big[\sigma(\alpha, \beta) + \sigma(\alpha, \beta + \pi) - \sigma(\alpha + \pi, \beta) - \sigma(\alpha + \pi, \beta + \pi)\Big] \\
&\quad + \frac{1}{4} cIJP^b\Big[\sigma(\alpha, \beta) - \sigma(\alpha, \beta + \pi) + \sigma(\alpha + \pi, \beta) - \sigma(\alpha + \pi, \beta + \pi)\Big] \\
&\quad + \frac{1}{4} cIJP^a P^b\Big[\sigma(\alpha, \beta) - \sigma(\alpha, \beta + \pi) - \sigma(\alpha + \pi, \beta) + \sigma(\alpha + \pi, \beta + \pi)\Big] \\
&= L\sigma_0\left[1 + (P^a_L + P^b_L)A_L + (P^a_T + P^b_T)A_N + P^a_L P^b_L A_{LL} + P^a_T P^b_T A_{TT}\right],
\end{aligned} \tag{A.27}$$

where P_L and P_T are the longitudinal and transverse component of the beam polarization, and defined as;

$$P_L^a = P^a \cos\alpha, \qquad P_T^a = P^a \sin\alpha \tag{A.28}$$

for the beam a. They are similarly defined for the beam b.

A.4 Other PHENIX detectors

A.4.1 Drift chambers (DC)

The major role of the drift chamber (DC) is to measure the trajectory of charged particles and determine their momentum. To determine the momentum precisely, the position resolution along the azimuthal direction is important since the field of the central magnet is oriented parallel to the beam axis. DC has cylindrical shape with the beam axis as the central axis and the distance of inner plane from the collision point is 2.0 m. The geometry of DC is 2 m along the beam axis, 90 degrees in the azimuthal angle and 0.4 m deep in the radial direction. The residual magnetic field in the coverage of DC is 0.06 T or less. The structure of east and west DC is identical but mirror symmetric. An 130 μm Al-mylar is used as the window (cylindrical plane) of DC, which limits the gas volume radially. Each DC is segmented into 20 pieces, each of which covers an azimuthal angle of 4.5 degrees and 2 m length along the beam axis. Each segment has 4 anode planes and 4 cathode planes which are parallel to the plane produced by the beam axis and radial direction, and therefore the drift space between cathode and anode plane is 2.0 – 2.5 cm depending on the location of particle hit. One anode plane includes 40 readout sense-wires. Twenty-four wires are oriented parallel to the beam axis and 16 wires are tilted to the azimuthal direction by ± 6 degrees from the anode plane to determine 3 dimensional track of particle hits. To eliminate the left-right ambiguity of the particle hit, 3 kinds of supporting wires are stretched. The single wire resolution of 165 μm is achieved and hence the spacial resolution in the beam axis direction is $\sim$2 mm. The track-finding efficiency of better than 99 % is obtained.

A.4.2 Pad chambers (PC1, PC2 and PC3)

Three layers of pad chambers are constructed in the west central arm, which are named PC1, PC2 and PC3 from inner layer, while two layers except for PC2 are installed in the east arm. PC1 is located at 2.5 m from the collision point and just behind DC and in front of RICH, and PC2 is at 4.2 m behind RICH, and PC3 is at 4.9 m in front of EMCal. The signals are read out via the cathode plane which is segmented into pad shape and provide 3 dimensional position. Therefore, unlike the case of 2 dimensional strip readout, the pad chambers can provide 3 dimensional position without ambiguity when multiple clusters are found. The important role of PC1 is to disentangle the multiple hits in DC, which cannot separate more than two hits along the beam axis because the readout anode wires are oriented parallel to the beam axis. PC2 and PC3 define the particle position at the entrance and the exit of the detectors for the particle identification like RICH and EMCal. For these reasons, low occupancy of individual channels and high detection efficiency are required.

Basic parameters of the pad chambers are listed in Table A.1. Each layer of the pad chambers is divided into sectors. PC1 has 8 sectors each for west and east arms and they are arranged along the azimuthal direction. In PC2 and PC3, the segmentation along the azimuthal direction is rougher than PC1, while they are divided at the median plane of the

Parameter	PC1	PC2	PC3
Number of sectors	16	8	16
Sector size $L \times W \times H$ (cm^3)	$198 \times 50 \times 6.0$	$151 \times 157 \times 7.2$	$177 \times 185 \times 9.0$
Anode wire pitch (mm)	8.4	13.6	16.0
Cathode cell pitch (mm)	8.45	14.2	16.7
Radiation length (%)	1.2	2.38	2.37
Position resolution (mm)	1.7	2.7	3.2

Table A.1: The design parameters of the pad chambers. L, W and H is the length along the beam axis, azimuthal direction and radial direction, respectively. The position resolutions are the values in the direction along the anode wires. The resolution was measured using cosmic rays for PC1 and PC2, while that for PC3 was evaluated by the simulation. The requirement for the radiation length is severer for the most inner PC1 than PC2 and PC3.

arm (z=0) because of their large size. The orientation of the anode wires is parallel to the beam axis in all chambers. It should be noted that minimal radiation thickness is desirable in particular for PC1 to minimize the photon conversion into electron positron pair because converted electrons generate background hits in RICH, which is the main detector for the electron identification. Meanwhile, the requirement for PC2 and PC3 is less crucial.

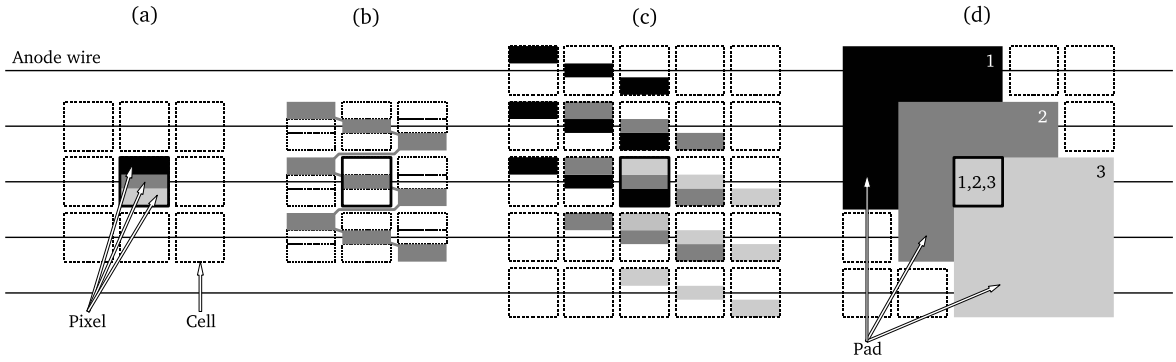

Figure A.2: The schematic diagram of the pad chambers. (a) Each cell is divided into 3 pixels. (b) 9 pixels are electrically connected to form one pad. (c) Pixels are connected to provide pads shifted each other. (d) The layers of the pads are virtually produced. The signals from three overlapped pads identify the hit in the corresponding cell.

The geometry of the cathode segments is designed specially to reduce the number of readout channels from a point of economical view, keeping the resolution, instead of simply producing the chamber with cathode segmented into "cell" whose size is defined to satisfy the position resolution. The principle of the pad geometry is displayed in Figure A.2. One cell is divided into 3 "pixel"s and then 9 pixels from neighboring 3-by-3 cells are electrically connected to make 1 "pad" layer, which is the unit to read out signals. The size of the center pixel in the cell, which is nearest to the anode wire, is smaller than two adjacent pixels to make induced charge on each pixel comparable. When a particle goes through a certain cell, the signals from corresponding three pads should be read out. The relationship between the

cell and three pads to respond is unique, and hence the cell on the particle path can be determined explicitly. This geometrical design saves the number of channels by a factor 3 because 1 cell is divided into 3 pixels and meanwhile 9 pixels are connected to be 1 pad. Moreover, the decision of the particle hit is less affected from electrical noise by requiring the coincidence of three pads. On the other hand, a disadvantage is poorer ability to separate double hits in near pads.

The performance of the pad chambers is evaluated during real data taking and test experiment using cosmic ray. The efficiency of more than 99.5 % is achieved for all layers. The obtained position resolution along the orientation of the anode wires (the beam axis) is summarized in Table A.1, where the resolution is better than that expected from single cell size because a large fraction of events have multiple hits in adjacent cells along the anode wire. On the other hand, the position resolution perpendicular to the anode wire is most likely the cell size divided by $\sqrt{12}$.

A.4.3 Ring image Cherenkov counter (RICH)

Ring image Cherenkov counter (RICH) is installed in both PHENIX central arms, and located between PC1 and PC2 (PC3) in west (east) arm. They occupy the region of 2.6 – 4.1 m from the beam axis and cover the acceptance of the central arm, 0.7 in pseudorapidity and 90 degrees in azimuthal angle. The role of RICH is the identification of electrons and it is required to limit the false identification of hadrons to less than 10^{-4} below the Cherenkov threshold for pions. The radiation thickness is a great concern of RICH because the major background source in RICH is electron pairs from the photon conversion and the pad chambers and EMCal behind RICH are also affected. Finally the radiation length of 2.5 % is achieved with the following condition. Aluminized Kapton with thickness of 125 μm is selected for the entrance and exit window. The spherical mirror in each RICH to reflect Cherenkov light is divided into halves at the plane of z=0 and each mirror is focused on the RICH's side near the mirror. Therefore, PMT arrays to detect reflected Cherenkov light are located on both side of RICH. The array on each side is comprised of 1280 PMTs; 16 along the beam axis and 80 along the azimuthal angle. RICH employs 25 mm-diameter PMTs with UV glass window and each of PMTs is attached to a 50 mm-diameter Winston cone. The coverage of each PMT is approximately 0.02×0.02 in the area of pseudorapidity and azimuthal angle. As the Cherenkov radiator, CO_2 is filled at a pressure of 1.3 cm of water in addition to the atmospheric pressure and provides the Cherenkov threshold of 4.65 GeV/c for pions. The thickness of the radiator gas varies from 87 cm to 150 cm depending on the path of the particle. A single charge particle with light velocity passing through 1.2m thick radiator gas generates 12 photons on an average and produces the ring with a diameter of 11.8 cm. The performance of RICH is evaluated with real data and the requirement in the electron identification is satisfied.

A.4.4 Muon tracker (MuTr)

The muon trackers (MuTr) perform the tracking and the momentum measurement of charged particles. Because the magnetic field is radial and therefore charged particles from the collision point are bent to azimuthal direction, the position resolution in the azimuthal direction is important to measure the momentum precisely. MuTr in each arm comprises three stations of tracking chambers. The stations are placed perpendicular to the beam axis and divided into octants each. In the farthest station, 2 layers of "gap"s are assembled, while other two stations have 3 gaps each. The gap is the plane of the chamber, which consists of

1 anode-wire plane between 2 cathode-strip planes and measures one-dimensional position of the track by cathode-strip readout. The anode wires are oriented to the azimuthal direction with an interval of 1 cm. While, depending on the gap, the orientations of the cathode strips are perpendicular to the anode wires or tilted within ± 11.25 degrees with respect to the perpendicular strips. By combining gaps in one station, two-dimensional position is determined on the plane of the station. The width of the cathode strips is 5 mm and alternate strips are read out to avoid cross talk. The position resolution is evaluated using cosmic ray to be 130 μm for the azimuthal direction, which is translated into the momentum resolution of $\Delta p/p = 3$ – 5 % for muons with a momentum of 2 – 10 GeV/c.

A.4.5 Muon identifier (MuID)

Muon identifiers (MuID) are constructed behind both north and south MuTr. The mechanical structure of MuID is same in both arms and each consists of 5-layer chambers interleaved by steel absorbers. The concept of MuID is to identify charged particles which survive a hadron absorber of enough thickness to be muons. The coverage on the perpendicular plane to the beam axis is 13 m wide and 10 m high. The distance from the collision point is 7 m at the nearest chamber plane and the depth up to the farthest chamber is about 2 m. The role of the hadron absorber is played by the steel backplate of the magnet with thickness of 20 (30) cm for the south (north) arm and 60 cm-thick steel for all layers in each MuID. The absorbers correspond to 4.8 (5.4) interaction lengths for the south (north) arm.

In addition to the hadron rejection factor of $\sim$100 provided by the material between the collision point and the muon tracker, roughly the factor of 30 is obtained by the absorber of MuID. In terms of muons, the momentum of 2.5 (2.7) GeV/c is needed to penetrate the south (north) muon arm. As the chambers, Iarocci-type tubes [107] are adopted. The spatial acceptance for single electrical channel of the chamber corresponds to a width of 8.4 cm by reading out multiple neighboring anode-wires into single channel. Since both horizontal and vertical tubes are assembled in one layer, the layer has capability to determine the position of the track in a segmentation of 8.4 cm $\times$ 8.4 cm. The detection efficiency of $\sim$97 % for muons and the drift time of 60 nsec are obtained by the test experiment. The drift time is enough faster than the bunch interval of the RHIC beam and MuID is used as one of the triggers in PHENIX.

A.4.6 Other detectors

There are other detectors installed in the central arms. They include ToF [90] for the particle identification and TEC [108] for the tracking of the charged particles.

A.5 The uncertainty of the relative luminosity

In this thesis, the number of BBCLL1 is used for the relative luminosity (R) and that of ZDCLL1 is utilized for the reference of BBCLL1. The uncertainty of R is evaluated by looking at the beam crossing dependence of the ratio of BBCLL1 and ZDCLL1 (C). The relation between C and R is described in this section. The calculation is performed applying the approximation based on several assumption. The number of BBCLL1 or ZDCLL1 is described as follows.

$$n_i \equiv \bar{n}(1+\epsilon_i), \qquad \sum_i \epsilon_i = 0, \tag{A.29}$$

$$\Delta n_i = \bar{n}\Delta\epsilon_i \equiv \bar{n}\Delta\bar{\epsilon}(1+\delta_i), \qquad \sum_i \delta_i = 0, \tag{A.30}$$

where subscript i denotes the crossing number, $\bar{n}$ and $\Delta\bar{\epsilon}$ is the average of n_i and $\Delta\epsilon_i$, respectively. Therefore the sum of ϵ_i or δ_i is 0. The calculation is on the assumptions of $\epsilon_i \ll 1$ and $\delta_i \ll 1$, and the terms of more than the second order of them are ignored. R is defined as

$$R = \frac{\sum_{i=\text{like-helicity crossings}} n_i^A}{\sum_{i=\text{unlike-helicity crossings}} n_i^A}, \tag{A.31}$$

where the summation is performed over either like- or unlike-helicity crossings. The superscript A indicates the trigger name; A for BBCLL1 and B for ZDCLL1. The error of R is calculated as below.

$$\begin{aligned}
\left(\frac{\Delta R}{R}\right)^2 &= \left(\frac{\Delta\left(\sum_{++} n_i^A\right)}{\sum_{++} n_i^A}\right)^2 + \left(\frac{\Delta\left(\sum_{+-} n_i^A\right)}{\sum_{+-} n_i^A}\right)^2 \\
&= \frac{(\Delta\bar{\epsilon}^A)^2 \sum_{++}(1+\delta_i^A)^2}{(N_{++}+\sum_{++}\epsilon_i^A)^2} + \frac{(\Delta\bar{\epsilon}^B)^2 \sum_{+-}(1+\delta_i^A)^2}{(N_{+-}+\sum_{+-}\epsilon_i^A)^2} \\
&\sim \frac{(\Delta\epsilon^A)^2}{N_{++}}\left(1+\frac{2}{N_{++}}\sum_{++}\delta_i^A\right)\left(1-\frac{2}{N_{++}}\sum_{++}\epsilon_i^A\right) + \\
&\quad \frac{(\Delta\epsilon^A)^2}{N_{+-}}\left(1+\frac{2}{N_{+-}}\sum_{+-}\delta_i^A\right)\left(1-\frac{2}{N_{+-}}\sum_{+-}\epsilon_i^A\right) \\
&\sim \frac{2(\Delta\epsilon^A)^2}{N}(1-\alpha)\left(1+\frac{4}{N}\sum_{++}\delta_i^A\right)\left(1-\frac{4}{N}\sum_{++}\epsilon_i^A\right) + \\
&\quad \frac{2(\Delta\epsilon^A)^2}{N}(1+\alpha)\left(1+\frac{4}{N}\sum_{+-}\delta_i^A\right)\left(1-\frac{4}{N}\sum_{+-}\epsilon_i^A\right) \\
&\sim \frac{4(\Delta\epsilon^A)^2}{N}\left(1+\frac{2}{N}\sum\delta_i^A - \frac{2}{N}\sum\epsilon_i^A\right) \\
&= \frac{4(\Delta\epsilon^A)^2}{N}.
\end{aligned} \tag{A.32}$$

The summations for like- and unlike-helicity crossings are abbreviated as $\sum_{++}$ and $\sum_{+-}$, respectively. Another summation without subscript means the sum over all crossings. N is the number of crossings and the subscript denotes the beam helicity state as before; N_{++} for the like-helicity, N_{+-} for the unlike-helicity and N for the total ($N = N_{++} + N_{+-}$). At the step of the third to forth formula, $\alpha = \frac{N_{++}-N_{+-}}{N}$ is introduced and $\alpha \ll 1$ is assumed. Finally the first terms of ϵ, δ and α become 0.

Similarly, the ratio of BBCLL1 and ZDCLL1 is approximated and simplified. The crossing-by-crossing ratio is described as c_i and the average of c_i is C.

$$c_i = \frac{n_i^B}{n_i^A}, \qquad \Delta c_i = \left(\frac{n_i^B}{n_i^A}\right)\sqrt{\left(\frac{\Delta n_i^A}{n_i^A}\right)^2 + \left(\frac{\Delta n_i^B}{n_i^B}\right)^2} \tag{A.33}$$

$$C = \frac{\sum \frac{c_i}{(\Delta c_i)^2}}{\sum \frac{1}{(\Delta c_i)^2}}, \qquad \Delta C = \frac{1}{\sqrt{\sum \frac{1}{(\Delta c_i)^2}}} \tag{A.34}$$

The error of C is calculated as follows.

$$\begin{aligned}
\left(\frac{\Delta C}{C}\right)^2 &= \frac{\sum \frac{1}{(\Delta c_i)^2}}{\left(\sum \frac{c_i}{(\Delta c_i)^2}\right)^2} \\
&= \frac{\sum \left(\frac{n_i^A}{n_i^B}\right)^2 \left(\left(\frac{\Delta n_i^A}{n_i^A}\right)^2 + \left(\frac{\Delta n_i^B}{n_i^B}\right)^2\right)^{-1}}{\left[\sum \left(\frac{n_i^A}{n_i^B}\right) \left(\left(\frac{\Delta n_i^A}{n_i^A}\right)^2 + \left(\frac{\Delta n_i^B}{n_i^B}\right)^2\right)^{-1}\right]^2} \\
&\sim \frac{\left(\frac{\bar{n}^A}{\bar{n}^B}\right)^2 \frac{1}{(\Delta\bar{\epsilon}^A)^2+(\Delta\bar{\epsilon}^B)^2} \sum(1+O(\epsilon_i^A,\epsilon_i^B,\delta_i^A,\delta_i^B))}{\left[\left(\frac{\bar{n}^A}{\bar{n}^B}\right) \frac{1}{(\Delta\bar{\epsilon}^A)^2+(\Delta\bar{\epsilon}^B)^2} \sum(1+O(\epsilon_i^A,\epsilon_i^B,\delta_i^A,\delta_i^B))\right]^2} \\
&\sim \frac{(\Delta\bar{\epsilon}^A)^2+(\Delta\bar{\epsilon}^B)^2}{N}
\end{aligned} \tag{A.35}$$

After the simplification, The term $\sum(1+O(\epsilon_i,\delta_i))$ appears and the second order always becomes 0 due to the definition in Equation (A.29) and (A.30). By comparing Equation (A.32) and (A.35), the uncertainties of R and C are related as

$$\frac{\Delta R}{R} \sim \frac{2\Delta\bar{\epsilon}^A}{\sqrt{N}} \leq 2\sqrt{\frac{(\Delta\bar{\epsilon}^A)^2+(\Delta\bar{\epsilon}^B)^2}{N}} \sim \frac{2\Delta C}{C} \tag{A.36}$$

A.6 The error of the parameters on the bunch fitting

The bunch fitting is to fit the data to the function of i;

$$f_i = C[1+\epsilon_{LL}h_{Bi}h_{Yi}], \tag{A.37}$$

where h_{Bi} and h_{Yi} is the helicity of the blue and yellow beam for the i-th crossing. C and ϵ_{LL} are the fit parameters. The relationship between the error of C and ϵ_{LL} is discussed in this section.

Because $h_{Bi}h_{Yi}$ is $+1$ or -1, the bunch fitting can be divided into two constant fittings; one is for like-helicity crossings and the other is for unlike-helicity crossings. When the parameters of the constant fittings are described as r_+ for the crossings with $h_{Bi}h_{Yi}=+1$ and r_- for the crossings with $h_{Bi}h_{Yi}=-1$, the C and ϵ_{LL} are related to r_+ and r_- as $r_\pm = C[1\pm\epsilon_{LL}]$, in other words,

$$C = \frac{r_+ + r_-}{2}, \qquad \epsilon_{LL} = \frac{r_+ - r_-}{r_+ + r_-}. \tag{A.38}$$

Hence, the errors of both C and ϵ_{LL} can be also written by $r_\pm$ and their error. The error of C is

$$\Delta C = \frac{\sqrt{(\Delta r_+)^2+(\Delta r_-)^2}}{2}. \tag{A.39}$$

The error of ϵ_{LL} is

$$(\Delta\epsilon_{LL})^2 = \frac{4}{(r_+ + r_-)^4}\left[r_-^2(\Delta r_+)^2 + r_+^2(\Delta r_-)^2\right]$$

$$
\begin{aligned}
&= \frac{1}{4C^4}\left[C^2(1-\epsilon_{LL})^2(\Delta r_+)^2 + C^2(1+\epsilon_{LL})^2(\Delta r_-)^2\right] \\
&= \left(\frac{\Delta C}{C}\right)^2\left[1-\epsilon_{LL}\frac{(\Delta r_+)^2-(\Delta r_-)^2}{2(\Delta C)^2}+(\epsilon_{LL})^2\right] \\
&\sim \left(\frac{\Delta C}{C}\right)^2. \qquad \text{(A.40)}
\end{aligned}
$$

$\epsilon_{LL} \sim 0$ is assumed at the last step.

A.7 Probability of the multiple collisions

To estimate the probability of the multiple collision, we suppose that the multiplicity of the collisions follows the Poisson distribution,

$$P(r) = \frac{e^{-\mu}\mu^r}{r!}, \qquad \text{(A.41)}$$

where μ is the mean of the distribution. The probability of the multiple collision is written as

$$P(r>1) = 1 - P(0) - P(1) = 1 - (1+\mu)e^{-\mu}. \qquad \text{(A.42)}$$

The probability of the collisions obtained with the detector which is insensitive to the multiple collision, such as BBC, is $P(r>0) = 1-e^{-\mu}$. Hence $P(r>1)$ is rewritten using $P(r>0)$ as

$$P(r>1) = 1 - (1-\log(1-c))\,(1-c), \qquad \text{(A.43)}$$

where $c = P(r>0)$, which is 8.18 % in this thesis and $P(r>1) = 0.344$ % is obtained.

A.8 Optimization of the charged-particle veto cut

The cut value of the charged-particle veto cut is optimized to minimize the error of A_{LL}. As described in Section 3.6.1, the error of A_{LL} for pure π^0s is calculated based on Equation (3.23). Because the uncertainty of A_{LL} for a certain mass window is roughly written as $\frac{1}{\sqrt{N}}$, where N is the total yield in the window and the beam polarization is abbreviated, the error of π^0 A_{LL} for the yield after a certain PID (particle identification) cut is written as

$$\Delta A_{LL}^{\pi^0}(cut) = \left[\frac{1}{p^2 N_{cut}^{sig}} + \frac{(1-p)^2}{p^2 N_{cut}^{BG(side)}}\right]^{\frac{1}{2}}. \qquad \text{(A.44)}$$

The error from the π^0 purity is ignored in this equation. Instead of $BG(under)$, $BG(side)$ is used following the actual analysis procedure to calculate $A_{LL}^{\pi^0}$. In addition, N_{cut}^{sig} and $N_{cut}^{BG(side)}$ is rewritten as

$$N_{cut}^{sig} = \frac{1}{p}N_{cut}^{\pi^0} = \frac{\epsilon}{p}N_{org}^{\pi^0}, \qquad N_{cut}^{BG(side)} = \alpha N_{cut}^{BG(under)} = \frac{\alpha\epsilon(1-p)}{p}N_{org}^{\pi^0}, \qquad \text{(A.45)}$$

where the subscription org indicates the yield before the PID cut, α is the ratio between $N_{cut}^{BG(side)}$ and $N_{cut}^{BG(under)}$, and ϵ is the efficiency of π^0 by the PID cut. Using these relation, Equation (A.44) is rewritten as

$$\Delta A_{LL}^{\pi^0}(cut) = \sqrt{\frac{\alpha+1-p}{\alpha p\epsilon}}\frac{1}{\sqrt{N_{org}^{\pi^0}}}. \qquad \text{(A.46)}$$

The coefficient which consists of α, p and ϵ is named "error factor". As expected, high purity and high efficiency are preferred to reduce the uncertainty of A_{LL}. The parameters for the charged-particle veto cut is determined to minimize the error factor.

The charged-particle veto cut is performed to remove only charged hadrons keeping the electron-positron pairs from the conversion as described in Section 3.5.4. Therefore, the lower and higher threshold for the cut must be determined. In this analysis, the lower threshold is determined at first and then the higher threshold is optimized with the lower cut applied. The parameters for the optimization is extracted depending on the cluster energy as displayed in Figure 3.23. Figure A.3 displays the error factor for the clusters with a certain energy as a function of the lower (left figure) and higher (right figure) threshold of the cut. The optimized threshold is denoted by the blue point in the figures. The flat region in Figure A.3-right for the higher threshold indicates the unavailable threshold because it is below the lower threshold. Such analysis as displayed in these figures is performed for all energy region and the cluster energy dependence is parameterized.

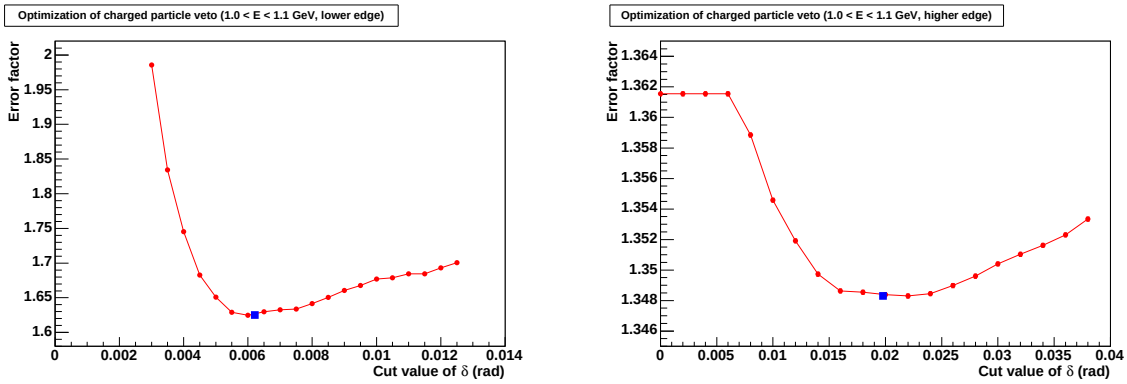

Figure A.3: The error factor as a function of the threshold of the charged-particle veto cut. The left is for the lower threshold and the right is for the higher threshold. The threshold for the minimum error factor is displayed as the blue point.

A.9 Run dependence of the ToF offset

Figure A.4 displays the EMCal sector-by-sector ToF offset as a function of the run number. The offset becomes shifted by ∼1 nsec at the latter period of the 2006 run.

A.10 Stability of the π^0 peak position and width

The run dependence of the π^0 peak position and width indicates the stability of EMCal. Figure A.5 and A.6 displays the peak position and the width as a function of the run number. The peak position is downside as the time goes. It indicates the shift of the EMCal energy gain. On the other hand, the peak width is stable during the 2006 run.

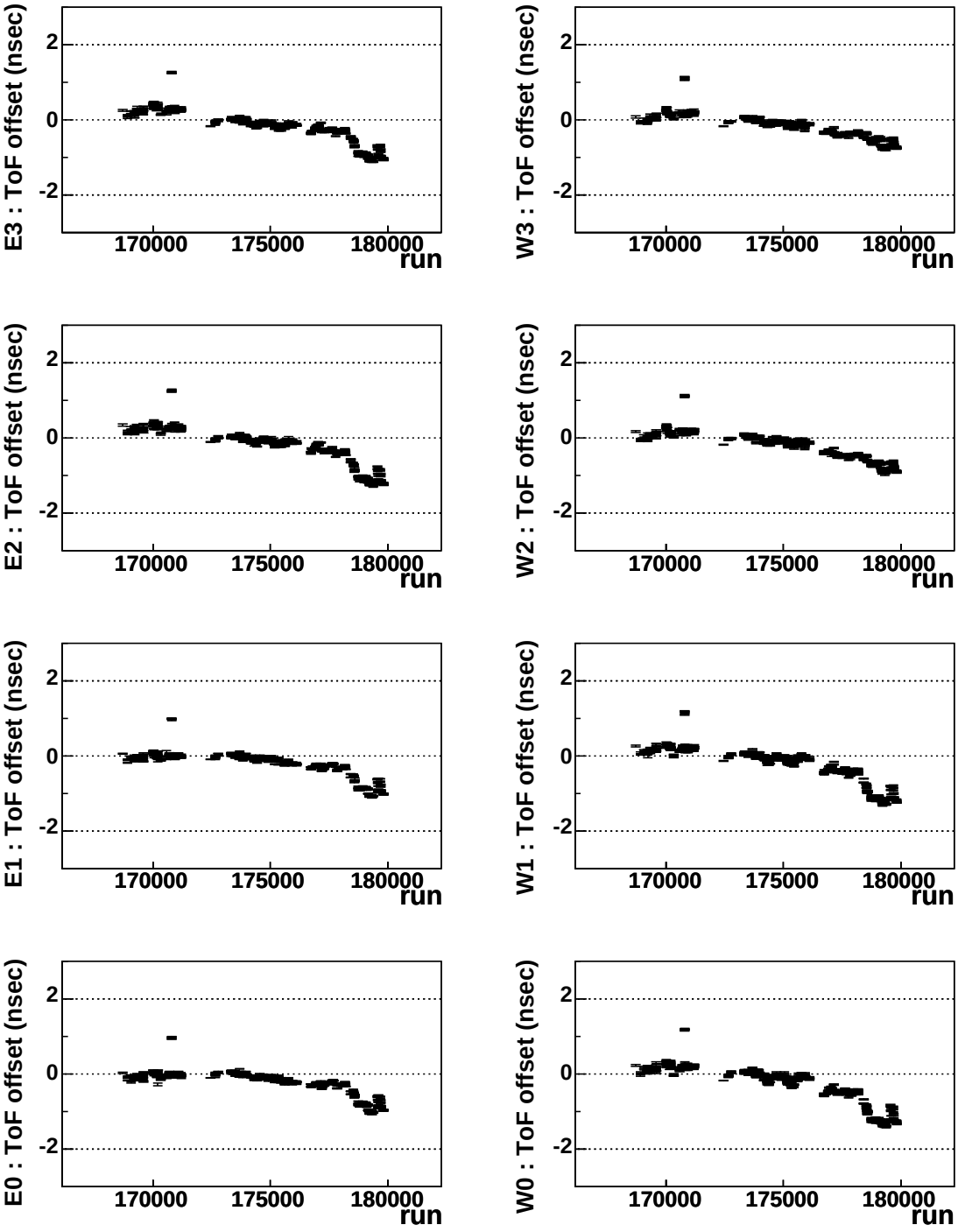

Figure A.4: The sector-by-sector ToF offset as a function of the run number.

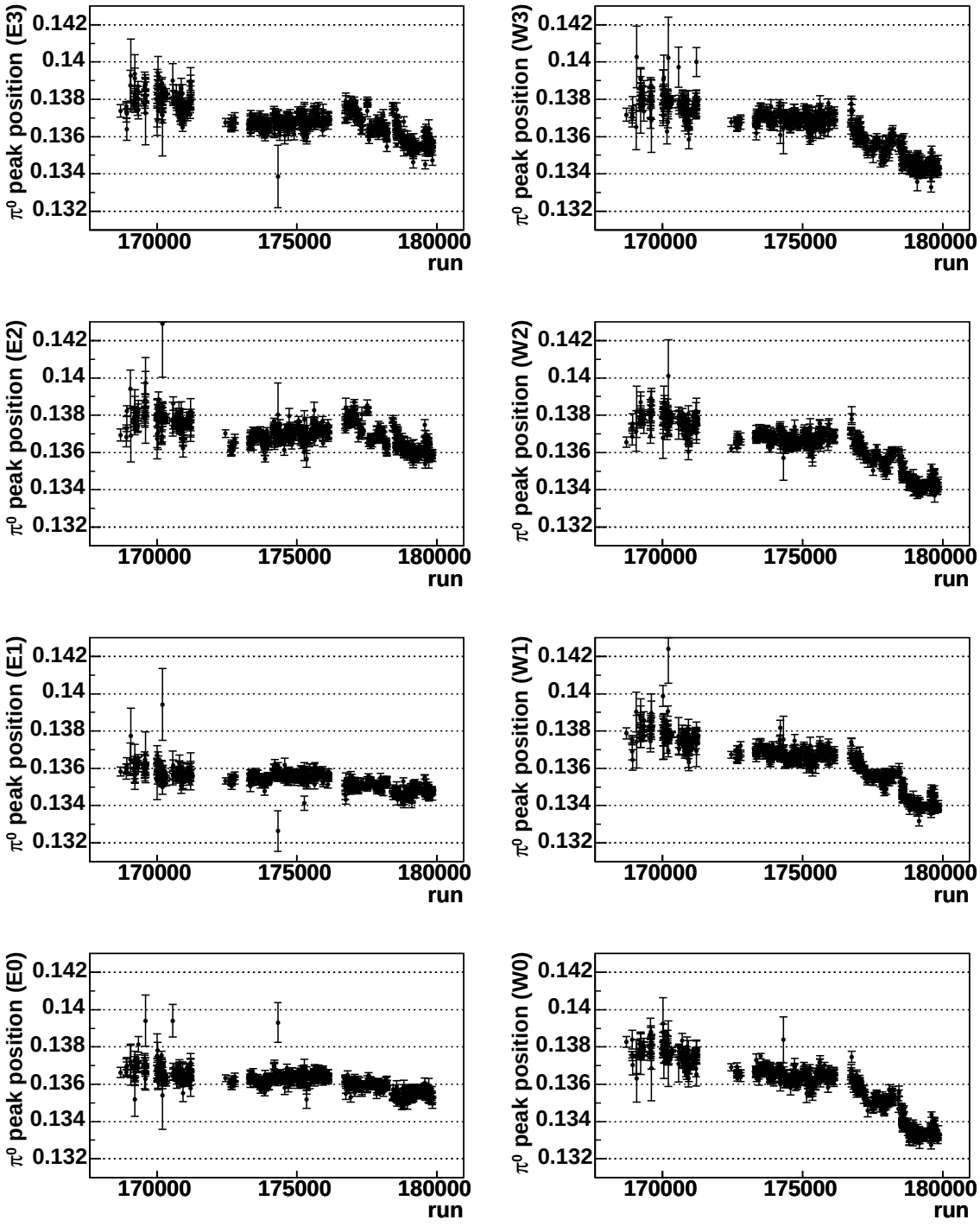

Figure A.5: The sector-by-sector position of the π^0 peak as a function of the run number before the energy calibration.

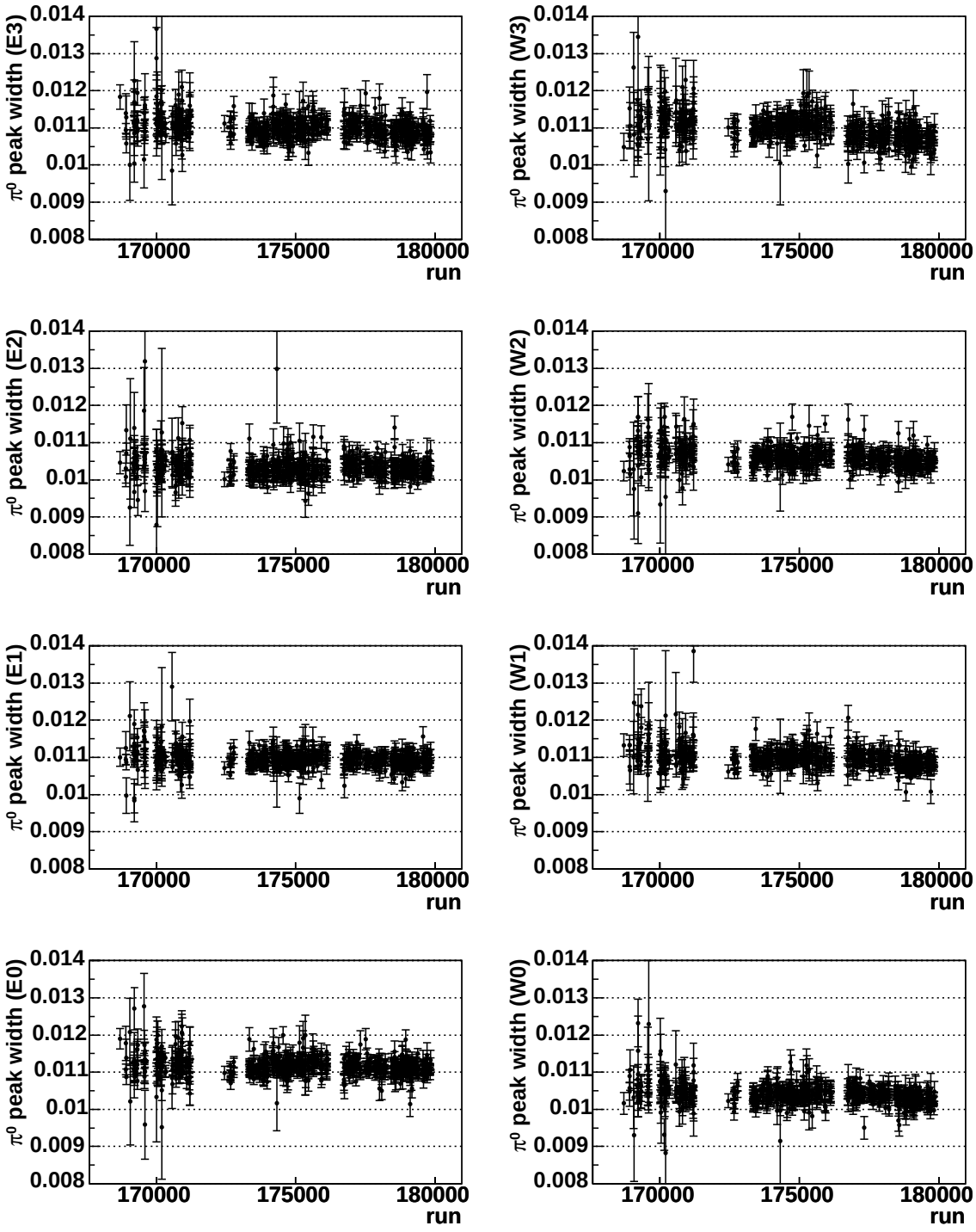

Figure A.6: The sector-by-sector width of the π^0 peak as a function of the run number before the energy calibration.

A.11 Comparison of the π^0 peak between the data and FastMC

The absolute energy scale of EMCal is determined by use of FastMC described in Section 3.5.6. The detail comparison between the data and FastMC is displayed in Figure A.7 and A.8. The non-linearity in the incident energy and the measured energy due to the tower-by-tower energy threshold is also evaluated by FastMC.

Figure A.7 displays the comparison without the correction of the energy non-linearity. The lower peak position in the lower p_T region is mainly because of this non-linearity since the percentage of the energy loss is larger in the lower energy clusters. The difference in the peak position between PbSc and PbGl is the result of the different clustering method. Because the cluster energy is calculated using only core towers in the cluster in PbSc, the towers with energy around the threshold are automatically removed in the energy measurement. Therefore, the p_T dependence of the peak position is more flat in PbSc than PbGl. See Section 3.5.2 about the clustering. The other source in the modification of the π^0 peak position is the shape of the p_T spectrum as described in Section 3.5.6. The difference between the ERT and MB sample is from the different shale.

The up trend of the π^0 peak width in the high p_T region is from the position resolution of EMCal. Two photons from the decay of π^0 with the higher momentum produce two clusters more closely on EMCal. Hence the resolution in the separation of two clusters becomes dominant in the mass resolution.

By the tuning of FastMC in Figure A.7, the fraction of the energy loss due to the energy non-linearity is obtained as a function of the cluster energy. The function and the parameters are described in Section 3.5.6. Figure A.8 displays the comparison between the data and FastMC after the correction of the energy non-linearity. FastMC reproduces the data well. The π^0 peak position becomes more flat than the case without the non-linearity correction. However, the peak position is still higher than the universal value of 0.135 GeV/c^2 due to the other effect from the p_T distribution.

A.12 Various crossing dependence

In this section, various crossing dependences are examined. They are on the rate of missing event, prescale of MB, efficiency of the event vertex cut and number of ERT. The crossing dependence over statistical fluctuation has possibility to affect the uncertainty of the asymmetries of π^0. However, such uncertainties are included in that evaluated by the bunch shuffle described in Section 3.7.8.

Contribution of the crossing dependences to the systematic uncertainty of asymmetries, A_{LL}, A_L and A_{TT}, is evaluated as follows. For example, if efficiency of the event vertex cut is not same between like-helicity and unlike-helicity crossings, it produces fake asymmetry in calculation of $A_{LL}^{\pi^0}$, where π^0s are counted with the vertex cut while GL1P scaler without the vertex cut are used for the relative luminosity.[2] Like this case, uncertainty of the crossing dependence can be translated into that of the relative luminosity. In the following discussion, the case of A_{LL} is taken for instance. The similar result is applicable for the case of A_L and A_{TT}.

We define the relationship between corrected luminosity (L), which should be used to calculate A_{LL} exactly, and uncorrected luminosity (L'), which is used in the actual calculation,

[2] If the efficiency of the event vertex cut is same in like- and unlike-helicity crossings, there is no problem because only ratio of the luminosity is used in the calculation of A_{LL}.

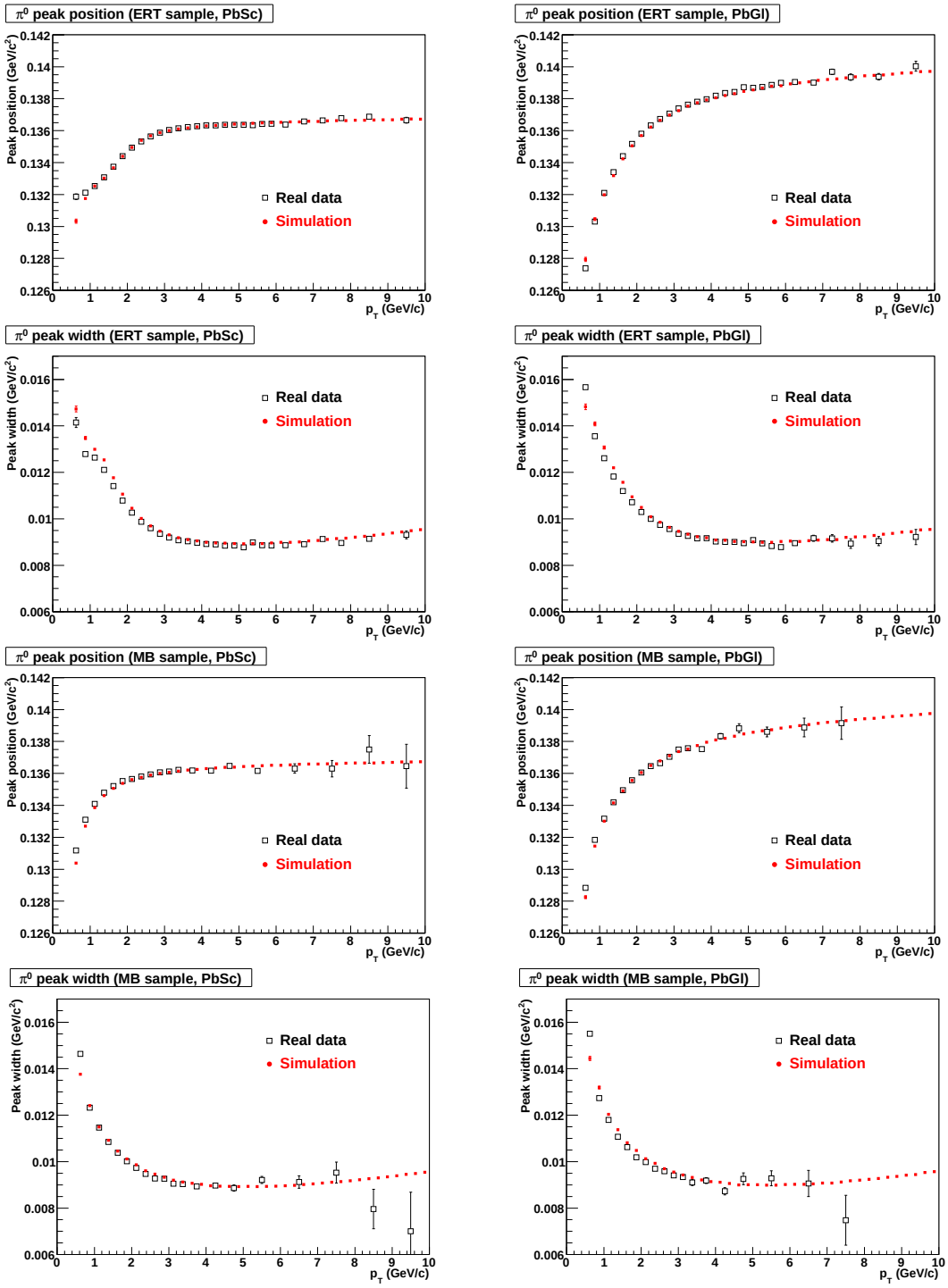

Figure A.7: The comparison between the data and FastMC before non-linearity correction. The top 4 plots is produced using the ERT data sample and the bottom 4 plots is for the MB data sample. The plots on the lest side is for PbSc and the right side is for PbGl. The first and the third rows show the π^0 peak position, and the second and the fourth rows show the π^0 peak width.

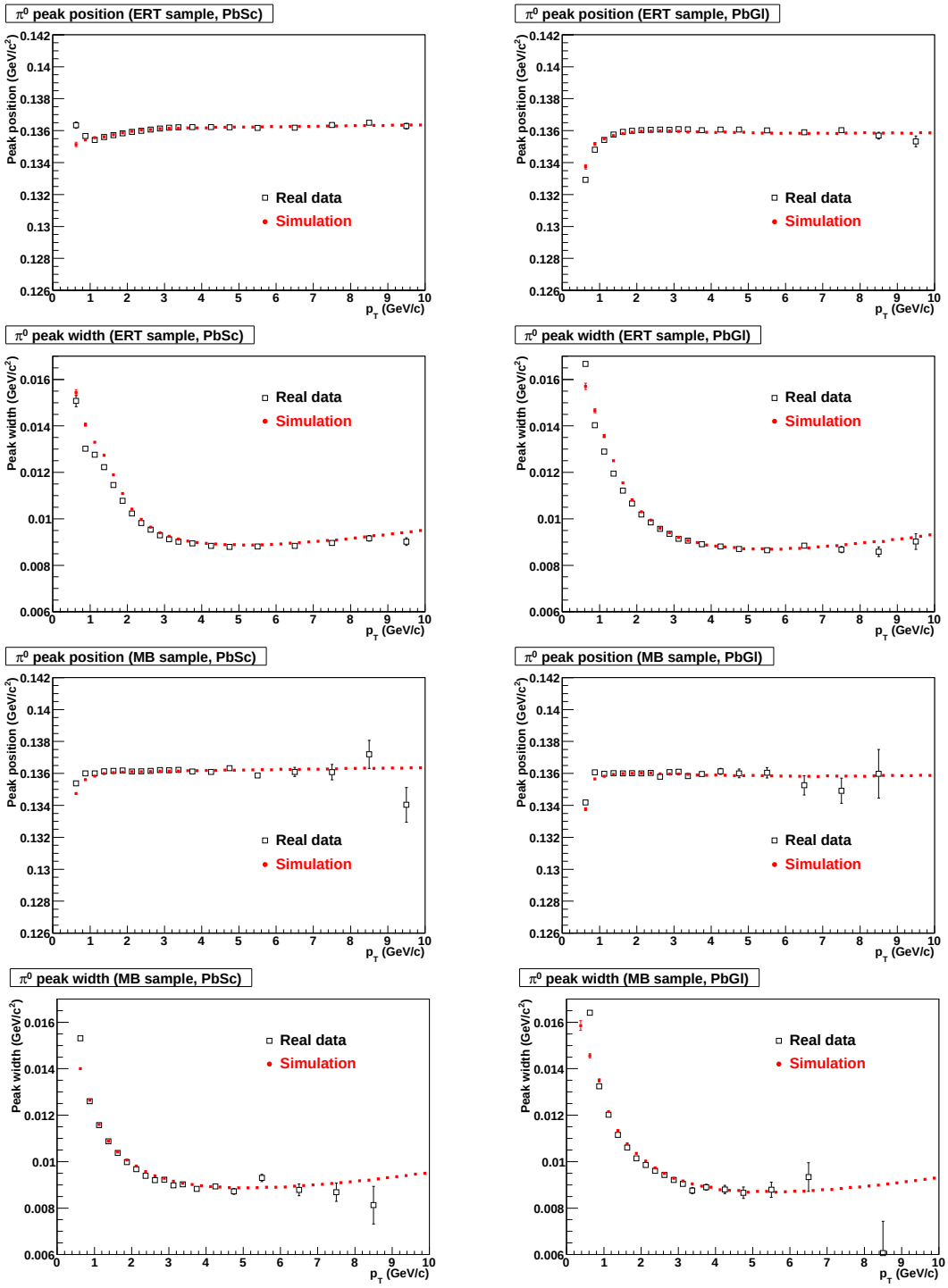

Figure A.8: The comparison between the data and FastMC after non-linearity correction. The top 4 plots is produced using the ERT data sample and the bottom 4 plots is for the MB data sample. The plots on the lest side is for PbSc and the right side is for PbGl. The first and the third rows show the π^0 peak position, and the second and the fourth rows show the π^0 peak width.

as follows.

$$L_{++} \equiv \beta_{++} L'_{++} \equiv r(1+a)L'_{++}, \qquad L_{+-} \equiv \beta_{+-} L'_{+-} \equiv r(1-a)L'_{+-}, \tag{A.47}$$

$$b = \frac{\beta_{++} + \beta_{+-}}{2}, \qquad a = \frac{\beta_{++} - \beta_{+-}}{\beta_{++} + \beta_{+-}}, \tag{A.48}$$

where $++$ and $+-$ at subscripts denote like- and unlike-helicity. β represents the difference between L and L', which is from the vertex cut efficiency for example. a and b are introduced for convenience. Therefore, the relation of the corrected relative luminosity (R) and uncorrected relative luminosity (R') is written as

$$\begin{aligned} R = \frac{L_{++}}{L_{+-}} = \frac{1+a}{1-a}\left(\frac{L'_{++}}{L'_{+-}}\right) = \frac{1+a}{1-a}R', \qquad R' \equiv \frac{L'_{+}}{L'_{-}}, \\ (\Delta R)^2 = R^2\left[\left(\frac{\Delta R'}{R'}\right)^2 + \left(\frac{2\Delta a}{1-a^2}\right)^2\right] \sim (\Delta R')^2 + (2\Delta a)^2, \end{aligned} \tag{A.49}$$

where we applied an approximation of $R \sim 1$, $R' \sim 1$ and $a \sim \Delta a \ll 1$ to obtain the second equation.

In terms of A_{LL}, the difference of R and R' introduces additional uncertainty.

$$\begin{aligned} A_{LL}^{corr} &= \frac{1}{P_B P_Y}\frac{N_{++} - N_{+-}R}{N_{++} + N_{+-}R} \\ &= \left(A_{LL}^{uncorr} - \frac{1}{P_B P_Y}\frac{2N_{+-}R'}{N_{++} + N_{+-}R'}\frac{a}{1-a}\right)\left(1 + \frac{2N_{+-}R'}{N_{++} + N_{+-}R'}\frac{a}{1-a}\right)^{-1} \\ &\sim A_{LL}^{uncorr} - \frac{1}{P_B P_Y}a, \end{aligned} \tag{A.50}$$

$$\Delta A_{LL}^{corr} \sim \frac{1}{2P_B P_Y}\Delta R \sim \sqrt{\left(\frac{1}{2P_B P_Y}\Delta R'\right)^2 + \left(\frac{1}{P_B P_Y}\Delta a\right)^2}, \tag{A.51}$$

where P_B and P_Y is the beam polarizations. N_{++} and N_{+-} indicate yield of π^0 by the collisions in like- and unlike-helicity crossings, respectively. A_{LL}^{uncorr} is A_{LL} calculated with the uncorrected relative luminosity, R' and is written as $A^{uncorr} = \frac{1}{P_B P_Y}\frac{N_{++} - N_{+-}R'}{N_{++} + N_{+-}R'}$. To obtain this results, we apply the approximation of $N_{++} \sim N_{+-}$, $R' \sim 1$ and $a \sim \Delta a \ll 1$. Therefore, it is found that size of the false asymmetry to the correct value, A_{LL}^{corr}, is $\frac{1}{P_B P_Y}a$ and contribution of Δa to ΔA_{LL}^{corr} is $\frac{1}{P_B P_Y}\Delta a$. In this thesis, R' is used in the calculation of A_{LL} as the relative luminosity. The uncertainty of the relative luminosity obtained in Section 3.4, which is $\sim 2 \times 10^{-4}$ for A_{LL} and A_L, and $\sim 1 \times 10^{-3}$ for A_{TT}, is for R'. Therefore, the additional uncertainty in Equation (A.50) and (A.51) need to be considered as the systematic uncertainty.

In this analysis, bunch fitting explained in Section 3.4 was applied to the crossing dependence of the various variables like Figure A.10. The fitting was performed fill by fill because such crossing dependences can be correlated between runs in the same fill. The effect of the systematic uncertainty is estimated following Equation (A.50) and (A.51) using a obtained by the fitting. In addition, chi-square of the fit is also useful to assess the existence of the systematic uncertainty.

A.12.1 GL1Pres and GL1Psum

GL1P scaler counts are used for the relative luminosity in the $A_{LL}^{\pi^0}$ calculation. As introduced in Section 2.3.5, the scaler counts are recorded event by event with two ways, which are named GL1Psum and GL1Pres. In the former way, the counts accumulated from the start of DAQ are recorded, while they are reset at each reading in the latter way. Ideally, these two types of scalers indicate identical counts by accumulating events. However, because a part of the events are discarded in the analysis code, they do not agree each other.

In this section, the crossing dependence of the ratio of GL1Pres/GL1Psum for BBCLL1 is examined. Figure A.9 displays recorded event number in a run. The dent period is due to the loss of the event during processing the data through the analysis code. Figure A.10 displays the crossing dependence of the ratio of GL1Pres/GL1Psum for the run and no crossing dependence is found by fitting the ratio to a constant and looking at the chi-square. In the actual analysis, bunch fitting explained in Section 3.4 is performed instead of the fitting to a constant. Figure A.11 and A.12 display reduced chi-square of the bunch fitting and the ratio of GL1Pres/GL1Psum as a function of fill number. There are fills with reduced chi-square far from unity. Meanwhile, the reduced chi-square in run-by-run analysis is nearer to unity as displayed in Figure A.13. Because the event loss should not correlate over runs, it is considered that the reason of the large chi-square is due to time dependence of the shape of the beam crossings. On the other hand, the chi-square is small for the fill or run with almost no lost events, where it is difficult to calculate the statistical error exactly.

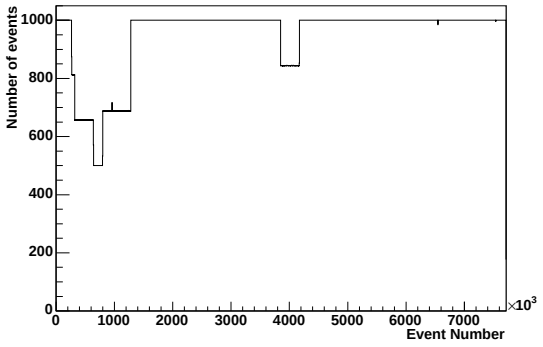

Figure A.9: Number of recorded events as a function of event number. One bin of the histogram consists of 1000 events.

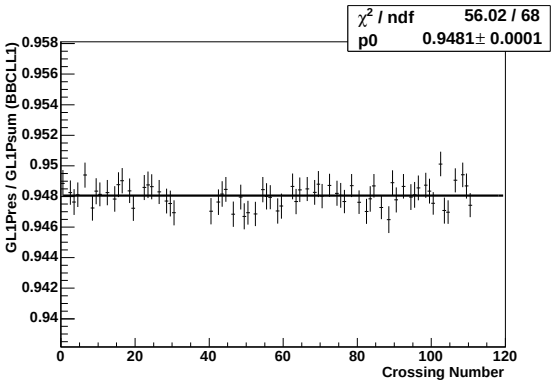

Figure A.10: Crossing dependence of GL1Pres/GL1Psum for a run. No crossing dependence is found in the run.

In the calculation of $A_{LL}^{\pi^0}$ in this thesis, GL1Pres scaler count of BBCLL1 is used for the relative luminosity. Since the number of π^0 is counted using same events as those for GL1Pres, there should be no systematic uncertainty in $A_{LL}^{\pi^0}$ from the discrepancy of GL1Pres and GL1Psum. However, considering a possible contribution to the $A_{LL}^{\pi^0}$ uncertainty, the systematic error is evaluated following Equation (A.49) and Equation (A.50). Figure A.14 displays double helicity asymmetry without normalization by the beam polarization (ϵ_{LL}) for the ratio of GL1Pres/GL1Psum. The asymmetry corresponds to a in Equation (A.48). Effect of large chi-square is corrected by enlarging the error bars of Figure A.10 to make the reduced chi-square unity. Average a is obtained by fitting Figure A.14 to a constant to be $(0.6 \pm 1.3) \times 10^{-7}$ with reasonable chi-square. The asymmetry is consistent with 0 within error and it is negligible compared with uncertainty of the relative luminosity.

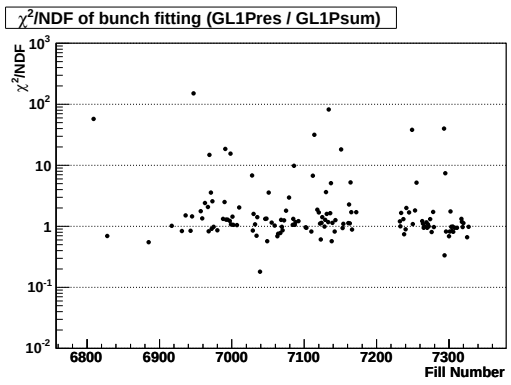

Figure A.11: Reduced chi-square of bunch fitting of GL1Pres/GL1Psum as a function of fill number.

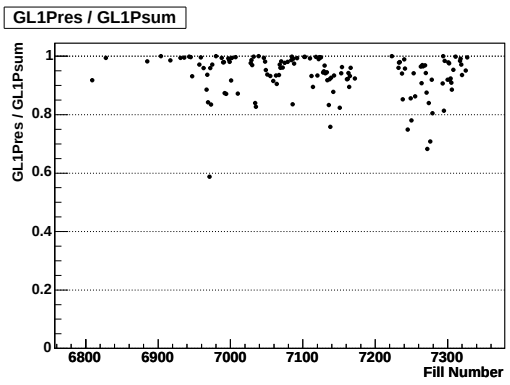

Figure A.12: Ratio of GL1Pres/GL1Psum as a function of fill number.

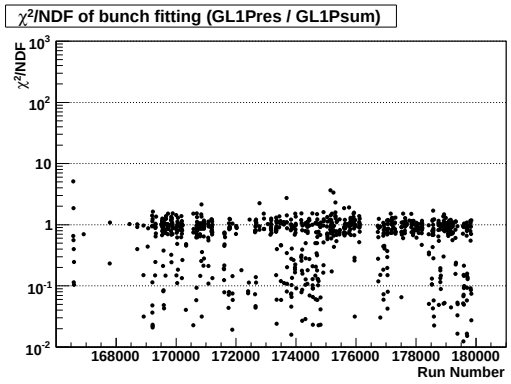

Figure A.13: Reduced chi-square of bunch fitting of GL1Pres/GL1Psum as a function of run number.

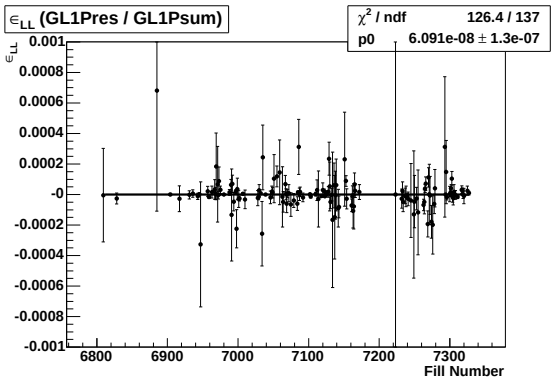

Figure A.14: Double helicity asymmetry of GL1Pres/GL1Psum without normalization of the beam polarization as a function of fill number. Correction due to large chi-square in the bunch fitting is applied.

A.12.2 Recorded MB and GL1P scaler count

In this section, the number of recorded MB (BBCLL1) events, which is prescaled from live MB events, and GL1P scaler count of MB are compared. See Section 2.3.5 about type of trigger and Section 2.3.5 about the scaler. For the scaler counts, GL1Pres is used for the comparison. The analysis is performed fill by fill, and therefore recorded BBCLL1 events are normalized by run-by-run prescale factor and summed up over runs in the same fill. Ratio of GL1P scaler to recorded MB ($\mathrm{GL1P/MB_{rec}}$) is calculated crossing by crossing and bunch fitting is applied as in the previous section.

Figure A.15 and A.16 display the reduced chi-square and the ratio of $\mathrm{GL1P/MB_{rec}}$ obtained by the bunch fitting. The ratio should be unity and it is true in most of the fills, while there are some fills with small ratio, where the chi-square is large up to ~ 9. In these earlier fills, statistics is also large since prescale factor of MB trigger is small during the period. Figure A.17 is the scatter plot of the reduced chi-square and the error of $\mathrm{GL1P/MB_{rec}}$. Moreover, when the analysis is performed run by run, the reduced chi-square is $\sim$4 at most, in which it is $\sim$9 in fill-by-fill analysis, and this indicates that the crossing dependence of $\mathrm{GL1P/MB_{rec}}$ is correlated over runs.

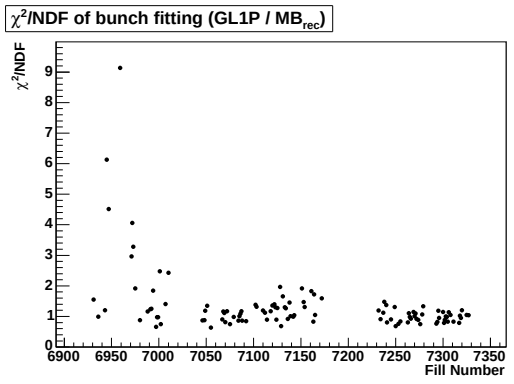

Figure A.15: Reduced chi-square of the bunch fitting of $\mathrm{GL1P/MB_{rec}}$ as a function of fill number.

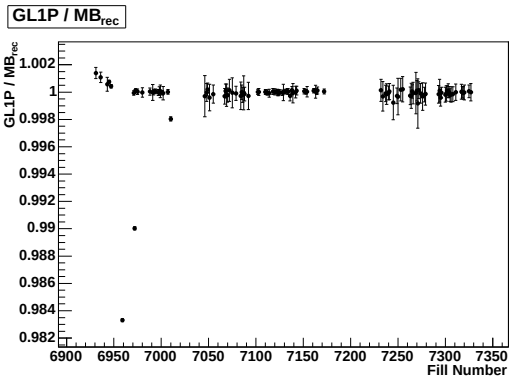

Figure A.16: Ratio of $\mathrm{GL1P/MB_{rec}}$ as a function of fill number.

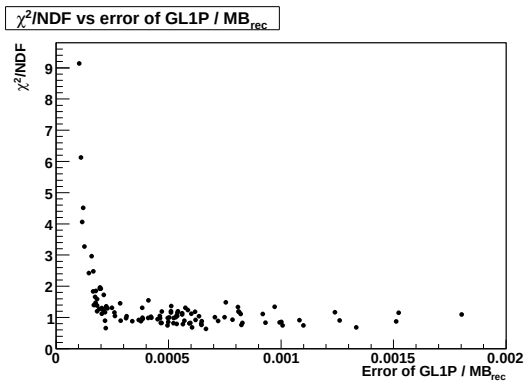

Figure A.17: Scatter plot of the reduced chi-square and the error of the ratio of $\mathrm{GL1P/MB_{rec}}$ by the bunch fitting.

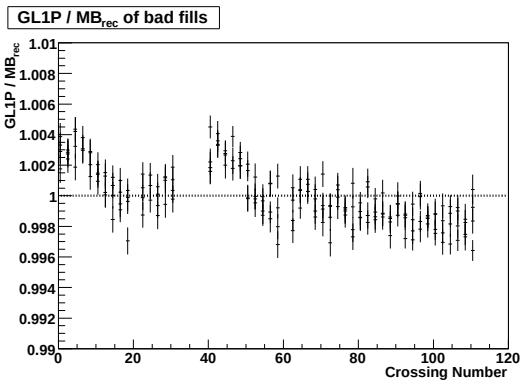

Figure A.18: Ratio of $\mathrm{GL1P/MB_{rec}}$ as a function of crossing number. 5 plots for bad fills are superposed.

In addition, it is observed that the crossing dependence is correlated over early bad fills. Figure A.18 displays GL1P/$\mathrm{MB_{rec}}$ as a function of crossing number. In Figure A.18, 5 plots for the fills in which the reduced chi-square of bunch fitting is larger than 3 are superposed after normalization. These fills have similar crossing dependence; the ratio is larger than other crossings in the crossings after empty crossings. This tendency is seen in only earlier fills and the crossing dependence is well randomized in other fills. Figure A.19 displays GL1P/$\mathrm{MB_{rec}}$ as a function of crossing number after summing up counts in all fills. The fit of Figure A.19 to a constant provides reduced chi-square of 180/99.

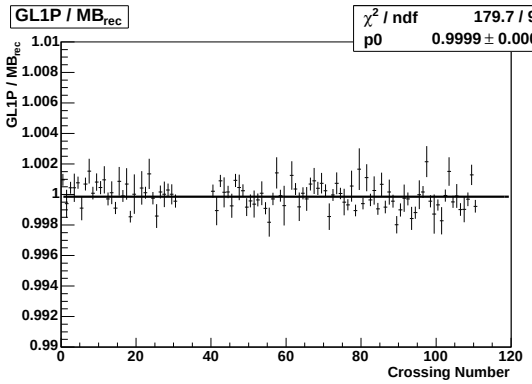

Figure A.19: Crossing dependence of GL1P/$\mathrm{MB_{rec}}$ after summing up all fills.

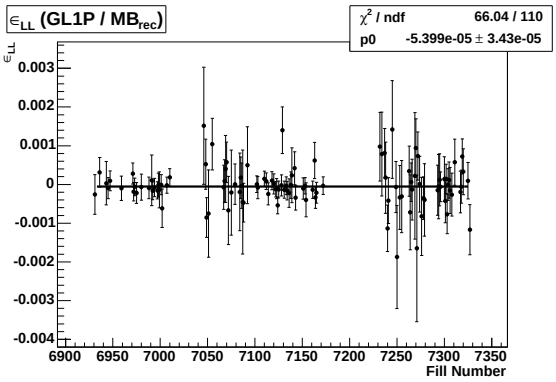

Figure A.20: Double helicity asymmetry of GL1P/$\mathrm{MB_{rec}}$ without normalization by the beam polarization as a function of fill number. Correction due to large chi-square in the bunch fitting is applied.

Though reason of the crossing dependence in early fills is unknown, the contribution from the systematic uncertainty to $A_{LL}^{\pi^0}$ is evaluated using Equation (A.49) and Equation (A.50). Figure A.20 displays double helicity asymmetry without normalization by the beam polarization (ϵ_{LL}) for GL1P/$\mathrm{MB_{rec}}$. The correction due to large chi-square of bunch fitting is applied for the asymmetry. The asymmetry a in The asymmetry a in Equation (A.48) is obtained by fitting Figure A.20 to a constant to be $(-5.4 \pm 3.4) \times 10^{-5}$, whose effect is smaller than uncertainty of the relative luminosity.

A.12.3 Event vertex cut

In this section, crossing dependence of efficiency of the event vertex cut in offline analysis is studied. As described in Section 2.3.5, we selected event vertex within a range of -30 cm to $+30$ cm from the collision point. The vertex cut efficiency depends on the vertex distribution of corresponding crossing, and therefore crossing to crossing variation of the efficiency is possible depending on the operation of RHIC. The ratio of the number of MB events with vertex cut to that without vertex cut ($\mathrm{MB_{cut}}/\mathrm{MB_{no\ cut}}$) is calculated for each crossings and bunch fitting is performed fill by fill. Since the vertex distribution is correlated over runs in same fill, the analysis must be carried out fill by fill. MB events are used for the analysis instead of ERT events because the vertex cut efficiency was difference between even and odd crossing as described later.

Figure A.21 and A.22 display the reduced chi-square and the value of $\mathrm{MB_{cut}}/\mathrm{MB_{no\ cut}}$ by the bunch fitting as a function of fill number. Cliff around fill 6970 in Figure A.22 is

because the vertex cut parameters of BBCLL1 was changed online. Though the reduced chi-square is better in the latter period, it is just due to smaller statistics of MB events. Figure A.23 displays the relation of the reduced chi-square obtained by the bunch fitting and the statistical error of $\mathrm{MB_{cut}/MB_{no\ cut}}$. It is seen that the reduced chi-square becomes worse in small statistical error in Figure A.23. After the correction to make the reduced chi-square unity, the double helicity asymmetry without normalization by the beam polarization (ϵ_{LL}), which is a in Equation (A.48), is displayed in Figure A.24 as a function of fill number. Average of a is $(-3.0 \pm 2.3) \times 10^{-5}$ and it is enough smaller compared with the uncertainty of the relative luminosity, and therefore the systematic error from the vertex cut can be ignored in extracting $A_{LL}^{\pi^0}$.

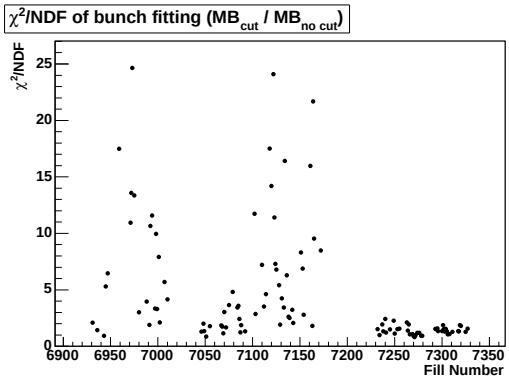

Figure A.21: Reduced chi-square of bunch fitting of the vertex cut efficiency as a function of fill number.

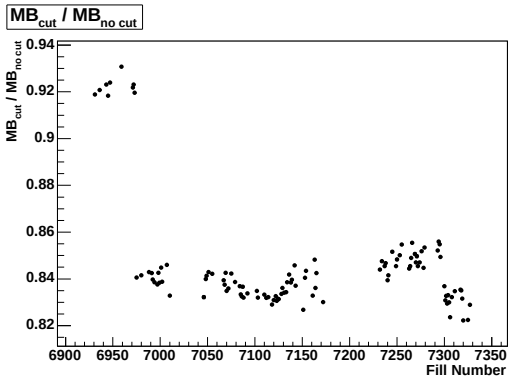

Figure A.22: $\mathrm{MB_{cut}/MB_{no\ cut}}$ as a function of fill number.

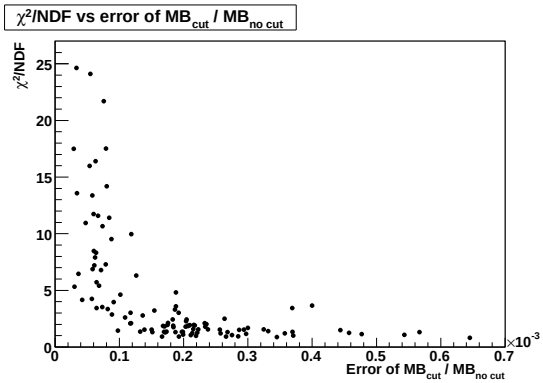

Figure A.23: Scatter plot of the reduced chi-square and the statistical error of the vertex cut efficiency.

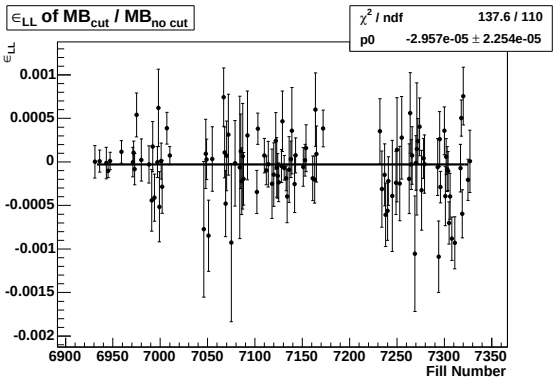

Figure A.24: Double helicity asymmetry of the vertex cut efficiency without normalization by the beam polarization after correction based on the chi-square.

As described above, the efficiency of the vertex cut for ERT events depends on whether the crossing is even or odd. Figure A.25 displays the ratio of events with the vertex cut to events without the cut as a function of the crossing number for a certain run as a sample of bad run. Red and blue points in Figure A.25 are corresponding to the ERT and MB events, respectively. Clearly two categories can be seen for the ERT events. It is also notable that

the vertex cut efficiency is lower in the MB events than the ERT events in any fills. Crossing distribution without the vertex cut for the run is displayed in Figure A.26. Red and blue histograms are for the ERT events and the MB events, respectively. Rejection power of ERT is obviously different between even and odd crossings because ERT has two alternative circuit for even and odd crossings as explained in Section 2.3.4.

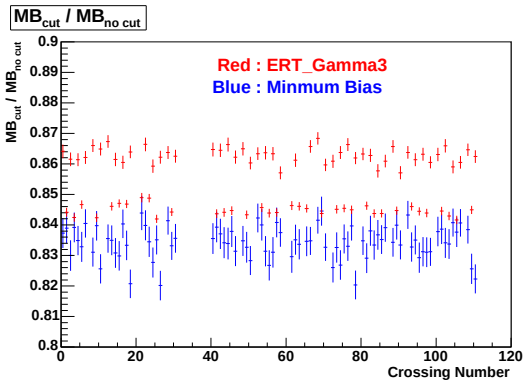

Figure A.25: The crossing dependence of the vertex cut efficiency for a certain run. Red points are for the ERT events and blue points are for the MB events.

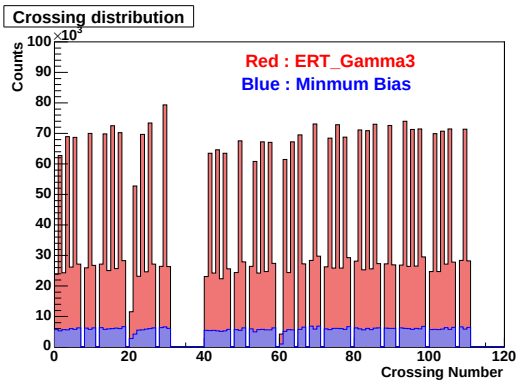

Figure A.26: Crossing distribution for the run corresponding to Figure A.25. Red histogram is for the ERT events and blue one is for the MB events.

The phenomenon of the different vertex-cut efficiency for ERT is understood by effective acceptance of EMCal due to the central magnet. ERT requires high energy photon and it can roughly come from the event vertex within ± 40 cm because photons from the outside are disturbed by the central magnet. In this reason, data of the ERT events have smaller tail in the event vertex distribution than that of MB events. Hence, the efficiency of the vertex cut for the ERT events is higher than MB events relatively. The difference between even and odd crossings in the ERT events can be also explained in the same way. Because of alternative circuits of ERT, the energy threshold is slightly different between even and odd crossings. In the crossings with lower threshold, performance of ERT is less effective than that in the other crossings and becomes closer to MB. That's why the efficiency of the vertex cut should be lower in the crossings for the ERT events with lower threshold than the other. In fact, as shown in Figure A.25 and A.26, the vertex cut efficiency is lower in the crossings with higher event rate, which is due to the lower threshold, and the efficiency is higher with lower event rate.

The contribution of the systematic uncertainty by the vertex cut for the ERT events is assumed to be same as the case of the MB events because variation of the vertex distribution is over the statistical fluctuation and the systematic error is dominant. a in Equation (A.48) for even and odd crossings for the ERT events are $(-0.9 \pm 3.1) \times 10^{-5}$ and $(-2.8 \pm 3.8) \times 10^{-5}$, and the average is $(-1.7 \pm 2.4) \times 10^{-5}$. Therefore, the systematic uncertainty by the vertex cut does not appear in the $A_{LL}^{\pi^0}$ results.

A.12.4 ERT and GL1P (A_{LL} of ERT)

In this section, crossing dependence of the ratio of the ERT events and BBCLL1 GL1P-scaler counts (ERT/GL1P) is studied. It is same as calculating double helicity asymmetry of ERT. As in the previous sections, ERT/GL1P is calculated crossing by crossing and bunch fitting

is performed for each fill. The analysis is carried out in even and odd crossings separately because of the specification of the ERT circuit described in Section 2.3.4.

Figure A.27 and A.28 display the reduced chi-square and ERT/GL1P obtained by bunch fitting as a function of fill number. Red and blue points correspond to the data of even and odd crossings, respectively, in both plots. Some reasons of the large chi-square are thought; for example, the vertex cut efficiency as described in Section A.12.3, the difference of scaler events and recorded events by DAQ as shown in section A.12.2, error of the scaler itself (it is same as error of the relative luminosity), noise of EMCal and so on. We don't discuss the reason in detail and just show the result of the asymmetry after chi-square correction. Figure A.29 and A.30 display double helicity asymmetry without normalization of the beam polarization for even and odd crossings, respectively. The crossing-by-crossing uncertainty of ERT/GL1P is enlarged to make the reduced chi-square of bunch fitting unity in the calculation of the asymmetry. The fit to a constant is applied for each plot and average over all fills is obtained to be $(-0.7 \pm 1.9) \times 10^{-4}$ for the even crossings and $(2.7 \pm 3.0) \times 10^{-4}$ for the odd crossings. Average of the even and odd crossings is $(0.3 \pm 1.6) \times 10^{-4}$.

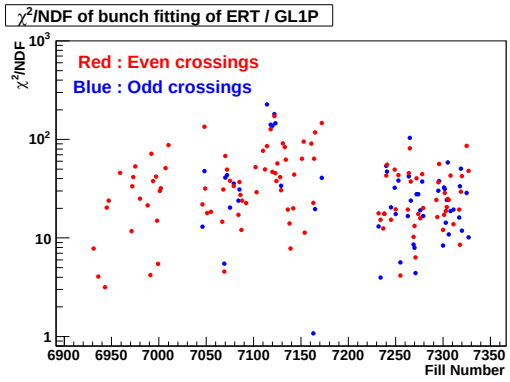

Figure A.27: Reduced chi-square of bunch fitting of ERT/GL1P as a function of fill number. Red points are for even crossings and blue for odd crossings.

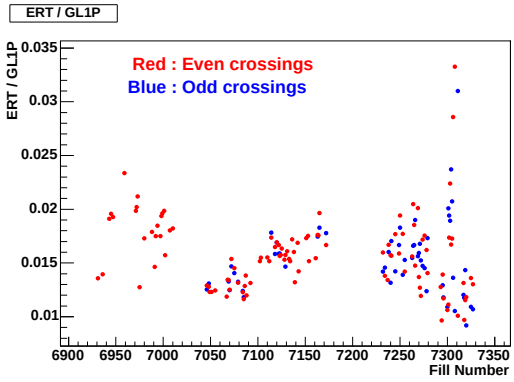

Figure A.28: ERT/GL1P as a function of fill number. Red points are for even crossings and blue for odd crossings.

Though the asymmetry is consistent with 0 within the error, size of the error is large compared to the uncertainty of the relative luminosity based on Equation (A.49). In terms of the uncertainty of $A_{LL}^{\pi^0}$, possible contribution from the crossing dependence of ERT/GL1P is 0.064 based on Equation (A.51) assuming beam polarization of 50% and it is comparable to the statistical uncertainty of $A_{LL}^{\pi^0}$ when events in all p_T bins are summed up. However, this estimation does not appear necessarily and, in fact, such large systematic uncertainty is not seen in the bunch shuffle for the counts of π^0. This is explained by the reason that π^0 candidates are collected by applying various cuts for particle identification and selecting reasonable mass window unlike just collecting triggered events.

A.13 Residual asymmetry in the bunch shuffle

When a finite asymmetry is observed, it affects an accuracy of the bunch shuffle described in Section 3.7.8. In this section, the estimation of the residual asymmetry in the bunch shuffle

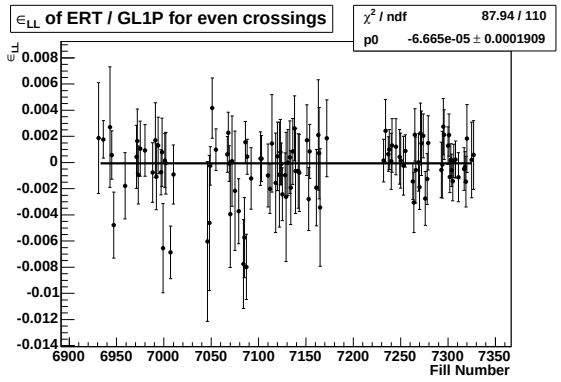

Figure A.29: Double helicity asymmetry without normalization of the beam polarization for even crossings. Correction based on the chi-square is applied.

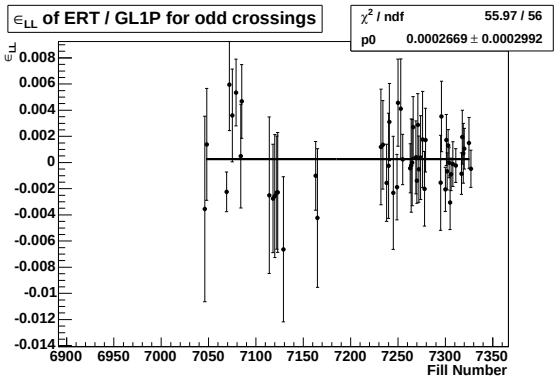

Figure A.30: Double helicity asymmetry without normalization of the beam polarization for odd crossings. Correction based on the chi-square is applied.

is described. The asymmetry after the bunch shuffle ($A^{shuffle}$) is calculated as follows.

$$\begin{aligned} A^{shuffle} &= \frac{\frac{N_+^+ + N_-^+}{L_+^+ + L_-^+} - \frac{N_+^- + N_-^-}{L_+^- + L_-^-}}{\frac{N_+^+ + N_-^+}{L_+^+ + L_-^+} + \frac{N_+^- + N_-^-}{L_+^- + L_-^-}} \\ &= \frac{A\left(\frac{L_+^+ - L_-^+}{L_+^+ + L_-^+} - \frac{L_+^- - L_-^-}{L_+^- + L_-^-}\right)}{2 + A\left(\frac{L_+^+ - L_-^+}{L_+^+ + L_-^+} + \frac{L_+^- - L_-^-}{L_+^- + L_-^-}\right)} \\ &\sim \frac{1}{2}A\left(\frac{L_+^+ - L_-^+}{L_+^+ + L_-^+} - \frac{L_+^- - L_-^-}{L_+^- + L_-^-}\right) \\ &= A\frac{L_+^+ L_-^- - L_+^- L_-^+}{(L_+^+ + L_-^+)(L_+^- + L_-^-)} \\ &\equiv AB_{lum}, \end{aligned} \tag{A.52}$$

where N and L indicates the yield and the integrated luminosity. $+$ and $-$ at the subscript denote the actual helicity combination, where $+$ $(-)$ corresponds to the (un)like-sign helicities in the case of A_{LL}. Similarly, the superscript denotes the helicity combination after the shuffle. From the first to the second equation, a relation of $N_\pm^h = CL_\pm^h(1 \pm A)$ is utilized for $h = +or-$ in the same way as Equation (1.54). This means that the statistical fluctuation of the yield N is ignored in this equation. The polarization is abbreviated in this section. At the second to the third step, the approximation of $A \ll 1$ is applied B_{lum} is defined as the luminosity part of the 4th equation. Therefore, the residual asymmetry remains as far as the helicity dependent luminosities are unbalanced. In the analysis, B_{lum} can be calculated in the bunch shuffle and the fluctuation of B_{lum} is summarized as a width of the Gaussian distribution in Table A.2.

B_{lum} is estimated numerically as follows. With an attention that $L_+^+ + L_+^-$ and $L_-^+ + L_-^-$ are conserved respectively, they are approximated as

$$L_+^+ + L_+^- \sim L_-^+ + L_-^- \sim \frac{1}{2}L, \tag{A.53}$$

	Longitudinal Pol.			Transverse Pol.		
	MB	ERT(even)	ERT(odd)	MB	ERT(even)	ERT(odd)
B_{lum}	0.023	0.016	0.027	0.068	0.082	0.163
n	6489	5014	1642	244	199	45

Table A.2: B_{lum} and the number of all crossings (n).

where L is the total integrated luminosity; $L \equiv L_+^+ + L_+^- + L_-^+ + L_-^-$. B_{lum} is rewritten using this relation as

$$B_{lum} \sim \frac{\frac{1}{2}L(L_+^+ - L_-^+)}{L(L_+^+ + L_-^+) - (L_+^+ + L_-^+)^2}. \tag{A.54}$$

Obviously, since the mean values of L_+^+ and L_-^+ are identical ($= \frac{1}{4}L$) in the approximation of Equation (A.53), the mean value of B_{lum} is 0. To calculate the fluctuation of B_{lum} (ΔB_{lum}), B_{lum} is differentiated with respect to L_+^+, for example.

$$\begin{aligned} \frac{\partial B_{lum}}{\partial L_+^+} &= \frac{\frac{1}{2}L[L(L_+^+ + L_-^+) - (L_+^+ + L_-^+)^2] - \frac{1}{2}L(L_+^+ - L_-^+)[L - 2(L_+^+ + L_-^+)]}{[L(L_+^+ + L_-^+) - (L_+^+ + L_-^+)^2]^2} \\ &= \frac{2}{L} \quad \text{at} \quad L_+^+ = L_-^+ = \frac{1}{4}L. \end{aligned} \tag{A.55}$$

The differential with respect to L_-^+ lead to the same result. Finally ΔB_{lum} becomes as follows;

$$\Delta B_{lum} = \frac{2}{L}\sqrt{(\Delta L_+^+)^2 + (\Delta L_-^+)^2}. \tag{A.56}$$

Then, the fluctuation of L_+^+ and L_-^+ (ΔL_+^+ and ΔL_-^+) is estimated. The mean and fluctuation of L_+^+ can be described as;

$$\langle L_+^+ \rangle = \langle n_+^+ \rangle \langle l \rangle, \tag{A.57}$$

$$\begin{aligned} (\Delta L_+^+)^2 &= \langle l \rangle^2 (\Delta n_+^+)^2 + \langle n_+^+ \rangle^2 (\Delta \langle l \rangle)^2 \\ &= \langle l \rangle^2 (\Delta n_+^+)^2 + \langle n_+^+ \rangle (\Delta l)^2 \end{aligned} \tag{A.58}$$

where l is the integrated luminosity for each beam crossing and Δl corresponds to the crossing-to-crossing fluctuation of l. n_+^+ is the number of the crossings where both initial and shuffled helicity combination is like-sign. The mean value and the fluctuation of n_+^+, $\langle n_+^+ \rangle$ and Δn_+^+, follows the binomial distribution and are written as

$$\langle n_+^+ \rangle = \frac{1}{2}(n_+^+ + n_+^-) \sim \frac{1}{4}n \tag{A.59}$$

$$(\Delta n_+^+)^2 = (n_+^+ + n_+^-)\frac{1}{2}(1 - \frac{1}{2}) \sim \frac{1}{8}n, \tag{A.60}$$

where n is defined as $n = n_+^+ + n_+^- + n_-^+ + n_-^-$ and the approximation of $n_+^+ + n_+^- \sim \frac{1}{2}n$ is used. $frac12$ in this equation is the probability of whether the helicity combination is kept or not in the shuffle. Therefore, ΔL_+^+ becomes

$$\Delta L_+^+ = \frac{L^2}{8n}\left[1 + 2\left(\frac{\Delta l}{\langle l \rangle}\right)^2\right], \tag{A.61}$$

where the relation of the total luminosity L is equal to $n\langle l\rangle$. The same result is obtained for ΔL^{+}_{-}. Finally, ΔB_{lum} can be described as

$$\Delta B_{lum} \sim \sqrt{\frac{1}{n}\left[1+2\left(\frac{\Delta l}{\langle l\rangle}\right)^{2}.\right]} \tag{A.62}$$

Therefore, the residual asymmetry in the bunch shuffle becomes smaller at the larger number of the all crossings n. In addition, the crossing-to-crossing fluctuation of the integrated luminosity makes it large. n used in the analysis is listed in Table A.2.

A.14 Fill-merging A_{LL}

In our standard analysis, asymmetries are calculated fill by fill (fill-by-fill asymmetry) as described in Section 3.6.1. In this section, the asymmetries calculated with fills merged (fill-merging asymmetry) is discussed. This method is useful when the statistics in one fill is too small to evaluated the yield as the Poisson distribution such as in the higher p_T bins. The method described in this section is for A_{LL}. However, it is applicable to other asymmetries like A_L. When fills are merged, what should be considered is the fill dependence in the calculation. Particularly in this analysis, the background fraction under the π^0 peak fluctuates fill by fill due to a little noisy towers of EMCal, which are not masked in the analysis and slightly unstable during the data taking. This causes that the ratio of the background yields and the luminosity depends on the fill. This effect is evaluated in this section.

Let us start from the definition of variables used in this section and the basic relationship between them. N^i_+ (N^i_-) is defined as the yield in a certain mass window, such as the signal window and the background window, for the collisions with like-sign (unlike-sign) helicities. See Section 3.6.1 about the mass window for the asymmetry calculation. i at the superscript represents the fill number. Similarly, the integrated luminosity in i-th fill is defined as L^i_+ and L^i_-. The relationship between N and L can be described as

$$N^i_{\pm} = L^i_{\pm}\epsilon^i(1 \pm A^i), \tag{A.63}$$

where ϵ^i indicates fill dependence of N/L and we assume that ϵ^i is independent of the beam helicity state. Ideally, ϵ^i should be constant over all fills in the 2005 run and should be the product of the cross section, the detector acceptance, the trigger efficiency and so on. A^i denotes A_{LL} for N and may depend on the fill number. The beam polarization is abbreviated in this section. The fluctuation of the polarization can be finally ignored in this calculation as pointed out below. In this analysis, N is the number of the cluster pairs in the selected mass window. For example, when the signal window is selected, A^i is the combined asymmetry for π^0 (A^{π^0}) and the background under the π^0 peak (A^{BG}).

$$A^i = p^i A^{\pi^0} + (1-p^i)A^{BG}, \tag{A.64}$$

where p^i is the purity of π^0 for i-th fill. See Section 3.6.1 about this relationship. p^i can be expressed by the average purity (p^0) and the relative deviation from the average (α^i); $p^i = p^0(1+\alpha^i)$. Therefore, A^i is rewritten as

$$\begin{aligned} A^i &= p^0 A^{\pi^0} + (1-p^0)A^{BG} + (A^{\pi^0} - A^{BG})p^0\alpha^i \\ &\equiv A^0(1+\beta^i), \end{aligned} \tag{A.65}$$

where

$$A^0 \equiv p^0 A^{\pi^0} + (1-p^0)A^{BG} \quad \text{and} \quad \beta^i \equiv \frac{A^{\pi^0} - A^{BG}}{A^0}\alpha^i \tag{A.66}$$

From Figure3.32, the fluctuation of p^i can be evaluated and $p^0\alpha^i$ is estimated to be a few %. The second term is also expected to be the order of a few % and it is the second order in this calculation as shown below. In any case that the fluctuation of A^i is small, it is negligible. In this reason, the fill dependence of the beam polarization is also ignored in this calculation. The validity of this approximation can be evaluated by the bunch shuffle and the result is shown later.

Using Equation (A.63) and (A.65), A_{LL} is calculated after summing up N^i and L^i over all fills. Merged variables N^{merge} and L^{merge} are defined as

$$N_\pm^{merge} = \sum_i N_\pm^i = \sum_i L_\pm^i \epsilon^i (1 \pm A^i), \tag{A.67}$$

$$L_\pm^{merge} = \sum_i L_\pm^i. \tag{A.68}$$

Then, fill-merging A_{LL} (A^{merge}) is calculated as follows.

$$A^{merge} = \frac{\left(\frac{N_+^{merge}}{L_+^{merge}}\right) - \left(\frac{N_-^{merge}}{L_-^{merge}}\right)}{\left(\frac{N_+^{merge}}{L_+^{merge}}\right) + \left(\frac{N_-^{merge}}{L_-^{merge}}\right)} \tag{A.69}$$

$$= \frac{A^0 + \Delta + A^0\left(\frac{\epsilon_{\beta+}+\epsilon_{\beta-}}{\epsilon_+ + \epsilon_-}\right)}{1 + A^0\Delta + A^0\left(\frac{\epsilon_{\beta+}-\epsilon_{\beta-}}{\epsilon_+ + \epsilon_-}\right)}$$

$$\sim A_0 + \Delta, \tag{A.70}$$

where

$$\epsilon_\pm = \frac{\sum_i L_\pm^i \epsilon^i}{\sum_i L_\pm^i}, \qquad \epsilon_{\beta\pm} = \frac{\sum_i L_\pm^i \epsilon^i \beta^i}{\sum_i L_\pm^i}, \qquad \Delta = \frac{\epsilon_+ - \epsilon_-}{\epsilon_+ + \epsilon_-}. \tag{A.71}$$

Because $\Delta = 0$ with $L_+^i = L_-^i$ or constant ϵ^i over all fills, $\Delta \ll 1$ is assumed. Moreover, $\epsilon_{\beta\pm} \ll \epsilon_\pm$ is expected. This assumption is applied at the last step in Equation (A.70) and the only leading order is left. As described above, the term including β^i disappears in this approximation.

When A_{LL} is calculated fill by fill and then averaged over all fills, the result becomes A^0. The discrepancy between fill-merging A_{LL} and fill-by-fill A_{LL} is Δ, which originates in the fill dependence of $\epsilon^i \sim N^i/L^i$. In other words, A^{merge} fluctuates from the real asymmetry A^0 by Δ (when the fluctuation of ϵ^i is much small, the term with β^i becomes significant). Since ϵ^i can be written by N^i and L^i using Equation (A.63) as follows,

$$\epsilon^i = \frac{1}{2}\left(\frac{N_+^i}{L_+^i} + \frac{N_-^i}{L_-^i}\right), \tag{A.72}$$

the fluctuation of A^{merge} from A_0 (Δ) can be calculated using N^i and L^i, which is obtained by the data.

The uncertainty of A^{merge} comes from the statistical error of N^{merge} and the systematic error of Δ in this framework. The validity of this model is evaluated by the bunch shuffle. See Section 3.7.8 about the bunch shuffle. The distribution of A^{merge} by the bunch shuffle

is compared with the expectation of Equation (A.70). Figure A.31 displays the A^{merge} distribution for the signal window and 2.5 – 3.0 GeV/c in p_T using the ERT data sample. This distribution is normalized by the average beam polarization weighted by fill-by-fill integrated luminosity. The red Gaussian has a width of the statistical error of A^{merge}. The blue one is obtained by fitting the A^{merge} distribution. For the green one, the statistical error and the fluctuation of Δ by the bunch shuffle is quadratically summed and it is used as a width of the Gaussian curve. The narrower width of the red curve than the blue one indicates the existence of some systematic fluctuation over the statistics and the good agreement between the blue and green Gaussian proves that the systematic error is well explained by the fill-by-fill fluctuation of ϵ^i. In the bunch shuffle, the fluctuation of Δ itself is also obtained to be smaller than a few %, therefore, the assumption for the approximation at Equation (A.70) is confirmed.

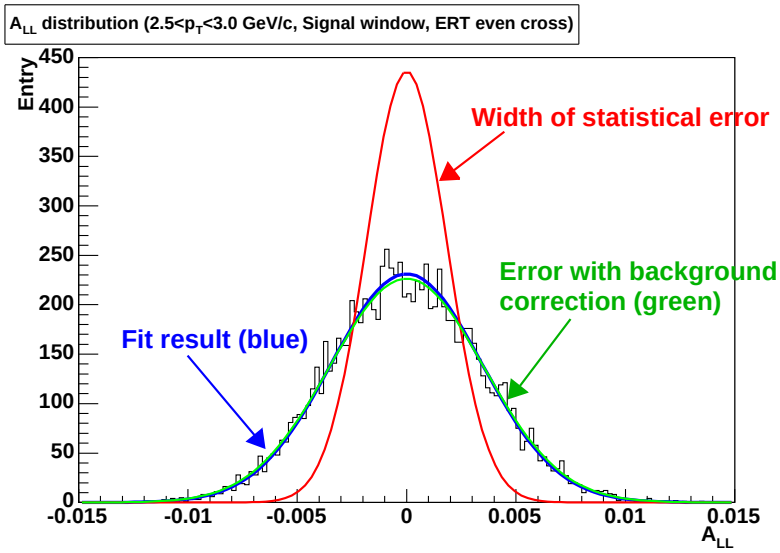

Figure A.31: The A^{merge} distribution by the bunch shuffle for the signal window and 2.5 – 3.0 GeV/c in p_T using the ERT data sample. Red Gaussian has a width of the statistical error of A^{merge}. Blue Gaussian is obtained by fitting the distribution. Green Gaussian has a width of the quadratic sum of the statistical error and the fluctuation of Δ defined Equation (A.70).

The ratio of the width between the red Gaussian and the blue Gaussian (the blue width divided by the red one) is displayed as blue points in Figure 3.46. In the low p_T region, the width of the A^{merge} distribution is much wider than the statistical error and it indicates that the fluctuation of the background level is larger than the statistical error. On the other hand, the width of the A^{merge} distribution is well represented by the statistical error in high p_T region, where the statistical uncertainty is larger than the systematic fluctuation. Similarly the ratio of the width between the green and blue Gaussian (the blue divided by the green) is displayed in Figure 3.46 as black points, which is almost 1 over all p_T range measured. This means that the width of the A^{merge} distribution is well represented by the statistical error and the systematic error from the fill-by-fill fluctuation of N^i/L^i. The results of the bunch shuffle prove that the uncertainty of A^{merge} is understandable by the framework described in this section.

In Figure 3.46, the results for A_{LL} calculated fill by fill is also displayed as red points. See

Section 3.7.8 about the bunch shuffle for the fill-by-fill calculated A_{LL}. These points represents the ratio of the width of the A_{LL} distribution by the bunch shuffle to the statistical error of A_{LL}. The points with the rate more than 1 in the high p_T region is caused by the too small statistics. This statement is confirmed by the bunch shuffle for the fill-merging A_{LL}, where the statistics is enough even in the high p_T bins by merging all of the statistics in the 2005 run. Moreover, while black points in Figure 3.46 is around 1 in any measured p_T bins and any data set, the red points for the MB sample have the values more than 1 in the low p_T region. This implies that the systematic error for the MB data evaluated by the bunch shuffle with fill-by-fill calculated A_{LL} originates in the fluctuation of ϵ^i in Equation (A.63).

At the last of this section, A_{LL} for the signal and background window are compared between A_{LL} calculated fill by fill and fill-merging A_{LL}. Figure A.31 displays A_{LL} as a function of p_T. The black and blue points are the results of A_{LL} with calculated fill by fill and A_{LL} calculated merging fill, respectively. The error bar for these points denotes the statistical error, while the error bar colored with red for fill-merging A_{LL} denotes the quadratic sum of the statistical error and the systematic error from Δ in Equation (A.70). The results from these two methods are consistent with each other in all p_T range measured considering the uncertainty from the fluctuation of the background level Δ.

A.15 Combining A_L for the blue and yellow beam polarization

Because both beams are polarized at RHIC, A_L can be extracted using either beam polarization and it is necessary to combine their results. The combined A_L can be calculated as usual as follows.

$$A_L = \frac{w_B A_{L,B} + w_Y A_{L,Y}}{w_B + w_Y}, \qquad w_{B(Y)} = \frac{1}{(\Delta A_{L,B(Y)}^{uncorr})^2} \tag{A.73}$$

$A_{L,B}$ and $A_{L,Y}$ is A_L extracted using blue and yellow beam polarization, respectively. $\Delta A_{L,B}^{uncorr}$ or $\Delta A_{L,B}^{uncorr}$ indicates the uncertainty of A_L which is uncorrelated between $A_{L,B}$ and $A_{L,Y}$. Though, in principle, ΔA^{uncorr} should includes both statistical and systematic uncertainties, systematic uncertainty is ignored in this thesis. The reason is because (1) currently the statistical uncertainty is dominant and the effect from the systematic one is small, and (2) the weight by the statistical and systematic uncertainty must be equal, but it is quite difficult to estimate systematic error as root-mean-square like statistical error.

A.15.1 Uncertainty from polarization

To consider the uncertainty of A_L from the beam polarization, Equation (A.73) is rewritten as

$$A_L = r_B \frac{\epsilon_B}{P_B} + r_Y \frac{\epsilon_Y}{P_Y}, \quad \text{where} \quad r_{B(Y)} = \frac{w_{B(Y)}}{w_B + w_Y} \quad \text{and} \quad A_{L,B(Y)} = \frac{\epsilon_{B(Y)}}{P_{B(Y)}}. \tag{A.74}$$

P_B and P_Y are the polarization of the blue and yellow beam, respectively. ϵ indicates raw asymmetry and does not include P. The uncertainty from the beam polarization is calculated as follows.

$$\Delta A_L|_{pol} = \left[r_B^2 A_{L,B}^2 \left(\frac{\Delta P_B}{P_B} \right)^2 + r_Y^2 A_{L,Y}^2 \left(\frac{\Delta P_Y}{P_Y} \right)^2 + 2 r_B r_Y A_{L,B} A_{L,Y} \frac{(\Delta P^{corr})^2}{P_B P_Y} \right]^{\frac{1}{2}} \tag{A.75}$$

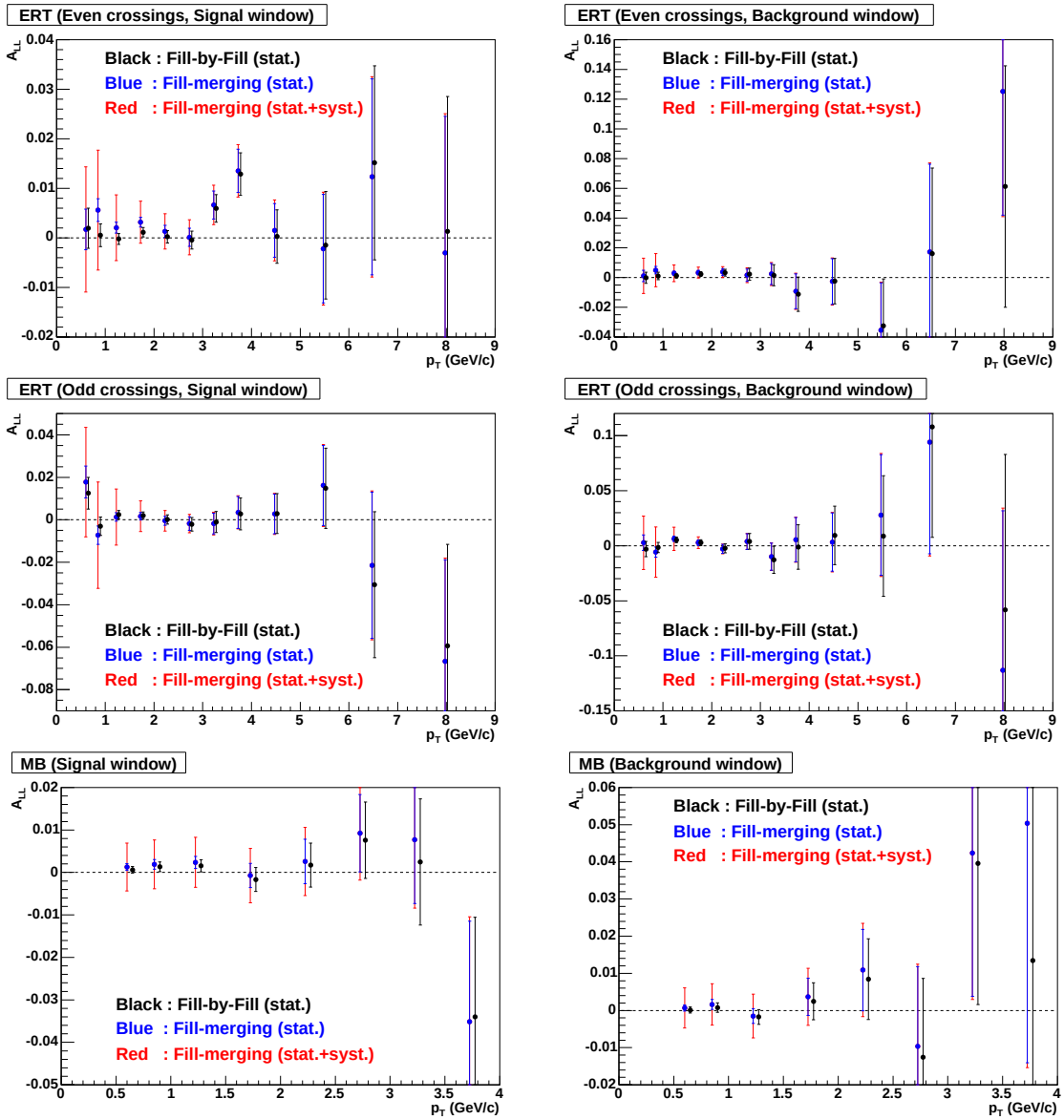

Figure A.32: A_{LL} as a function of p_T. The plots on the left side is for the signal window and the right is for the background window. The top, middle and bottom plots are obtained using the ERT even crossings, the ERT odd crossings and the MB sample, respectively. Black points are obtained by calculating A_{LL} fill by fill and then averaged over all fills in the 2005 run. Blue points are obtained by calculating A_{LL} after merging the yield and luminosity over all fills. Red error bars indicates the quadratic sum of the statistical error and the systematic error from the background fluctuation represented as Δ in Equation (A.70).

ΔP^{corr} denotes the correlated error between P_B and P_Y. For simplicity, we assume $A_L = A_{L,B} = A_{L,Y}$ and $r_B = r_Y = \frac{1}{2}$. Then $\Delta A_L|_{pol}$ can be approximated as;

$$\begin{aligned}\Delta A_L|_{pol} &\sim \frac{1}{2}A_L\left[\left(\frac{\Delta P_B}{P_B}\right)^2 + \left(\frac{\Delta P_Y}{P_Y}\right)^2 + 2\frac{(\Delta P^{corr})^2}{P_B P_Y}\right]^{\frac{1}{2}} \\ &= A_L\frac{\Delta(P_B P_Y)}{2P_B P_Y}. \end{aligned} \tag{A.76}$$

Therefore, the uncertainty from the beam polarization behaves as the scale error for combined A_L.

A.15.2 Uncertainty from relative luminosity

The relative luminosity in the calculation of $A_{L,B}$ (R_B) is not same as that of $A_{L,Y}$ (R_Y). However, R_B and R_Y are calculated from the same source and their uncertainties are approximately fully correlated. R_B and its error are evaluated as

$$R_B = \frac{L_{++} + L_{+-}}{L_{-+} + L_{--}} \tag{A.77}$$

$$\begin{aligned}\frac{\Delta R_B}{R_B} &= \left[\frac{(\Delta L_{++})^2 + (\Delta L_{+-})^2}{(L_{++} + L_{+-})^2} + \frac{(\Delta L_{-+})^2 + (\Delta L_{--})^2}{(L_{-+} + L_{--})^2}\right]^{\frac{1}{2}} \\ &\sim \frac{4}{L^2}\sqrt{(\Delta L_{++})^2 + (\Delta L_{+-})^2 + (\Delta L_{-+})^2 + (\Delta L_{--})^2}. \end{aligned} \tag{A.78}$$

$L_{h_B h_Y}$ indicates spin-dependent integrated luminosity and h_B (h_Y) is the helicity state of the blue (yellow) beam. In the approximation, $L_{++} = L_{+-} = L_{-+} = L_{--} = \frac{1}{4}L$ is applied. In the same way, R_Y and its error are obtained to be

$$R_Y = \frac{L_{++} + L_{-+}}{L_{+-} + L_{--}} \tag{A.79}$$

$$\begin{aligned}\frac{\Delta R_Y}{R_Y} &= \left[\frac{(\Delta L_{++})^2 + (\Delta L_{-+})^2}{(L_{++} + L_{-+})^2} + \frac{(\Delta L_{+-})^2 + (\Delta L_{--})^2}{(L_{+-} + L_{--})^2}\right]^{\frac{1}{2}} \\ &\sim \frac{4}{L^2}\sqrt{(\Delta L_{++})^2 + (\Delta L_{+-})^2 + (\Delta L_{-+})^2 + (\Delta L_{--})^2}. \end{aligned} \tag{A.80}$$

Hence, R_B and R_Y are fully correlated.

In terms of the uncertainty of A_L combined from $A_{L,B}$ and $A_{L,Y}$, from Equation (3.11), the uncertainties of the raw asymmetries from the relative luminosity,

$$\Delta\epsilon_B|_{R.L.} = \frac{1}{2}\left(\frac{\Delta R_B}{R_B}\right) \quad \text{and} \quad \Delta\epsilon_Y|_{R.L.} = \frac{1}{2}\left(\frac{\Delta R_Y}{R_Y}\right), \tag{A.81}$$

are fully correlated. The uncertainty of the combined A_L is calculated from Equation (A.74) as follows.

$$\begin{aligned}\Delta A_L &= \left[\frac{1}{4}\left(\frac{r_B}{P_B}\right)^2\left(\frac{\Delta R_B}{R_B}\right) + \frac{1}{4}\left(\frac{r_Y}{P_Y}\right)^2\left(\frac{\Delta R_Y}{R_Y}\right) + \frac{1}{2}\left(\frac{r_B}{P_B}\right)\left(\frac{r_Y}{P_Y}\right)\frac{(\Delta R^{corr})^2}{R_B R_Y}\right]^{\frac{1}{2}} \\ &\sim \frac{1}{4}\left[\frac{1}{P_B} + \frac{1}{P_Y}\right]\left(\frac{\Delta R}{R}\right). \end{aligned} \tag{A.82}$$

ΔR^{corr} indicates the correlation term between R_B and R_Y. Based on the discussion above, $\frac{\Delta R_B}{R_B} = \frac{\Delta R_Y}{R_Y} = \frac{\Delta R^{corr}}{\sqrt{R_B R_Y}} \equiv \frac{\Delta R}{R}$ is used in the calculation. In addition, the approximation of $r_B = r_Y = \frac{1}{2}$ is adopted.

A.16 Summary of the systematic error for A_{TT} and A_L

The systematic uncertainties from each source are tabulated for A_{TT} and A_L in this section. The label in the table indicates the source of the error, which is listed in Section 3.7.9. See Section 3.3 about the error from the beam polarization.

p_T (GeV/c)	C	D	E	F	G	H	I	total
				(10^{-5})				(10^{-5})
0.5 – 0.75	408	108	81	11	28	3258	0	3286
0.75 – 1.0	408	108	13	47	27	425	0	602
1.0 – 1.5	408	108	6	82	26	0	0	431
1.5 – 2.0	408	108	6	129	692	0	0	821
2.0 – 2.5	408	108	11	176	1188	0	0	1273
2.5 – 3.0	408	108	18	224	4325	0	0	4351
3.0 – 3.5	408	108	29	273	1589	0	0	1667
3.5 – 4.0	408	108	44	322	4759	4262	0	6411

Table A.3: The summary of the systematic errors for π^0 A_{TT} with MB sample. The unit for the numbers is 10^{-5}. The quadratic sum of the systematic errors is put in the last column as the total systematic error. The scale uncertainty from the beam polarization of 10.7 % is not included in the table.

p_T (GeV/c)	C	D	E	F	G	H	I	total
				(10^{-5})				(10^{-5})
0.5 – 0.75	395	108	54	28	2128	0	0	2168
0.75 – 1.0	395	108	2	57	488	0	0	640
1.0 – 1.5	395	108	5	98	24	671	0	793
1.5 – 2.0	395	108	2	144	23	0	0	435
2.0 – 2.5	395	108	1	188	11	0	0	451
2.5 – 3.0	395	108	1	232	9	567	0	737
3.0 – 3.5	395	108	2	277	58	0	0	498
3.5 – 4.0	395	108	3	325	15	0	0	523
4.0 – 5.0	395	108	7	391	46	0	0	568
5.0 – 6.0	395	108	15	495	178	1726	0	1850
6.0 – 7.0	395	108	27	600	111	5211	0	5263
7.0 – 9.0	395	108	74	739	27	0	0	849

Table A.4: The summary of the systematic errors for π^0 A_{TT} with ERT sample. The unit for the numbers is 10^{-5}. The quadratic sum of the systematic errors is put in the last column as the total systematic error. The scale uncertainty from the beam polarization of 10.7 % is not included in the table.

p_T (GeV/c)	B	C	D	E	F	G	H	I	total
					(10^{-5})				(10^{-5})
0.5 – 0.75	1	20	5	4	1	6	49	66	85
0.75 – 1.0	0	20	5	1	2	2	0	41	46
1.0 – 1.5	0	20	5	0	4	0	0	23	31
1.5 – 2.0	1	20	5	0	6	2	0	10	24
2.0 – 2.5	1	20	5	0	9	0	125	0	127
2.5 – 3.0	1	20	5	0	11	3	0	0	24
3.0 – 3.5	7	20	5	0	13	26	40	0	54
3.5 – 4.0	11	20	5	0	16	23	0	0	36

Table A.5: The summary of the systematic errors for π^0 A_L with MB sample. The unit for the numbers is 10^{-5}. The quadratic sum of the systematic errors is put in the last column as the total systematic error. The scale uncertainty from the beam polarization of 4.7 % is not included in the table.

p_T (GeV/c)	B	C	D	E	F	G	H	I	total
					(10^{-5})				(10^{-5})
0.5 – 0.75	2	19	5	1	1	12	0	0	23
0.75 – 1.0	2	19	5	0	3	12	0	0	23
1.0 – 1.5	0	19	5	0	5	1	0	0	20
1.5 – 2.0	0	19	5	0	7	0	14	0	25
2.0 – 2.5	1	19	5	0	9	0	0	0	22
2.5 – 3.0	0	19	5	0	11	0	0	0	23
3.0 – 3.5	0	19	5	0	14	0	23	0	33
3.5 – 4.0	0	19	5	0	16	1	0	0	25
4.0 – 5.0	2	19	5	0	19	1	82	0	86
5.0 – 6.0	1	19	5	0	24	6	48	0	57
6.0 – 7.0	4	19	5	0	29	52	0	0	63
7.0 – 9.0	0	19	5	1	36	19	0	0	45

Table A.6: The summary of the systematic errors for π^0 A_L with ERT sample. The unit for the numbers is 10^{-5}. The quadratic sum of the systematic errors is put in the last column as the total systematic error. The scale uncertainty from the beam polarization of 4.7 % is not included in the table.